acta physica slovaca vol. 57 No. 6, 911 – 1074 **December 2007**

ADVANCED NANOMETER-SIZE STRUCTURES

Eva Majkova[a,1] , Matej Jergel[a], Masaki Yamamoto[b], Toshihide Tsuru[b], Stefan Luby[a], Peter Siffalovic[a]

[a] *Institute of Physics, Slovak Academy of Sciences, 845 11 Bratislava, Slovakia*
[b] *IMRAM, Tohoku University, 2-1-1 Katahira, Sendai 980-8577, Japan*

Received 10 March 2008, accepted 17 March 2008

Solid state physics made a considerable progress towards nanometer- and subnanometer-size structures during the last decade. The structures encompass ultra thin films, multilayers, tubes, pillars, particles, clusters, etc. In this work, we address some of them. In particular, multilayers and spin valves with nm and sub-nm thickness of individual layers and ordered monolayers of nanoparticles are discussed in detail. These structures are at the forefront of further progress in the soft X-ray and extreme ultraviolet optics, spintronics and the whole emerging nanotechnology era. Attention is paid to the design, layer growth control with picometer resolution, interface phenomena and interlayer formation which is also responsible for thermal stability of both multilayers and spin valves. Interfaces are characterized by a full set of parameters including various types of roughness, its lateral and vertical correlations and fractal dimension. For the analyses of interfaces, X-ray diffraction, X-ray reflectivity and diffuse scattering have been elaborated in detail. The results are completed by local methods, like electron and atomic probe microscopies. Layered structures are studied in view of their applications in X-ray and extreme ultraviolet mirrors, giant magnetoresistance and spintronics devices. Development of novel nanosized structures with embedded arrays of magnetic nanoparticles is a challenging task nowadays. Magnetic nanoparticles offer a possibility of quantized electron tunneling and additional spin blockade. An ordered array of such nanoparticles can be used as natural double tunnel barrier of novel tunnel magnetoresistance devices. The Co, Fe_3O_4, $CoFe_2O_4$ magnetic nanoparticles prepared in colloidal solutions are of main interest for us. The process of spontaneous nanoparticle self-assembly leads to well correlated nanoparticle arrays. Such bottom-up approach presents a fast and cost-effective way of fabrication of nanoparticle monolayers. It will be shown that the grazing incidence small-angle X-ray scattering is a powerful technique for characterization of nanoparticle arrays, allowing *in-situ* studies of the ordering process. In particular, it can resolve the problem whether the arrays are formed on the substrate surface or on the surface of the drop of the colloidal solution. We hope that tutorial style of our presentation with insight into basic theories and experimental approaches completed by simulations will result in a useful introduction into some areas of the nanometer world.

PACS: 61.10.Eq, 61.46.Df, 72.25.-b, 75.75.+a, 81.15.-z, 81.16.-c, 85.75.-d

KEYWORDS: Multilayers, Interfaces, Magnetic nanoparticles, X-EUV optics, GMR, Spin valves, Nanoparticle self-assembly, X-ray reflectometry, GISAXS

[1]E-mail address: majkova@savba.sk

Contents

List of basic symbols and abbreviations

Symbols

d_{A}, d_{B}, d_{m} [nm]	thickness of the respective layers in multilayer
d [nm]	thickness of multilayer period, spacing, bilayer thickness
e [As]	electron charge, 1.602×10^{-19} As
f [Hz, s^{-1}]	frequency
h	Hurst or fractal parameter
h [Js]	Planck constant, 6.624×10^{-34} Js
$\mathrm{k_B}$ [J/K]	Boltzmann constant, 1.38×10^{-23} J/K
m	diffraction order, number of the respective layer in multilayer
n	index of refraction
p [Pa]	pressure
$\vec{q}$ [nm^{-1}]	wave vector transfer, scattering vector
q_{x}, q_{y}, q_{z} [nm^{-1}]	components of the scattering vector
$\vec{r}$ [nm]	position vector
x, y, z [nm]	components of the position vector
r	Fresnel reflection coefficient
t	Fresnel transmission coefficient
t [s]	time
C	correlation function
D [cm^2/s]	diffusion coefficient
D	topological dimensionality (D = 0, 1, 2, 3)
D^f	fractal dimensionality ($D^f = 3 - h$)
DWF	Debye-Waller factor
E [eV]	energy
F [J/cm^2]	laser fluence
H [Am^{-1}]	magnetic field
I [A]	electric current
L_{vert} [nm]	vertical correlation length of roughness
M [T]	magnetization
N	number of layers, periods, pulses, etc.
N_{at} [cm^{-3}]	atomic density
NCF	Nevot-Croce factor
ΔQ [J/g.at]	heat of mixing
R, R_o	reflectivity (reflectance), reflectivity from an ideal surface (interface)
T [K]	temperature
λ [nm]	wavelength of radiation
ξ [nm]	lateral correlation length of roughness
ρ [g/cm^3]	density
σ, σ_N [nm]	interface roughness, substrate surface roughness
σ_{eff} [nm]	effective interface roughness (interface width)
ϕ [°]	angle of incidence of radiation with respect to the surface normal
θ [°]	angle of incidence of radiation with respect to the surface
θ_c [°]	critical angle
Δ	ellipsometric parameter
ψ	ellipsometric parameter

Abbreviations

bcc	body-centered cubic
fcc	face-centered cubic
e-beam evaporation	electron beam evaporation
hcp	hexagonal close-packed
rms	root mean square
AES	Auger electron spectroscopy
AFM	atomic force microscopy
ALE	atomic layer epitaxy
BA	Born approximation
BL	maxima Bragg-like maxima
CIMS	current induced magnetization switching
CIP	current-in-plane (configuration)
CPP	current-perpendicular-to-plane (configuration)
CVD	chemical vapour deposition
DECR	distributed electron cyclotron resonance
DWBA	distorted-wave Born approximation
ED	electron diffraction
EDX	energy-dispersive X-ray spectroscopy
EUV	extreme ultraviolet region of radiation
EUVL	extreme ultraviolet lithography
EW	Edwards-Wilkinson equation
FEG	field emission gun
FM	ferromagnetic metal
FWHM	full width at half-maximum of a peak
GISAXS	grazing-incidence small-angle X-ray scattering
GI XRD	grazing incidence XRD
GMR	giant magnetoresistance
HS	heated substrate
IBP, IBS	ion beam polishing, sputtering
KPZ	Kardar-Parisi-Zhang model
ML, MLs	multilayer, multilayers
NM	non-ferromagnetic metal
PLA, PLD	pulsed laser ablation, deposition
PSD	power spectral density (function)
PVD	physical vapour deposition
RM	refractory metal
RBS	Rutherford backscattering spectroscopy
RSM	reciprocal space map
RT	room temperature
RTA	rapid thermal annealing
SEM	scanning electron microscopy
SIMS	secondary ion mass spectrometry
STM	scanning tunneling microscopy
SV	spin valve
TEM, CS TEM	transmission electron microscopy, cross-sectional TEM
TER	total external reflection
TMR	tunnel magnetoresistance
UHV	ultrahigh vacuum
X-EUV	X-ray – ultraviolet region of radiation
XFA	X-ray fluorescence analysis
XPS/ESCA	X-ray photoelectron spectroscopy/electron spectroscopy for chemical analysis
XRD	X-ray diffraction
XRIDS	X-ray interface diffuse scattering
XRR	X-ray reflectivity

1 Introduction

Advanced nanometer-size thin film structures with characteristic dimensions in the nm range have found wide interest both in research and applications. In this work, we pay attention to three types of such structures: multilayers for X-ray and extreme ultraviolet (X-EUV) optics [DUM40], magnetic multilayers (MLs) and spin valve (SV) structures with giant magnetoresistance (GMR) effect [BAI88, BIN89], and magnetic nanoparticles assemblies [CAO].

The main motivation for the expanding research of multilayers is the possibility to combine various materials and layer thicknesses in wide range of scales - from tenths of nm to several hundreds of nm – and thus to create structures with new physical properties. We discuss here only thin layer systems with the individual layer thicknesses in a multilayer stack below 10 nm.

The most important application fields of metallic multilayers are:

a) multilayer mirrors (Bragg reflectors) as elements for EUV and soft X-ray optics,

b) magnetic multilayers and spin valves for recording/reading systems of magnetic information storage media and various sensors.

In addition to X-EUV optics and GMR applications, we should mention a solid state amorphization reaction observed for the first time in metal/metalloid multilayers [SCHW83] as another ML application field.

Using the multilayer technology, it is possible to affect the anisotropy of layered structures in a particular way. For example, in superconductor/non-superconductor multilayers or in metal/insulator multilayers, the degree of anisotropy can be easily affected by changing the non-superconductor or insulator layer thickness [RUG85].

There are also other areas where the multilayer structures bring new interesting results, e.g. in multilayer coatings with good mechanical properties [TSA86].

In spite of the fact that different physical phenomena are exploited in X-EUV and magnetic multilayers, interfaces critically determine their properties and applications in both of them, though in different ways. The role of interfaces increases when the layer thicknesses scale down to few nm or even less. The quantitative characterization of interfaces is important for a deeper understanding of the interplay between structure and properties of layered systems and also for further improvement of particular structures and devices. Interface morphology is determined by various processes and parameters. The most important of them are type of deposition technique, deposition temperature and material combinations, discussed in the following sections.

With decreasing size of characteristic dimensions of thin film structures (first of all the layer thickness), new or modified analytical techniques for interfaces studies with resolution in 0.1 nm range or below are developed. Here both direct and reciprocal space analytical methods applied for interface studies are introduced.

Nanostructuring, i.e. fabrication of layered structures with lateral dimensions of several hundreds of nm or less launched intense research activity, especially in the field of magnetic nanostructures. Analogically to the development in semiconductor microelectronics, mostly top-down approach was used for the nanostructuring of layered structures so far. Typical lithographic techniques accessible in research laboratories usually do not allow resolution below 100 nm over large areas and this is often not sufficient. New phenomena have been observed in magnetic

thin film structures with the lateral size well below 100 nm [STO]. Therefore, new progress was achieved by nanoparticle synthesis and a shift from magnetic layered nanostructures to magnetic nanoparticles (bottom-up approach) with the size in 10 nm range [SCHM]. The preparation and properties of magnetic nanoparticles and their tendency to form ordered $2D$ arrays is included into this paper as well.

2 Basic principles and applications of X-EUV mirrors

2.1 Principles

Multilayers are artificially produced structures consisting of periodically alternating layers of two or more materials without any closer specification of the crystalline structure of the individual layers. When a multilayer consists of single crystalline layers and the atomic planes are coherently stacked, it is customary to label the structure as a superlattice. The periodic modulation of chemical composition along the direction perpendicular to the layers plane is a significant property of such systems and in the early stage of multilayer research they were also named compositionally modulated structures [MCW]. Nowadays besides layered systems of strict periodicity (e.g. multilayer interference mirrors), also non-periodic multilayers are developed. In this paper only few examples of non-periodic multilayer structures will be given. Absence of periodicity in layered structures is more frequent for magnetic structures. A typical example is spin valve as it will be discussed in Sec. 4. In addition to simple periodic structures of A/B type, also more sophisticated systems were reported [LEV89, MIK95, MAT06] where the layers alternate according to a deterministic rule (e.g. Fibonacci rule). However, these structures are beyond the scope of this work.

The artificial periodicity is a decisive property of most multilayers. Generally, it enables us to observe phenomena which are weak (e.g. interface phenomena) or which do not exist in structures with low number of interfaces or in non-periodic systems (e.g. constructive interference of the radiation diffracted at interfaces). This is the reason why also other types of multilayers are often prepared and studied. On the other hand, especially the X-EUV multilayers have initiated an extensive research of interface phenomena both in theory and experiments.

Soft X-ray multilayer mirror is considered as the most attractive optical element developed during the last two decades of the past century [YAM92]. This mirror, called also Bragg mirror, opened a lot of new applications of soft X-rays and EUV radiation in various analytical and technology equipments. The authors have published recently an extensive review on X-EUV interference mirrors [MAJ08].

In the visible light optics, two basic optical elements - lenses and mirrors - are used to process the light beam. For lenses it is necessary to use transparent material with index of refraction n larger than 1. Such materials could be found in the nature and have been used for several centuries. In a classical mirror, the light is absorbed in the near-surface region $\approx 1/\lambda$. Usually metals fulfil this condition.

In the X-EUV wavelength range, the refractive index of common materials is lower than 1, $n = 1 - \delta - \mathrm{i}\beta$. Here, the real decrement δ represents scattering and the imaginary part β represents absorption. The behaviour of refractive index in the X-ray region is given as

$$\begin{aligned} \delta &= (\mathrm{r_o}/2\pi)\lambda^2 N_{at} f_1, \\ \beta &= (\mathrm{r_o}/2\pi)\lambda^2 N_{at} f_2. \end{aligned} \tag{2.1.1}$$

Here, $\mathrm{r_o} = 2.82 \times 10^{-13}$ cm is the classical electron radius, λ stays for wavelength, N_{at} is the atomic density in the film, f_1, f_2 are real and imaginary parts of atomic scattering factor ($f = f_1 + \mathrm{i}f_2$). As follows from Eq. (2.1.1), δ, β decrease quadratically with decreasing wavelength [JAM].

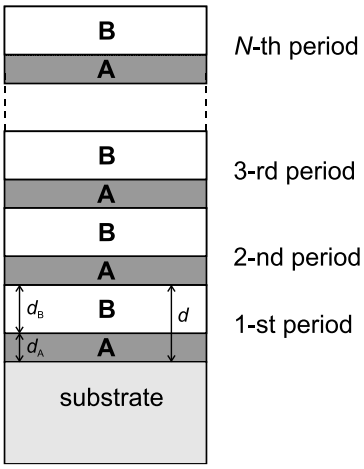

Fig. 2.1.1. Scheme of A/B multilayer with the period $d = d_{\mathrm{A}} + d_{\mathrm{B}}$. The d_{A} and d_{B} are the thicknesses of layers A and B, respectively, N is the number of periods.

Using the Fresnel equations (derived from the Maxwell equations), the amplitude r of the X-ray beam at normal incidence reflected at the interface of materials with optical indices n_1 and n_2 is given as

$$r = \frac{n_1 - n_2}{n_1 + n_2} \approx \frac{\delta_2 - \delta_1}{2}. \tag{2.1.2}$$

For all available material combinations, the difference $(\delta_2 - \delta_1)$ is extremely small in X-EUV region. Therefore, high normal incidence reflectivity cannot be obtained at a single boundary between any two materials. Considering the above mentioned facts, classical lenses and mirrors cannot be used. Another principle should be used to process the beam: either total external reflection discovered by Compton [COM23] or the interference principle (Fresnel optics) [SPI72].

The phenomenon of total external reflection (TER) has been used in optical elements for the X-EUV region. Considering that $n < 1$, the radiation is totally reflected (reflectivity $\cong 1$) for the angle of incidence $\theta < \theta_c$ where θc is a critical angle. For $\theta > \theta_c$, the radiation penetrates into the material and the reflectivity decreases as $\sin^{-4}\theta$. The value of θ_c depends on the wavelength λ of the beam $(\theta_c \approx \sqrt{2\delta})$ outside the regions close to the K, L, and M absorption edges. For hard X-rays, θ_c is of a few tenths of degree, for soft X-rays it does not exceed 30° as a rule. Consequently, optical elements utilizing the TER phenomenon work in the region of grazing incidence. The beam can be only deflected. The mirrors and size of the whole equipment are large. When more TER mirrors are used, the random phase relation exists between the waves reflected from different mirrors [SPI].

Multilayer interference mirrors are thin film stacks composed of two materials with alternately high and low scattering power (electron density) [ATT]. The number of periods (bilayers, repetitions, spacing) is from tens to hundreds. The period thickness $d = d_{\mathrm{A}} + d_{\mathrm{B}}$ where d_{A} and d_{B} stay for thickness of the respective layers. Sometimes sequences of three or four different materials can be used in the stack. In a simple multilayer (Fig. 2.1.1) the stack is periodic along

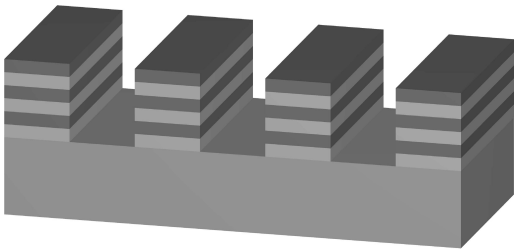

Fig. 2.1.2. Scheme of laterally modulated multilayer.

z axis whereas there is no periodicity along the x and y directions. Therefore, these multilayers are sometimes called 1-dimensional $(1D)$ crystals, independently of the structure of their individual layers which could be even amorphous. It is possible to create an additional artificial periodic structure in x or y direction, too. This is the case of laterally modulated (nanostructured) multilayers (Fig. 2.1.2).

The idea that multilayers can act as inference mirrors reflecting X-EUV radiation at normal incidence was suggested almost a century ago. The first Au/Cu mirror reflecting at the wavelength $\lambda \approx 7$ nm was prepared by DuMond and Youtz in 1940 [DUM40]. The structure was designed as dispersion element of soft X-rays. The quality of the structure (period accuracy) was not sufficient but the compositional modulation was observed by X-ray diffraction. The structure was not stable due to the interdiffusion between Au and Cu. The authors analyzed the diffusion process and they established the basis for studies of diffusion effects in compositionally modulated materials. In this way it was possible to determine much lower diffusivities than by any other technique. Since this pioneering work, the diffusion studies in compositionally modulated films became a subject of wide interest. Up to now the X-ray diffraction method for determining the interdiffusivity in compositionally modulated films enables to detect subtle profile changes involving atomic jumps of one per hundred atoms [GRE85, GRE88].

In 1970 Esaki and Tsu [ESA70] prepared the first semiconductor multilayers and a new complex program of multilayer structures for electronic and optoelectronic devices was launched. At that time, real development of X-EUV multilayer mirrors, based on deposition techniques providing good quality and high accuracy (± 0.1 – 0.3 nm) of layering, started.

The interfaces in a multilayer are an analogy of the atomic planes in a crystal. Diffraction on such a structure obeys the Bragg equation modified for refraction [ALS]

$$m\lambda = 2d\sqrt{n^2 - \cos^2\theta}, \tag{2.1.3}$$

where m is the diffraction order and θ is the angle of incidence of radiation. Only the first few peaks have the intensity appropriate for practical application [ATT]. For $\theta = 90^\circ$ the multilayer period $d = \lambda/2$. The $\theta = 90^\circ$ corresponds to normal incidence mirrors which are of the highest importance. However, θ only approaches to 90° in practical applications. Therefore, d is slightly higher than $\lambda/2$.

The X-EUV interference mirror spectral region shown in Fig. 2.1.3 is approximately defined as 40 – 0.2 nm (25 eV – 6 keV). EUV range covers 40 – 10 nm. From 10 to 1 nm, there is soft-X ray region. Under 1 nm, hard X-rays may be reflected by interference mirrors in grazing

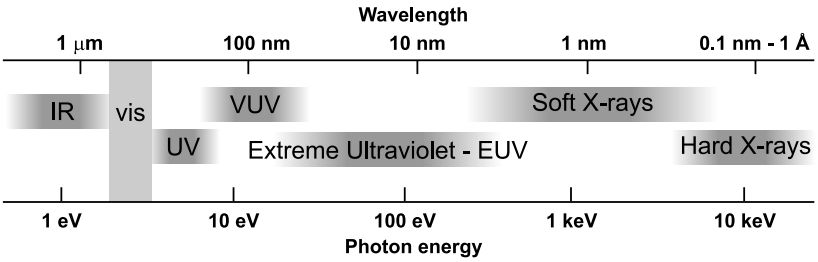

Fig. 2.1.3. The spectrum of electromagnetic radiation.

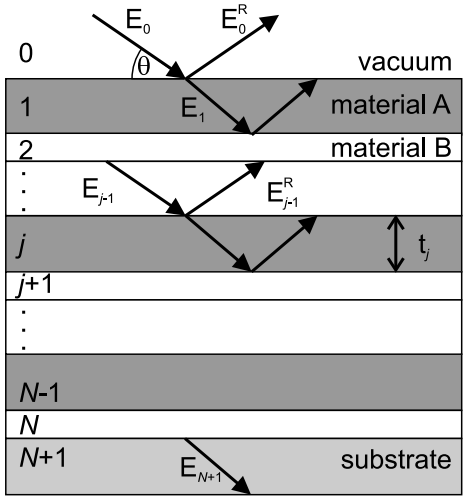

Fig. 2.1.4. Propagation of X-ray radiation in a multilayer.

incidence regime [ATT] or by single crystals at higher angles of incidence.

Assuming the given wavelengths, the thickness of mirror layers ranges from several nm to few atomic planes. Typical multilayer mirror consists from thirty up to several hundreds of periods. At each transition from one material to another one, a partial reflection of the incoming radiation appears. Although the reflectivity from each interface is small, a constructive interference occurs when the thickness of layers is properly designed and all partial reflections add together (Fig. 2.1.4). To achieve the reflectance near the theoretical value, the thickness errors must be minimized and compositionally sharp and atomically smooth interfaces are required. Roughness and intermixing suppress the reflectivity of a mirror. At shorter wavelengths, they should be as low as a few tenths of nm.

In the literature it is often simply stated that one should use a combination of high- and low atomic number materials, i.e. high and low absorbing layers. Spiller [SPI72] proposed that a multilayer composed of high Z (Z is the atomic number) and low Z materials with precise layer thicknesses can be used as an interference mirror in the soft X-ray and EUV ranges.W, Mo, Nb, Pt, Ru, Rh, Ni, Co, Fe, Tb, Gd, Cr are examples from the first group, C, Si, B, Al, Be, Sc,

Ti, B_4C, BN, SiC represent the second group [BHA06]. Absorber limits the number of periods which in turn limits the selectivity or bandwidth of the reflection peak. More exact criterion is that the material with the lowest possible absorption be selected first as a spacer material and then the second material – absorber - be selected with the largest possible reflection coefficient at the boundary with the first one [SPI94].

Modeling of the properties of the mirrors can be done using atomic or macroscopic approach. In the first one, each atom is considered to scatter or absorb the radiation, in the second one, the complex refractive index is attributed to each layer.

Unlike single layer- or bulk X-ray mirrors operating below critical angle θ_c (in the total reflection region), multilayer mirrors operate at near-normal incidence of the radiation and therefore, the optical systems are much smaller in comparison to the grazing incidence optics. Therefore, they open the way for diverse equipments applicable directly on laboratory tables [SAT55].

2.2 Applications

In the EUV wavelength region, ML mirrors are successfully utilized for various normal incidence imaging optics [ATT, KIN86, SPI94] such as microscope, telescope and a next generation lithography tool. Multilayer interference mirrors provide a well-defined bandpass with relatively high throughput. Besides mirrors and common antireflection coatings, optical elements with various spectral functions are developed (filters, beam splitters, polarizers, phase retarders). These elements are important in surface science instrumentation, astronomy, plasma diagnostics, X-ray fluorescence analysis (XFA), X-ray photoelectron spectroscopy/electron spectroscopy for chemical analysis (XPS/ESCA) equipments, synchrotron facilities, etc. These applications were developed especially in the 90-ies of the previous century (e.g. [BAR81, BAR85, BAR90, SEE93]). It should be noted that air is absorbing between 1 and 190 nm, therefore EUV and soft X-ray mirrors should work in vacuum. Grazing incidence multilayer mirrors are used as beam compressors, collimators and monochromators in laboratory diffractometers.

Important advantage of multilayer mirrors is that they can be fabricated on specially figured substrates. These applications for beam conditioning in X-ray diffractometry became very successful since the introduction of "Göbel" mirror [MIC00]. Being covered by multilayer with layer thickness gradient (laterally-graded), the mirror fulfills Bragg law for the wavelength of interest across the entire mirror length. Most important is the multilayer mirror curved into the form of parabola which allows the conversion of divergent beam into a parallel one [MIC00].

Potentially the most important application of multilayer mirrors is the extreme ultraviolet lithography (EUVL). Currently this technique, based on the reflection optics operating near 13.4 nm, is developed using Mo/Si multilayers. They achieve the reflectivity of $\approx 70\%$ in the case of interface engineered stacks [LAR02, CHA03]. This value is close to the theoretical limit of 74% at the given wavelength [SKU95, LAR02]. Mo/Be multilayer provides a higher theoretical reflectivity of 80% provides at 11.1 nm [SKU95]. However, beryllium is toxic. Further increase of Mo/Si mirror reflectivity is based on Mo/X/Si/X multilayers with interposed diffusion barriers X. An example is a multilayer with the Mo/B_4C/Si period [PAT04]. If interdiffusion is suppressed, the interfaces and the respective change in the refractive index are sharper. In the EUVL, up to ten mirrors are used including the lithography mask. Therefore, further increase of the reflectivity of Mo/Si is desirable. For example, an increase from 70 to 72% in the system with ten elements would correspond to the $(72/70)^8 = 32\%$ increase of the photon throughput.

This improvement is important because at the reflectivity of 70% and ten elements, the overall efficiency is only 3%.

Another important area of multilayer mirror applications is the soft X-ray microscopy of biological objects in the water window range between the K absorption edges of carbon at the photon energy of 283 eV and of oxygen at 523 eV [MAC] which corresponds to wavelengths from 4.4 to 2.4 nm, respectively. In this range, the water is transparent for radiation whereas the C containing organic or biological materials are absorbing. Using a soft X-ray microscope working in this wavelength range, it is possible to observe living cells *in vivo* in their natural environment [PAL]. The short period multilayer mirrors are a key factor for the development of laboratory microscopes independent of the synchrotron radiation source. Here, multilayers with Sc spacer (absorption edge at 3.11 nm) combined with Ni, Cu, Cr, Co, Fe, Mn or V are possible candidates.

Multilayer mirrors achieved a wide range of applications. They can be produced with high quality performance which will be further improved. In the field of non-periodic mirrors, depth-graded structures like broad-band multilayer mirrors important for astronomy and/or chirped MLs for reflection of soft X-ray attosecond pulses are developed [SPI94, ATT].

3 Design and *in-situ* fabrication control of X-EUV mirrors

3.1 Physical optics of multilayer mirrors

Extreme ultra-violet light having photon energy of approx. 100 eV is attenuated by material because of the interaction with the core electrons of atoms of the material. The light is absorbed by air within a few mm which requires technical means to avoid the absorption along the optical path. There is neither transparent material nor "reflector" in this wavelength range, even with metals having refractive indices close to unity. Therefore, as already mentioned, an X-ray multilayer utilizing constructive interference of the electro-magnetic waves is used for a mirror.

X-ray multilayer development for practical use was started by the forefront research by Spiller [SPI74]. He used the electron beam deposition combined with *in-situ* X-ray reflectometry for the thickness monitoring and period thickness control with sufficient accuracy. Spiller [SPI81, SPI88] described the theoretical background in his review on X-ray multilayers where he makes use of the absorption contrast based on a combination of light and heavy elements, unlike the high reflectance multilayer for visible region utilizing the contrast in refractive indices. As the materials pairs to be used, he concentrated on materials with high-melting points forming the smallest crystallites. Several pairs with C as the light element were used, e.g. combination of C(light)/W(heavy).

Barbee Jr., on the other hand, used magnetron sputtering method having high stability of the deposition rate and enabling the thickness control via the deposition time. With this method, he made a break-through for practical applications of Mo/Si multilayers showing reflectance above 60% at the wavelength of 13 nm [BAR85]. This allowed for the development of the Extreme-Ultraviolet Lithography (EUVL) technique started by Kinoshita et al. [KIN89].

The combination of Si/Mo does not fulfill the Spiller's criterion mentioned above since both materials have a low absorption and show low contrast. As it will be shown in the following sections, these elements fulfill the optical criteria for high reflectance X-ray multilayer mirror [YAM92] which are well described by the theory of the electro-magnetic waves used in the visible region with the accuracy sufficient for various practical applications [ATT].

X-ray multilayer mirror criteria for high reflectance

In comparison to the multilayers in the visible region, the X-ray multilayer has characteristics as follows:

a) much smaller (by two orders of magnitudes) period thickness, typically of 7 nm because of the short wavelength,

b) much larger number of periods from a few tens to several hundreds because of the smaller Fresnel reflection coefficients (by several orders of magnitude) at the surfaces and boundaries (interfaces),

c) no transparent material is available and the extinction coefficients k of the materials are of the order of 0.01 or less,

d) design principle for the mirror is a constructive interference with weakly absorbing materials which limits the maximum theoretical reflectance well below 100%,

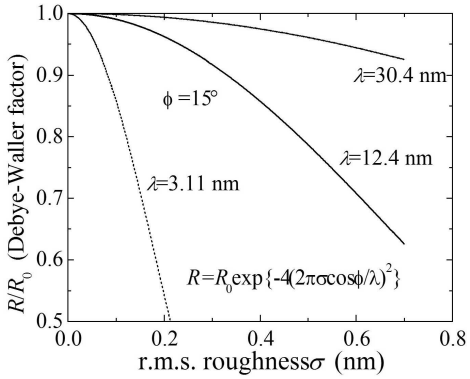

Fig. 3.1.1. Reflection loss factor by surface roughness σ at three wavelengths of soft X-rays.

e) short wavelength of light enhances scattering effects by the surface and interface roughness which are the dominant source of deterioration of the achievable reflectance.

For theoretical description of scattering losses by the roughness, the Debye-Waller factor, commonly used in the X-ray diffractometry, is used in the form of $DWF = \exp\left[-2\left(\frac{2\pi\sigma\cos\phi}{\lambda}\right)^2\right]$ where σ denotes the root mean square (rms) roughness of the surface. The Debye-Waller factor was introduced originally to describe the scattering effect by the lattice vibrations. The equation of the same form can be used to derive reflectivity attenuation by the rough surface where the surface topology has a Gaussian distribution within the surface area of coherence of the illuminating light [CAO94]. However, the *DWF* should be used as a qualitative measure of performance since the verification of its applicability by a quantitative analysis is still needed. For example, it has been known that the surface roughness should be evaluated with its spatial frequency for the explanation of the flare observed in the EUVL images. In fact, usually different roughness values are obtained from the measurements by the AFM, a visible light scatterometer, profiler, X-ray diffractometry at grazing incidence, and the soft X-ray reflectometry at normal incidence. In addition, the reflection loss by the scattering of the surface and interface roughness shows substantial differences depending on the coherence of the illuminating light [YAN96].

Common rms surface roughness of an optically super-polished substrate and the thin films fabricated on it are found in a range from 0.2 nm to 0.8 nm. Such a roughness σ gives a considerable effect on the loss of reflectance in the soft X-ray region as shown in Fig. 3.1.1. It can be seen that the reflectance reduction by the roughness dramatically increases as the wavelength decreases. At an angle of incidence of 15° with a wavelength $\lambda = 12.4$ nm (the photon energy is λ(nm)$/0.124 = 100$ eV), the roughness σ of the surface and interfaces should be smaller than 0.3 nm as can be seen in the figure. In fact, when the multilayer is fabricated for the use at $\lambda = 3.11$ nm in a so-called water window region, the scattering loss of the reflectance by the roughness reaches from 50 to 80% since it is not possible to reduce the roughness below 0.2 nm. Thus the compositionally abrupt and flat surface and interface formation is of primary importance

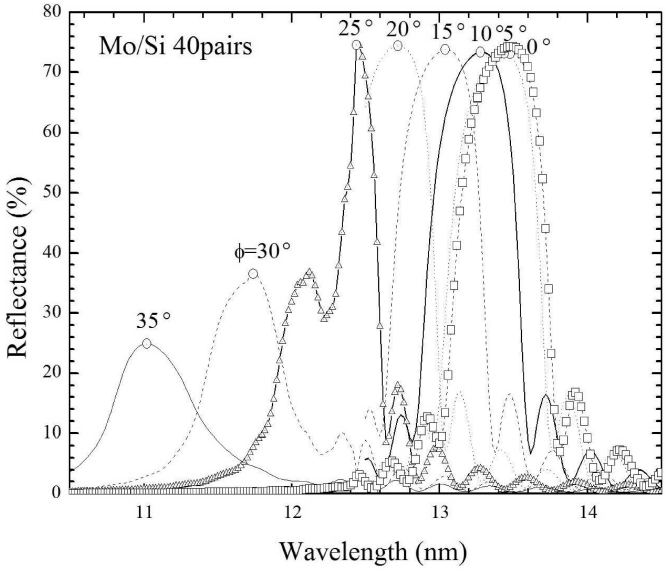

Fig. 3.1.2. Soft X-ray spectral reflectance of Mo/Si periodic multilayer (period 6.9 nm) calculated at various angles of incidence [YAM01].

in addition to the period thickness control. The highest reflectance multilayer mirror fabrication requires four items, namely: (1) a low absorption material pair, (2) the exact thickness, (3) layers with flat and smooth interfaces, and (4) super polished substrate.

Optical characteristics of multilayers

For fabrication of high performance X-ray multilayer mirrors, it is of primary importance to establish the methodology of smooth and flat multilayers by improving the fabrication conditions. However, prior to the detailed studies for improving interface smoothness and stability in the viewpoints of material science, optical simulations should be useful to know about the suitability of the material combination for the highest reflectance, the best thickness ratio within the multilayer period and the number of pairs needed for practical use. Such calculations can be done by using optical simulation codes for the visible region accepting weakly absorbing elements with external optical constant tables. Among optical simulation methods available, a layer-by-layer method [YAM92] is particularly useful for soft X-ray multilayer designing and simulation. By this method, the optimal thickness structure for a given pair of layer materials can be calculated to show the absolute theoretical maximum reflectance. Selection criteria of materials based on the optical constants or the Fresnel reflection coefficients can also be discussed easily. A typical example of Mo/Si multilayers will be taken to show the basic characteristics and design examples.

Figure 3.1.2 shows the theoretical spectral reflectance of a typical Mo/Si multilayer with the period thickness of 6.90 nm. For calculation, a periodic layered structure with a 2.76 nm thick

Mo layer and a 4.14 nm thick Si layer as a pair stacked to 40 periods on a Si substrate was assumed. Optical constants available at the web page of Lawrence Berkeley National Laboratory [CXRO] were used for Mo and Si. In Fig. 3.1.2, the reflectance spectra at various angles of incidence from 0° to 85° are shown with different marks. Reflectance above 70% is expected at the angles from 0° to 25°. The spectrum shows characteristics of a reflection filter with the full width half maximum FWHM $\Delta\lambda$ of 0.6 nm, which corresponds to the resolution $\lambda/\Delta\lambda$ of approx. 20. In general, the resolution increases as the number of periods but the absorption of the layers saturates the reflectance increase. Practical resolution with the effect of fabrication error causing period thickness variation would be from 10 to 50.

Fig. 3.1.2 also shows that the peak wavelength of the multilayer moves to shorter wavelength with the increase of the angle of incidence following the 1^{st} order Bragg equation of diffraction. Since the refractive index in the soft X-ray is close to unity, the peak wavelength λ_P may follow $2d\cos\phi = \lambda_P$ with d being the period thickness (6.90 nm in Fig. 3.1.2) and ϕ being the angle of incidence. At the normal incidence with $\phi = 0^\circ$, the peak wavelength is proportional to the period thickness as $\lambda_P \approx 2d$.

Peak reflectance, on the other hand, shows dependence on the interface roughness, the thickness ratio γ within the period, the total number of periods and the dispersion of the refractive index. As an example, the parameter γ defined as the ratio of the high absorption layer thickness to the multilayer period was taken as $\gamma = 0.4$ since the Mo layer has higher absorption. As shown in the spectrum for the angles of 25°, 30°, and 35°, the peak reflectance drops to a half as the interference peak crosses the absorption edge of Si $\mathrm{L_{II,III}}$ at the wavelength of 12.5 nm. This drop at the higher photon energy side indicates the large effect of the optical constant variation caused by the absorption increase.

Reflection increase and layer-by-layer method of calculation

For calculation of the X-ray multilayer mirror reflectance, the Fresnel equation in the visible region and the Bragg equation of the X-ray diffraction theory are used as equivalent methods. In the following, Fresnel equation is used to describe and discuss constructive interference of the light.

In the multilayer systems including X-ray range, the amplitude reflectance for p- and s-components can be written in the same form. Let us suppose we fabricate the multilayer up to the $(m-1)^{\mathrm{th}}$ layer as shown on the left-hand side of Fig. 3.1.3, and let the complex amplitude reflectance be R_{m-1}. By adding a layer of material with the complex refractive index $\tilde{n}_m = n_m - \mathrm{i}k_m$ as shown on the right-hand side of Fig. 3.1.3, the complex amplitude reflectance R_m and the complex amplitude transmittance T_m can be written with the Fresnel reflection coefficient r_m of the material surface to the vacuum as

$$R_m = \frac{r_m\left(1 - r_m R_{m-1}\right) + \left(R_{m-1} - r_m\right)\exp\left(-\mathrm{i}\delta_m\right)}{1 - r_m R_{m-1} + r_m\left(R_{m-1} - r_m\right)\exp\left(-\mathrm{i}\delta_m\right)}, \tag{3.1.1}$$

$$T_m = \frac{T_{m-1}\left(1 - r_m^2\right)\exp\left(-\mathrm{i}\delta_m/2\right)}{1 - r_m R_{m-1} + r_m\left(R_{m-1} - r_m\right)\exp\left(-\mathrm{i}\delta_m\right)}, \tag{3.1.2}$$

where

$$\delta_m = \left(4\pi/\lambda\right)\tilde{n}_m d_m \cos\phi_m \tag{3.1.3}$$

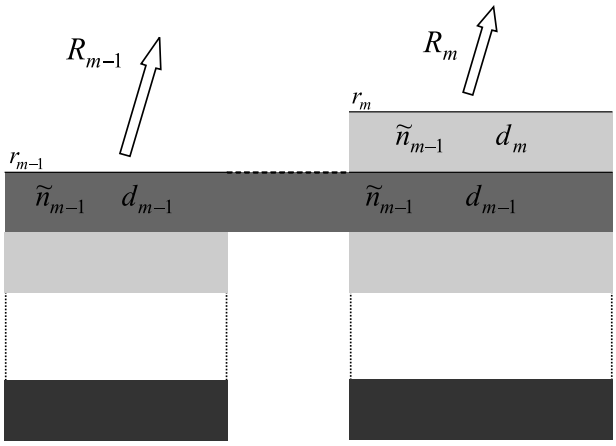

Fig. 3.1.3. Multilayer model for the layer-by-layer calculation.

is the phase delay by the return passage within the layer. Parameters λ, ϕ_m, d_m denote the wavelength of light, the complex angle of refraction to the layer, and the thickness of the layer, respectively.

The equation (3.1.1) represents complex amplitude reflectance R_m of the m-layer system by the complex amplitude reflectance R_{m-1} of the $(m-1)$-layer system before adding the m^{th} layer and the parameters determined solely by the m^{th} layer. It should be noted that in the ordinary calculation of optical thin films, the interface Fresnel reflection coefficient at the boundary r_{m-1} is used to represent the buried interface between $(m-1)^{\text{th}}$ and the m^{th} layer on the top. Exclusion of such interface parameters renders the above equations to be useful in the layer-by-layer designing when the material of the m^{th} layer on the top needs to be tested.

For $m = 0$, the thickness of the substrate is much larger than the wavelength of light and the substrate absorbs completely in the X-ray range. Then the equation above is simplified as $R_0 = r_0$ with $\exp(-\mathrm{i}\delta_0) = 0$. Recursive application of this equation from $m = 1$ to $m = m$ will result in the complex amplitude reflectance R_m for the m-layer system. The intensity reflectance can be calculated as $|R_m|^2$.

In the calculation process described above, the variation of R_m directly shows the complex amplitude variation during the multilayer fabrication. The amplitude and the phase can be seen directly. The same procedure for the amplitude transmission will give the variation during the multilayer fabrication from the substrate.

Complex plane representation

Fig. 3.1.4 shows an example of the complex plane plot of Mo/Si multilayer growth as observed by the growth curve of the complex amplitude reflectance. The calculation corresponds to a point at the wavelength of 13.5 nm on the curve in Fig. 3.1.2 with the angle of incidence of 10°. At this point outside the peak, the reflectance value is 48.5% since the peak wavelength is located at 13.2 nm. The complex refractive index (n-ik) for Si $(0.998994 - 0.001827\mathrm{i})$ and for Mo $(0.92377 - 0.006439\mathrm{i})$ are used for the calculation. The Fresnel reflection coefficient of Si

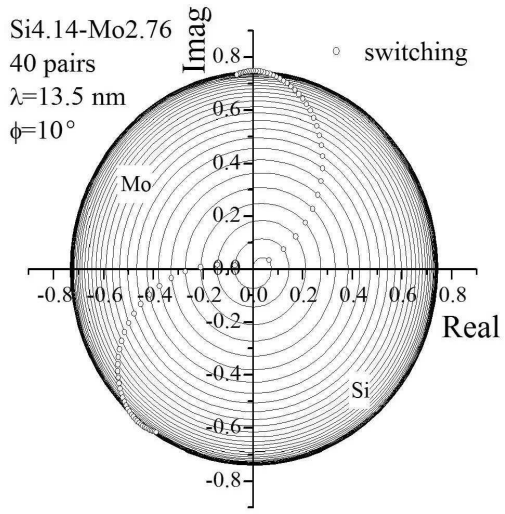

Fig. 3.1.4. Mo/Si multilayer growth as seen by the amplitude reflectance for 10° angle of incidence in Fig. 3.1.2.

coincides with the origin since the value is very close to zero. As the fabrication proceeds from Mo (2.76 nm), Si(4.14 nm), Mo(2.76 nm), and so on, the amplitude reflectance R_m spirals out by turning right and saturates radial expansion at $R_m = 0.8$. The Mo layers appear in the left-upper region in the figure, being shown by the material switching points (open circles) aligning on a curve in the complex plane. The reflectance varies as the fabrication proceeds as shown in Fig. 3.1.5 where the total thickness is taken as horizontal axis. On the upper horizontal axis, the number of period is shown. In this calculation with the condition of off-peak, the reflectance reaches the maximum at 200 nm total thickness and then decreases. A similar calculation with the condition of the reflectance peak shows also saturation in reflectance but fine oscillations remain.

Fine oscillations within 3% reflectance variation corresponding to the growth of one period, as expected by the off-centered circle movement of the amplitude reflectance variation, are plotted in Fig. 3.1.5. The fine structure is shown enlarged in the inset of the figure from the 36^{th} to the 40^{th} periods. It is shown that the local maximum in reflectance is observed at the switching from Mo to Si and then the reflectance decreases as the Si layer grows.

In general, for a given pair of layer 1 and layer 2, or more specifically for a given pair the complex refractive indices, the absolute maximum reflectance achievable by the pair and the corresponding structure thickness are given as a unique solution. The ideal thickness structure is aperiodic and is approaching to the periodic one as the number of pairs approaches or surpasses 10 [YAM92]. The resulting periodic structure coincides with that obtained by the standard designing of the ideal periodic multilayers for the maximum reflectance. It should be noted here, that for an exact discussion of the highest reflectance within a few % accuracy, the last layer thickness should be controlled separately. In the case of the extreme ultra-violet lithography (EUVL), where the gain of a few % has important consequences, the last layer should be opti-

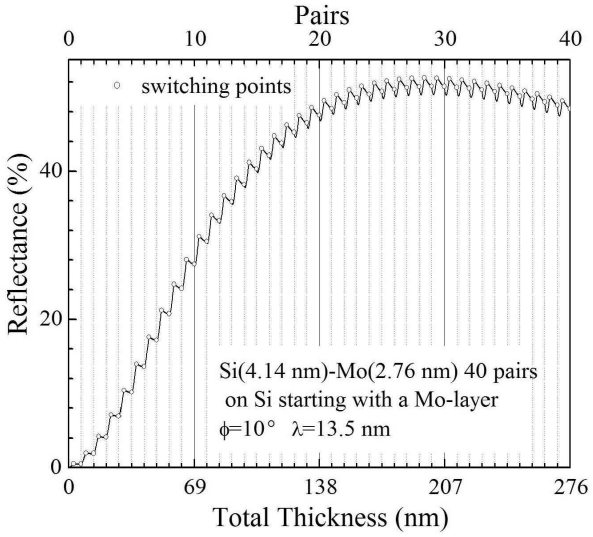

Fig. 3.1.5. Mo/Si multilayer growth as seen by the amplitude reflectance for 10° angle of incidence in Fig. 3.1.2.

mized to the next layer, i.e. hypothetical vacuum layer, according to the best thickness condition for the highest reflectance as discussed in the next section. In other words, even in the optimized periodic multilayer structures, the last layer should be treated separately.

Growth curve and the maximum reflectance

The curve in Fig. 3.1.4 can be called as a growth curve which is characterized by the Fresnel reflection coefficient of the material with "vacuum". In Fig. 3.1.6, the region close to the origin in Fig. 3.1.4 is shown in detail to depict the character of the growth curve.

In the complex plane, the reflectance amplitude is represented by the radial distance from the origin. The task to increase the reflectance is the task to depart the growth curve from the origin as effectively as possible. The growth curve starts from the Fresnel amplitude reflectance point of the Si substrate shown by a cross mark and moves to the right along the solid curve as the Mo layer grows. This curve continues to form a spiral curve shown by the dashed curve for a few spiral movements. Because of the weak absorption of Mo, this Mo continuation curve gently spirals in to reach the open triangle at the infinitely thick growth, which is the Fresnel amplitude reflection point of Mo.

Now by switching the material to Si at the switching point shown by the open circle, the growth curve turns the direction. Although the growth curve comes inside the Mo continuation curve in the initial stage, it eventually goes outside and goes along the Si growth forming a Si continuation curve till the next switching point. The Si continuation curve also spirals in to the Si Fresnel reflection point close to the origin, though the curve looks like a circle because of the much smaller absorption of Si. After the material switching to Mo, the multilayer growth

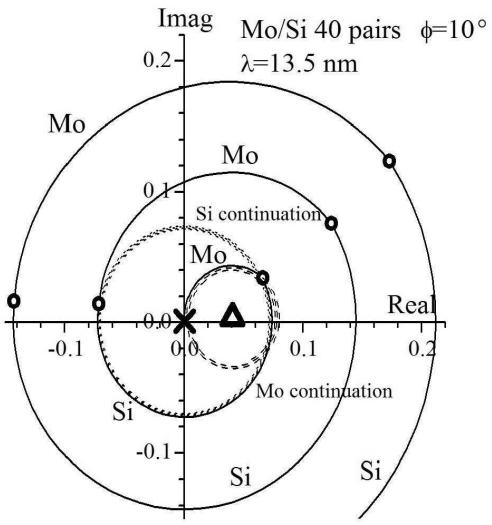

Fig. 3.1.6. Enlarged view of the Mo/Si multilayer growth by the amplitude reflectance in Fig. 3.1.4.

curve now swings outwards by the Mo growth forming another Mo growth curve with a different starting point. The process is thus repeated till the outward expansion reaches saturation as shown in Fig. 3.1.4

As expected by the symmetry in the Mo growth segments shown in Fig. 3.1.6, all forming the initial part of different Mo continuation curves, the growth curves of a specific material with a specific complex refractive index never cross each other regardless the starting or switching point location in the complex plane. Therefore, the most effective increase of the reflectance should be defined by the tangential condition at the switching point. In other words, the multilayer growth curves should be formed by smooth connections between the current growth curve and the continuation curve of the next material. According to the smooth connection criterion of the best switching, the $1^{\rm st}$ switching should be delayed with a thicker Mo since the bending is obvious at the switching point shown. Similarly, the $2^{\rm nd}$ switching should be earlier with a thinner Si layer because the bending of the growth curve is opposite for the case at the $1^{\rm st}$ switching.

The growth curve shown in Fig. 3.1.4 indicates that the effect of changing the substrate material is manifested within a few layers. In particular, the shape of the growth curves in the saturation region is not affected by the optical constants of the substrate but by the Fresnel reflectance amplitude points r_A and r_B of materials A and B. The maximum reflectance achievable by a given pair is thus given by the smooth connection point of the saturated growth curve to a circle, which is the growth curve of the next hypothetical layer of vacuum. Therefore, the last layer thickness is decisive independently of other layer thicknesses and the last switching point to the vacuum should be located in the $1^{\rm st}$ quadrant.

Selection of materials

In the visible region, the multilayer mirror is formed by a material pair of high and low refractive indices. As mentioned earlier, Spiller described the material selection criteria of the X-ray multilayer mirror as "select spacer material by the smallest possible k and pair material of the highest $|n - \mathrm{i}k|$ difference with the spacer material." By expanding the equation for R_m and ignoring the 3$^{\mathrm{rd}}$ and higher order terms, we obtain

$$R_m = r_m + (R_{m-1} - r_m) \exp(-\mathrm{i}\delta_m) . \tag{3.1.4}$$

Assuming the normal incidence for simplicity, this can be written as

$$R_m = r_m + (R_{m-1} - r_m) \exp(-4\pi k_m d_m/\lambda) \exp(-i4\pi n_m d_m/\lambda) . \tag{3.1.5}$$

In Fig. 3.1.6, the growth curve of the m^{th} layer can be understood by referring to the equation above as a circular curve drawn with a radial line connecting the origin r_m and the switching point R_{m-1} rotated by a specific angle defined by the thickness. The radial line of $(R_{m-1} - r_m)$ $\times \exp(-4\pi k_m d_m/\lambda)$ is rotated by the angle $(-4\pi n_m d_m/\lambda)$ for the m^{th} layer. For the alternating layer of two materials, the complex amplitude reflectance point R_m will draw a curve with the centers of rotation of r_A and r_B alternatively which are the Fresnel reflectance amplitudes of the two materials A and B. Therefore, the distance $|r_A - r_B|$ should be as large as possible. At the same time, the damping of the radial length should be small which requires small k_m. There is a simple relation between the complex refractive index $n - \mathrm{i}k$ and the Fresnel amplitude reflectance. At normal incidence, the amplitude reflectance

$$r_{m0} = \frac{1 - \tilde{n}}{1 + \tilde{n}} = \frac{\delta + \mathrm{i}k}{2 - \delta - \mathrm{i}k} \cong \frac{\delta + \mathrm{i}k}{2} \tag{3.1.6}$$

is located in the complex plane at a point $\left(\frac{\delta}{2}, \frac{k}{2}\right)$. This shows that the material with a smaller k_m will be located at r_m close to the real axis in the complex plane. Thus, the selection criterion can be written as:

(I) among the plots of the Fresnel amplitude reflectance in the complex plane, choose two materials located both close to the real axis and far apart from each other.
Another formulation of the criterion can be based on the complex refractive index of the materials -

(II) materials both having small k but with the largest difference in n.
Finally, a practical description utilizing the characteristics of anomalous X-ray dispersion in materials can be -

(III) select material A having absorption edge on the shorter side of the wavelength region to be used and select material B having small absorption and small refractive index n (large δ).

At the wavelength of 12.4 nm close to the Si absorption edge, material A can be e.g. Si and Be and material B can be e.g. Rh, Ru, and Mo. Another example can be found for the case of CuK$_\alpha$ radiation at the wavelength of 0.154 nm [MAJ03a]. The layer-by-layer design principle shown here is effective for multilayers in the visible region. An example can be the

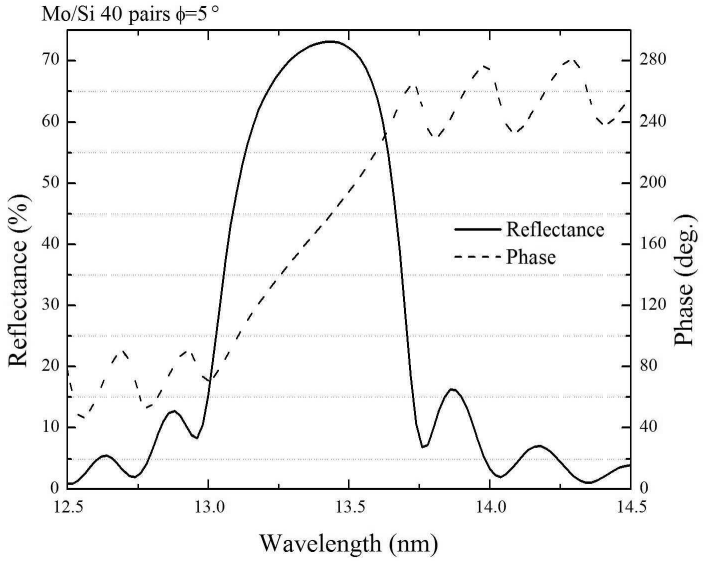

Fig. 3.1.7. Spectral reflectance and reflection phase as calculated for the Mo/Si multilayer.

laser mirror for high power application where the weak absorption should be taken into account in the design. Our method gives such a solution easily and with high accuracy as demonstrated by the case treated by Carniglia and Apfel [YAM89]. Their design is based on a pair of materials as a unit while in our design each layer includes three or more elements.

Reflection phase of the multilayer

The multilayer mirrors can be used for imaging by applying the multilayer on a curved substrate with appropriate period thickness distribution [HAT03]. The reflection phase of the multilayer structure has consequence for imaging application. In Fig. 3.1.7, spectral reflectance and the reflection phase are plotted for an angle of incidence of 5°. The reflection phase is symmetric around the reflection peak wavelength. The absolute reflection phase shown here depends strongly on the thickness and material structure. As expected from Fig. 3.1.4, the thickness of the last layer also shifts the phase linearly with the thickness. In Fig. 3.1.8, the reflection spectra data of Fig. 3.1.7 are traced back to the amplitude reflectance and shown in the complex plane. The data points for the wavelength from 10.5 nm to 14.5 nm are shown at every 0.02 nm. The numbers in the figure show the wavelength. The maximum reflectance is obtained at the 4^{th} quadrant where the complex amplitude reflectance spectrum meets the circle as a tangential condition. As seen in Fig. 3.1.7, the reflectance peak is located at the wavelength of 13.4 nm. In Fig. 3.1.9, the data shown in Fig. 3.1.2 were traced back to the amplitude reflectance to show the spectral evolutions at various angles of incidence. With the scale of Fig. 3.1.9, the data of 0°, 5°, 10°, 15° and 20° are overlapping with each other. The open circles close to -0.9 on the real axis show points of the peak reflectance. At 25°, large variation is induced at the absorption edge by the change of the optical constants of Si, which continues to the angles 30° and 35°. The curve

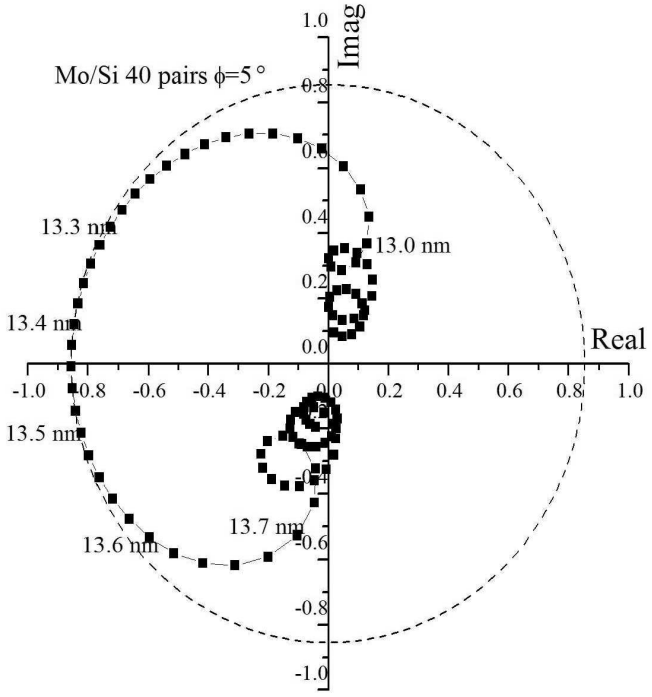

Fig. 3.1.8. Complex plane representation of the reflection peaks and phase of the Mo/Si multilayer.

shown by open squares in Fig. 3.1.9 represents the switched material multilayer starting with Si and ending with Mo. As can be seen in Fig. 3.1.2, the spectral reflectance of both structures shows no obvious change of amplitude but the reflection phase is much different.

Reflection phase compensation by milling

The tolerated wavefront error of the imaging optics for illumination wavelength λ is defined as $\lambda/4$ for the micro-focus optics of paraxial rays (Rayleigh criterion). For wide field imaging, the error should be within $\lambda/14$ known as Marechal criterion. For the mirror optics with the reflection imaging, the wavefront errors should be a half of these, i.e. $\lambda/8$ and $\lambda/28$, respectively, for the micro-focus and imaging optics. These values show that at the typical application wavelength of 13 nm, the wavefront error should be of the order of 0.1 nm. This extreme accuracy is difficult to achieve in combination with the most advanced super-polishing technique and the evaluation techniques.

Correction by physical optics

An alternative method can be the wave front error correction based on physical optics. In general, the shape error ε of an optical element causes wavefront errors of 2ε and $2(1-n)\varepsilon$ in the reflection

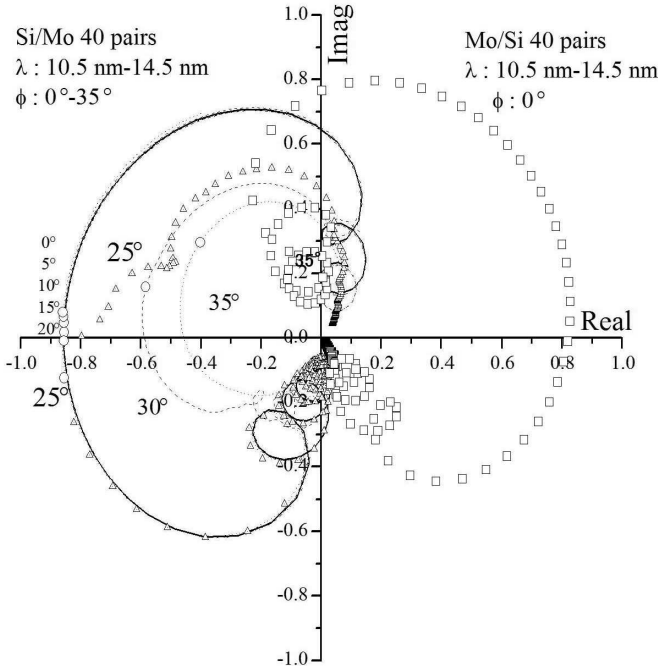

Fig. 3.1.9. Complex plane representation of the spectral reflectance at various angles of incidence calculated for the same conditions as in Fig.3.1.2.

optics and the transmission optics of refractive index n, respectively. In the soft X-ray region, the term $(1 - n) = \delta$ is of the order of 10^{-2} to 10^{-4}. This means that the transmission optics in the X-ray can tolerate large shape errors in principle. Here, the multilayer mirror function is based on a constructive interference of weak reflections at the multilayer boundaries. Thus the reflection is the volume effect of the whole multilayer stack which indicates that the layers at the surface should behave as the transmission layer even for the soft X-rays. In fact, the reflectance will saturate with an increase of the number of layers as it can be seen in Fig. 3.1.4. In the saturation, the surface layers are actually found to work as the transmission layer for the expected phase error correction [YAM01].

In Fig. 3.1.10, the effect of milling of the surface of the Mo/Si multilayer mirrors is shown for the wavelength of 12.78 nm at normal incidence. In this simulation, the layer-by-layer calculation is very effective and straightforward:

1) Calculation of the amplitude reflectance of the growing multilayer system at every 0.1 nm increase by using Eqs. (3.1.1) and (3.1.3) where the thickness d_m is varied and recorded as a data file. After the calculation, the last data for the top surface is referred to the origin of the reflection phase before the milling of the surface.

2) The reflection phase after milling can be traced back in the data file stored but by adding the exact thickness of "vacuum layer" added on top of the back-traced data. This addition

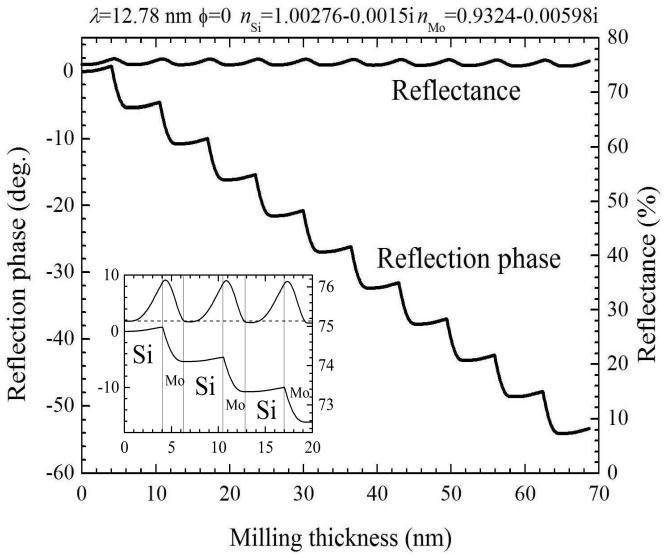

Fig. 3.1.10. Reflection phase and reflectance variation by milling from the surface of the Mo/Si multilayer providing the means of digital phase correction (simulation).

of the vacuum layer is necessary to keep the reference of the reflection phase to the surface before milling. This process is essential to find the real effect of the milling without changing the reference surface of reflection phase because the multilayer top surface is always referred to as the origin of the calculation in usual optical reflection calculation of the phase.

The reflection phase variation by milling calculated in the method above shows a stepwise decrease as seen in Fig. 3.1.7. The averaged rate of decrease in the reflection phase is around $-1°$/nm whereas the reflectance does not change except for the small sinusoidal variation of amplitude of 1%. A detailed inspection of the milling shows that a large change in phase and amplitude is caused by the milling of Mo layers whereas much smaller variation is seen in the Si layer milling. This means that a digital milling correction of phase with a step of $6°$ can be realized by detection of the surface appearance of Si, which can be done by utilizing ions, electrons, or visible light reflectance. The reflection phase of $6° = 360°/60$ for the wavelength of 13 nm corresponds to the required shape error correction at the mirror substrate surface of $13\ \mathrm{nm}/(2 \times 60) = 0.1$ nm. The reflectance variation by the digital milling will be within 0.1% as shown by the dashed lines showing the regions finished by milling which is controlled by the detection of Si appearance.

The reflection optics by the multilayer mirror thus converts the standard error term of 2ε to the term of $2(1-n)\varepsilon$, equivalent to the error term of transmission optics in general. In the X-ray applications, the multilayer mirror is particularly effective since the refractive index is very close to 1, making the $(1-n)$ small enough to control the minute phase. Another advantage applicable to all electromagnetic wavelength regions is the realization of an accurate phase manipulation

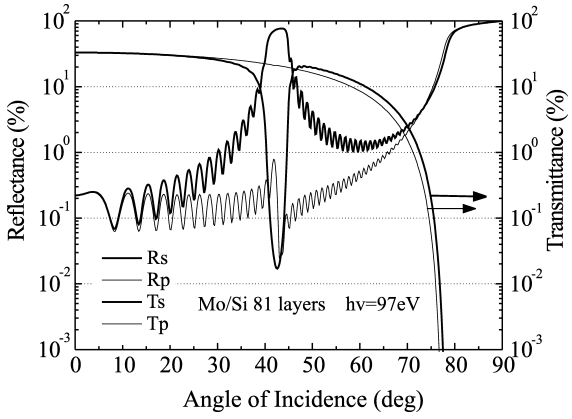

Fig. 3.1.11. Theoretical reflectance and transmittance of a free standing Mo/Si multilayer at a photon energy of 97 eV. Thick curves are for the s-polarization components.

such as in reflection filtering and holography. Particular emphasis should be put on the large area application which could only be realized by the mirror optics with a multilayer coating on a large substrate.

Polarization characteristics and devices

One of the new important application fields of the X-ray multilayer structures are the polarization measurements in the soft X-ray region. In the vacuum ultraviolet wavelength range, reflection polarizers were used for a long time. However, the poor reflectance of such reflection polarizers at the polarization angle limited their use in the soft X-ray range [HUN78]. The polarization angle of incidence in the soft X-ray range is around 45° since the Brewster angle is defined as $\tan^{-1} n$ and the refractive index n is very close to unity. As it was shown above, the multilayer structure can be designed with a sufficiently high reflectance at a desired wavelength and angle of incidence. Using the multilayer structures, the polarization measurements in the soft X-ray range are available at present.

The multilayer reflection polarizers utilize the difference in Fresnel reflection coefficients between the p- and s-polarization components at the Brewster angle or, more specifically, at the pseudo Brewster angle where the p-reflectance reaches the minimum value. Design calculation examples are shown in Fig. 3.1.11 for the photon energy of 97 eV with a multilayer composed of 81 alternative layers of Si and Mo (i.e. 40 periods and one additional layer of Si). The refractive indices and thicknesses used for the calculation are $(0.9324 - 0.00598\mathrm{i})$ and 3.09 nm for the Mo layers, and $(1.00276 - 0.00150\mathrm{i})$ and 5.93 nm for the Si layers, respectively. The calculation of transmittance is also shown and indicated by the arrows with the scale at the right-hand axis.

As it can be seen in Fig. 3.1.11, the peak region of the s-reflectance R_s is above 10% while the p-reflectance R_p stays small of approx. 0.2%. Therefore, a single reflection at the peak angle results in the linear s-polarization reflection with the reflectance ratio to the p-polarization of the order of 10^3. With an analyzer unit composed of the polarizing multilayer mirror and a detector mounted to receive the s-reflection at the polarization angle of approx. 42°, the incoming

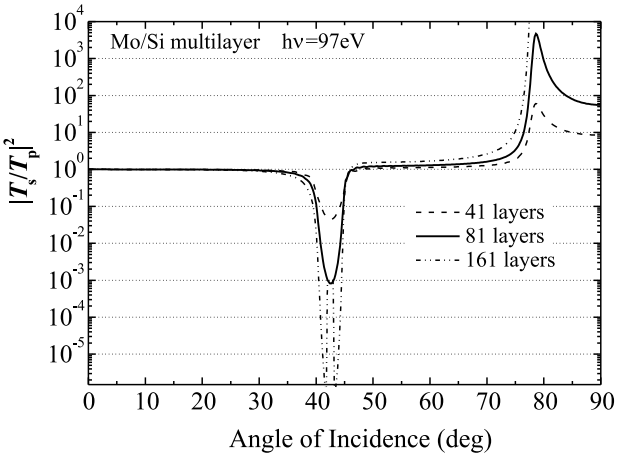

Fig. 3.1.12. Theoretical transmittance ratio between the p- and s-polarization components as calculated for the free standing Mo/Si with the number of layers of 41, 81, and 161.

polarization can be analyzed by the azimuthal rotation of the unit. With this high performance polarization analyzer unit, a so called "rotating analyzer" method can be realized [DHE87].

The single reflection polarization inevitably changes the direction of the incoming light and therefore, it is not convenient for the use as a standard polarizer for production of the linear polarization from the unpolarized light. In Fig. 3.1.11, the s-transmittance T_s curve shows a deep minimum (which coincides with the R_s maximum) whereas the p-transmittance T_p does not show any obvious effect. This confirms that a multilayer can also be used as a transmission polarizer suitable for applications requiring a straight light path. However, special techniques should be used to prepare the freestanding structures [FU96, NTT-AT].

Figure 3.1.12 shows calculation examples of the polarization function $\left|\frac{T_s}{T_p}\right|^2$ for a transmission polarizer. The calculations were performed for multilayers with the number of layers 41, 81, and 161 (i.e. 20, 40, and 80 periods, and Si cover layer). As it follows from the figure, the minimum at 42.6° becomes deeper when increasing the number of layers. For 81 layers, the p-transmittance of 21% with the transmission ratio of 10^{-3} is achieved. By doubling the number of layers, the transmission ratio can be better than 10^{-6} with the p-transmittance of 4.4%. For 41 layers, the transmission ratio is 0.04 only but the p-transmittance is of 46% (the total thickness of the multilayer is 186 nm). Further advantage of the transmission multilayers is in the phase shifting function.

Figure 3.1.13 shows the relative phase shift between the p- and s-transmissions calculated at the same conditions as for Fig. 3.1.12. The phase shift starts from zero at the normal incidence since there is no relative difference between the p- and s-components of the transmission amplitude. A typical behaviour can be described for the multilayer with 81 layers shown by the solid curve in the figure. As the angle of incidence increases, the phase gradually becomes more negative and shows a large resonance like a deflection centered at the polarizing angle of 42.6° with a negative peak of $-108.3°$ at the $40.4°$ incidence angle followed by a positive peak of 192.2°

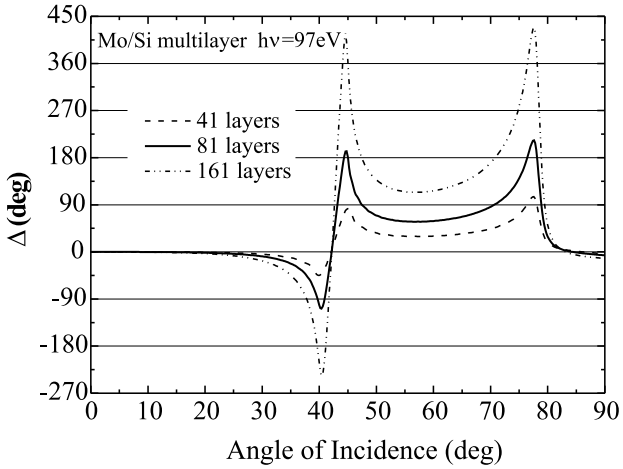

Fig. 3.1.13. Theoretical relative phase shift between the p- and s-polarization components of the free standing Mo/Si multilayers. Calculation conditions are the same as in Fig. 3.1.12.

at the 44.8° incidence angle. Between the peak at 44.8° and the next positive peak of 213.2° at the 77.6° incidence angle, there is a plateau region with a phase shift larger than 57.5°. If the deviation of the phase angle of 2° is allowed, the angles of incidence from 53.8° to 60.6° with the phase shift of $58.5 \pm 1°$ can be used for the phase shifting. This large acceptance range of the angles of incidence could be useful in imaging optics with a large numerical aperture. Figure 3.1.13 also shows that the phase shift is proportional to the number of layers. For 161 layers, the phase shift of 113.8° can be obtained which implies that the phase shift of 0.71° per layer can be expected.

These theoretical expectations have been proved by the fabrication of free standing transmission multilayers [NOM92, YAM99a]. With the multilayer polarizers and phase shifters, various polarization measurements and control are now realized including the most advanced soft X-ray ellipsometry [YAM93, TSU08].

3.2 *In-situ* ellipsometric monitoring

Multilayers of several tens of periods are formed by depositing alternate layers composed of two materials of appropriate optical constants. For the constructive interference of specific EUV radiation, individual layers should be controlled to the exact thickness of around $\lambda/4$. Thus, in the EUV region, each layer thickness of a few nanometers should be controlled precisely over several tens up to hundreds periods. To achieve high reflectance, the thickness error over layers should be within the inverse of a number of layers because the top layer should be in a constructive interference condition. For example in the water window region, since a large number of layers > 200 is required for practical use, the thickness error should be within 0.5% which means that each layer is monitored and controlled with a thickness accuracy better than 0.005 nm [TSU04]. Furthermore, for imaging optics composed of multiple mirrors, the reflection peak wavelength should be matched by controlling the period thickness to attain a high throughput [HAT99].

In addition to the period thickness control, a smooth and sharp interface at every boundary is required for high reflectance. However, a real multilayer has some imperfections at the boundaries due to interdiffusion, intermixing of materials and interface roughness [SPI94, SLA94, ISH02] which reduce the reflectance. When the wavelength of the employed EUV light becomes shorter, suppression of such imperfections is still more urgently required.

Preparation conditions are carefully optimized to achieve stable operation in the multilayer fabrication by sputtering. Consequently, the layer thickness control by the duration of deposition is possible assuming that the sputtering rate is constant. However, it is found that a thickness deviation from the designed value can be caused by any slight fluctuation in the environmental temperature, target surface erosion and ion beam current. To control the period thickness exactly, the sputtering rate monitor with the sensitivity better than 0.01 nm (described above) is necessary. Since each layer is only a few atoms thick in the EUV wavelength region, commercially available thickness monitors are lacking sufficient sensitivity for the sputtering fabrication.

Ellipsometry [AZZ, TOM] exhibits a high sensitivity to thickness and optical properties of thin films. Therefore, a carefully tuned ellipsometer is adequate to study ultra thin film fabrication for EUV multilayer optics. Although many designs of ellipsometers are in use, these are generally classified into two types: a null instrument and a photometric instrument. In the measurement by the null ellipsometer, the null position is found by adjusting alternately the polarizer and the analyzer. In the photometric instrument, the sinusoidally varying light intensity is recorded during the rotation of the polarizer or the analyzer. In principle, null ellipsometer can easily realize a high thickness sensitivity because careful calibrations such as nonlinearity of detector, fluctuations of light intensity and so on are of less importance.

Automatic null ellipsometer by two-phase modulations

The null ellipsometer developed by us has a standard polarizer (P) – sample (S) – compensator (C) – analyzer (A) configuration. For automation, two Faraday rotators operated at a common frequency with 90° phase difference are installed [LAY69, MAT74, YAM03, TSU03, TSU04, TSU05]. Two Glan-Thompson polarizers with an extinction ratio better than 10^{-7} and a mica quarter wave plate as a compensator are mounted on optical rotary encoders with an angular resolution of 0.0001°. A power stabilized He-Ne laser of a wavelength of 632.8 nm irradiates the sample at an angle of incidence of 75°.

Since the azimuthal angles of P and A are modulated by the Faraday rotators, the effect of a small sinusoidal optical vibration of azimuths by the rotators is equivalent to an additional small mechanical vibration of P and A azimuths. The output signal I_{out} in the P-S-C-A configuration is expressed as

$$I_{out} = I_0\{\sin^2(P - P_n) + \sin 2P_n \sin 2P \sin^2(A - A_n)\}, \tag{3.2.1}$$

where P_n and A_n are the azimuths at the null positions. By setting the sinusoidal modulation signal of P in sine form and of A in cosine form at the angular frequency of ω, the output signal I_{out} can be expressed with Bessel function J_n as

$$I_{out} = 2I_0\{J_0(\alpha_0)J_1(\alpha_1)\sin 2\alpha_0 \sin \omega t + J_0(\beta_0)J_1(\beta_1)\sin 2\beta_0 \cos \omega t + ...\}. \tag{3.2.2}$$

Here we use the following relations with respective azimuthal miss-settings of α_0 and β_0 from

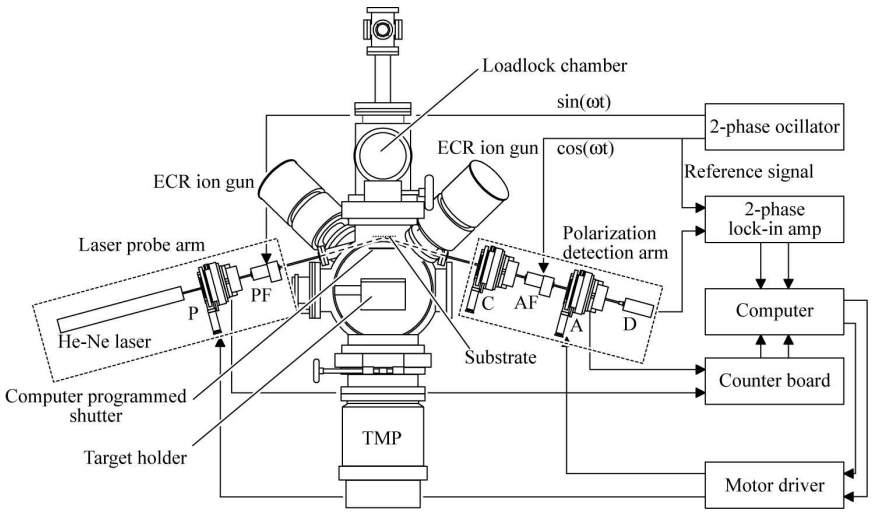

Fig. 3.2.1. Schematic drawing of an *in-situ* automatic null ellipsometer mounted on an ion beam sputtering system for fabrication of EUV multilayer mirrors. P: polarizer, PF: polarizer Faraday rotator, C: compensator, AF: analyzer Faraday rotator, A: analyzer, D: detector.

the null positions of P_n and A_n:

$$P - P_n = \alpha_0 - \alpha_1 \sin \omega t, \tag{3.2.3}$$

$$A - A_n = \beta_0 - \beta_1 \cos \omega t. \tag{3.2.4}$$

As can be seen in the first and second terms on the right-hand side of Eq. (3.2.2), the output signal near the null position is proportional to the errors α_0 and β_0 of the azimuthal settings of P and A. Therefore, the relative azimuth displacements α_0 and β_0 from the null position can be directly measured with no cross-talk as the outputs of cosine and sine phase with plus and minus signs by a two-phase lock-in amplifier tuned to the fundamental frequency.

Schematic drawing of the automatic null ellipsometer attached to the ion beam sputtering system for the multilayer fabrication is shown in Fig. 3.2.1. This system can be operated in two modes, i.e. a standard mechanical servo-mode and a mechano-electronic tracking mode. In the servo-mode, the error signals are used with the repetition of 150 ms as feed back signals for the stepping motor drives to eliminate the errors of the azimuthal setting. In the tracking mode, the error signals near the null position are used to calculate the relative azimuth displacement from the current origin of the azimuthal angles. The origin can be renewed by driving small and appropriate angles when necessary.

In the *in-situ* ellipsometric measurement, the azimuths of P and A are recorded by the control system and used for the plotting the complex relative amplitude attenuation ρ in a Gaussian plane which directly represents the properties of the thin film during fabrication. The complex relative

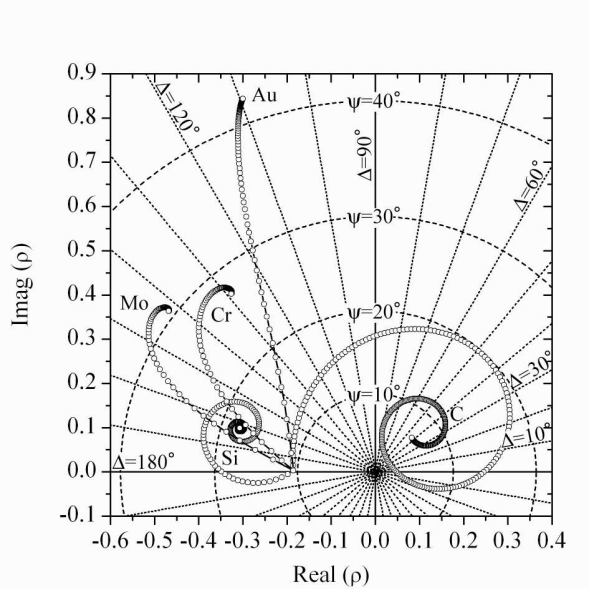

Fig. 3.2.2. Theoretical ellipsometric growth curves of Au: $n = (0.44 - 3.50\mathrm{i})$, $d = 100$ nm, C: $n = (2.25 - 0.37\mathrm{i})$, $d = 300$ nm, Cr: $n = (3.13 - 3.31\mathrm{i})$, $d = 100$ nm, Mo: $n = (4.08 - 4.47\mathrm{i})$, $d = 100$ nm and Si: $n = (4.81 - 1.02\mathrm{i})$, $d = 300$ nm single layers on a Si substrate: $n = (3.875 - 0.0205\mathrm{i})$ in the complex plane. A wavelength of 632.8 nm and an angle of incidence of 75° are chosen for the calculations. The circle marks are distributed with 1 nm interval. The broken and dotted lines indicate the ellipsometric parameters Ψ and Δ, respectively.

amplitude attenuation is defined as

$$\rho = \frac{R_p}{R_s} = \tan\Psi \exp(\mathrm{i}\Delta), \tag{3.2.5}$$

where R_p and R_s are the complex amplitude reflectances for the p- and s-components and Ψ and Δ are the relative amplitude attenuation and relative phase shift, respectively. In the null ellipsometry, actual null conditions exist as a combination of the azimuthal settings falling in the symmetric halfspace separated by the plane of incidence. Rotational symmetry of the polarizing elements by 180° also gives more read-outs for the single state of polarization. Azimuth selection of the compensator at $\pm 45°$ provides plural read-outs. Such combination is classified into 4 groups and called "zones" [AZZ] which define the relation between the azimuthal angles and the ellipsometric parameters. For zone 3 used in our measurement, ρ is calculated by the azimuths of P and A as $\tan(-P)\exp\{\mathrm{i}(2A - 90°)\}$.

In the ellipsometry, we can not directly measure the thickness and the optical constants of films. Ellipsometers measure the complex relative amplitude attenuation ρ or the ellipsometric parameters ψ and Δu Therefore, prior to the experiment, it is helpful to know the ρ trajectories of the films as the growth curves simulated by model calculation with expected film thickness and optical constants. Fig. 3.2.2 shows the ρ trajectories for several absorbing materials on a

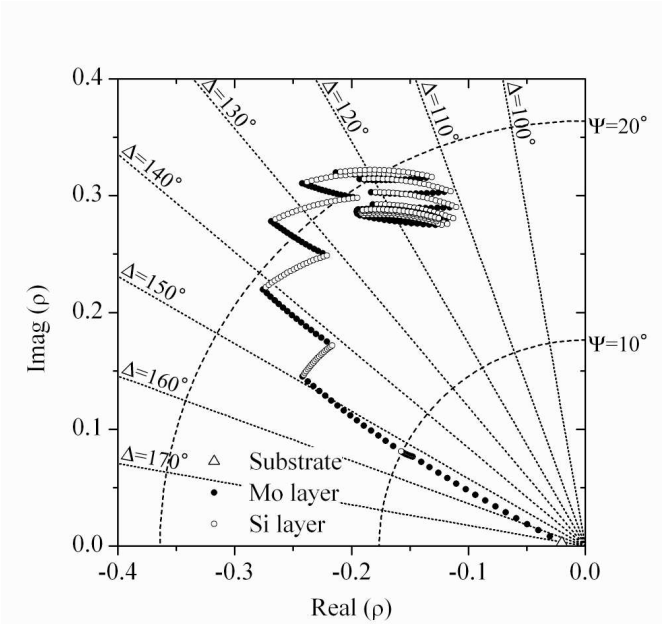

Fig. 3.2.3. Theoretical ellipsometric growth curve of a Mo/Si multilayer composed of 40 periods on a Si substrate with a wavelength of 632.8 nm and an angle of incidence of 75°. Solid marks (•) and open marks (○) indicate 3 nm Mo layer formation and 4 nm Si layer formation, respectively, both at every 1 nm thickness increment.

Si substrate at angle of incidence of 75°. A standard single layer model was used for the calculation with the optical constants of Au $(0.44 - 3.50\text{i})$, C $(2.25 - 0.37\text{i})$, Cr $(3.13 - 3.31\text{i})$, Mo $(4.08 - 4.47\text{i})$ and Si $(4.81 - 1.02\text{i})$. When the thickness is zero, ρ represents the substrate. Although the circle marks are separated from each other in the early stage, ρ proceeds gradually towards the value of the bulk material as the thickness increases. Consequently, the trajectories depict spirals towards the bulk value. The extinction coefficient k determines how fast the spiral converges into the bulk value. As shown in Fig. 3.2.2, the direction and the length of the trajectories qualitatively correspond to the optical constants and the thickness, respectively. Fig. 3.2.3 shows the theoretical growth curve of Mo/Si multilayer composed of 40 periods on Si substrate simulated with the optical constants and thickness of $(4.08 - 4.47\text{i})$ and 3 nm for Mo layers and $(4.81 - 1.02\text{i})$ and 4 nm for Si layers, respectively. The angle of incidence and the irradiation wavelength are 75° and 632.8 nm, respectively. The circle marks are distributed with 1 nm intervals. Starting from the substrate, the ρ trajectory of Mo appears to form a smooth line of which the direction and interval are the same as for Mo single layer shown in Fig. 3.2.2. Therefore, the direction is changed at the material switching point from Mo to Si. Such alternate movements of the Mo and Si segments continue up to the final layer. As the deposition proceeds, the multilayer is stacked beyond the penetration depth of the probing light and the bottom part of the multilayer stack ceases to contribute to ρ variation. At the final stage the growth curve moves between two points as a closed-loop, since the light probes the top part of the multilayer due to the lack of con-

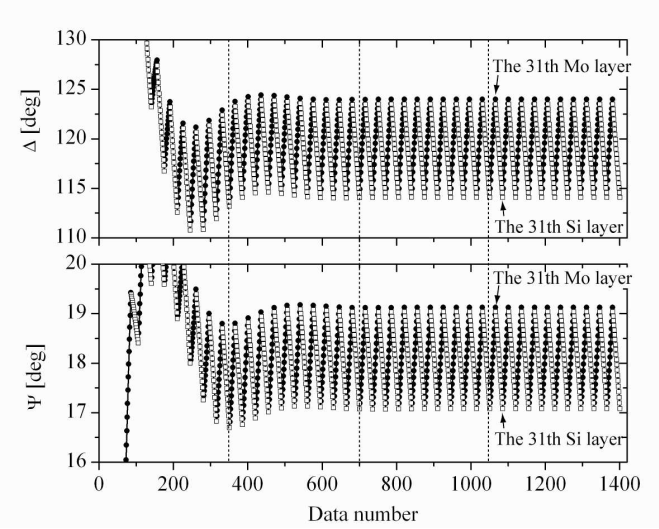

Fig. 3.2.4. Theoretical variations of the ellipsometric parameters Ψ and Δ of a 40 period Mo/Si multilayer shown in Fig. 3.2.3. Solid marks (•) and open marks (○) indicate formation of 3 nm Mo layer and 4 nm Si layer at every 1 nm interval, respectively. The horizontal axis corresponds to the growth duration.

tribution of the reflected light from the substrate [YAM03, TSU04, TSU05 TSU06]. Fig. 3.2.4 shows simulated variations of the ellipsometric parameters Ψ and Δ at this stage. As can be seen in this figure, the periodicity directly follows that of the fabricated multilayer. The simulation software programmed by JAVA applet is available at the web site [YAM_1].

Layer-by-layer analysis of multilayers

To determine the thickness and the optical constants of every layer in a multilayer structure, we devised a layer-by-layer method of *in-situ* ellipsometric data analysis [TSU04, TSU06]. Although many methods have been utilized to analyze *in-situ* data measured by an ellipsometer including a spectroscopic ellipsometer [ASP84, ASP93, COL00], our method is applicable for a multilayer structure consisting of absorbing materials with no pre-determination of the dielectric functions. We assume that (1) a homogeneous, isotopic and parallel-plane layer is growing regardless the growth stage, (2) variations of the optical constants are negligible when the layer thickness increases by a very small amount. Since our automatic null ellipsometer can detect and record the null positions in a sequence with an interval of less than 150 ms during multilayer fabrication, two neighbouring *in-situ* data should satisfy the assumptions formulated above, having common optical constants n and k and a slight difference in thickness. The method is described in detail in refs [YAM92, URB94, COM95, TSU06].

In the ellipsometric measurement, the j^{th} *in-situ* data of the complex relative amplitude attenuation within the m^{th} layer is defined by the amplitude reflectance for the p- and s-components

as

$$\rho_{m,\,j} = \frac{R_{p,\,m,\,j}}{R_{s,\,m,\,j}}. \tag{3.2.6}$$

When the p- and s-polarized light of the wavelength λ irradiates a multilayer composed of m layers at an angle of incidence ϕ, the j^{th} amplitude reflectance of the m^{th} layer for both p- and s-components is expressed as

$$R_{m,j} = \frac{r_{m,j} + R'_{m-1}\exp(-i\delta_{m,j})}{1 + r_{m,j}R'_{m-1}\exp(-i\delta_{m,j})}, \tag{3.2.7}$$

$$\delta_{m,\,j} = \frac{4\pi d_{m,\,j}}{\lambda}\sqrt{\tilde{n}^2_{m,\,j} - \sin^2\phi}, \tag{3.2.8}$$

where $r_{m,j}$ is the j^{th} Fresnel reflection coefficient at the vacuum/m^{th} layer interface, R'_{m-1} is the resultant amplitude reflectance including the effect of the multiple reflection in the layer beneath, $d_{m,j}$ and $\tilde{n}_{m,\,j}$ are the j^{th} thickness and optical constant of the m^{th} layer, respectively. If we take the infinitesimally small limit for the thickness in Eq. (3.2.7), the multilayer composed of the m layers is converted into a $(j-1)$ structure which yields the following relation

$$R_{m-1,j} = \frac{r_{m,j} + R'_{m-1}}{1 + r_{m,j}R'_{m-1}}. \tag{3.2.9}$$

Equation (3.2.9) can be rewritten to calculate $R'_{m-1,j}$ with $R_{m-1,j}$ and $r_{m,j}$ as

$$R'_{m-1} = \frac{R_{m-1,j} - r_{m,\,j}}{1 + r_{m,j}R_{m-1,j}}. \tag{3.2.10}$$

By *in-situ* ellipsometric data acquisition, a series of the complex relative amplitude attenuations starting as ($\rho_{1,1}$, $\rho_{1,2}$, $\rho_{1,3}$, …, $\rho_{1,j}$) for the first layer till ($\rho_{m,1}$, $\rho_{m,2}$, …, $\rho_{m,j}$) for the m^{th} layer can be obtained where the first and second subscripts indicate the layer number and the data number in the m^{th} layer, respectively. To determine the four unknown parameters of ($n_{m,j}$, $k_{m,j}$, $d_{m,j}$, $d_{m,j-1}$) from $\rho_{m,j}$ and $\rho_{m,j-1}$, the following procedure is used. (1) $R'_{1,j}$ for the first layer in Eq. (3.2.7) can be easily derived by using the optical constants of the substrate measured separately, where the R_0 in Eq. (3.2.10) can be calculated as the Fresnel reflection coefficient of the substrate. Thus, a set of solutions can be determined by Eqs. (3.2.6) – (3.2.8) and (3.2.10). (2) From the second layer, Eq. (3.2.10) can be calculated by the last set of solution of the preceding layer. For example, in the second layer, the last solution ($n_{1,j}$, $k_{1,j}$, $d_{1,j}$ is used for calculation of R'_1. A set of solutions for each data point in the current top layer can be iteratively derived by employing Eqs. (3.2.6) – (3.2.8) and (3.2.10). This layer-by-layer procedure is graphically shown in Fig. 3.2.5.

With the theoretical growth curve of Mo/Si multilayer shown in Fig. 3.2.3, the layer-by-layer analysis is demonstrated to determine the optical constants and the thickness. The results of the analysis plotted as a function of data number are shown in Fig. 3.2.6. The values coincide well with the values used for the simulation within the calculation precision. Therefore, this method was applied for a detailed analysis of the multilayer fabrication.

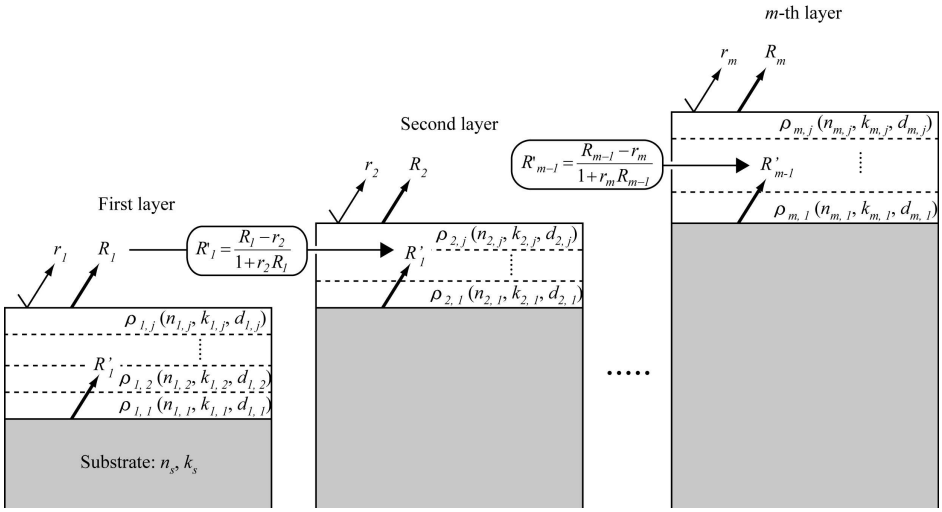

Fig. 3.2.5. The layer-by-layer analysis diagram to determine the optical constants and thickness of each layer in a multilayer. R_m, r_m and R'_{m-1} are, respectively, the amplitude reflectance for the p- and s-components, the Fresnel reflection coefficient at the vacuum/$m^{\rm th}$ layer interface and the resulting amplitude reflectance including the effect of the multiple reflection in the layer beneath. $d_{m,j}$, $n_{m,j}$ and $k_{m,j}$ are the $j^{\rm th}$ thickness, the refractive index and the extinction coefficient of the $m^{\rm th}$ layer.

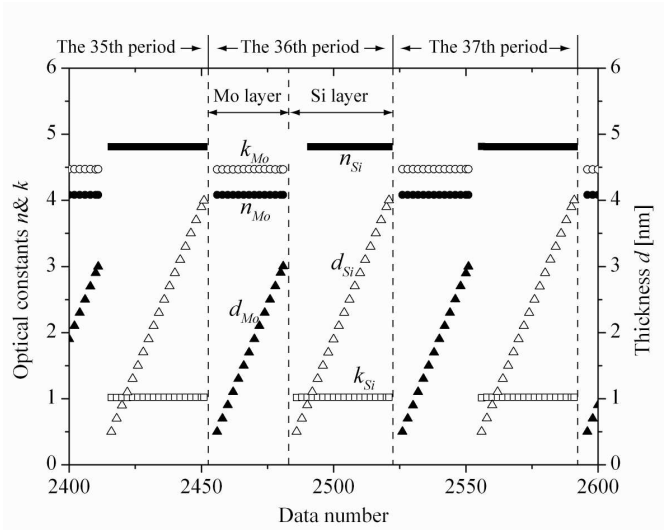

Fig. 3.2.6. Proof of the correctness of the optical constants and thickness determination by the layer-by-layer analysis. The theoretical complex relative amplitude attenuations of the Mo/Si multilayer shown in Fig. 3.2.3 were used for the analysis.

Ellipsometric *in-situ* monitoring of Mo/Si multilayer fabrication

As shown in Fig. 3.2.1, an ion beam sputtering system equipped with two electron cyclotron resonance type ion guns is used for our multilayer fabrication. The system is pumped down to a base pressure less than 10^{-5} Pa and is operated with Ar gas at 3.5×10^{-3} Pa. A triangular prism shape target holder is rotated by 120° for switching the deposition materials by a sequencer timer. In the automatic operation mode with sequential target switching, the period thickness is controlled by the deposition time. The target holder position is sent to the computer of the ellipsometer for recording the target materials. Vacuum windows of BK7 glass plates of 3 mm thickness, which were annealed to remove the residual birefringence, are used for the precise ellipsometric measurement [YAM80]. Since the deposition rate is directly affected by the fluctuation of the ion beam intensity, the stabilization of the ion beam intensity during the fabrication is essential for the periodicity of the multilayer structure. By careful optimization of several parameters of operation and employment of a stabilized AC power supply, fluctuations of the ion emission current as monitored by the current at the acceleration electrode was suppressed within ± 0.2 %.

In this study, two Mo/Si multilayers were fabricated at Ar ion acceleration voltages of 1400 V and 900 V while other sputtering conditions were kept constant. The *in-situ* monitoring enables us to characterize variation of the layer properties and boundary structure formations. By the ion beam sputtering system, two Mo/Si multilayer composed of 30 periods were stacked on Si wafers. Using multiple-angle-of-incidence ellipsometer, the optical structure of Si substrate was determined independently to be $n_{Si} = (3.87 - 0.0292\mathrm{i})$. For a native oxide on the substrate, $n_{\mathrm{SiO_2}} = 1.45$ and $d_{\mathrm{SiO_2}} = 1.79$ nm values were found. In the preparation runs, the deposition rates of Mo and Si as determined by X-ray diffractometry were 1.958 and 3.382 nm/min, respectively, at 1400 V. The respective rates at 900 V were 1.252 and 2.256 nm/min. The sputtering times for Mo and Si were set to 120 s at 1400 V and 140 s at 900 V to compensate for the deposition rate difference.

Figure 3.2.7 shows the ellipsometric growth curves observed at different acceleration voltage settings. Starting from the Si substrates, both growth curves are drawn by alternating Mo and Si segments up to the final layer, behaviour of which is qualitatively explained by the theoretical curve shown in Fig. 3.2.3. However, the curves follow different paths depending on the optical constants of layers in the multilayer. As mentioned above, the direction and length of each segment in the complex plane represent the optical constants and layer thickness. Therefore, the ellipsometric growth curves visualize differences of layer properties and directly give the information on the behaviour at the layer boundaries related to layer structure and/or mixed layer formation.

The 27^{th} periods of the two multilayers are compared in Fig. 3.2.8 where both growth curves move repeatedly between two points forming closed loops. The thickness determined by the layer-by-layer analysis is plotted by triangular marks on the curves. A clear difference is observed between the growth curves just after the target switching points. On every Mo layer deposited at 1400 V, downward movement was observed in the earliest stages after the target material was changed from Si to Mo. Judging from the characteristic shape of the curve, this movement corresponds to an island structure formation [YAM92]. When the layer was deposited up to thickness of approx. 1.5 nm at 1400 V, the island structure formation was over and the growth process was converted to homogeneous and optically isotropic layer formation. At 900 V on the other hand, no island structure formation was observed below 1 nm and ho-

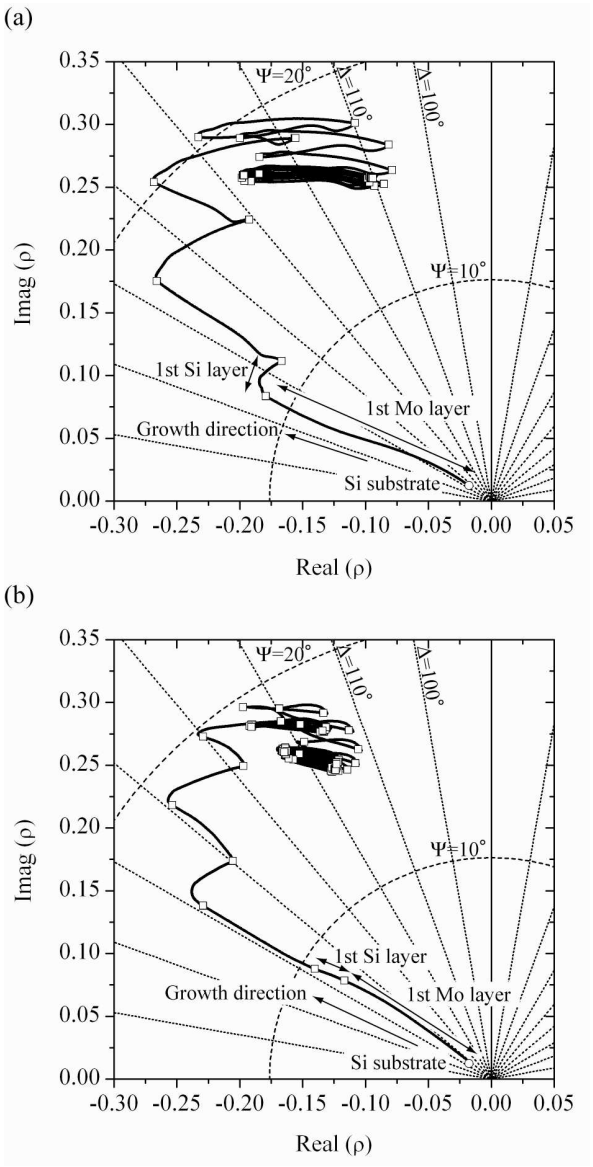

Fig. 3.2.7. Measured ellipsometric growth curves of Mo/Si multilayers composed of 30 periods fabricated at Ar ion acceleration voltages of (a) 1400 V and (b) 900 V. Squares indicate target switching points. Sputtering times of one period were for 240 sec at 1400 V and for 280 sec at 900 V.

mogeneous layer was formed as deposition proceeded. Therefore, a silicide layer is likely to be formed on Si without Mo island growth at 900 V. Sharper and smoother interfaces suited for the

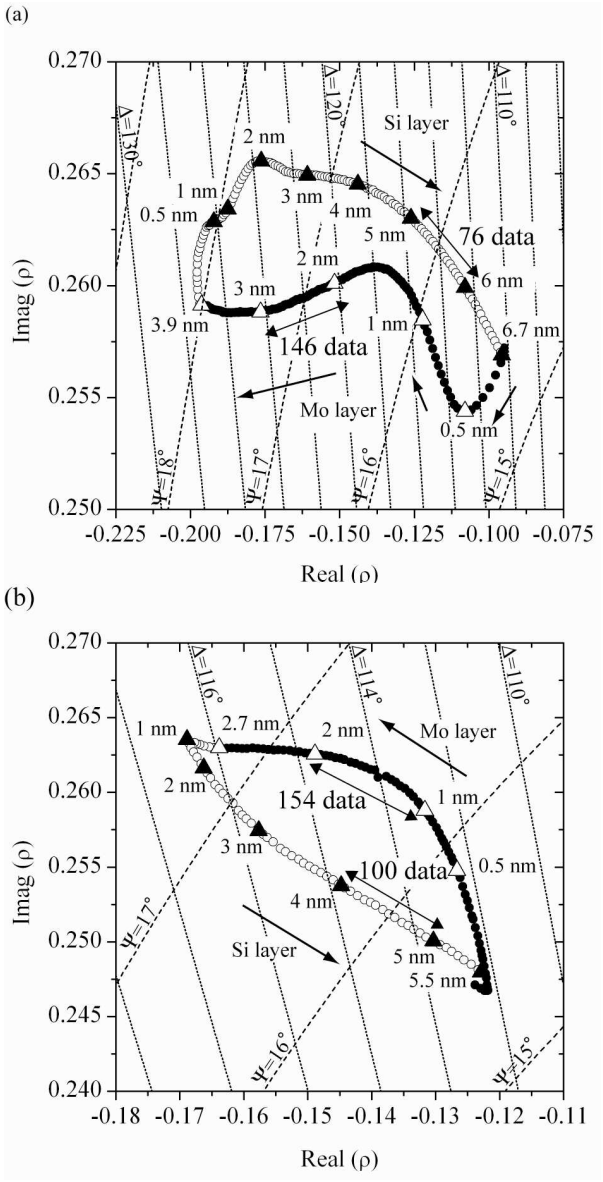

Fig. 3.2.8. Close-up view of the ellipsometric growth curves at the 27^{th} period of Mo/Si multilayers fabricated at Ar ion acceleration voltages of (a) 1400 V and (b) 900 V. Solid marks (●) and open marks (○) denote data points for Mo layers and Si layers, respectively. The thicknesses determined by the layer-by-layer analysis are indicated by triangular marks. There are 146 and 76 data points in 1 nm growth of Mo and Si layers at 1400 V, and 154 and 100 data points at 900 V, respectively.

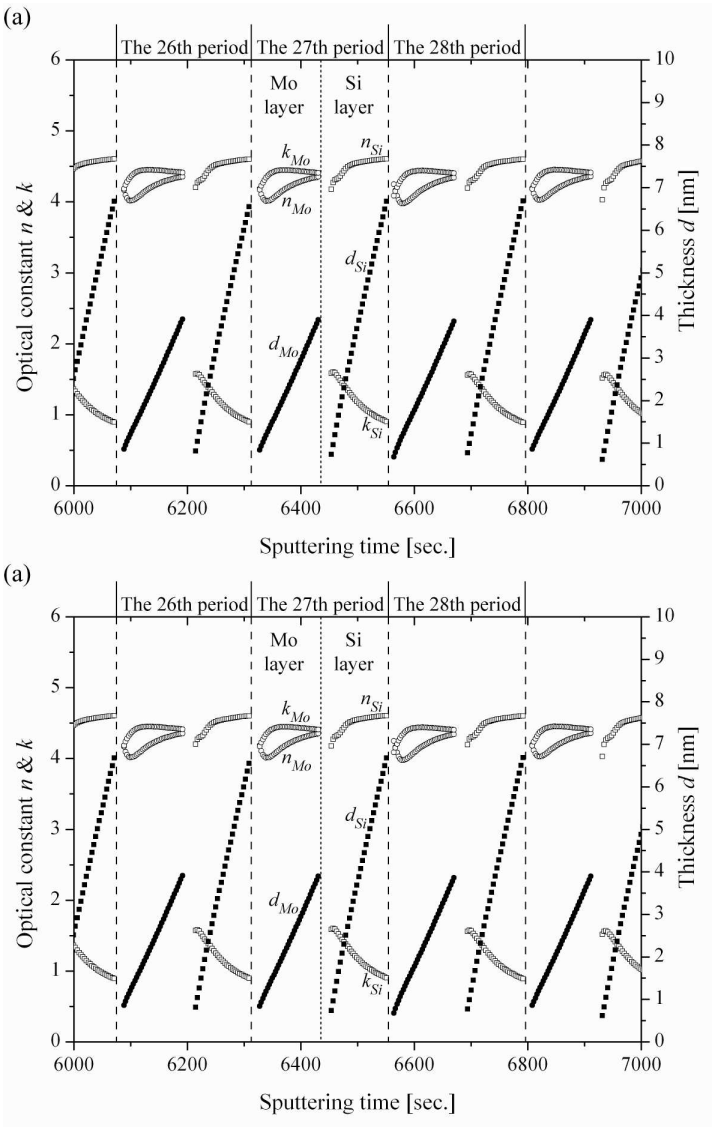

Fig. 3.2.9. The refractive index n, extinction coefficient k and thickness d values for a 30 period Mo/Si multilayer, determined by the layer-by-layer analysis, as a function of the sputtering time. Ar ion acceleration voltages were set to (a) 1400 V and (b) 900 V.

EUV multilayer are expected to be formed at 900 V rather than at 1400 V.

To determine the optical constants and the thicknesses of individual layers in Mo/Si multilayers fabricated at 1400 V and 900 V, the ellipsometric growth curves in Fig. 3.2.7 were analyzed layer-by-layer. Fig. 3.2.9 shows the results from the 26^{th} to 28^{th} period as a function of the

sputter-deposition time. During these periods, the growth curves draw the closed-loops in the complex plane as shown in Fig. 3.2.8. While an island structure and/or a mixed layer formation is expected just after the target material switching, no solution was found for the optical constants which indicates that they are not constant in reality. However, as the deposition proceeds, solutions with the optical constants can be found implying a stable morphology or growth phase in the initial growth. Later, the optical constants gradually change and become stable at certain values. An exception can be found for Mo layer deposited at 900 V. It is quite likely that the layer was still in the stage of silicide layer growth. Averaging from the 21^{st} to 30^{th} periods, where the closed loops are formed, the optical constants of the layers were found to be $n_{Mo} = 4.35 \pm 0.01$, $k_{\mathrm{Mo}} = 4.41 \pm 0.01$ and $n_{\mathrm{Si}} = 4.60 \pm 0.01$, $k_{\mathrm{Si}} = 0.89 \pm 0.01$ at acceleration voltage of 1400 V and of $n_{\mathrm{Mo}} = 3.87 \pm 0.09$, $k_{\mathrm{Mo}} = 3.62 \pm 0.05$ and $n_{\mathrm{Si}} = 4.53 \pm 0.05$, $k_{\mathrm{Si}} = 1.61 \pm 0.04$ at 900 V. Judging from the growth curves, the Mo/Si multilayer fabricated at 900 V was expected to have sharper interface than that at 1400 V as described above. Contrary to the expectation, the quantitative layer-by-layer analysis shows that the Si layer deposited at 1400 V became optically isotopic already at 1 nm which could also be useful to fabricate short period multilayers.

As for the thickness sensitivity, since there are 146 data points within 1 nm growth of Mo layer at 1400 V, the distance between the data points is equal to $1/146 = 0.007$ nm $= 7$ pm. This sensitivity achieved in the EUV multilayer fabrication should be high enough to be applied to the *in-situ* monitoring of ultra-thin multilayer fabrication in general.

The averaged thicknesses of Mo and Si layers in the last 10 periods are found to be $d_{\mathrm{Mo}} = 3.92 \pm 0.01$ nm and $d_{\mathrm{Si}} = 6.72 \pm 0.01$ nm at an acceleration voltage of 1400 V, and $d_{\mathrm{Mo}} = 2.70 \pm 0.02$ nm and $d_{\mathrm{Si}} = 5.54 \pm 0.02$ nm at 900 V. The period thickness as a sum of Mo and Si thicknesses determined by the ellipsometric analysis is close to that of 9.894 nm at 1400 V and 8.154 nm at 900 V determined by X-ray diffractometry. This slight variation of the thickness is likely to be caused by an ambiguity in the start and end points assignments as shown in the growth curves.

In summary, we have successfully applied an *in-situ* ellipsometric monitoring with a picometer thickness sensitivity for EUV multilayer fabrication. The automatic null ellipsometer can clearly distinguish growth curves as demonstrated by two different deposition conditions. The information accumulated by the *in-situ* monitor with quantitative layer-by-layer analysis should be useful for controlling nanometre layer thickness and also for interface engineering to form sharp and smooth boundaries required for the EUV multilayer optics.

4 Basic principles of giant magnetoresistance multilayers and spin valves

4.1 Principles

Magnetic multilayers with Giant Magnetoresistance (GMR) effect are another type of thin film layered systems discussed in this paper. With the discovery of the GMR effect in metallic magnetic multilayers in 1988/1989 [BAI88, BIN89], the era of spintronics was launched. Spintronics (spin-based electronics) represents a new branch of electronics which employs the spin of electron as the carrier of information in addition to its charge [WOL01].

In pioneering papers [BAI88] it was observed that the resistance of thin ferromagnetic (FM) films separated by non-magnetic metallic layer (NM) – spacer – changes as a function of mutual magnetization orientations of FM layers as it is shown in Fig. 4.1.1. The early GMR structures employed thin spacer layers providing the indirect exchange coupling with antiferromagnetic alignment of FM layers which are antiparallel in zero magnetic field [GRU86, PAR90]. In FM/NM MLs, the spontaneous alignment of magnetic moments depends on the NM metal layer thickness d_{NM}. This is a result of exchange interaction which oscillates as $\cos(2k_F/d_{NM})$ where k_F is the Fermi wave vector. Magnetic configuration can be changed by applying an ex-

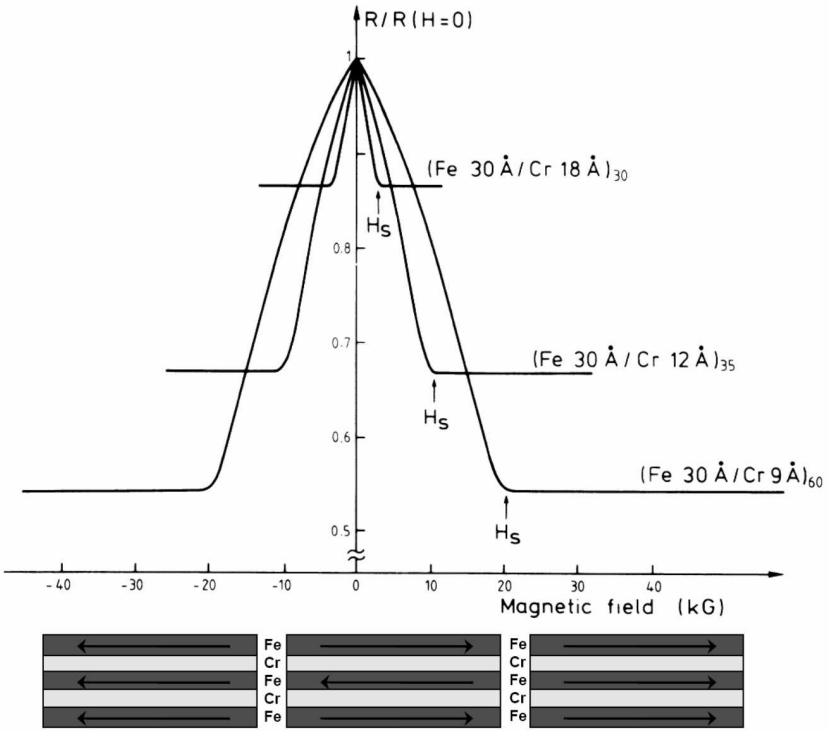

Fig. 4.1.1. GMR effect in Fe/Cr multilayers. The curves show relative changes of the resistance vs. an external magnetic field intensity [BAI88].

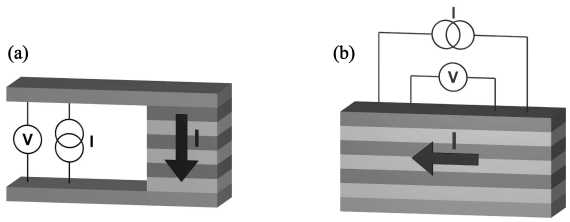

Fig. 4.1.2. CPP (a) and CIP (b) configurations of GMR.

ternal magnetic field. The magnetizations of magnetic layers rotate to align with the field and ferromagnetic configuration is achieved, i.e. magnetizations of magnetic layers become parallel. This process results in a lower resistance with the relative difference even larger than 100%. GMR is usually expressed as a ratio $\Delta R/R = [R(H) - R(H_s)]/R(H_s)$ where $R(H)$ is the resistance value at the magnetic field H and H_s is the saturation field. GMR ratio increases with decreasing temperature and growing number of multilayer periods.

GMR effect belongs to the most important discoveries in the solid state physics and material research in the last 30 years. The leading personalities in GMR research — P. Grünberg and A. Fert — were awarded by Nobel Prize in physics in 2007. Simultaneously with the research of GMR structures, the first applications of the GMR effect appeared. The main reason is that the GMR value is considerably larger than that of anisotropic magnetoresistance utilized at that time. At present, various sensors, magnetometers and reading heads of high density hard-discs based on GMR elements are produced [IBM03]. The GMR discovery renewed also interest in properties of magnetic systems and in the interplay between the spin and electronic transports [TSY01].

The GMR effect has been investigated in two basic configurations shown in Fig. 4.1.2. In the CIP (Current In Plane) geometry, the loading current flows in plane of layers, in CPP (Current Perpendicular to Plane) geometry it flows perpendicularly to the layers. The effect is stronger in the CPP geometry because of a more effective spin-dependent scattering of electrons. However, the CIP geometry is applied in practice because of a very small resistance of the structure in CPP configuration. Magnetic coupling between the FM layers and complex micromagnetic effects pose also some problems.

As it was mentioned above, in the first GMR multilayers the antiferromagnetic alignment of the layers in zero magnetic field was obtained by indirect exchange coupling. Exchange coupling oscillates between the parallel and antiparallel orientations in dependence on the thickness of the spacer layer (Fig. 4.1.3) [MTA99]. To observe the GMR effect, multilayers with the nonmagnetic layer thickness corresponding to the antiparallel alignment of the FM layer magnetizations are to be prepared. Fig. 4.1.3 demonstrates that spacers must be deposited with sub-nm precision. Consequently, the parallel alignment could be achieved and the drop of resistance is observed under an external magnetic field. However, as it was proved experimentally, any other method of the reorientation of mutual magnetizations of FM layers will result in GMR [TSY01].

Also mechanical straining of coupled magnetostrictive–magnetoresistive structures results in a change of magnetization direction which in turn leads to a change of magnetoresistance. The promise of these magnetic layer sensor structures lies in the coupled inherent sensitivity of the

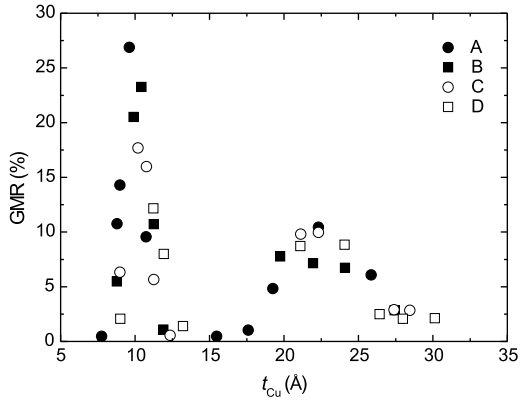

Fig. 4.1.3. Measured magnetoresistance versus thickness of the non-magnetic spacer layer for NiFeCo/Cu multilayers with different composition of magnetic layers. A, B, C, D correspond to the magnetic layer composition A - $Ni_{44}Fe_{10}Co_{45}$, B - $Ni_{48}Fe_{11}Co_{41}$, C - $Ni_{57.5}Fe_{13}Co_{29}$, D - $Ni_{59}Fe_{16}Co_{25}$. The thickness of magnetic layers is A - 2.1 nm, B - 2.4 nm, C - 2.5 nm, D - 1 nm. Number of periods is 12 [MTA99].

magnetostrictive layer, i.e., rotation of magnetic moments even at small amounts of stress and the associated large changes of resistance [DUE02].

An essential starting point of the existing, yet not well developed, theory of GMR is the two-current model [CAM], i.e. the existence of two types of conducting electrons (minority and majority) with different scattering mechanisms. A simple model of GMR origin in multilayers based on Fuchs-Sondheimer theory was worked out by Barnas and Camley [BAR89]. Later Zhang [ZHA92] presented a semiclassical model based on Kubo formula. In general, the basic aspects of GMR are understood qualitatively. The present discussion is focused on whether bulk or interfacial scattering is the dominant process. While the bulk spin dependent scattering is basically well understood, its interfacial counterpart is still subject of thorough studies. The importance of scattering at the interfaces was experimentally demonstrated [FUL92, PAR93] and its role in the bulk scattering models was put forward [PRA99]. According to this paper, the carriers responsible for GMR are flowing in a narrow strip in FM layer close to the FM/NM interface when only the bulk scattering is considered. Consequently, regardless whether either bulk or interface scattering processes or both of them are considered, the interface roughness will play a crucial role in the GMR effect.

To understand the origin of GMR, a simple resistor model is useful [EDW91]. However, it explains only the GMR behaviour in CIP geometry in a qualitative way. Here, each layer is represented by an independent resistor. If we consider that the mean free path of electrons is short in comparison with the layer thickness, the layers conduct the current independently and the corresponding resistors are added in parallel. In this case the ferromagnetic and antiferromagnetic alignments provide the same resistance and the GMR is zero. This is in agreement with experimental observations that for GMR the mean free path of electrons must be long in comparison to the layer thicknesses. The total resistance of the multilayer is related to the sum of scattering probabilities in each layer and each interface. This means that the resistors should be added in series [TSY01].

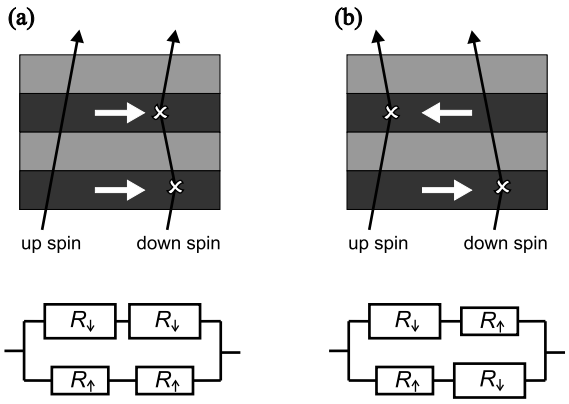

Fig. 4.1.4. Scheme of the electron scattering in the magnetic multilayer with parallel and antiparallel magnetization configurations as depicted by the arrows. The electron mean free path is longer than the layer thickness.
(a) The majority spin electrons pass the layered structure almost without scattering. The minority spin electrons are scattered by both ferromagnetic layers.
(b) In antiferromagnetic configuration, both majority and minority spin electrons are strongly scattered and the resistance of the system is larger.

The spin of an electron can be oriented as parallel (majority spin direction called spin up $\uparrow$) or antiparallel (minority spin direction called spin down $\downarrow$) with respect to the magnetization direction of a ferromagnetic layer. The resistance of the bilayer composed of a magnetic layer and a spacer in the direction perpendicular to the layers (CPP) is

$$R_{\uparrow\downarrow} = r_{NM} d_{NM} + r_{\uparrow\downarrow} d_{FM}, \tag{4.1.1}$$

where r_{NM} and d_{NM} are the resistivity and thickness of the nonmagnetic layer, respectively, and $r_\uparrow, r_\downarrow$ denote the majority and minority spin resistivities, respectively. The d_{FM} is the thickness of the FM layer. The resistance of the layered structure in Fig. 4.1.4 for FM configuration is

$$R_{parallel} = 2\frac{R_\uparrow R_\downarrow}{R_\uparrow + R_\downarrow} \tag{4.1.2}$$

and for antiferromagnetic alignment it is

$$R_{antiparallel} = \frac{R_\uparrow + R_\downarrow}{2}. \tag{4.1.3}$$

The GMR ratio is expressed as

$$\frac{R_{antiparallel} - R_{parallel}}{R_{parallel}} = \frac{(R_\downarrow - R_\uparrow)^2}{4R_\downarrow R_\uparrow}. \tag{4.1.4}$$

From this relation it is easy to show that a large spin asymmetry is necessary for large GMR. Low resistivity of the spacer layer is another important condition for large GMR value. The

effect of multilayer interfaces on GMR can be easily taken into account in the resistor model by adding additional resistors.

The first GMR structures were epitaxially grown Fe/Cr multilayers. It was shown by Parkin [PAR90] and later by other authors that good GMR multilayers can be prepared also by magnetron sputtering or by other physical vapor deposition techniques. In general, the GMR multilayers with antiparallel alignment of magnetic moments are not the most suitable structures for applications. They are technologically complicated because the layers 1 - 3 nm thick have to be deposited sequentionally with high precision and relatively high magnetic fields are necessary to rotate the magnetization. Shortly after the discovery of GMR, a new structure known as spin valve (SV) with the magnetization of one FM layer pinned and another one free to move in an external magnetic field was proposed by Dieny et al. [DIE91]. The magnetic moment can be pinned e.g. by an antiferromagnetic layer attached closely to the FM one or by an artificial antiferromagnet. Simple spin valve structures with magnetic layers of different coercivities were reported as well [WAN00]. When the magnetic system consists of materials with different coercivities, one of the layers switches into the direction of the external field before the others follow. The antiparallel alignment will not be reached at zero field but at the external field value which corresponds to the coercivity field of the soft magnetic material. The spin valve effect allows to switch easily between the parallel and antiparallel configurations.

Example of the spin valve structures are shown in Figs. 4.1.5 and 4.1.6. In Fig. 4.1.5, a structure with different coercivities of Co FM layers is shown. The structure in Fig. 4.1.6 consists of a magnetically soft ferromagnetic layer (free layer), a non-magnetic spacer layer and a pinned ferromagnetic layer which is exchange-coupled to the antiferromagnetic layer. The exchange coupling pins the magnetization of the ferromagnetic layer in a particular direction. The magnetic hysteresis loop of the pinned ferromagnetic layer is centered about a non-zero bias field, HB. The magnetic hysteresis loop of the free layer is centered close to zero field. The magnetic moments of two ferromagnetic layers are antiparallel in the field range between zero and HB.

In the field of GMR research, also granular films should be mentioned. Granular films with magnetic clusters embedded in a non magnetic matrix exhibit the GMR effect as well [BER92]. The magnetic clusters are usually distributed randomly in the bulk and have randomly oriented magnetic moments. When an external magnetic field is applied, the magnetic moments are aligned along the field direction and a drop of the resistance is observed. Granular films can be easily prepared from immiscible combinations of materials by codeposition. Usually, a post deposition heat treatment is necessary to improve the phase separation. However, large size dispersion of magnetic clusters is typical. This results in a lower sensitivity of the GMR vs. field (in [%/Oe] units) and high magnetic fields are necessary to align the magnetic moments.

A quasi-granular structure can be prepared by an appropriate thermal treatment of GMR multilayer composed of immiscible material pairs. Procedure proposed by Hylton [HYL93] to prepare discontinuous MLs (DMLs) allows to control the composition, to minimize the effects of shape and size distribution of magnetic clusters and thus to overcome the disadvantages of granular structures. The discontinuity arises from the break-up of magnetic layers upon annealing due to the grain boundary diffusion of atoms of NM layers into FM layers. Consequently, separated islands are formed. Here, the immiscibility is the unavoidable condition. It this case, the distribution of the islands is quite uniform and a lower size dispersion is achieved. DMLs have low saturation and larger sensitivity (given in [%/Oe] units) when magnetic field is applied along the easy direction of pancake shaped magnetic islands. The first DMLs were reported by

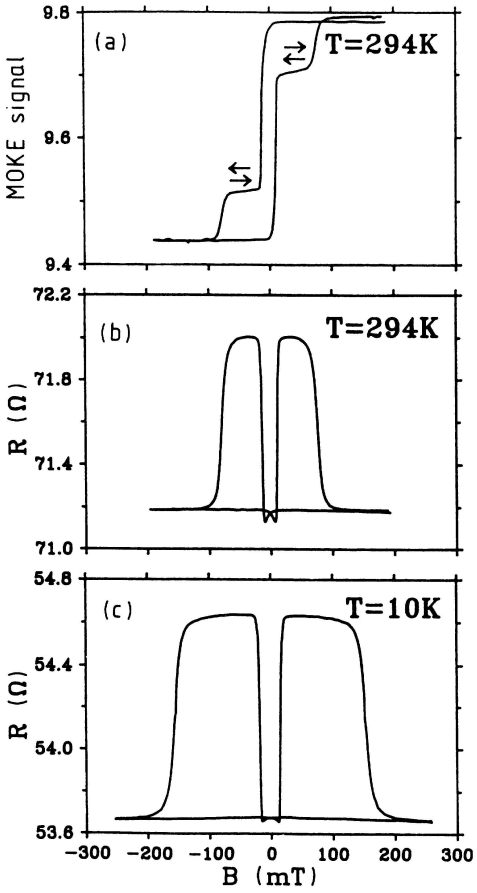

Fig. 4.1.5. An example of the pseudo spin valve Co(10 nm)/Au(6 nm)/Co(10 nm) [BAR90b]. The Co layers have different coercive fields. (a) $M(H)$ curves measured by MOKE, (b) and (c) $R(H)$ dependences.

Hylton et al. [HYL93] for Fe-Ni/Ag MLs, later Co-Ag/Cu, Fe-Co/Ag and Co/Ag DMLs [VIE97] were prepared. The GMR in DMLs is explained as a result of antiferromagnetic coupling between the magnetic islands in magnetic layers. Another way of preparation of granular films with uniformly distributed granular magnetic phase of low size dispersion could be the application of magnetic nanoparticles, as it will be shown later.

It should be mentioned that both the ordinary and anisotropic magnetoresistances are present in magnetic multilayers as well. Ordinary magnetoresistance is the result of the Lorenz force action upon the trajectory of an electron moving in the magnetic field. Anisotropic magnetoresistance originates from the dependence of the electrical resistance on the angle between magnetic field and direction of electric current as a consequence of the spin-orbit interaction. It should be noticed that both ordinary and anisotropic magnetoresistance values are about 1 - 2% whereas for GMR ration values of several tens of percents are common at RT [TSY01].

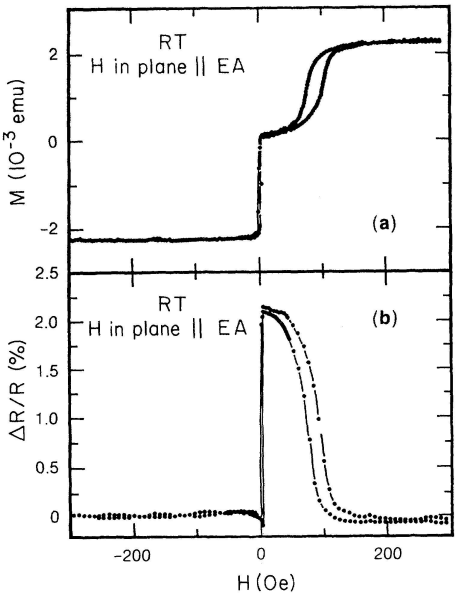

Fig. 4.1.6. $M(H)$ (a) and GMR vs H (b) dependences for Si/$Ni_{80}Fe_{20}$(15 nm)/Cu(2.6 nm)/ $Ni_{80}Fe_{20}$(l5 nm)/$Fe_{50}Mn_{50}$(10 nm)/Ag(2 nm) spin valve. HB denotes the exchange-bias field [DIE91].

The GMR was observed for several material combinations like Fe/Cr [SCHA94, SCHA95], Co/Cu [PAR91a], Co/Ag [ARA93, LUB98], Ni/Ag [ROD93a], Ni/Cu [SAT94], $Ni_{80}Fe_{20}$/Cu [TAK93], $Ni_{80}Fe_{20}$/Ag [ROD93b], $Ni_{80}Fe_{20}$/Au [PAR94] to mention some of them. On the other hand, there are various examples of magnetic multilayers without any GMR effect, like NiFe combined with Ta, Al, Cr or Pd [PAR90, BRU91, SHI93, JIN95, YAN97]. Recently it was shown that the features of the electronic band structures of FM and spacer materials are important for GMR observation. As it is pointed in Ref. [TSY01], a good band matching for one spin orientation between FM and NM materials and lattice matching of the subsequent layers are necessary for high GMR. The most studied GMR systems Fe/Cr and Co/Cu fulfill these conditions. One can assume that in the systems with a good band matching for one spin orientation, the scattering at the interface imperfections will be also spin dependent. Nevertheless, there are several types of structural defects present at the interfaces (grain boundaries, stacking faults, misfit dislocations, roughness) and the resulting scattering potential will be only weakly spin dependent. The scattering on the lattice imperfections in NM layers is spin independent and reduces the GMR value. The effect of the interface roughness on GMR will be discussed in the next section.

CIMS structures

The GMR effect is nowadays broadly applied in read heads of hard disks and in sensors of magnetic field. However, switching of free FM layer in GMR spin valves by an external magnetic

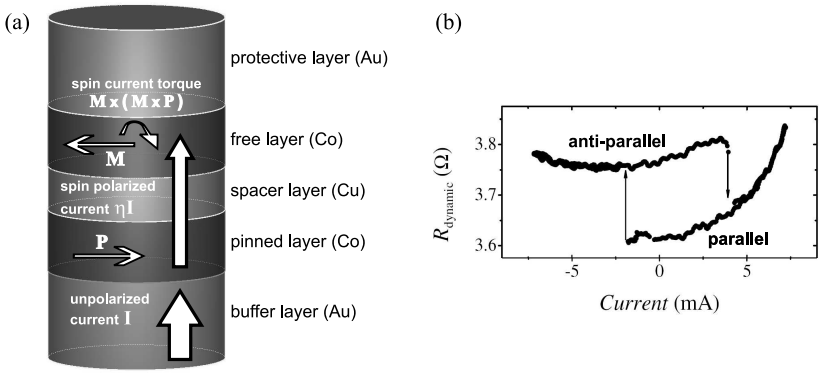

Fig. 4.1.7. (a) Principle of the GMR spin-valve current induced magnetization switching. (b) Spin-valve resistance vs. switching current (CPP geometry) [KOCH04].

field sets the limit for their further miniaturization. Therefore, the spin valve structures utilizing the current induced magnetization switching (CIMS) structures are studied and developed nowadays. A switching effect was theoretically predicted by Slonczewski [SLO96] and Berger [BER96]. Later it was experimentally confirmed [KAT00] and it has attracted a great deal of interest in many laboratories. Although the CIMS structures are beyond the scope of this paper, some basic information is presented below.

The dynamics of the magnetization $\vec{M}$ switching of the free layer in an external magnetic field $\vec{H}$ and the current I flowing through the layers (in the CPP geometry) is described by the generalized Landau-Lifshitz-Gilbert equation [SLO96, BER96, LIF, KOCH04] supposing monodomain nanomagnet structure

$$\frac{d\vec{M}}{dt} = \gamma\vec{M}\times\vec{H} - \left(\frac{\alpha\gamma}{\mathrm{m}}\right)\vec{M}\times(\vec{M}\times\vec{H}) - \left(\frac{\gamma\eta\hbar I}{2\mathrm{em}^2}\right)\vec{M}\times\left(\vec{M}\times\vec{P}\right). \qquad (4.1.5)$$

Here, $\vec{P}$ is the magnetization of the pinned layer, γ is the gyromagnetic ratio, α is the damping parameter, η is the spin-polarization factor, e and m are the electron charge and mass, respectively. The first term on the right side describes the precession of $\vec{M}$ in the magnetic field $\vec{H}$ and the second term, corresponding to the damping, aligns the magnetization $\vec{M}$ with the magnetic field $\vec{H}$ direction. The third spin-current torque term tends to flip the magnetization $\vec{M}$ into the $\vec{P}$ magnetization direction.

The classical GMR spin valve effect describes the first limiting case where the spin-current torque term is negligible with respect to the damping term. Here, the magnetization $\vec{M}$ of the free layer aligns into the external magnetic field $\vec{H}$ direction resulting in a change of the spin-valve magnetoresistance.

The second limiting case, when the spin-current torque term dominates over the damping term, corresponds to the discussed CIMS behaviour [FUC04, BHU]. The unpolarized current flowing through the pinned ferromagnetic layer gets spin-polarized along the $\vec{P}$ magnetization direction (Fig. 4.1.7a). In the free ferromagnetic layer, the spin-polarized current exerts the torque on its magnetization $\vec{M}$ flipping it in parallel with the magnetization $\vec{P}$ of the pinned

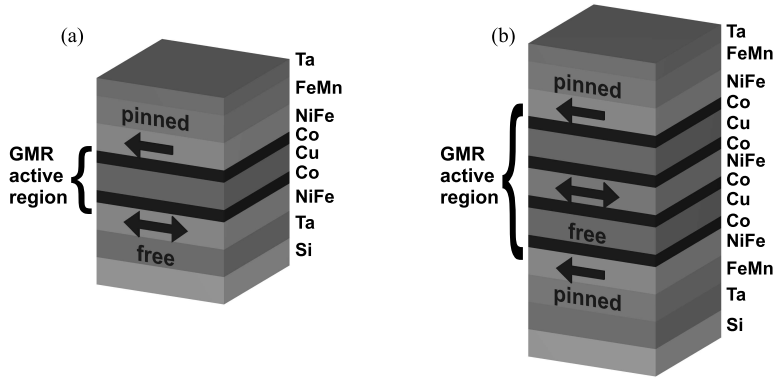

Fig. 4.2.1. Examples of SV structures used in GMR sensors.

layer. The process results in a change of the measured spin valve resistance (Fig. 4.1.7b). The switching current densities for CIMS devices are of the order of 10^7 A/cm^2 and must be lowered by two orders of magnitude for applications. Here, the structure and composition of individual layers, interface properties, layering, etc. have to be optimized.

The GMR CIMS devices are intensely investigated at present. The potential applications with high added value include magnetic field sensors, read heads for hard drives, galvanic isolator, etc.

4.2 Applications

As it was mentioned in the previous text, until the discovery of GMR, the anisotropic magnetoresistance (AMR) effect was utilized in magnetic sensors and read heads of magnetic disks. AMR was discovered already in 1857 by W. Thomson [THO57]. Here, the resistance change is a few percents only.

The first commercial applications of GMR appeared in the first decade after its discovery in 1988. In particular, we can mention the monitoring of machinery operations in mechanical and automotive industries (Non-Volatile Electronics in 1996, Siemens in 1997). An example is a GMR sensor which is placed close to a rotating ferrous gear. The direction of the magnetic moment of the soft magnetic sensor layer can be switched any time when a gear tooth passes the sensor if the field induced by the gear exceeds a critical value. Such sensors can be used as contactless potentiometers or for measurements of angles or distances. There are many other interesting applications of GMR sensors, e.g. in combination with magnetostrictive layers for strain sensing, as actuators or as magnetocouplers for the galvanic separation of signals (presently the domain of optocouplers) [NVE]. Wheel speed sensing for ABS brakes, low field detection in banking, vehicle detection for traffic counting, magnetic encoder detection for secure safes are other applications. High sensitivity/low field GMR materials will be used also in high accuracy compasses and in geophysical applications like magnetic field anomaly detection in the earth crust. Examples of SV structures used in sensors are shown in Fig. 4.2.1.

The employment of GMR effect in read heads of computer hard-disk drives introduced in

1997 by IBM is the most important application. These sensors replaced the AMR heads not only because the GMR effect is larger but also because it scales better. A typical structure of the spin valve used in the read head is 5 nm Ta/10 nm NiFe/2.5 nm Cu/2.2 nm Co/11 nm FeMn. Whereas in 1991 using the AMR heads the areal density of hard disk drives was 0.132 Gbites/inch^2, soon after the introduction of GMR read heads it increased up to 10 Gbites/inch^2 in 1999 and nowadays it reaches approx. 300 Gbites/inch^2.

GMR sensors are important also for bio-medical applications. As an example, a biosensor system based on the detection of magnetic beads can be mentioned. The chip consists of an array of GMR sensors able to capture and detect magnetic particles [RIF03].

5 Preparation of multilayer structures

Modern methods of X-ray multilayer fabrication were introduced at the beginning of 80-ies by Spiller [SPI80] and Barbee [BAR81]. The basic demands on the MLs preparation techniques are:

a) tight control of deposition process,

b) stability of deposition,

c) fast switching from one to another material,

d) high density of layers,

e) sharp boundaries of the width of atoms between layers.

Thermal (e-gun) evaporation and sputter deposition are the most widely used methods belonging to the category of physical vapor deposition (PVD). They produce multilayers with amorphous structures if the layers are thin enough which is especially true for semimetals, like C, Si, but also for metals as it was shown for tungsten ≤ 4 nm [LUB92].

The energy of condensing species associated with the process is of primary importance for deposition. For evaporation, it can be calculated as $E = \mathrm{k_B}T$, where $\mathrm{k_B}$ is the Boltzmann constant and T is the temperature of evaporation. Boiling temperatures of the respective elements like Be, Si, Mo, C, W at 10^{-7} Pa range from ≈ 1200 K to 2850 K [NES]. Therefore, the energy of evaporation is estimated to range from 0.1 to 0.25 eV and higher. For sputtering, typical energies are ≈ 10 eV which are acquired due to momentum transfer from bombarding ions with energies in the range of 1 keV.

Kinetic energies ≤ 10 eV create favourable deposition conditions for the growth of clean, dense and continuous layers with sharp interfaces. These energies allow decontamination of surface from adsorbed species and provide enhanced surface mobility of adatoms without considerable penetration into the structure. A further increase of these energies to 100 eV, which is much higher than the cohesion energy of lattice, leads to a deeper penetration and intermixing of deposited atoms across the interfaces. This phenomenon precludes e.g. application of cathodic arc deposition as a method of production of MLs for X-ray mirrors [SWI03].

On the other hand, kinetic energies at evaporation are too low and therefore evaporation is combined with ion bombardment. For example, Voorma et al. [VOO97] applied Kr^+ (300 eV - 2 keV) ion bombardment of every Si layer during Mo/Si ML deposition at an angle of incidence of 20° or 50° with respect to the substrate surface. This technique has been broadly studied also by other teams using also Ar^+ ions with energies between 200 eV and 1.5 keV and angles $\leq 45^o$ measured from the substrate surface [SCHL94, JER00]. A more simple approach how to increase the surface adatom mobility is *in-situ* substrate heating (e.g. to 160°C at Mo/Si evaporation [JER98]), however, here the intermixing should be born in mind.

The magnetron dc or rf sputtering became the most frequent method of ML deposition at present. The main advantage of sputtering is the stability of the sputtering rate which allows to minimize thickness errors. In comparison with the e-beam deposited MLs, lower roughness, mixing and interlayer formation due to the interpenetration and interdiffusion is observed in sputtered samples. This is explained by a longer distance surface migration of energetic sputtered

atoms. Sputtering can be used also on curved substrates [ATT], providing films with homogeneous thickness. In the case of evaporation, the distribution of deposited material follows a cosine law [SZE]. The thickness deposited per unit area is $\approx \cos\phi\cos\theta$. Here, ϕ is the angle between the (vertical, as a rule) axis of symmetry of the deposition system and the direction of deposition and θ is the angle between the axis and surface normal of the substrate. If evaporation source and deposition surface are both mounted onto a spherical surface, the mass deposited per unit area of the sphere is constant. Therefore, it is far from constant on the surface of large planar substrate. In both PVD methods, planetary rotations and shadow masks are used to improve the uniformity of depositions.

Besides magnetron sputtering, also ion beam sputtering has been successfully applied. The electron cyclotron resonance ion guns can operate at the Ar gas pressure of 10^{-7} Pa which is by two orders of magnitude lower than that at magnetron sputtering [SAK99]. It will be shown later that this method provides the best layered structures at present.

Multilayers composed of amorphous layers have almost reached their inherent maximum performance. Therefore as a technology for future, the growth of short-period epitaxial superlattices by molecular beam epitaxy (MBE) or other methods like atomic layer epitaxy (ALE) were considered and reviewed [KIN02]. In particular, Al-based metallic superlattices with ultrashort periods (less than 1.5 nm) were prepared by ALE and MBE. Such structures would allow further progress in mirror performance where amorphous MLs approached their inherent limits. The main problem is severe restriction in selecting suitable material pairs which leads also to compromising optical criteria. Compatibility of ALE and MBE techniques with pre-figured substrates is another issue to solve. Interdiffusion is prevented in immiscible combinations of materials. If such materials do not satisfy optical criteria at given wavelengths, interdiffusion of an optically suitable but miscible couple can be suppressed using a pair of materials in thermodynamic equilibrium or using compound layers instead of elemental ones. As an example, CrN/ScN superlattice mirrors for water window prepared by dc magnetron sputtering could be mentioned [BIR06]. Superlattice with 61 periods showed reflectivity comparable with Cr/Sc mirrors (7% at 398 eV and $\theta = 63.25°$), although the optical contrast must be lower because of nitrogen content. However, also interface width is low (0.2 nm) and thermal resistance and mechanical properties are much better because of nitrogen superhardening effect.

Pulsed laser ablation (PLA) is another deposition technique which is used for MLs fabrication. During 90-ies it moved from coating of small areas of ≈ 1 cm^2 [MAI92] to wafers with diameter of 4 - 6$''$ [DIE88, PAN96]. This progress has been achieved by dual (multi)-beam PLA in combination with rotating targets, motion of substrates and computer-controlled operation of lasers (e.g. Nd:YAG [DIE88]). Sophisticated target and substrate handling regime allows even deposition of graded period ML across 4$''$ substrate [HOLZ97]. The PLA Mo/Si MLs with 50 periods have shown the reflectivities of 60% at near-normal incidence of 13 nm radiation [BRA01].

Ablation is a complex mechanism of target erosion accompanied by the formation of dense plasma (plume) over it, hydrodynamic phenomena in the melted pool on the target, and ejection of debris. The temperatures of the target surface are computed to be over 5000 K at the fluences of 1 - 10 Jcm^{-2} per pulse but the kinetic energy of ablated species may be even 1 keV. This energy is much higher than the basic energy $\mathrm{k_B}T$ of ≈ 0.5 eV. The big kinetic energy of the species is not very appropriate for the ML deposition, as it was discussed earlier. Nor the second advantage of PLA – the stoichiometric transfer of multicomponent material from the target onto the substrate

(due to short localized interactions of laser beam with the target) [ACQ03] is substantial for the ML deposition. Moreover, it has been shown [ACQ05] that the transfer of a multicomponent material from the target onto the substrate is not completely stoichiometric and some deviations are observed due to the interactions between heavy and light elements in the plasma region. Following the model of hard sphere collisions, the light elements are expelled sideward from the axis of the deposition which was indeed observed. Therefore, deposited films are enriched in the higher atomic mass elements, especially at lower laser fluences. At the same time, PLA is quite expensive technique. Therefore, it cannot be expected that PLA can compete with well-established PVD techniques.

Much less has been published about the deposition of multilayers by chemical vapor deposition (CVD). Some results on the fabrication of MoO_x/SiO_x and WO_x/SiO_x oxide MLs in O_2 remote plasma are in papers [HAM00, HAM06]. Advantages are uniform deposition on shaped substrates and very smooth interfaces (rms roughness < 0.2 nm) due to the isotropic nature of CVD process. However, a heating of the substrate is needed in most cases and the layer thickness control on a nm scale is missing.

Up to now the problems of preparation of X-EUV multilayers were discussed. The strict conditions for performance of X-EUV multilayers to achieve the highest possible reflectance stimulated an intense development of thin film and multilayer deposition. At present, the best parameters are obtained for amorphous multilayers with layer thicknesses even below 1 nm prepared by sputtering techniques. For thicker metallic layers, small crystallites are sometimes observed (Mo layers in Mo/Si).

Different situation is for GMR and SV layered structures. As mentioned in Sec. 4, the first GMR multilayers were epitaxially grown structures. Later it was shown that the comparable results can be obtained by magnetron sputtering.

MBE was introduced in 1968 for the growth of thin films of $A_{III}B_V$ semiconductors. For the first time, film growth was controlled with atomic monolayer precision, being *in-situ* monitored with electron beam probes (high energy electron reflection and SEMPA-scanning secondary electron microscopy with polarization analysis). In this way, it was possible to control the film growth and composition in real time at the atom level. Utilization of MBE led to significant improvements in the performance of semiconductor devices. In late 1970-ies, MBE was applied to metal epitaxy and in 1986, high quality epitaxial magnetic rare earth superlattices were prepared [KWO87].

It was expected that MBE would enable preparation of high quality magnetic metallic structures which could exhibit new magnetic phenomena. These expectations were fulfilled. The rare earth superlattices Gd/Y and Dr/Y allowed to study the indirect exchange coupling through the nonmagnetic Y layers via RKKY interaction [KWO87]. Later superlattices and epitaxial sandwiches containing 3d transition metals were prepared and studied. Using MBE, artificially layered structures with antiferromagnetic interlayer exchange coupling [GRU86, CAR87], enhanced magnetoresistance [BIN89], and GMR [BAI88] were discovered.

In 1991, Parkin [PAR91a] showed that magnetron sputtered polycrystalline multilayers Fe/Cr, Co/Cr, Co/Ru exhibited antiferromagnetic interlayer exchange coupling which oscillated with spacer layer thickness. The value of GMR was comparable with that of MBE samples. This observation was important for the application of GMR as magnetron sputtering is widely used in the production. On the other hand, it opened the question about the role of structural defects and interface roughness on GMR. This question is not fully replied yet.

Whereas for the Fe/Cr multilayer systems, similar results of exchange interlayer coupling for sputtered and MBE samples are observed, the situation is more complicated for Co/Cu multilayers [PAR91b]. Clear oscillatory exchange coupling is observed for sputtered Co/Cu samples. However, for MBE grown samples, especially those grown as Co/Cu111, the results indicate the presence of growth-induced defects which can result in ferromagnetic bridging between the FM layers [HEI91, CAM96]. Permalloy/Au multilayers show GMR and oscillatory exchange coupling for both MBE and sputtered samples, nevertheless, their behaviour is not the same implying a strong effect of structural details on magnetic properties [FAR98].

In summary, MBE enabled to develop high quality magnetic superlattices, to understand the antiferromagnetic exchange coupling and it led to GMR discovery. For practical application it is important that sputtered multilayers can be used because sputtering is a production technology with high throughput. Therefore, both deposition techniques can be viewed as complementary for magnetic multilayers fabrication.

It should be noted that epitaxially grown metallic structures have usually compositionally sharp interfaces (not mixed), however, the interface roughness of such structures ranges between 0.3 - 0.9 nm. This means that it is comparable or even higher than for X-EUV multilayers prepared by sputtering or e- beam deposition.

6 Interface roughness and diffusion

6.1 Roughness as a result of growth process, roughness replication

Various geometrical imperfections of a surface or interface are generally referred as roughness. Substrate roughness and statistical nature of the flux of deposited entities (atoms, ions, molecules, clusters) are ever present extrinsic and intrinsic factors, respectively, which build up the roughness of a growing film surface. Roughness may have a significant effect on physical properties of the film if its lateral dimension is close to the characteristic length scale involved in the respective application. It should be noted that mainly roughness "on atomic scale" is considered in the following. The roughness evolution is generally governed by an interplay between kinetic energy of the deposited entities (referred further as adatoms) and their interaction with the growing surface which is controlled by thermodynamic properties of the materials involved. In particular, deposition conditions (energy, deposition angle, substrate temperature) interact with thermodynamic driving forces for $2D$ condensation or $3D$ cluster formation and shadowing effects.

For the deposition conditions close to thermodynamic equilibrium, the adatoms have sufficient time to relax into equilibrium lattice positions and to form monocrystalline-like structure. A structure prepared by molecular beam epitaxy (MBE) is a typical example. Further from equilibrium, different scenarios of the film structure formation are possible with an impact on the surface morphology. For $T/T_M < 0.5$, amorphous or columnar fine grain structure is obtained depending on the film thickness while for $T/T_M > 0.5$, there is enough adatom mobility for nucleation and crystallization and columnar structure disappears [PHA93]. Here, T and T_M are the substrate and melting temperatures, respectively. Amorphous films exhibit smaller roughness than polycrystalline ones as they are not affected by crystalline grains close to the surface. Amorphous films are formed at small thicknesses of several nm. Epitaxial films grown close to equilibrium on vicinal monocrystalline substrates also exhibit small roughness within terraces formed by step bunching.

Generally, surface diffusion length of atoms or molecules before a sticking site is reached controls the growing surface morphology. High-energy deposition, such as sputtering at a low working gas pressure below thermalization threshold, promotes lateral mobility of the adatoms and "heals" the roughness of the growing surface (conservative growth mode). On the other hand, a short diffusion length results in a formation of voids and overhangs enhancing the roughness (non-conservative growth mode) [SWA94]. UHV evaporation is an example. The former case occurs when the surface diffusion length is large enough to fill surface valleys [SAV92] while the latter one is typical for low lateral mobility of atoms or molecules and is well described by Kardar-Parisi-Zhang (KPZ) model of kinetic roughening [KAR86] or its older linear version worked out by Edwards and Wilkinson for small surface slopes [EDW82].

A generalization of the KPZ model describes the spatial and temporal behaviour of the surface growing in z direction by a Langevin equation [STE98]

$$\frac{\partial z(\vec{r},t)}{\partial t} = \nu \nabla^N z(\vec{r},t) + \frac{\partial \eta(\vec{r},t)}{\partial t}. \tag{6.1.1}$$

Here, ν is the relaxation coefficient controlling the surface diffusion length of adatoms and $\frac{\partial}{\partial t}\eta(\vec{r},t)$ is the white noise term describing the statistical nature of the adatom flux which results in the intrinsic roughness. The first term on the right-hand side describes the evolution of

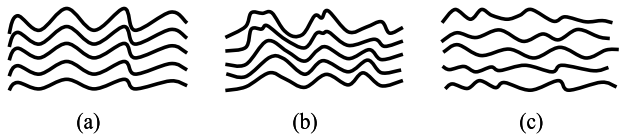

Fig. 6.1.1. Types of the interface roughness replication : maximum (a), partial (b), none (c).

the roughness inherited from the substrate (extrinsic roughness). The integer exponent N depends on the relaxation mechanism of adatoms, namely viscous flow ($N = 1$), evaporation and condensation ($N = 2$), bulk diffusion ($N = 3$) and surface diffusion ($N = 4$). For example, for high-energy deposition the case $N = 2$ corresponds to the sputter and redeposition of adatoms via atomic bombardment of the surface. Theoretically the growth becomes stationary for $t \to \infty$ but in practice it is reached at large length scales when the roughness gets saturated.

In the case of nanometer-scale ML structures, replication of the interface roughness is another important issue to consider. For example, interfaces with replicated roughness should be avoided in ML interference mirrors because they produce resonant diffuse scattering which lowers the optical performance [HOL94]. Replicated interface morphology in magnetic MLs produces Néel magnetostatic coupling [NEE62] which reduces the GMR effect and switching efficiency in spin valves.

The lateral adatom mobility is one of the factors controlling the roughness replication. There are different degrees of the interface roughness replication ranging from the maximum to zero one (Fig. 6.1.1). Low surface diffusion results in a better interface roughness replication. Moreover, the roughness inherited from the substrate (extrinsic roughness) propagates from the below lying to the above lying interfaces with the ever present intrinsic roughness produced by the stochastic nature of the deposition process, hence, the interface roughness is gradually accumulated towards the ML surface. Therefore totally correlated (identical) interfaces are never realized, even when the replication is at maximum (zero adatom mobility). On the other hand, high-energy deposition with long surface diffusion paths provides less replicated and less cumulative interface roughness.

In addition to the growth mechanism, different interface phenomena between constituting layers (see Sec. 6.2) may affect the surface diffusion of adatoms and thus contribute to the build-up of the interface roughness. Therefore roughness propagation in a ML is more complicated than in a single film and different scenarios are possible. If the interface phenomena do not dominate, the roughness evolution is directly related to the total thickness of the ML structure at a given instant of deposition. In this case, the replication of the roughness across particular interfaces, which were formed at different instants of time, reflects the growth mechanism and the KPZ model can be applied. Conservative growth mode has scarcely been observed in MLs (e.g. [HOU88]), the non-conservative one is a more frequent case (e.g. [FUL92, MIL92]). If the interface phenomena are of more importance, build-up of the interface roughness scales with individual layer thicknesses rather than with the total ML thickness [SAV92].

6.2 Interdiffusion, mixing and grain boundary diffusion

An interface between the layers of two different materials with a steep concentration gradient is a highly non-equilibrium structure. Miscibility, interdiffusion coefficients, compound formation ability and layer structure in terms of crystallinity are important factors determining interface stability at a given temperature. Typically, some interdiffusion and/or mixing at interfaces occur already during the deposition even at room temperature.

Interface phenomena are of special importance for thermal stability of ML structures with many interfaces, especially for those with small layer thicknesses approaching several nm, such as interference mirrors. Here, any compositional smearing at the interfaces lowers reflectivity. Yet, the interface phenomena are less detrimental than the roughness itself because smooth interdiffused interfaces only decrease reflectivity but do not contribute to the diffuse scattering [STE90]. Suppressed compound formation, low miscibility and low interdiffusion coefficients are general requirements for a material pair to form stable interfaces. The most stable interfaces are provided by material pairs in thermodynamic equilibrium which are formed by neighbouring crystalline phases in a phase diagram of a binary system separated by their own eutectic. High melting temperatures and similar thermal expansion coefficients of the constituents extend interface stability to high temperatures [KNI88, YAM92, ZIE92]. Amorphicity of the layers is an advantage not only because of smooth interfaces but also because of absence of grain boundary diffusion which is the fastest diffusion channel with the activation energy of 0.3 - 0.6 eV.

At elevated temperatures, interdiffusion followed by chemical reaction at interfaces may form interlayers which is typical e.g. for metal/silicon pairs in interference ML mirrors. Thin silicide interlayers may either act as amorphous diffusion barriers and stabilize the ML structure or they grow continually via interdiffusion and crystallize under a thermal treatment. Mo/Si and Co/Si pairs [PET87, HOL89a, STE90, WAN99] are the examples of the former group and Ni/Si [HOL89a], Ti/Si [HOL88] and W/Si [DUP90a, BRU93] of the latter one. Chemical reaction can immobilize adatoms and cause roughening which depends in a complex way on deposition angle, shadowing and agglomeration effects. Depending on an interplay of all these phenomena with the surface diffusion of adatoms, different scenarios are possible in different temperature ranges. Surface of the ML structure is the only interface exposed to the open air. To prevent chemical reactions with oxygen and/or water vapour, a protective capping layer is used. In metal/metalloid MLs, a metalloid layer (e.g. C, Si) is used as the top layer to avoid surface tarnishing.

If mutually immiscible materials are not applicable, interface phenomena may be suppressed by modification of a material pair to approach thermodynamic equilibrium, e.g. by lowering the concentration gradients. A way to do it is an admixing of one constituent into another one during the deposition which proved to be effective for metal/silicon pairs such as Mo/Si [KON93, STO93] or W/Si [DAN96, SEN97]. A negative consequence of using such compound layers instead of elemental ones, which is relevant for optical applications, is a reflectivity decrease. Application of thin interposed diffusion barriers (< 1 nm) at all interfaces or at every second one is another method (with a similar disadvantage) how to increase thermal stability. The Mo/C/Si/C [TAK96] and Mo/SiC/Si [MUR00a] are examples of the former and the latter, respectively. In both cases, the structures are stable up to 700°C instead of typical deterioration which begins in Mo/Si system already at 300°C. B_4C or Ru are other examples of diffusion barriers. Compound spacers are generally considered to be better following a simple argument that their decomposition is required before a new compound formation at interfaces begins [JAN90].

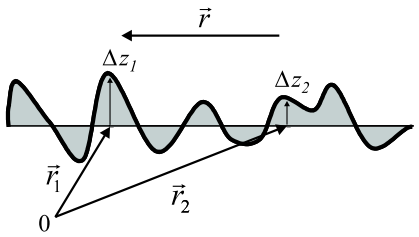

Fig. 6.3.1. To the definition of the autocorrelation function of an interface.

The most stable MLs are structurally coherent heteroepitaxial ones called superlattices which are grown at equilibrium conditions from compatible material pairs with the phase diagram as described above. The interfaces between monocrystalline-like layers are extremely flat and resistant against grain boundary diffusion. While such semiconductor superlattices are common, metallic ones are scarce due to the character of metallic bondings which aggravates preparation. For example, Al-based epitaxially grown metallic superlattices were successfully applied as soft X-ray short-period ML mirrors [KIN02] but a choice of convenient materials is rather limited.

6.3 Quantitative characterization of interface roughness

A proper quantitative description of the interface roughness and its replication is of primary importance for evaluation of the results of analytical non-destructive techniques for surface/interface characterization (see Sec. 7). There are different mathematical descriptions of the interface morphology depending on the interface type. For amorphous or polycrystalline layers, which are most common in magnetic and optical ML structures, randomly rough isotropic interfaces are typical and the concept of correlation functions may be applied. The autocorrelation function of a single interface

$$C(r) = \langle \Delta z(r_1) \Delta z(r_2) \rangle \tag{6.3.1}$$

describes the probability that the interface deviations Δz from a reference ideal interface with zero roughness are correlated over a certain lateral spacing $r = r_1 - r_2$ (Fig. 6.3.1). The averaging is done over all distances and directions along the interface. The asymptotic behaviour of the correlation function

$$\begin{aligned} \lim_{r \to 0} C(r) &= \sigma^2 \\ \lim_{r \to \infty} C(r) &= 0 \end{aligned} \tag{6.3.2}$$

is independent of the interface type. Here, σ is the root-mean-square (rms) value of the interface roughness. Fourier transform of the autocorrelation function, called power spectral density (PSD), describes the frequency spectrum of the interface roughness in terms of $f = 1/r$ values. The shape of the autocorrelation function or PSD between the asymptotic values is not known *a priori* and has to be postulated. Alternatively, the PSD in a frequency range may be found

experimentally (see Sec. 7) and the rms interface roughness may be then calculated as

$$\sigma^2 = \int_{f_{\min}}^{f_{\max}} \mathrm{PSD}(f)df. \tag{6.3.3}$$

The rms interface roughness represents a cutoff due to which the interface morphology scales differently in the lateral and normal directions. Therefore real interfaces are never true fractals but are self-affine.

Different types of self-affine autocorrelation functions for solid interfaces were proposed. The autocorrelation function

$$C(r) = \sigma^2 e^{-\left(\frac{r}{\xi}\right)^{2h}} \tag{6.3.4}$$

proved to be a good approximation in many cases [SIN88]. Here, ξ is the effective cutoff or lateral correlation length which determines how fast $C(r)$ approaches zero with increasing r. For $r \ll \xi$, the interface appears as true fractal while for $r \gg \xi$, the roughness goes to saturation value σ. Generally, low frequency components of the interface roughness favour large ξ values and *vice versa* while h parameter (Hurst or fractal parameter) is related to the "jaggedness" of the interface profile and determines the fractal dimension of the interface which is $D^f = 3 - h$. The autocorrelation function given by Eq. (6.3.4.) has no analytical expression of the Fourier transform and hence the PSD. This disadvantage is overcome by a so called K-correlation function [PAL93]

$$C(r) = P\xi^h r^h K_h\left(r/\xi\right), \tag{6.3.5}$$

where K_h is the modified Bessel function of the order determined by the Hurst parameter h and P is a constant related to σ as $\sigma^2 = P\xi^{h-1}2^{h-1}\Gamma(1+h)/h$. For the PSD this yields

$$PSD(f) = \frac{4\pi h\sigma^2\xi^2}{\left(1 + 4\pi^2 f^2\xi^2\right)^{1+h}}. \tag{6.3.6}$$

This PSD has a bell-like shape centered at $f = 0$ with the height and width proportional to $\sigma^2\xi^2$ and $1/\xi$, respectively. An alternative approach to scaling theories to express the PSD is based on the KPZ kinetic roughening model (see Sec. 6.1) which provides

$$PSD(f) = \Omega\frac{1 - e^{-2\nu(2\pi f)^N d}}{2\nu(2\pi f)^N}. \tag{6.3.7}$$

Here, Ω is the volume of the constituent element of the film (e.g. atom, molecule, cluster), d is the film thickness and the meaning of other parameters is the same as in Eq. (6.1.1).

In the ML structure, the cross-correlation function between the i^{th} and j^{th} interfaces reads

$$C_{ij}(r, z) = \langle \Delta z(r_1, z_i)\Delta z(r_2, z_j)\rangle. \tag{6.3.8}$$

The averaging is done over all distances connecting the two interfaces in all directions (Fig. 6.3.2). Specifically, the averaging can be decomposed into the lateral and vertical parts

$$C_{ij}(r, z) = \sqrt{C_i(r)C_j(r)}C\left(z\right), \tag{6.3.9}$$

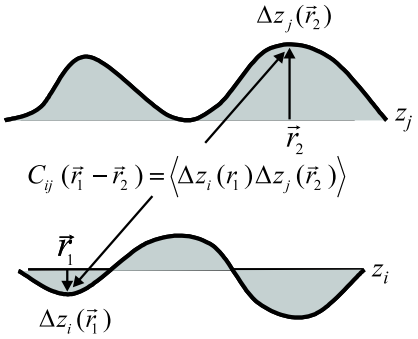

Fig. 6.3.2. To the definition of the cross-correlation function between two interfaces.

where $C(r)$ are the isotropic autocorrelation functions of the respective interfaces and $C(z)$ is the vertical correlation function where variable $z = z_i - z_j$ is the distance between the interfaces. The vertical correlation function describes the degree of replication of the interface morphology. A simple phenomenological model [MIN93]

$$C(z) = \mathrm{e}^{-\frac{z}{L_{vert}}} \tag{6.3.10}$$

with a single vertical correlation length $L_{vert} = \mathrm{const}$ postulates the same decay of the vertical interface correlation across the ML for all roughness frequencies. If applicable (see Sec. 6.1), a more realistic model of the interface replication relies on a microscopic model of the thin film growth. Using the Galileo transformation from the time to thickness scale at a constant film growth velocity, Salditt et al. showed [SAL96] that stationary solution (for $t \to \infty$) of the Edwards-Wilkinson (EW) equation [EDW82] provides the vertical correlation length

$$L_{vert}(f) = \frac{1}{\nu (2\pi f)^2}, \tag{6.3.11}$$

where the exponent of 2 may be generally replaced by an integer N of the same meaning as that in Eq. (6.1.1). It can be seen that a low value of the relaxation coefficient ν favours the interface replication for a given f value (large L_{vert}) and *vice versa*. On the other hand, the replication decays faster for higher roughness frequencies.

Alternatively, the cross-correlation function is not divided into lateral and vertical parts but the recursive approach is applied to describe evolution of the interface morphology. The approach via PSD provides a simple formula

$$\mathrm{PSD}_i(f) = a_i(f)\mathrm{PSD}_{i+1}(f) + \mathrm{PSD}_{\mathrm{int}}(f), \tag{6.3.12}$$

where indexing starts from the ML top, $a_i(f)$ is a replication factor and $\mathrm{PSD}_{int}(f)$ refers to the film grown on a perfectly smooth substrate (intrinsic roughness). Relying on Eq. (6.1.1), the replication factor for layer thickness d_i reads [SPI93]

$$a_i(f) = e^{-4\pi^2 \nu d_i f^2}. \tag{6.3.13}$$

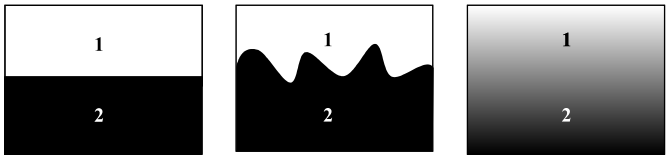

Fig. 6.4.1. Different interface types - ideal (a), geometrically rough and compositionally sharp (b), compositionally graded and geometrically smooth (c). The real interfaces are geometrically rough and compositionally graded simultaneously.

Obviously, putting Eq. (6.3.11) into Eq. (6.3.10) gives the same replication decay as that described by Eq. (6.3.13) so that both approaches are equivalent. The first term on the right-hand side of Eq. (6.3.12) describes the contribution partly inherited from the below lying interface. It can also be seen that the interfaces are not identical even for zero relaxation coefficient ν because of the intrinsic roughness. The roughness evolution across N interfaces reads in that case [HOL94]

$$\sigma_i = \sqrt{\sigma_N^2 + (N-i)\sigma_{int}^2}, \tag{6.3.14}$$

where indexing i starts from the top and σ_N refers to the substrate roughness.

6.4 Effect of interface roughness and diffusion on optical properties of X-EUV multilayers

Different types of interfaces can be seen in Fig. 6.4.1. Compositionally sharp and topologically smooth interfaces (Fig. 6.4.1a) with good optical contrast are required for high reflectivity of X-EUV MLs. Typical combinations are W, Mo, Nb, Pt, Ru, Rh, Ni, Co, Fe, Tb, Gd, Cr with C, Si, B, Al, Be, Sc, Ti, B_4C, BN, SiC. The absorber limits the number of periods which in turn limits the selectivity or bandwidth of the reflection peak. A more exact criterion says that the material with the lowest possible absorption be selected first as a spacer material and then a second material (absorber) be selected with the largest possible reflection coefficient at the boundary with the first one [SPI].

Atomic-scale surface or interface roughness (Fig. 6.4.1b) causes scattering losses and lowers the specular reflectivity but more importantly, it produces non-specular (diffuse) scattering. This scattering concentrated around Bragg reflections of the periodic ML (see Sec. 7) reduces the imaging contrast when it falls into the field of view. On the other hand, interdiffusion and chemical reactions at the interfaces are less detrimental for the optical performance because diffuse but smooth interfaces (Fig. 6.4.1c) only decrease the reflectivity [SPI, STE90]. Moreover, these reflectivity losses may be compensated by reflection from deeper interfaces if a large enough number of interfaces are penetrated. Because a ML with steep concentration gradients at the interfaces is inherently unstable, it may experience interface degradation under heavy-duty operation conditions (e.g. at synchrotron beamlines, intense plasma source diagnostics) with an irreversible loss of reflectivity. Therefore a reasonable interface quality must be preserved also at elevated temperatures. Thermal stability of MLs is enhanced by a proper material choice or

by application of barrier layers as described in Sec. 6.2. Thermodynamic and optical criteria are often contradictory and the choice depends on a particular application.

As mentioned before, amorphous layers are generally preferred in X-EUV MLs as crystalline grains may contribute to the interface roughness and mediate the grain boundary diffusion resulting in discontinuous layers. Atomically flat stable interfaces were achieved in metallic superlattices which were tested for mirror applications. In particular, Al-based metallic superlattices with ultrashort periods (less than 1.5 nm) prepared by atomic layer epitaxy (ALE) and MBE [KIN02] show the way for a further progress in optical performance where amorphous MLs approached their inherent limits. The main problems are a limited material choice compromising the optical criteria and compatibility of ALE and MBE techniques with pre-figured substrates.

The attenuation factor for the X-ray reflectivity (XRR, see Sec. 7) characterizing the interface roughness increases rapidly with reduction of the ML period if the effective interface roughness (interface width) is not reduced in the same way. Therefore the interface quality becomes inherently crucial for the layer thicknesses below 1 nm which become comparable to the interface roughness itself. For example, the rms interface roughness of 0.1 nm reduces the reflectivity by $\approx 50\%$ for the period of 1 nm. Actually, the ability of a material pair to yield structures with minimum interface roughness rather than X-ray optical constants is important for ultrashort period MLs [SCH00]. The materials must also provide continuous layers. The critical thickness is mostly 0.5 - 1 nm. No less is important the uniformity of the interfaces and the ML stack as a whole. It was shown [BIB05] that period fluctuations should not exceed $\approx d/N$ (d - period, N - number of periods) which gives fluctuations less than 0.0025 nm for $d = 1$ nm and $N = 400$. The issue of thermal stability is also more critical than in conventional MLs. Therefore ultrashort period MLs are challenging for thin film technology and materials science generally. The deposition process requires a tight control, stability and fast switching between the materials. The application field of ultrashort period MLs encompasses soft X-ray microscopy in the water window between K absorption edges of oxygen and carbon (2.33 - 4.36 nm) (e.g. V/Al_2O_3 [NEF01], Ni/C/Ti/C [TAK01], W/Sc and Cr/C [AND03]) and coatings of hard X-ray telescopes above 50 keV (e.g. W/Si and Pt/C [MAO99]). As it follows from the attenuation factor for the XRR (Sec. 7), the interface roughness is more detrimental for hard X-rays.

Potentially the most important optical application of MLs is the extreme ultraviolet lithography (EUVL). It is based on the reflection optics operating near 13.4 nm. Quality of the respective mirrors in terms of the overall efficiency and photon throughput of the exposition equipment was discussed in Sec. 2.2.

7 Reciprocal space analysis techniques

For the analysis of interfaces and ML structure in the reciprocal space, X-ray scattering is the most widespread method. Collecting the signal from a large sample volume, it is statistical in the direct space but local in the reciprocal space of scattering vectors. In this aspect, it is complementary to local direct space methods such as different kinds of microscopies. Moreover, the X-ray scattering is a non destructive method, probing simultaneously the surface and buried interfaces. The information obtained is indirect so that the interpretation of the results requires application of underlying theories of the X-ray scattering to proper structural models.

X-ray diffraction (XRD) is a well established method based on constructive interference of X-rays produced by spatial correlations of the electronic density on the atomic scale. It gives insight into atomic structure of the layers in a ML. If the layers are polycrystalline, lattice parameters, microstrain and stress may be determined in standard ways from diffraction patterns [SNY99]. However, the signal from thin layers is often very low which aggravates the analysis. Grazing incidence (GI) geometry is helpful in that case. Firstly, the substrate signal is suppressed or eliminated and secondly, the X-ray beam path in the layer is prolonged and the irradiated volume is larger. Texture produced by the asymmetry of the deposition process and influenced by the substrate crystalline structure is often present in polycrystalline layers. Usually, the film grows as a stack of planes with the largest atomic density, typically (111) and (110) for body-centered cubic (bcc) and face-centered cubic (fcc) structures, respectively. If all layers in the ML are grown in that way, structural coherence resembling the superlattice is established between the layers. In the diffraction pattern of such a periodic multilayer, satellites (Laue oscillations) around a central peak appear. While the position of the central peak depends in a complex way on the lattice parameters of the constituent layers, the satellite distance is related to the ML period.

Specular X-ray reflectometry came to common use some 30 years ago as a convenient tool for the determination of thin film parameters such as roughness, thickness and density. The evaluation of the specular X-ray reflectivity (XRR) could profit from the well established Fresnel optical theory elaborated originally for visible light. Parrat proposed an optical recursive algorithm for the calculation of the specular XRR from stratified media many years ago [PAR54] and nearly 30 years later, Underwood and Barbee applied it to ML structures [UND81]. The Fresnel approach inherently includes refraction, extinction and absorption effects but no interface roughness and for the XRR of an ideal interface with zero roughness it leads to the $1/\sin^4\theta$ decay above the critical angle for the total external reflection where θ is the angle of incidence measured from the sample surface. Therefore, the XRR is measured not far above the critical angle in grazing incidence geometry with laboratory X-rays sources (wavelength $\lambda = 0.1$ - 0.2 nm). The critical angle θ_c takes up the values of several tenths of degree in this wavelength range.

The calculation of the XRR of a ML with ideal interfaces (periodic or non-periodic) starts at the substrate which is considered to be semi-infinite, i.e. the reflectivity from its bottom is zero. The reflected amplitude from a particular interface is calculated by summation of its Fresnel reflection coefficient and the reflectivity contribution from the below lying interface which is modified by a phase shift across the involved layer -

$$R_{i,i+1} = a_i^4 \left(r_{i,i+1} + \frac{R_{i+1,i+2} t_{i,i+1} t_{i+1,i}}{R_{i+1,i+2} r_{i,i+1} + 1} \right). \tag{7.1}$$

Here, the indexing starts at the ML top, r, t are the Fresnel reflection and transmission coeffi-

cients, respectively, and the phase factor a_i reads

$$a_i = \exp\left(-\frac{i\pi d_i\sqrt{n_i^2-\cos^2\theta}}{\lambda}\right) \quad \text{and} \quad a_i = \exp\left(-\frac{i\pi d_i\sqrt{n_i^2-\cos^2\theta}}{n_i^2\lambda}\right) \tag{7.2}$$

for s and p polarization, respectively, where d_i and n_i are the layer thickness and refractive index, respectively. The calculation proceeds separately for both polarizations up to the ML top giving the resulting amplitude and subsequently the specular XRR as $R_0 = R_{12}R_{12}^*$. It is a good approximation at grazing incidence which is the geometry applicable for XRR measurements.

To apply this recursive approach to real MLs, interface imperfections discussed in Sec. 6 have to be incorporated. In a kinematical theory of the X-ray scattering (the first Born approximation), the reflectivity of a real interface is governed by the Fourier transform of the partial derivative of the interface profile function expressed via the refractive index

$$R = R_0\,\mathrm{FT}\left(\frac{\partial n(x,y,z)}{\partial z}\right), \tag{7.3}$$

where the z coordinate is perpendicular to the averaged interface. Both the geometrical roughness (Fig. 6.4.1b) and compositional grading (Fig. 6.4.1c), which are usually present simultaneously, enter this z projection. Therefore the two effects cannot be practically distinguished from the specular XRR measurement though higher-order effects do cause some subtle difference ([DEB94, DEB96]). The most common error function interface profile provides a Gaussian attenuation factor of the Debye-Waller type [STE89]

$$DWF = \mathrm{e}^{-q_z^2\sigma_{eff}^2}, \tag{7.4}$$

which was defined in Sec. 3.1. in a different but complementary way. Here, $q_z = 4\pi\sin\theta/\lambda$ is the normal component (perpendicular to the interface) of the scattering vector $\vec{q} = \vec{k}_2 - \vec{k}_1$ (wave vector transfer from the incoming wave vector $\vec{k}_1$ to the outgoing one $\vec{k}_2$) and σ_{eff} is the rms effective interface roughness (interface width) including all types of the interface imperfections. A steeper exponential interface profile leads to the Lorentzian attenuation factor giving a slightly higher reflectivity. Other interface profiles [STE89] are less common. Nevot and Croce treated the problem within a dynamical scattering theory which takes into account multiple scattering effects [NEV80] and arrived at a more precise expression

$$NCF = \mathrm{e}^{-q_z q_z^t \sigma_{eff}^2}, \tag{7.5}$$

where q_z and q_z^t are the normal components of the scattering vector above and below the involved interface, respectively, which are different due to the refraction. The *NCF* is general because it transforms into *DWF* far above the critical angle for the total external reflection where the refraction plays a negligible role.

The simplest way to include the attenuation factor into the recursive formula (7.1) is to multiply the total specular XRR from ideal interfaces which inherently implies a perfect replication. Another possibility is the multiplication of each Fresnel reflection coefficient with a simultaneous modification of each transmission coefficient by a corresponding factor (graded interfaces with no scattering losses into non-specular directions) as it was discussed by De Boer [DEB95].

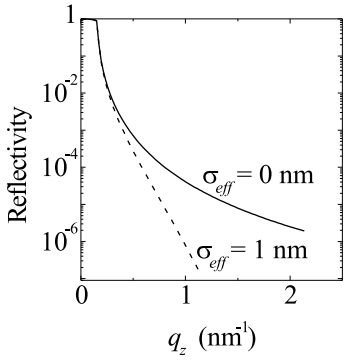

Fig. 7.1. Effect of the effective interface roughness on the specular XRR of silicon at CuK_α wavelength.

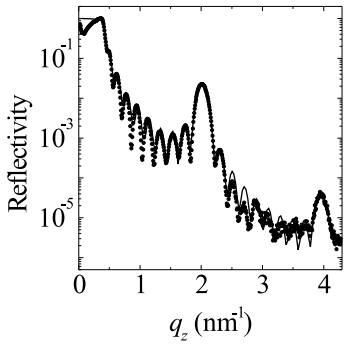

Fig. 7.2. Specular XRR of the nominally (1.2 nm Cu/2.2 nm Si)×10 ML measured using CuK_α radiation $\lambda = 0.154$ nm (dots — measured points, line — fit).

Finally, the modification of the transmission coefficients may be omitted (geometrically rough interfaces producing the diffuse scattering). The way of incorporation of the attenuation factor plays a role only close to the critical angle where the compensation of the reflectivity loss due to graded interfaces by an increased number of the penetrated interfaces may be effective [SPI88].

Figure 7.1 demonstrates that already $\sigma_{eff} = 1$ nm produces a much steeper XRR decay than that for the ideal single interface. It follows also from the expressions for *DWF* and *NCF*, that the detrimental effect of the effective interface roughness on the XRR increases with decreasing wavelength. The specular XRR of a periodic ML (Fig. 7.2) exhibits larger Bragg maxima and smaller finite-size Kiessig fringes connected with the ML period and total thickness, respectively, by the Bragg equation corrected for refraction

$$m\lambda = 2d\sqrt{n^2 - \cos^2\theta}, \tag{7.6}$$

where m is the interference order and $n = 1 - \delta - \mathrm{i}\beta$ is the mean (volume weighted) refractive index of the multilayer. The square root in Eq. (7.6) becomes real above the critical angle θ_c for

the total external reflection which gives

$$\sin\theta_c \approx \sqrt{2\delta} \tag{7.7}$$

neglecting absorption ($\beta = 0$). The decrements δ, β of the refractive index are proportional to atomic densities of the constituting layers so that the position of the critical angle is controlled by the layer densities while the positions of Bragg maxima and Kiessig fringes give access to the ML period and total thickness, respectively. Therefore, some parameters of the ML may be evaluated also directly from the XRR curve but the most precise and complete evaluation is based on the fitting of the measured XRR based on the Fresnel theory as that shown in Fig. 7.2. The attenuation factor incorporating the interface roughness causes a gradual damping of Bragg maxima towards higher angles but does not cause any additional peak broadening. The *DWF* for the m^{th} Bragg order belonging to the ML period d can be written as

$$DWF = e^{-\left(\frac{2\pi m\sigma_{eff}}{d}\right)^2}, \tag{7.8}$$

which shows an enhanced detrimental effect of the interface roughness for ultrashort period MLs.

Geometrical interface roughness (Fig. 6.4.1b) causes a redistribution of a part of the scattered intensity away from the specular direction. The effect is called X-ray interface diffuse scattering (XRIDS). Spatial distribution of the XRIDS bears wealth of information on the morphology and replication of the interface roughness. Being sensitive only to geometrical interface features, the XRIDS allows also to extract the geometrical (i.e. genuine) interface roughness from the total width of real interfaces as determined by the XRR. However, the underlying theory of the XRIDS was worked out much later than that of the XRR which prevented from its practical utilization for a long time. Sinha et al. [SIN88] were the first to calculate the XRIDS from a single interface (surface) both within the Born approximation (BA) and a so called distorted-wave BA (DWBA). Soon afterwards, Stearns extended the theory to a ML within the BA [STE89] while the DWBA extension was done later by Holý et al. for uncorrelated [HOL93] as well as correlated [HOL94] interface roughness. Some time later, De Boer refined the DWBA to the second order for a single interface [DEB94] and for a ML [DEB96].

The calculation of the XRIDS relies on the wave equation for an elastic scattering process

$$(\Delta + \vec{k}^2)E(\vec{r}) = V(\vec{r})E(\vec{r}) \tag{7.9}$$

where $\vec{k}$ is the wave vector in vacuum, $E(\vec{r})$ is the amplitude and $V(\vec{r})$ is the scattering potential proportional to the electronic density. The solution in vacuum ($V(\vec{r}) = 0$) leads to plane waves which may be used to start the solution in real systems ($V(\vec{r}) \neq 0$) in the form of Born series (Fraunhofer approximation). In the first BA (kinematical solution), multiple scattering effects are neglected and the solution diverges when the incidence angle approaches zero. A better approach is the DWBA where the scattering potential is expressed as $V(\vec{r}) = V_{id}(\vec{r}) + V_d(\vec{r})$ where $V_{id}(\vec{r})$ and $V_d(\vec{r})$ are the scattering potentials of an ideal system and a disturbance, respectively. Consequently, the perturbation theory is applied. While in the BA the ideal system is vacuum and the whole sample (multilayer with the substrate) is the disturbance, the DWBA considers the multilayer with ideal interfaces and the interface roughness as the ideal system and the disturbance, respectively. Fresnel theory yields exact eigenstates for the undisturbed system (ideal ML) where only the specular XRR occurs while in presence of the interface roughness,

the solution is composed of the coherent (specular XRR) and incoherent (XRIDS) parts. It is more practical to calculate the coherent part by means of the complex Fresnel and attenuation coefficients (see above) while the incoherent part must be calculated by the DWBA.

In the DWBA, the incoherent scattering cross-section for a random disturbance potential $V_d(\vec{r})$ is given by the covariance [HOL93]

$$\left(\frac{d\sigma}{d\Omega}\right)_{\text{incoh}} = \frac{1}{16\pi^2}\text{Cov}(W) = \frac{1}{16\pi^2}(\langle WW^*\rangle - \langle W\rangle^2) \tag{7.10}$$

of the matrix element

$$W = \sum_i \langle E_i^{(2)}|V_d|E_i^{(1)}\rangle = \langle E_{id}^{(2)}|V_d|E_{id}^{(1)}\rangle \tag{7.11}$$

obtained by the summation over particular interfaces. This matrix element gives the probability of the scattering from the initial state $|E_{id}^{(1)}\rangle$ into the final state $\langle E_{id}^{(2)}|$ on the disturbance potential V_d. Because these states correspond to two different wave fields of the undisturbed system, the XRIDS is calculated in the basis of the eigenstates of the ideal ML. Furthermore, as multiple scattering effects in the incoherent part of the scattering cross-section are neglected, the DWBA treats the XRIDS kinematically while the coherent part is calculated fully dynamically. The disturbance potential V_d of randomly rough interfaces is included into calculations via lateral and vertical correlation functions (see Sec. 6.3). The lateral component of the scattering vector $q_{lat} = \sqrt{q_x^2 + q_y^2}$ is connected with a particular frequency of the PSD, on which the wave vector transfer takes place, as $q_{lat} = 2\pi f$. The resulting XRIDS intensity is then obtained as a configurational average of the differential scattering cross-sections over randomly rough interfaces.

It is worth noting that the DWBA describes not only the diffuse scattering of the transmitted component of $|E_{id}^{(1)}\rangle$ into the transmitted component of $\langle E_{id}^{(2)}|$ (direct scattering) but also the diffuse scattering from (and/or into) the reflected components (*Umweganregung* effect). These secondary processes correspond to the diffuse (incoherent) scattering of a specularly (coherently) reflected wave and/or coherent reflection of the diffusely scattered wave and give rise to sharp XRIDS spikes which are called Bragg-like (BL) maxima. This situation occurs as soon as the angle of incidence or exit fulfills the Bragg Eq. (7.6). The BL maxima are of dynamical origin and their occurrence indicates a regular good-quality periodic ML. Another distinct XRIDS effect is the resonant diffuse scattering (RDS) due to the constructive interference of the waves scattered diffusely on at least partially replicated interfaces which is a purely kinematical effect. In the reciprocal space, banana-shaped sheets of enhanced XRIDS intensity around the ML Bragg maxima can be seen (Fig. 7.3). The RDS reduces the specular contrast for imaging in the ML mirrors, hence, the interface replication should be minimized here. The vertical interface correlation affects also the BL maxima. For uncorrelated roughness, the BL maximum follows the intensity of the standing wave field at the interfaces and is typically S-shaped but different for different Bragg orders. Even a slight vertical interface correlation [KAG96] as well as an asymmetry between the A/B and B/A interfaces [SIN95] changes the shape of the BL maximum depending on the order of the RDS sheet where the BL maxima are superimposed.

When the secondary scattering effects such as the BL maxima are weak, a semikinematical approach to the DWBA is sufficient [JER98]. Here, the substrate is taken as the undisturbed

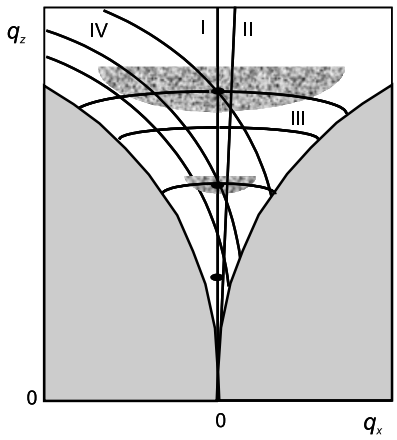

Fig. 7.3. Trajectories of different scans in the reciprocal space : I - specular scan, II - offset scan, III - sample scans (rocking curve scans), IV - detector scans. All scans start at limiting Ewald spheres and intersect in different ways the sheets of the RDS around the ML Bragg points.

system and the whole ML including the interface roughness is considered as a disturbance. Then, the eigenstates contain only one plane wave (the transmitted one propagating in the substrate) and the matrix element of the disturbance V_d describes only one primary scattering process between these components which facilitates the calculation.

From the principle of the perturbation theory putting some restrictions on the disturbance it follows that the DWBA works well for $q_z^2\sigma^2 \ll 1$ [SIN88, DAI99] where q_z and σ are the normal component of the scattering vector and the rms geometrical interface roughness, respectively. For the wavelengths of 0.1 - 0.2 nm provided by laboratory X-ray sources, the condition $\sigma \leq 5$ nm in the common q_z interval should be fulfilled [NEV88]. Regardless this condition, the DWBA fails also at large q_z values where the Fresnel eigenstates are not a proper description of the system any more and the BA is applicable instead.

The specular XRR and XRIDS are measured on common X-ray diffractometers in reflection geometry. Parallel beam with a low divergence as that provided by Göbel mirrors is an advantage owing to the typical grazing incidence geometry. Interference features in the XRR and XRIDS usually do not put strong requirements for the experimental resolution but a large dynamic range of the measured intensity approaching 8 - 9 orders of magnitude is necessary due to a rapid intensity decay with increasing incidence angle. In terms of the reciprocal space, the XRR and XRIDS measurements probe the intensity distribution close to the origin by different types of scans (Fig. 7.3). The specular XRR is measured in the symmetrical reflection geometry while the XRIDS may be traced by a series of the sample (detector) scans with the detector (sample) fixed and the sample (detector) moving or by a specular scan with an offset. Intensity distribution over a part of the reciprocal space (reciprocal space map - RSM) can be obtained by a series of such scans. The evaluation starts with the specular XRR which provides basic ML parameters in terms of the layer thicknesses, layer densities and effective interface roughnesses (interface widths). These parameters are further used for a simultaneous fitting of several XRIDS curves which provides the geometrical interface roughness in terms of the rms values, scaling properties

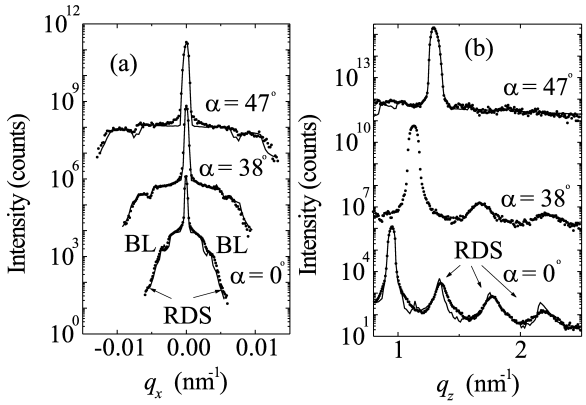

Fig. 7.4. Sample scans (a) and detector scans (b) taken on a series of W/Si MLs deposited by electron beam UHV evaporation under different angles α from the substrate normal as indicated [JER95]. The curves for nonzero α values are shifted upwards for clarity. The RDS brings about a strong diffuse background around the specular peak in the rocking curves and non-specular peaks in the detector scans which extinct with increasing deposition angle indicating a replication decay. The S-shaped BL maxima on the rocking curves (a) are clearly visible (dots — measurement, line — fit). The results reflect the influence of a shadowing effect of surface roughness on the ML growth.

and lateral and vertical correlation parameters depending on the autocorrelation and vertical correlation functions, respectively, used (see Sec. 6.3). These correlations modulate the otherwise monotonous distribution of the XRIDS as it is schematically shown in Fig. 7.3 and experimentally demonstrated in Fig. 7.4 where both RDS sheets and BL maxima are visible. Comparing the values of the effective and geometrical interface roughness, a compositional grading at the interfaces may be detected.

Figure 7.3 refers to the mostly used coplanar geometry where the scattering plane given by the $\vec{k}_1$ and $\vec{k}_2$ wave vectors is perpendicular to the sample surface. Here, the limiting Ewald spheres restrict considerably the lateral wave vector transfer q_x ($q_y = 0$) and thus also the accessible frequency range of PSD. The detector slit is positioned normal to the scattering plane, hence, the intensity along the q_y axis is integrated. Utilization of a pinhole collimator allows to obtain resolution and to perform measurements also along the q_y axis in a non-coplanar (out-of-plane) geometry with a much larger lateral wave vector transfer. However, the DWBA evaluation is more complicated in this case. In the case of a single interface (surface), the PSD can directly be obtained from such a measurement at a constant q_z.

It has to be stressed that the XRIDS, being distributed over the whole solid angle, enters always the specular XRR measurements depending on the slit width. Moreover, the specular XRR itself decays with the angle of incidence faster than the XRIDS as it was shown theoretically [DAI99] and observed before experimentally [KOR97]. In the result, the contribution of the XRIDS to a measured XRR curve increases with increasing q_z. In a coherent scattering approximation, this effect is neglected because the specular XRR is at least by 2 orders of magnitude larger than the XRIDS close to the critical angle. If it is not applicable, the true specular XRR must be extracted from the measured XRR by subtraction of an additional offset scan.

8 Examples of EUV multilayers

8.1 Mo/Si and W/Si based multilayers

The Mo/Si MLs are the most widely studied systems due to their high reflectivity at 13 nm (up to 70%) at normal incidence. They are used as reflective mirrors for EUV wavelengths in EUVL, astronomy, X-ray microscopy and spectroscopy, and in X–ray laser cavities [ATT]. Various methods of deposition were utilized for Mo/Si MLs. The highest reflectivities close to the theoretical limit were obtained by e-beam evaporation combined with ion beam polishing of the deposited layers [SCHL95, LOU05], magnetron and ion beam sputtering [SKU95, ULY00, SHI03, RAV04, YUL05]. The W/Si MLs are applied in astronomy, both in hard and soft X-ray range, and in mirror optical elements used for laboratory diffractometers [WIN99, WIN00, MIC02].

For Mo/Si similarly as for W/Si, the CS TEM studies showed that amorphous interlayers were formed at metal/Si interfaces during the deposition [PET87, HOL89a, HOL89b, MEY90, STE90, WAN94]. The width of the intermixed region is lower for Si on W (Mo) than for W (Mo) on Si interfaces [PET87]. This is because of a deeper penetration of the more energetic Mo atoms into the amorphous Si layer in comparison to the penetration of Si atoms into the relatively more densely packed metallic layer. However, other mechanisms like diffusion of Si upwards into the metallic layers or interdiffusion induced by the latent heat of condensation (which is large for refractory metals) could contribute to the above-mentioned effect.

It was suggested by Bene [BEN87] that rather kinetics aspects than the minimization of the free energy determine the processes at metal/Si interfaces. At elevated temperatures, two types of reaction are observed:

i) growth of amorphous interlayer, as reported for Ni/Si, Ti/Si [HOL88, HOL89a] or W/Si [KIN02] MLs.

ii) crystallization of amorphous interlayer and growth of silicides, e.g. in Mo/Si or Co/Si MLs [PET87, HOL89a, STE90, WAN94].

Whereas in the case i) the interdiffusion proceeds without stopping, in the case ii) the process stops because the interlayer acts as a diffusion barrier. The behaviour i) is typical for the W/Si interface whereas the Mo/Si interface follows the mechanism ii).

In refractory metal (RM)/Si MLs, also the formation of refractory silicides at elevated temperatures is expected. Typically, the transformation RM $\rightarrow$ $RMSi_2$ is accompanied by large volume changes (Table 8.1.1) [MUR83]. This results in the change of ML period with increasing temperature. A way to stabilize the ML structure is to use immiscible pairs of materials.

Tab. 8.1.1. Amount of silicon required to form silicide and resulting silicide thickness [MUR83].

metal	silicide	thickness of Si per 1 nm of metal [nm]	resulting silicide thickness [nm]
Mo	$MoSi_2$	2.56	2.59
W	WSi_2	2.53	2.58
Co	Co_2Si	0.91	1.47
Co	CoSi	1.82	2.02
Co	$CoSi_2$	3.64	3.52

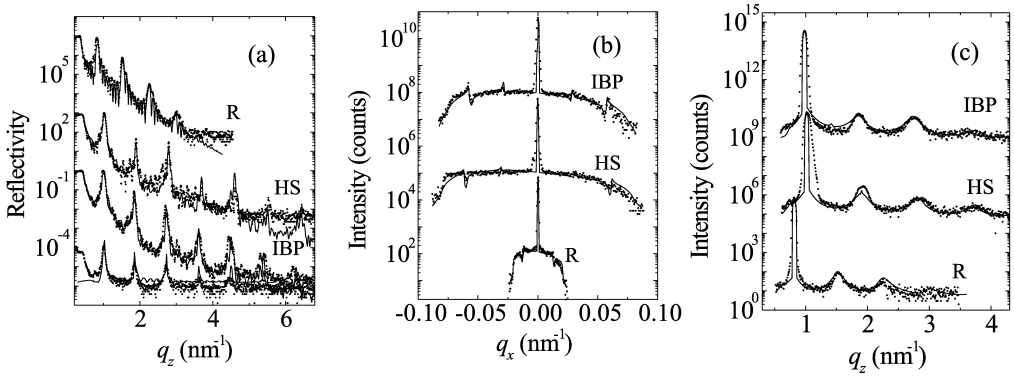

Fig. 8.1.1. (a) Measured specular X-ray reflectivities (dots) and their simulations (lines). The HS and R curves are shifted upwards by the factors of 10^3 and 10^7, respectively. (b) Rocking curves measured around the second (R) and third (HS) ML Bragg maximum (dots) and their simulations (lines). The HS and IPB curves are shifted upwards by the factors of 10^3 and 10^6, respectively. (c) Detector scans taken on the first ML Bragg maximum (dots) and their simulations (lines). The HS and IPB curves are shifted upwards by the factors of 10^4 and 10^8, respectively [ANO01].

However, here the crystallization and the following fast grain boundary diffusion can increase the interface roughness and damage the ML structure considerably.

The interface roughness characteristics of Mo/Si MLs of similar periods in dependence on the deposition methods were studied in our laboratory [ANO01]. Mo/Si MLs prepared by standard e-beam evaporation at RT (R), e-beam deposition on the substrate heated to 170°C (HS), e-beam evaporation combined with ion polishing (IBP) of amorphous Si layers with Ar^+ ions of 800 eV energy were studied by X-ray reflectivity and XRIDS (Fig. 8.1.1). For simulations of the experimental data, the interlayers of Mo_5Si_3 composition [LIM01] were incorporated into the simulation model (Table 8.1.2).

The interface morphology parameters were found close for IBP and HS indicating a similar relaxation mechanism of the growing surface. The main difference is a larger thickness of the Mo_5Si_3 interlayer at the substrate heating which has a direct implication for peak reflectivity (at normal incidence). At room temperature e-beam deposition, the interface roughness is nearly doubled at 3-times smaller number of ML periods. A suppressed interface roughness replication across the MLs for IBP and HS samples was found which means that more layers may be deposited maintaining a high interface quality. The replicated interfaces produce a so called resonant diffuse scattering around the ML Bragg maxima which deteriorates the imaging contrast of the mirror.

In Fig. 8.1.2, the cuts of the GISAXS spectra across the $2^{\rm nd}$ Bragg maximum for PVD-Mo/Si multilayers prepared by the standard UHV e-beam deposition, e-beam deposition on heated substrate, ion beam assisted PVD (ion polishing) and ion beam sputtering are shown. These spectra correspond to non-coplanar XRIDS on large length scales (see Sec. 7) and demonstrate that IBS technique provides the best multilayer in terms of the interface roughness with severely suppressed parasitic diffuse scattering.

To achieve the theoretical reflectivity value, the details of interlayer formation as well as

Tab. 8.1.2. ML parameters derived from the X-ray reflectivity and XRIDS simulations. N, d, Δ, σ, ξ and L_{vert} stand for the number of periods, layer thicknesses and ML period, layer thickness fluctuations, effective interface roughness, lateral and vertical correlation lengths, respectively. The ratio L_{vert}/Nd characterizes the interface replication across the whole ML stack. The fractal parameter $h = 1$ was used for all samples [ANO01].

ML	N	d_{Mo} [nm]	$d_{Mo-on-Si}$ [nm]	d_{Si} [nm]	$d_{Si-on-Mo}$ [nm]
R	10	0.9	0.7	6.5	0.5
HS	30	1.0	1.5	3.5	0.9
IBP	30	1.5	1.0	3.8	0.7

ML	Δ [%]	d [nm]	σ [nm]	ξ [nm]	L_{vert} [nm]	L_{vert}/Nd
R	8.6	0.50 $\pm$0.05	20 $\pm$10	50 $\pm$10	0.58	5
HS	6.9	0.35 $\pm$0.05	20 $\pm$10	65 $\pm$30	0.31	7
IBP	7.0	0.35 $\pm$0.05	20 $\pm$10	75 $\pm$25	0.36	7

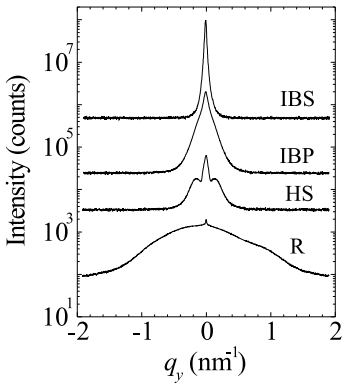

Fig. 8.1.2. Cuts of the GISAXS pattern across the 2$^{\rm nd}$ Bragg maximum of Mo/Si multilayers prepared by UHV e-beam deposition (R), e-beam deposition at heated substrate (HS), ion beam polishing (IBP) and ion beam sputtering (IBS). These cuts correspond to non-coplanar XRIDS measurements (see Sec. 7) and demonstrate superior quality of the IBS prepared multilayer.

crystallinity of Mo layers are studied. The formation of $MoSi_2$ instead of Mo_5Si_3 was reported [DIE88, STE91]. Formation of crystalline grains in Mo layers resulting in a rapid increase of the Mo layer surface roughness in dependence on deposition method and Mo layer thickness were recently thoroughly analyzed [DIE02, ABD02]. Mo/Si ML mirrors systems with very thin diffusion barriers increasing the thermal stability were also prepared. Examples are B_4C [BOT03, PAT04, KJO04], C [TAK01, YUL03, YUL05] and Ru [MAT06].

The interface characteristics and thermal stability of W/Si MLs (periods 2 - 12 nm) with tungsten layer thickness 1 and 2 nm prepared by e-beam deposition were studied in papers [BRU93, JER93, JER97]. Formation of an amorphous W-Si mixture at W/Si interfaces during the depo-

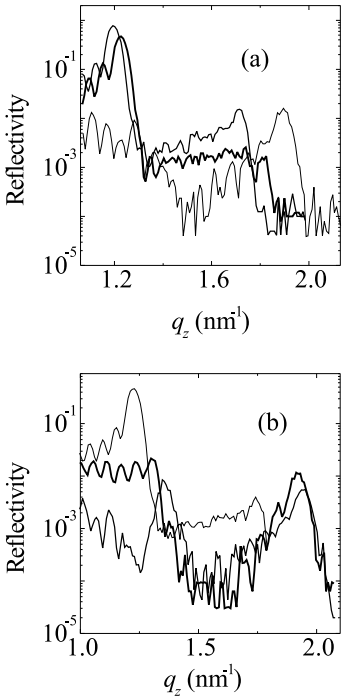

Fig. 8.1.3. (a) Evolution of the 2^{nd} and 3^{rd} ML Bragg maxima during a $430°$C isothermal annealing of a (8 nm Si/2 nm W)$\times$10 ML – the beginning (medium line), after 0.5 h (thick line), and after 2.5 h (thin line). Disappearance and re-appearance of the 3^{rd} maximum is observable suggesting an interface shift. (b) The same phenomenon observed on the 2^{nd} maximum as the interface shift proceeds. A total shift exceeding 1 nm is observed in still a well-preserved multilayer structure [JER96].

sition was evidenced. The interface roughness and mixing increase above $250°$C while the ML period decreases. The ML structure persists up to $650°$C annealing for 30 s. It is known that Si is the main diffuser in the W/Si couple [MUR83]. Therefore one can expect that Si layers become thinner and W (in fact W-Si) layers become thicker at elevated temperatures and a shift of the ML interfaces could be observed [MEY90] before the collapse of the ML structure. This effect was evidenced by the hard X-ray reflectivity behaviour of W/Si MLs during an isothermal *in-situ* annealing [JER96]. The effect was manifested by the successive disappearance and re-appearance of the Bragg ML maxima in the reflectivity curves measured *in-situ* (Fig. 8.1.3). The change takes place without smearing-out the interfaces. The shift is connected with a substantial decrease of the electronic density of the expanding W layers and the ML period, too. The diffusion of Si into W layers already during the deposition has been observed also for magnetron sputtering [WIN99], therefore the interface width of a typical W/Si ML is larger than that of Mo/Si one at comparable nominal parameters. Moreover, as mentioned above, diffusion of Si extends across the whole W layer. Suppressed interdiffusion and increased thermal stability can be achieved by using already mentioned B_4C layer instead of Si [JIA01, OHI03].

Thermal stability of MLs could be promoted using the pairs of materials close to thermo-

Tab. 8.1.3. Soft X-ray reflectivity (R) data of RTA treated samples at the first Bragg peak (BP) position measured at the angles of incidence $36^\circ - 43^\circ$ with respect to the normal. λ is the wavelength [SEN97].

annealing	W/Si λ [nm]	R [%]	$W_{0.5}Si_{0.5}$/Si λ [nm]	R [%]	$W_{0.33}Si_{0.66}$/Si λ [nm]	R [%]
as-deposited	13.1	6.8	13.4	2.4	13.0	1.0
500^{o}C/30 s	13.2	6.1	13.3	2.4	12.9	1.0
850^{o}C/30 s	—	no BP	13.3	2.1	13.0	0.6

dynamic equilibrium. In the case of Mo/Si and W/Si combinations, an effective way is to dope metal by silicon. Consequently, the consumption of Si due to the silicide formation is partly or fully suppressed. Some results of the interface stability in $Mo_{1-x}Si_x$/Si MLs were published by Kleineberg et al. [KLE94]. Here the MLs were prepared by two e-guns and they were annealed in vacuum chamber for 20 minutes at different temperatures. It was found that Mo/Si and $Mo_{0.5}Si_{0.5}$ MLs were destroyed at 600°C and 900°C, respectively, but $Mo_{0.33}Si_{0.66}$/Si MLs destruction started at 900°C only.

Similar results were obtained with W/Si system in our laboratory. W/Si, $W_{0.66}Si_{0.33}$/Si, $W_{0.5}Si_{0.5}$/Si and $W_{0.33}Si_{0.66}$/Si MLs were prepared by dual e-gun evaporation onto oxidized Si substrates. The nominal thickness of Si spacer and W or $W_{1-x}Si_x$ reflector were 5.5 and 2.5 nm, respectively. Ten bilayers were deposited.

i) The samples were processed by a halogen lamp rapid thermal annealing (RTA) between 500°C and 1000°C/30 s in vacuum [SEN97]. The rise time of temperature was 1 - 2 s. We have observed that for $x = 0$, MLs were heavily distorted already at 750°C and for $x = 0.33$, it occurred at 850°C. For $x = 0.5$ and 0.66, the change of period was only around 5% even at 850^{o}C. All structures collapsed at 1000^{o}C. However, the reflectivity of mirror decreases inherently with increasing x because the optical contrast between the reflector and spacer becomes lower. These results are shown in Table 8.1.3.

ii) For comparison, same samples were treated by high intensity pulses of excimer XeCl laser (wavelength 308 nm) at the fluences $F = 0.075$ - 0.6 cm^{-2} [DAN96]. The number of pulses of 30 ns duration used for the irradiation of samples were $N = 1, 10$ or 100. After irradiation at $F = 0.6$ Jcm$^{-2}/N = 1$, some changes were observed in all samples, but they were not detrimental. After $N = 100$ pulses of the same fluence, W/Si and $W_{0.33}Si_{0.66}$/Si MLs collapsed, $W_{0.66}Si_{0.33}$/Si ML was heavily distorted, however, $W_{0.5}Si_{0.5}$/Si ML was practically unchanged in terms of period thickness. These results confirm that the resistance against laser irradiation increases with x from 0 to 0.5. The unexpected decrease at $x = 0.66$ is explained by a gradual loss of the refractory nature of tungsten when it is diluted by Si. The corresponding reflectivity data are shown in Table 8.1.4.

In conclusion, it was observed that the thermal stability of W/Si MLs may be increased by appropriate doping of W by Si. It has been shown that $W_{0.66}Si_{0.33}$/Si MLs have also outstanding smoothness and conformity in periodicity and therefore they were used for the fabrication of curved graded ML mirrors instead of standard W/Si structures [MICH02].

Tab. 8.1.4. Soft X-ray reflectivity data of laser treated samples at the first Bragg peak (BP) position measured at the angles of incidence 36° - 43° with respect to the normal. λ is the wavelength. Samples were treated by XeCl laser pulses at the fluence $F = 0.6$ Jcm^{-2} by $N = 1$ or 100 pulses [DAN96].

annealing	W/Si λ [nm]	R [%]	$W_{0.5}Si_{0.5}$/Si λ [nm]	R [%]	$W_{0.33}Si_{0.66}$/Si λ [nm]	R [%]
as-deposited	13.1	6.8	13.4	2.4	13.0	1.0
N = 1	13.3	2.4	13.3	0.5	13.5	0.5
N = 100	—	no BP	13.6	0.5	—	no BP

Tab. 8.1.5. The layer thicknesses d_{Co}, d_W and d_{Si}, period $d = d_{Co} + d_W + 2d_{Si}$, geometrical interface roughness σ, lateral correlation length ξ and vertical correlation length L_{vert} of the interfaces in Co/Si/W/Si MLs obtained by simulation of the reflectivity and XRIDS spectra of the as-deposited and RTA treated ML1 and ML2 [LUB99].

ML	d_{Co} [nm]	d_W [nm]	d_{Si} [nm]	d [nm]	σ [nm]	ξ [nm]	L_{vert} [nm]
ML1 as-deposited	2.1	1.6	5.1	13.9	0.65	20	50
500° C/30 s	3.1	1.6	4.5	13.7	0.60	20	50
ML2 as-deposited	3.8	2.0	6.8	18.0	0.70	100	90
500° C/30 s	4.2	2.0	6.1	17.0	0.80	60	90

Another way to increase the thermal stability of W/Si MLs is to stabilize the ML structure by the combination with another reflecting element, e.g. with Co. In Co/Si couple, Co is the dominant diffuser. According to the thermodynamic parameters [MUR83], Co silicides should be formed prior to W silicides. Considering the amorphous interlayer formation at the interfaces, a layered structure composed of Co/Si/W/Si periods with appropriate Co, W and Si layer thickness could be more stable than simple W/Si ML. Two sets of MLs were investigated (Table 8.1.5). The sequence of layers within the period was Si/Co/Si/W starting from the substrate, the number of periods is $N = 5$ [LUB99, MAJ96, JER00].

We have shown that for appropriate Co, Si and W layer thickness, high thermal stability can be achieved. The ML1 persists up to 850°C for 30 s of RTA and the ML period changes only slightly up to this temperature. Our studies showed that during the deposition, an amorphous intermixed layer is formed at Co/Si interfaces and at elevated temperatures, the nucleation of various Co silicides takes place. The formation of Co-Si mixture is alleviated by thinner and partially discontinuous Co layers (ML1). According to the published data [HOL89b], the Co-Si interlayer does not grow under annealing but formation of silicides is observed instead. Crystallization of an amorphous phase of a close composition is not connected with a large volume change and usually does not exceed several %. Therefore, the ML1 period remains almost unchanged. Moreover, most part of Si is consumed by reaction with Co and thus the processes

at W/Si interfaces are suppressed. For ML2, the thicker Co layers are partially crystalline and crystallization of Co-Si at elevated temperatures was connected with larger volume changes. The large difference in lateral correlation lengths between the as-deposited ML1 and ML2 is explained by the break up of the lateral correlation due to the partial discontinuity of Co layers in ML1. The large decrease of the lateral correlation length for annealed ML2 in comparison to the as deposited state corresponds to the crystallization of CoSi evidenced also by X-ray diffraction.

8.2 Short period multilayers

Minimization of optical aberrations by maximizing the angle of incidence is general effort which results in near-normal incidence geometry. Differently to EUV region, such a geometry for soft X-rays can be realized only at extremely short ML periods down to 2 nm or less, soft X-ray mirrors working in a so-called water window 2.33 - 4.36 nm being a typical example. The water window is located between K absorption edges of oxygen and carbon where the absorption coefficient of water is very low while C containing organic or biological materials are absorbing. Consequently, living cells can be observed *in vivo* in their natural environment [PAL]. The examples are V/Al_2O_3 [NEF01], Ni/C/Ti/C [TAK01], W/Sc, Cr/C [AND03], Cr/Sc, W/B_4C [BIB05], CrN/ScN superlattice [BIR06], Sc/Cr [SAL97, YAM99b, KUH02, BIR03].

Another application example of ultra-short period MLs are coatings in hard X-ray telescopes working above 50 keV, e.g. W/Si and Pt/C [MAO99]. Here, the angle of incidence is inherently grazing even for ultra-short periods. Debye-Waller attenuation factor for the X-ray reflectivity *DWF* drops down rapidly with reduction of the ML period unless the interface width is reduced in the same way. Therefore, the interface quality becomes inherently crucial for the layer thicknesses below 1 nm. For example, the interface width of 0.1 nm reduces the reflectivity by $\approx 50\%$ for the period of 1 nm (the value of *DWF*). Actually, the ability of a material pair to yield structures with minimum interface roughness rather than X-ray optical constants is important for ultra-short period mirrors [SCHA00]. The materials must also provide continuous layers, the critical thickness being mostly 0.5 - 1 nm. No less important is the uniformity of the ML stack. It was shown [BIB05] that period fluctuations should not exceed $\approx 1/N$ (N - number of periods) which gives fluctuations less than 0.0025 nm for a period of 1 nm and $N = 200$ - 700. The issue of thermal stability is also more critical than in convenient MLs. Therefore, ultra-short period MLs are challenging for thin film technology and materials science generally. Deposition process requires a tight control, stability and fast switching between the materials. A detailed interface characterization provides a necessary feedback.

We present here several types of ultra-short period MLs with different miscibilities of the constituents which were presented in our recent paper [JER08]. They were fabricated by different techniques in order to study and to compare them in terms of the interface quality and thermal stability combining the methods of the specular/non-specular X-ray reflectometry, transmission electron microscopy and X-ray and electron diffraction. An insight into interface phenomena is a prerequisite for a proper material pair choice compatible with ultra-short periods and subsequently for a knowledge-based and targeted optimization of fabrication conditions resulting in high-performance interference mirrors.

Because of the lower absorption far above the K absorption edges, Cu and Ni are promising refractory metals to replace W or Pt in ultra-short period grazing incidence X-ray mirrors working close to 100 keV. When combining them with a low-absorption spacer, optical criteria

worked out for a proper material pair choice [YAM99b] are fairly satisfied.

Long-term room-temperature (RT) stability and narrow interfaces below 0.3 nm were reported for dc sputtered Cu/Si MLs with the period down to 2 nm [MAO99, WIN99]. However, a rather large solubility and diffusivity of Cu in Si of 75% and 1.6×10^{-10} cm^2/s, respectively, may pose a problem at elevated temperatures regardless the deposition technique, especially for ultra-short periods. As a part of our work, we inspected this issue in detail in the MLs prepared by electron-beam evaporation in ultra-high vacuum (UHV).

Ni/C MLs were studied more frequently, e.g. in connection with the development of Göbel mirrors for laboratory X-ray sources or normal-incidence mirrors working at C-K edge. Carbon-based MLs are known to have a good thermal stability. Ni/C mirrors were found to be stable up to 300°C [LOD96, NAK92] but the interface width in the as-deposited state proved to be larger than that in Cu/Si ones. Therefore, Ni/C mirrors with periods down to 3 nm are rather exceptional. Common Ni/C mirrors were prepared mainly by rf/dc sputtering [DUP90b, FRI97, BOR00, ULM00] or by pulsed laser deposition (PLD) [CHE00, DIE02, KOV03]. Energetic adatoms in these techniques result in rather smooth interfaces. On the other hand, PLD is known to produce mixing and interdiffusion which may broaden interfaces and deteriorate reflectivity. Electron-beam UHV evaporation is less prone to the these effects but being used for Ni/C mirrors, an *in-situ* ion-beam etching of Ni layers had to be applied to reduce the geometrical interface roughness [PUI91, PER02]. Energy dissipation from hot spots created by the ions impinging under particular angle smoothes the deposited surface. As a cheaper and simpler alternative to ion beam etching, we tested UHV electron beam evaporation with an *in-situ* substrate heating to prepare ultra-short period MLs from Ni/C couple. A larger surface mobility of adatoms is expected to heal the interface roughness and to obtain thin layers but the substrate temperature must be optimized to avoid an enhanced constituent mixing. A low solubility of C in Ni (0.55% at 1300°C) and practically zero one of Ni in C render Ni/C couple very suitable for such a technique. Moreover, bulk nickel carbides are formed far above 1000°C.

Cu/Si and Ni/C samples were deposited in a UMS 500 Balzers apparatus in a vacuum of 10^{-7} Pa onto silicon wafers with a native oxide layer. Typically, 10 - 15 periods of 1.5 - 3.2 nm were deposited starting with Si (Ni) and the same layer was used as a cover layer. Different deposition temperatures up to 160°C were tested for both couples to optimize the ML stack. A vacuum furnace annealing at 10^{-4} Pa was applied to test the thermal stability.

Thermal stability of MLs can be improved by compound layers following a simple argument that compound decomposition is required before the formation of new mixed phases [JAN04]. Recently, thin B_4C interlayers were applied as diffusion barriers for Mo/Si and Sc/Si systems [BOT03, JAN04]. We tested the merit of spacer compound layers by application of B_4C instead of C in combination with Ni. For compound layers, sputtering is necessary. A sputter deposition based on distributed electron cyclotron resonance (DECR) was used to prepare Ni/B_4C ML. The advantages of this method were discussed elsewhere [MOR99]. A low argon gas pressure of 10^{-1} Pa results in smooth interfaces so that a large number of periods is needed to utilize the X-ray diffuse scattering for interface characterization. In particular, 400 periods of 1.59 nm were coated on a Si wafer starting with B_4C, the spacer material being used also for the top protective layer of the double period thickness. A rapid thermal annealing in pure nitrogen in addition to the long-term vacuum one was applied to study the decay of the ML structure in detail.

For nanometer-scale period MLs it is useful to utilize mutually immiscible materials to reduce the mixing at interfaces. Sc/Cr couple with positive heat of formation was proposed several times

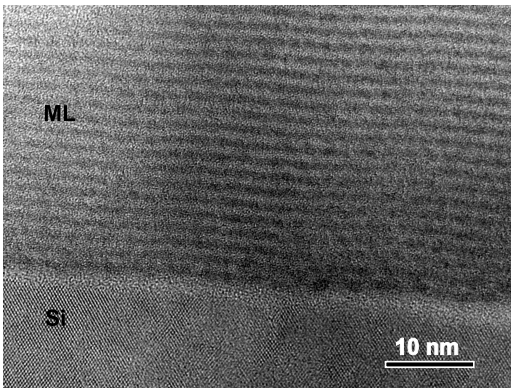

Fig. 8.2.1. High resolution CS TEM image of the Sc/Cr multilayer (period 1.75 nm) taken close to the substrate [MAJ06].

for microscopy in the water window [SAL97, SCHA98a, KUH02, BIR03] but the growth process and interface properties are not well understood yet. Particularly, a low solubility and mixing cannot be excluded as the heat of formation, though being positive, is rather small (1 kJ/g.at). Moreover, ultra-short period immiscible MLs are prone to degradation to granular systems under a thermal load via crystallization and grain boundary diffusion. We inspected the interface quality and thermal stability of Sc/Cr mirrors prepared by the ion beam sputtering of the ECR type operating at the lowest Ar gas pressure of 10^{-3} Pa. These mirrors were prepared at Tohoku University, Sendai. The details of the deposition may be found elsewhere [SAK99]. Up to 250 periods of 1.3 - 1.75 nm were deposited onto Si wafers starting with Sc. The thermal treatment was done in a vacuum of 10^{-4} Pa.

A comprehensive characterization of Sc/Cr MLs ($d = 1.75$ nm, $N = 250$) in terms of the intermixing, geometrical interface roughness, its replication and crystalline structure of the layers was performed [MAJ06]. This characterization relies on a single set of simulation parameters retrieved from the reflectivity and the reciprocal space map of the X-ray diffuse scattering. The ML parameters were further refined by the simulation of the soft X-ray reflectivity measured at near normal incidence. We demonstrated that such an approach overcomes ambiguities of the evaluation.

From the CS-TEM image of a part of the ML stack (Fig. 8.2.1), the regularity of the ML is clearly visible. The reciprocal space map of the diffuse scattered intensity at grazing incidence is shown in Fig. 8.2.2a, the simulation of the reciprocal space map in Fig. 8.2.2b. The high intensity band parallel to q_z for q_x close to 0 corresponds to the specular reflectivity scan. The region of enhanced diffusely scattered intensity outside the specular reflectivity line is evident (increased brightness) which suggests the correlation between the roughness of interfaces across the multilayer.

For a quantitative check of the simulation, the scans along q_x ($q_z = 0.362$ Å^{-1}) and q_z ($q_x = -0.005$ Å^{-1}) along with their simulations are shown in Figs. 8.2.3a and 8.3.2b, respectively. According to our simulations, $L_z = 35 \pm 2.5$ nm which corresponds to ≈ 20 periods and $\xi = 7 \pm 1.5$ nm (Table 8.2.1).

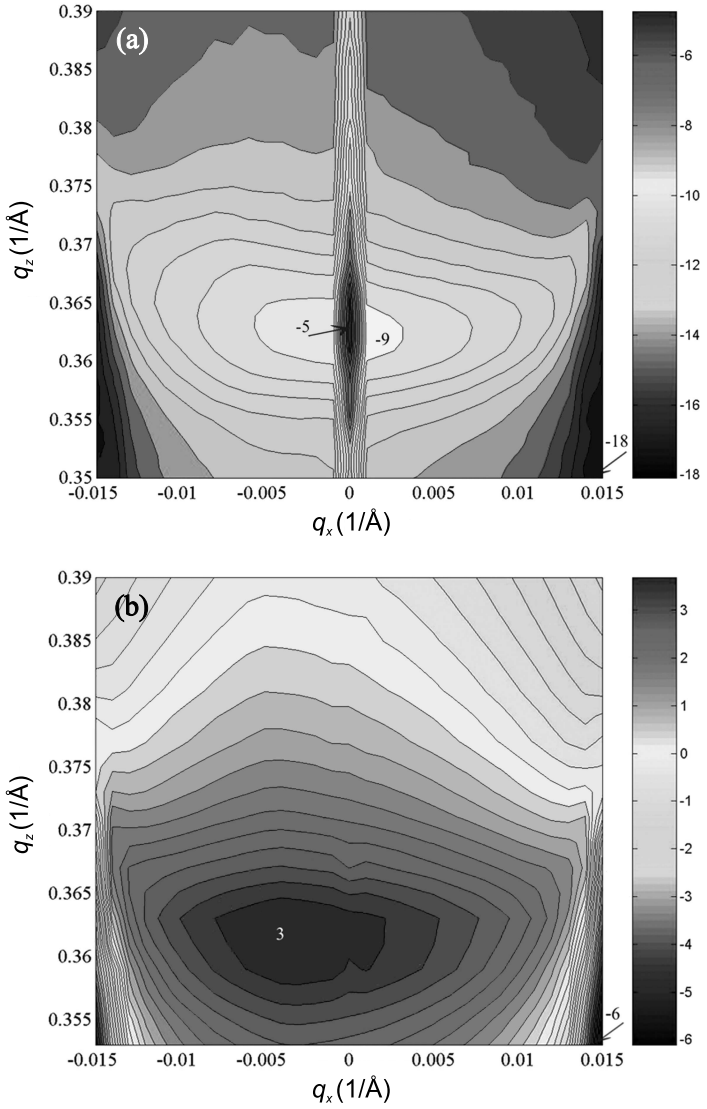

Fig. 8.2.2. (a) Reciprocal space map of the Sc/Cr multilayer measured around the first Bragg maximum. (b) Simulation of the reciprocal space map using the parameters given in Table 8.2.1 [MAJ06].

Although the interface roughness is small, it is about 20% of the layer thickness of Cr and Sc. It should be noted that for the layer thickness of 1 nm or less, the validity of the model might be questionable. Also, the optical constants of ultrathin layers may differ from those given in databases, especially near the absorption edge. However, an agreement between our

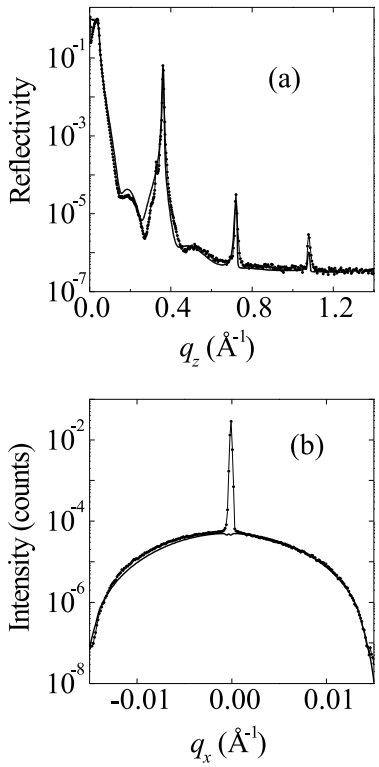

Fig. 8.2.3. The q_z scan at $q_x = -0.005$ Å^{-1} (a) and q_x scan at $q_z = 0.362$ Å^{-1} (b); the points are experimental data, the solid line is simulation [MAJ06].

Tab. 8.2.1. Parameters of the Sc/Cr ML obtained by reflectivity and reciprocal space map simulations. d-layer thickness, N-number of periods, σ_{eff}-effective interface roughness, ξ-lateral correlation length, L_{vert}-vertical correlation length, h-fractal parameter [MAJ06].

d_{Sc} [nm]	d_{Cr} [nm]	N	σ_{eff} Cr on Sc [nm]	σ_{eff} Sc on Cr [nm]	ξ [nm]	L_{vert} [nm]	h
0.834	0.932	250	0.28	0.25	7 ± 1.5	35 ± 2.5	1

experimental and calculated reciprocal space maps suggests that the calculated parameters are reasonable.

We compared the data of the soft X-ray reflectivity around the wavelength of 3.13 nm obtained on the same sample with our model. The agreement confirms the validity of the model. Additionally, a slight grading of the ML period across the stack, giving a 0.05 nm increase from the first to the last period, had to be introduced to obtain a reasonable simulation. The net change of the period was also assumed for simulations of the X-ray reflectivity and reciprocal space

Tab. 8.2.2. The XRR and XRIDS simulation parameters of several Cu/Si MLs (10 periods). d, σ_{eff}, σ, ξ, L_{vert}, h stand for the layer thickness or multilayer period, interface width, geometrical interface roughness, lateral and vertical correlation lengths, and fractal parameter, respectively. Bulk densities were used for the simulations. For $d < 2$ nm, the XRIDS around the 1^{st} Bragg peak was too low above the background to be simulated reliably (last column).

deposition temperature	RT	80°C	80°C
d_{Cu} [nm]	1.22	1.27	0.65
d_{Si} [nm]	2.25	1.9	0.98
d [nm]	3.47	3.17	1.63
$\sigma_{eff\ \ Si-on-Cu}$ [nm]	0.7	0.5	0.7
$\sigma_{eff\ \ Cu-on-Si}$ [nm]	0.6	0.45	0.6
$\sigma_{Si-on-Cu}$ [nm]	0.4	0.3	—
$\sigma_{Cu-on-Si}$ [nm]	0.35	0.25	—
ξ [nm]	10	10	—
L_{vert} [nm]	30	30	—
h	0.2	0.3	—

map measured with hard X-rays. However, this model refinement had a negligible effect on the grazing incidence spectra and demonstrates a complementarity between the grazing and normal incidence reflectivity measurements. From both reflectivity and reciprocal space map simulations, it follows that the effective interface roughness and geometrical roughness of Sc/Cr and Cr/Sc interfaces are identical which corresponds to the low mutual solubility of both components [MIE76].

The thermal stability of Sc/Cr ML was reasonable. A slight 2.4% increase of the period at 280°C can be attributed to some structural ordering in the Sc and/or Cr layers. The reflectivity of the ML decreased considerably only after a 3 hour annealing above 300°C, proving that the Sc/Cr combination is a good choice for mirrors in the water window region.

Cu/Si couple provided very regular UHV evaporated ML stacks with amorphous or microcrystalline layers at different deposition temperatures. The interface roughness σ and mixing quantified as $\sigma_{eff} - \sigma$ were minimized at 80°C. Examples of the XRR and XRIDS simulations of the optimized ML are shown in Fig. 7.2 and Fig. 8.2.4, respectively. The simulation parameters for RT and 80°C depositions are compared in Table 8.2.2. Below 2 nm ML period (last column), the ML gets discontinuous and the interface roughness increases.

An asymmetry between the roughness of Cu/Si and Si/Cu interfaces shows that Cu layers grow rougher while the mixing is comparable. The interface widths σ_{eff} are rather independent of the ML period down to $\approx$ 2 nm. Below $\approx$ 2 nm, the ML Bragg peak in the XRR curve is poorly resolved above the background while Kiessig fringes are still visible which indicates that mixing at interfaces destroys the ML stack. The vertical correlation length is comparable with the total multilayer thickness giving rise to a pronounced resonant diffuse scattering around the Bragg peaks. A quickly saturating reflectivity drop at RT, which reached $\approx 25\%$ on the 1^{st} Bragg peak 2 weeks after the deposition, was observed. A severe suppression of the ML Bragg peaks

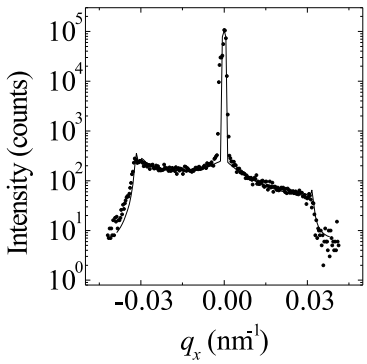

Fig. 8.2.4. Rocking curve simulation of the Cu/Si ML deposited at 80°C with the simulation parameters indicated in Table 8.2.2. The rocking curve was measured with the detector fixed at the 1^{st} Bragg maximum. The q_x stands for the lateral (along the surface) components of the scattering vector (wave vector transfer) (dots – measured points, line – simulation). The simulated specular reflectivity is shown in Fig. 7.2.

due to a strong mixing and interdiffusion was induced by the 100°C/1h annealing and the ML collapsed at the 200°C/1h one. Here, an onset of η'(Cu,Si) tetragonal phase formation (JCPD-ICDD data set file no. 23-0224) was revealed by the XRD, starting presumably in the mixed regions. Fast grain-boundary diffusion of Cu into Si layers mediated by this interface phase then accelerated the multilayer degradation. Nevertheless, the interdiffusion with the substrate was not developed yet after the 280°C/1h annealing as suggested by the presence of the Kiessig fringes in the XRR curve.

The quality of the ML stack proved to be more sensitive to the UHV deposition temperature for Ni/C couple where a well resolved ML Bragg peak in the XRR was observed only around 80°C. A comparison with Cu/Si MLs of similar periods shows slightly rougher and more mixed metalloid-on-metal interfaces and shorter correlation lengths after deposition (Table 8.2.3). HR TEM revealed that Ni layers contained grains with locally well ordered regions inside (Fig. 8.2.5) which control the interface morphology. The interface width obtained from the XRR reaches the value of 1 nm for the ML period below 3 nm suggesting agglomeration effects in Ni. This observation compares well with a percolation threshold around 2 nm found in sputtered samples [BOR00] at which Ni forms coalescent layers. The interface correlation lengths indicated by the XRIDS are much shorter in Ni/C than in Cu/Si MLs while fractal behavior ($h < 1$) is observed in all cases. Such a behaviour was reported for Ni/C MLs previously from post-deposition atomic force microscopy measurements [ULM00].

A step-like vacuum annealing from 100°C up to 350°C with 50°C steps and a duration of 4 hours at each step was applied to the sample with the nominal ML period of 3 nm. After each annealing, the sample was cooled down in vacuum and measured at RT. The XRR and XRIDS simulation parameters are also shown in Table 8.2.3. An increase of the σ and $\sigma_{eff} - \sigma$ values indicates an advanced interface roughening and interdiffusion, respectively, before the ML breakdown at 350°C. Cross-sectional HR TEM image of the collapsed ML showed well developed grains embedded in a disordered matrix (Fig. 8.2.5b). The grains are composed of Ni of fcc symmetry according to EDX and ED analyses while the matrix is formed by C and a small

Tab. 8.2.3. The XRR and XRIDS simulation parameters of a Ni/C ML (10 periods) deposited at 80°C. Four hour annealings at each temperature were successively applied to the same sample. The XRIDS was not measured in the temperature region where the XRR did not change qualitatively. The meaning of parameters is the same as in Table 8.2.2, ρ is the density of the respective element.

annealing temperature	as-dep.	100°C	150°C	200 ° C	250°C	300°C
d_{Ni} [nm]	1.26	1.26	1.28	1.32	1.33	1.34
d_C [nm]	1.89	1.89	1.92	1.98	1.99	2.01
d [nm]	3.15	3.15	3.2	3.3	3.32	3.35
ρ_{Ni} [g/cm^3]	8.9	8.9	8.9	8.5	8.5	8.0
ρ_C[g/cm^3]	2.2	2.2	2.1	2.0	2.0	1.8
$\sigma_{eff\ \ C-on-Ni}$[nm]	0.65	0.65	0.7	0.75	1.1	1.6
$\sigma_{eff\ \ Ni-on-C}$ [nm]	0.45	0.45	0.5	0.55	0.7	1.2
$\sigma_{C-on-Ni}$ [nm]	0.35	—	—	—	0.5	0.8
$\sigma_{Ni-on-C}$ [nm]	0.25	—	—	—	0.3	0.4
ξ [nm]	5	—	—	—	8	10
L_{vert} [nm]	10	—	—-	—	3	1
h	0.25	—	—	—	0.18	0.25

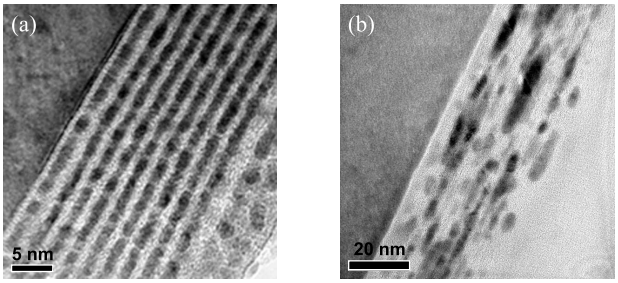

Fig. 8.2.5. Cross-section HR TEM images of the as-deposited (a) and collapsed (b) Ni/C ML whose XRR and XRIDS simulation parameters are given in Table 8.2.3.

fraction of fine granular fcc Ni. Obviously, the annealing stimulates the growth and coalescence of original Ni grains found in the as-deposited state which governs also interface morphology as reflected in an increase of the lateral correlation length and a decrease of the vertical correlation of the interface roughness (decay of interface conformality). As soon as Ni grains are well developed and the ML gets discontinuous, diffusion of C along Ni grain boundaries may also contribute to the ML breakdown. A complete diffusion of C into Ni layers was reported in the past [DUP90]. The observed thermal stability is comparable with sputtered and PLD Ni/C mirrors [NAK92, LOD96, CHE00].

It is worth noting that the ML period steadily increases and C layer densities decrease when increasing temperature above 100∘C. Similar effects were reported in sputtered Ni/C MLs with

Tab. 8.2.4. The XRR simulation parameters of the as-deposited Ni/B_4C ML (400 periods). Meaning of the parameters is the same as in Table 8.2.2.

d_{Ni} [nm]	d_{B4C} [nm]	d [nm]	$\sigma_{effNi-on-B4C}$ [nm]	$\sigma_{effB4C-on-Ni}$ [nm]
0.78	0.81	1.59	0.28	0.26

larger periods [DUP90, DJA00] and were attributed to a transformation of the amorphous into the graphitic-like structure. Though we were not able to trace this effect directly by HR TEM or XRD due to very thin C layers, the observed growth and coalescence of Ni grains connected with a long-distance collective diffusion of Ni atoms across C regions may induce graphitization. It was shown that such a metal-driven graphitization is preferred to carbide formation when C is in excess [SIN02] which explains also the absence of carbide formation in the temperature range applied. Once initiated, the graphitization due to Ni diffusion proceeds even at RT as evidenced by $\approx 8\%$ increase of the ML period which was observed on the sample annealed at 300°C after a 16 month RT storage.

Ni/B_4C MLs prepared by sputtering with distributed electron cyclotron resonance (DECR) ion source do not suffer from agglomeration effects in Ni as a ML with a period below 2 nm and extremely small interface width below 0.3 nm could be deposited (Table 8.2.4). Obviously, much higher adatom mobilities at DECR sputtering than at UHV deposition have a healing effect on the geometrical interface roughness and layer continuity at small thicknesses which goes in hand with amorphous character of the layers as confirmed by XRD and ED. On the other hand, the presence of compound layers does not favour mixing effects. No less is important the fact that substitution of C for B_4C has no detrimental effect on the theoretical optical contrast. Nevertheless due to very smooth interfaces, a large number of periods was necessary to visualize XRIDS effects in RSM. Only the XRIDS around the $1^{\rm st}$ ML Bragg maximum was usable (Fig. 8.2.6a) as the $2^{\rm nd}$ maximum emerges directly from the instrumental background and the higher orders cannot be seen at all. This fact is a consequence of the ultra-short ML period when the measurements of RSM are especially instructive. A concentration of XRIDS in the form of a sheet around the Bragg peak (resonant diffuse scattering) is a clear sign of a partial vertical correlation of the interface roughness while its distinct asymmetry is rather exceptional. HR TEM revealed that the interfaces are rather wavy and partly copy each other.

The as-deposited Ni/B_4C ML was first exposed to several isothermal annealings at 300°C up to 8 hours of total time with no significant changes of XRR but a slight improvement of the peak reflectivity on the $1^{\rm st}$ Bragg maximum. Contrarily, an additional annealing at 400°C/2 hours destroyed the ML completely and the Bragg peak disappeared. Therefore an intermediate 350°C/2h annealing, which brought about a decrease of the peak reflectivity by ≈ 1 order of magnitude, was done independently. Such a pre-annealed sample was then processed by a series of 5 or 10 minute rapid thermal annealings (RTA) with a step-like increase of temperature up to 520°C which resulted in a further severe reduction of the peak reflectivity and a reduction of the ML period from 1.59 nm to 1.54 nm, the $1^{\rm st}$ Bragg maximum being still well resolved. This reduction may be attributed to the annealing-out of the excess free volume typical for amorphous structure. HR TEM inspection showed that the layered structure without mixed regions but

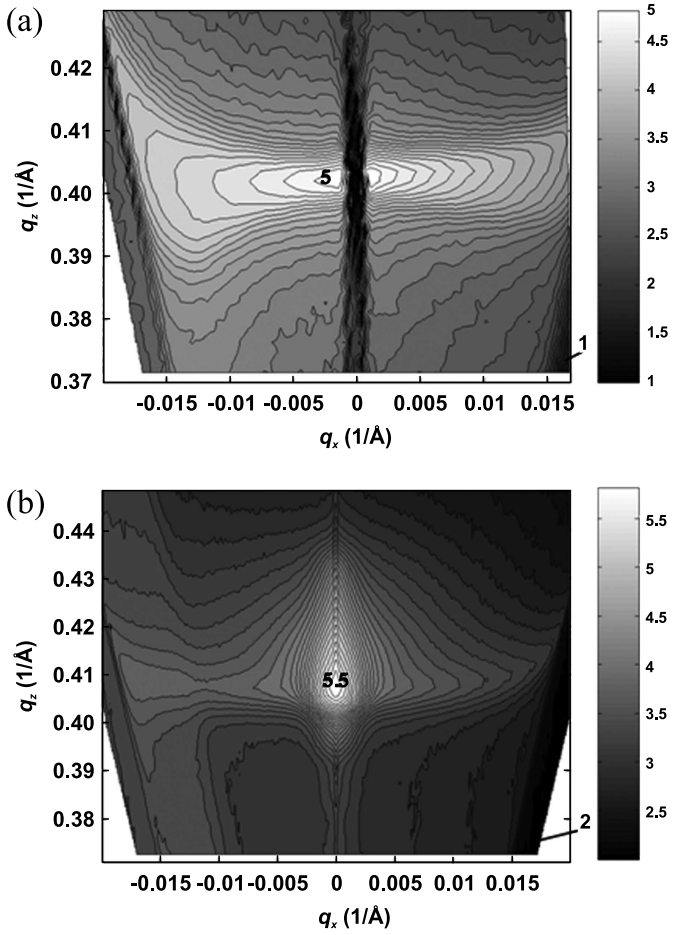

Fig. 8.2.6. Reciprocal space maps of the as-deposited (a) and annealed up to 520°C (b) Ni/B_4C ML around the 1^{st} Bragg peak. In the former map, the shadow of a beam stopper protecting a position-sensitive detector hides the XRR whose simulation parameters are shown in Table 8.2.4. The second map was measured with a point detector.

with many topological defects was still preserved. The RSM (Fig. 8.2.6b) exhibits substantial changes in comparison with the as-deposited state. Though it was not possible to simulate RSM with common correlation functions presented in the previous section, a qualitative change due to the annealing could be simulated when doubling the lateral correlation length from 10 nm to 20 nm. This increase cannot be attributed to the grain growth as in the case of Ni/C couple as no crystallization inside the ML was observed. However, large recrystallized regions in the substrate at the interface with the ML, presumably Ni silicide grains, could be seen locally by TEM. After the ML breakdown, the original layered structure was transformed into an inhomogeneous amorphous-like structure with only one diffuse ring in ED. This collapsed ML keeps still a sharp

interface with the substrate. HR TEM revealed a rare occurrence of crystallographically ordered regions, probably (111) planes of fcc Ni. This fact suggests that Ni diffusion controls the ML breakdown as in Ni/C couple but the mechanism of decay of the compound layers is rather unclear in the absence of a crystalline phase formation. Nevertheless, any deviation from the compound stoichiometry, which is common in extremely thin layers, may affect thermal stability of Ni/B_4C mirror adversely.

9 Examples of GMR structures

9.1 Effect of interface roughness on GMR behaviour

The GMR effect results from the fact that the electronic band structure of a defect-free system is different for majority and minority spins, and from the spin dependence of the electron scattering. The resistivity is determined by the bulk scattering (scattering by impurities and other defects inside the layers) and by the scattering on interfacial imperfections (roughness, intermixing) [BAR97]. Both contributions are important and their relative role depends on the details of the layered structure where also the crystallinity and crystalline phases are to be considered. The ratio of the bulk and interface scattering can be changed by variation of the layer thicknesses, roughness amplitude and impurity concentration. It was shown that for different ratios of the bulk and interface scattering, an enhancement or suppression of GMR is observed [BAR96].

From the experiments it is known that the GMR behaviour depends strongly on the above mentioned factors [PAR] but the experimental results are too complex for a straightforward interpretation. It is even not clear whether the bulk or interface scattering dominate. Nevertheless, in most GMR multilayered structures, the layer thicknesses are shorter than the electronic mean free path but longer than the spin relaxation length. Therefore, assuming homogeneous layers, the interface spin-dependent scattering should play the main role.

The apparent discrepancies of the published experimental data probably arise from the absence of detailed analysis of the interface roughness in the GMR samples. As it was shown in Sec. 7, a detailed quantitative description of the interface roughness of a multilayer (periodic or aperiodic) can be obtained by X-ray interface diffuse scattering (XRIDS) measurements. Combining the X-ray reflectivity and XRIDS, the intermixing and geometrical roughness at the interfaces can be distinguished. The theoretical approaches allowing simulation of the X-ray reflectivity and XRIDS data [SIN88, HOL93] were developed in the last decade of the 20^{th} century and were first applied to the EUV multilayer systems (Sec. 8).

For a full description of the multilayer interfaces, we need a set of parameters such as interface width, lateral correlation length of the roughness, Hurst (or fractal) parameter h of the interface and vertical correlation length of the roughness (see Sec. 6). Each of these parameters could influence the spin-dependent electron scattering in a different way. Mostly the X-ray reflectivity measurements were used to characterize the layered structure of magnetic multilayers. However, the X-ray reflectivity data do not allow a detailed interface roughness analysis including the roughness vertical and lateral correlations and fractal dimension. Therefore, combined reflectivity and diffuse scattering measurements should be performed in spite of the fact that the most GMR systems are combination of metals like Co/Cu, FeNi/Cu with very close optical constants in the hard X-ray range [CXRO]. This circumstance makes the analyses more complicated and usually less accurate.

It was often assumed that the interface roughness enhances the GMR because of the increased spin dependent scattering. An important role of the interface details affecting the interface scattering contribution to GMR was pointed out by Zhang and Levy [ZHA92]. Later, Barnas and Palasantzas analyzed the effect of the roughness correlation and fractal parameter h on GMR [BAR97]. They showed that when the spin asymmetry of the bulk scattering was of the same kind as that of the interface scattering, both contributions added constructively to build GMR. Here, the GMR ratio varies monotonously with increasing h. When the spin asymmetries for

Tab. 9.1.1. Heat of formation ΔH of immiscible combinations of elements often used in GMR research and applications [MIE76].

ΔH [kJ/g.at]	Fe	Co	Ni
Cu	+22	+13	+10
Ag	+39	+26	+26
Au	+12	+11	+11

the bulk and interface scattering are opposite, magnetoresistance varies with increasing h in a complex way, showing generally an extreme at a certain value of the roughness.

In this section, the most important results on the correlation between the interface roughness and GMR are presented. The most studied GMR systems are Fe/Cr multilayers, in which the GMR effect was discovered, followed by Co/Cu, Ag/Co, Au/Fe, permalloy/Cu and other multilayers and spin valves which are used for various applications. In general, these are the combinations of ferromagnetic elements Fe, Ni, Co and their compounds on one hand and noble metals Cu, Ag, Au on the other hand. These combinations are attractive because they belong to immiscible systems with a positive heat of formation (Table 9.1.1).

Fullerton et al. [FUL92], using the reflectivity data, reported an increase of GMR in Fe/Cr MLs due to an enhanced spin dependent scattering at rough interfaces. Similar results were reported by Belien et al. for polycrystalline Fe/Cr multilayers [BEL94]. They showed that the transport properties are governed by the interface scattering rather than by the bulk scattering inside layers. GMR values were higher for the samples with smaller interface roughness; however, a small amount of steps at the interfaces enhanced the GMR. A detailed analysis of the interface morphology of Fe/Cr epitaxial MLs was performed by Schad et al. [SCHA99]. The interface roughness was modified by the heat treatment at various temperatures and the structures were inspected by the X-ray reflectivity and diffuse scattering. The GMR increased with decreasing lateral correlation length of the interface roughness. As pointed out by the authors, it is impossible to separate the contributions of both interface and bulk scattering to GMR in polycrystalline samples. Only for a well ordered epitaxial structure, the bulk contribution could be almost eliminated. At higher annealing temperatures, the interface width increases causing a further increase of the GMR. However, a reduction of GMR with increasing interface roughness and constant lateral correlation length was observed by the same authors in polycrystalline Fe/Cr samples [SCHA98]. Here, the bulk and interface scattering contributions to GMR cannot be separated.

Santamaria et al. [SAN02] published a comparative study of the growth, structure, magnetization, and magnetotransport in Fe/Cr superlattices. They found a clear dependence of the resistivity and GMR on the long length-scale roughness of 10 - 20 nm. A long-scale roughness may be relevant not only because of its contribution to scattering but also because of its influence on magnetic properties at the interfaces. The saturation resistivity is determined by the lateral correlation length of the roughness whereas the GMR is determined by the interface width.

Roughness of the interfaces can be modified by high energy ion irradiation. Kopcewicz et al. [KOP03] studied the influence of 200 keV Ar-ion irradiation of sputtered Fe/Cr multilayers

on their GMR. They observed a GMR decrease accompanied by an increase of the interface roughness at the doses exceeding 53×10^{12}Ar/cm^2. The authors concluded that the main effect responsible for the GMR decrease was caused by a pinhole creation.

A similar approach was used by Gupta et al. [GUP06]. They modified the multilayer interfaces by 100 MeV Au ion irradiation and studied its effect on GMR in epitaxial [Fe (3 nm)/ Cr (1.2 nm)]$\times$20 multilayer. The interface was analyzed by the X-ray reflectivity and diffuse scattering measurements at the energy just below the absorption edge of Fe. The diffuse scattering measurements showed that the irradiation resulted in a substantial decrease of the lateral correlation length of the roughness while the rms roughness value changed only by a small amount. Giant magnetoresistance measurement of the irradiated multilayer suggests that GMR is sensitive mainly to the change of the rms roughness and only weakly to the variation of the lateral correlation length of the roughness. In particular, a decrease of GMR by 2% was observed for irradiated samples.

Kano et al. [KAN93] showed that in sputtered Co/Cu multilayers, the magnetoresistance ratio increased with decreasing substrate temperature at the deposition. From the analysis of the satellite peaks in the XRD pattern they concluded that the increase of GMR was connected with a decrease of the interface roughness which enlarged the antiferromagnetically coupled areas.

The effect of the interface roughness on GMR in epitaxial Co/Re MLs was studied by Xu et al. [XU04, XU07]. The roughness ranged between 0.3 and 1 nm and increased towards the top of the multilayer. The crystalline structure of individual layers was very regular which resulted in a low bulk scattering. The spin dependent scattering occurred mainly at the ML interfaces. The authors showed that the interface roughness plays a dominant role in the studied GMR structures.

Different effects of the interface roughness on GMR in the CIP and CPP geometries were reported by several authors [CHI98, CYR00, ZAM02]. Theoretical calculations showed [ALI03] that in the short mean-free path limit, the resistance decreases in the CPP geometry and increases in the CIP geometry. In the long mean-free path limit, the resistance increases in both configurations due to an enhanced surface scattering.

The effect of annealing on Co/Cu interfaces was studied by molecular dynamics simulations [SU03]. The results indicate that a pronounced interdiffusion appears, resulting in a long-range migration of the Co atoms in Cu layers at elevated temperatures.

Computer simulations [NAG03] of the intermixing in NiFe/Cu and Co/NiFe/Co/Cu multilayers explained experimentally observed variations of the resistivity and GMR with thickness of the NiFe, Cu, and Co layers and the variations of the interfacial intermixing and roughness, leading to an increase of the thickness of a paramagnetic interfacial layer.

Correlation between the interface structure and GMR behaviour of the single spin valve Co/Cu/Co structure with a NiO layer at the top or bottom was studied in ref. [ZHA04]. From the X-ray reflectivity and diffuse scattering studies it follows that the interface roughness of NiO on Co is much larger than that of Co on NiO. The interfaces become flatter under annealing. Different temperature dependences of GMR were observed for the top and bottom spin valves with the NiO pinned layer at the top and bottom, respectively. The authors assumed that this behaviour was a consequence of the competition between the roughness and exchange effects of the NiO/Co interface.

An et al. [AN06] analyzed the $(\mathrm{Cu/Ni_{70}Co_{30}}) \times 20$ and $(\mathrm{Cu/Ag/Ni_{70}Co_{30}}) \times 20$ multilayers. They reported a formation of intermixed regions at the $\mathrm{Ni_{70}Co_{30}}$-on-Cu interfaces. The results suggest that addition of Ag suppresses the interfacial intermixing. X-ray diffuse scattering pro-

files show that the interfacial lateral correlation length of the Ag-doped multilayer is longer than that of the undoped multilayer and it does not change significantly under annealing. The addition of Ag gives rise to smoother interfaces and results also in a good thermal stability.

The scattering at interfaces comes from the geometrical roughness with the lateral length scale of the order of the mean free path of electrons and from the atomic scale roughness due to the intermixing of atoms at interfaces. Impurity in the layer acts as a scatterer and affects the scattering process depending on the position in the multilayer. It was shown that the GMR ratio increased when impurities were introduced into the magnetic layers. Especially impurities at interfaces produce efficient spin-dependent scattering [ZAH98]. Impurities in nonmagnetic layers enhance the resistance whereas they do not produce a difference in the conductivity of the parallel and antiparallel configurations. Therefore, they decrease the GMR ratio.

In addition to roughness, the grain boundary diffusion should be also born in mind in polycrystalline samples. This phenomenon is of special importance for immiscible systems which exhibit the highest GMR, like Fe/Cr, Co/Cu, Ag/Co, $Ni_{80}Fe_{20}$/Au, and $Ni_{80}Fe_{20}$/Ag. Here, the grain boundary diffusion might be a decisive detrimental mechanism. On the other hand it can be employed for the improvement of GMR, as it was proposed by Hylton et al. [HYL93].

In general, it can be concluded that a broad variety of experimental results on GMR can be systemized using one common denominator – interface roughness. On the other hand, a coherent understanding of all effects was not achieved yet.

9.2 Orange peel coupling

One of the most important factors affecting the GMR behaviour in multilayers and spin valves is the interlayer coupling between two ferromagnetic layers separated by a non-magnetic spacer. This coupling is usually a sum of different mechanisms. Among them, the three most important are: pinhole coupling, RKKY interaction and Néel coupling. Pinhole coupling is caused by structural defects in the spacer layer. They can totally destroy the GMR. The RKKY interaction oscillates with the spacer layer thickness as mentioned in Sec. 4. This coupling is due to the indirect exchange mechanism. The third mechanism is the Néel coupling [NEE62], often named orange peel coupling. Néel as the first considered magnetic dipole coupling between the two ferromagnetic layers separated by nonmagnetic spacer. The interlayer morphology has an impact on the magnetic coupling of free and pinned layers due to the magnetostatic interaction of magnetic dipoles induced by the interlayer roughness (waviness). It is accepted that full or at least partial vertical correlation of rough interfaces in a spin valve system results in the Néel magnetostatic coupling. This means that not only the interface roughness but also its lateral and vertical correlations are important. The original Néel model was extended by Kools et al. [KOO99] for finite thickness of magnetic layers and for stacks with columnar structures typical for metallic layers.

Néel coupling is explained in Fig. 9.2.1 considering the ferromagnetic coupling between two interfaces separated by the non-magnetic spacer and the antiferromagnetic coupling between the upper free layer interface and the upper pinned layer interface. The magnetostatic coupling with the lower interface of the pinned layer is negligible. The Néel coupling field H can be thus written as

$$H_N = \frac{\pi^2}{\sqrt{2}\lambda t_F} M_s \left[4\sigma_P \sigma_S e^{\frac{-2\pi\sqrt{2}d}{\lambda}} - 4\sigma_P \sigma_F e^{\frac{-2\pi\sqrt{2}(t_F+d)}{\lambda}} \right] \tag{9.2.1}$$

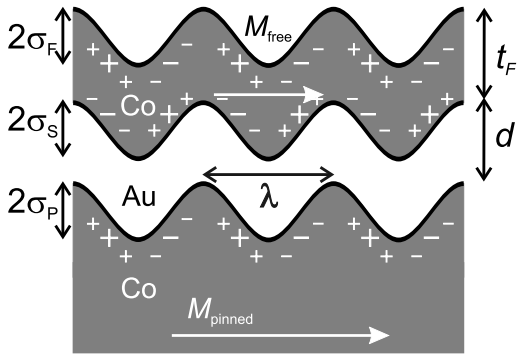

Fig. 9.2.1. Néel coupling principle.

where the first and second terms on the right-hand side correspond to the ferromagnetic and antiferromagnetic couplings, respectively. The M_s is the magnetization of the pinned layer, t_F is the thickness of the free layer, d is the thickness of the nonmagnetic spacer and σ_P, σ_s, and σ_F stand for the roughness of the pinned, spacer and free layers, respectively. The λ is here the period of the interface waviness which can be approximated by the lateral correlation length ξ (see Sec. 7).

One of the most important tasks in CIMS spin valve research and development is the minimization of the interlayer magnetic coupling between the free and pinned ferromagnetic layers in order to achieve their parallel as well as antiparallel orientations.

9.3 Ag/Co multilayers

As it was already shown, the growth conditions and the presence of structural defects significantly affect the AF alignment and thus also the magnitude of GMR in MLs. The quality of interfaces is another factor which influences the value of GMR. We showed already in previous sections that the interfaces can be modified by various types of heat treatment. Therefore, thermal processing can significantly influence the GMR in MLs. Generally, annealing-out of defects lowers the resistivity and, consequently, improves the GMR ratio. Another improvement of the GMR by annealing associated with a "back diffusion" was reported by Shelp et al. [SHE92] for Ag/Co MLs. Considering that Ag and Co are immiscible elements, smoothening of interfaces upon annealing due to the back diffusion process could be assumed. A different effect of heat treatment was reported by Dykes et al. [DIK90] for NiFeCo/Ag MLs with very thin magnetic layers. Here, the breaking-up of the thin magnetic layers due to grain boundary diffusion of Ag and formation of a discontinuous magnetic layer similar to granular structure [BER92] was suggested. The authors found that the GMR and field sensitivity varied widely as a function of annealing parameters.

In our works [LUB98, MAJ99, SPA99, JER00, LUB02], the effect of heat treatment on the GMR using the pulsed excimer laser irradiation of Ag/Co MLs was studied. The advantage of this type of heat treatment is the possibility to deposit a required amount of heat energy into the volume of the film without interaction with the substrate.

Tab. 9.3.1. The layer thickness d_{Ag}, d_{Co}, multilayer period d, number of periods N and effective interface roughness σ_{eff} determined from the X-ray reflectivity.

sample	d_{Ag} [nm]	d_{Co} [nm]	d [nm]	N	σ_{eff} [nm]
Ag2Co1	2.1	1.25	3.35	5	0.8
Ag3Co1	3.35	0.9	4.45	5	0.8
Ag4Co1	4.32	1.35	5.67	10	0.5
Ag6Co1	6.0	1.55	7.55	5	0.8

The samples were prepared in UHV apparatus (10^{-7} Pa and 10^{-6} Pa prior and during the deposition, respectively) by e-beam evaporation onto oxidized Si substrates at room temperature. SiO_2 thickness was 300 nm. The following MLs were prepared: (2 nm Ag/1 nm Co)×5, (3 nm Ag/1 nm Co)×5, (4 nm Ag/1 nm Co)×10 and (6 nm Ag/1 nm Co)×5. They will be denoted as Ag2Co1, Ag3Co1, Ag4Co1 and Ag6Co1, respectively. With regard to Ref. [LOL95], the 1 nm thick Co layers in Ag/Co MLs are assumed to be continuous.

The samples were processed with a Lambda Physik LPX 315i excimer XeCl laser with beam homogenizer in a chamber evacuated down to 10^{-3} Pa. The laser fluences F were 0.1, 0.15 and 0.2 Jcm^{-2}, the numbers of pulses directed to the same irradiation spot were $N = 1, 10, 20, 50, 100$ and 200. The pulse repetition rate was 10 Hz and the pulse duration 30 ns. The electrical resistance $R(H)$ was measured as a function of the applied magnetic field up to 50 kOe using a standard four-probe method with Ag contacts. Measurements were performed at 4.2 K in two geometries : magnetic field perpendicular ($\perp$) or parallel ($||$) to the film plane. The current was in the plane of the sample.

Since the direct measurement of temperature for the laser irradiated films is complicated due to very fast heating and cooling rates, numerical calculations were performed [DAN88]. The surface temperature and depth of melting were determined for each fluence. The results showed that at the fluences $F = 0.25$ Jcm^{-2} both Co ($T_{melt} = 1768$ K) and Ag ($T_{melt} = 1235$ K) melt in all types of MLs. For $F \leq 0.2$ Jcm^{-2}, Co layers remain solid. Ag layers remain solid in all samples at $F = 0.10$ Jcm^{-2}. They melt at $F = 0.15$ Jcm^{-2} in both Ag3Co1 and Ag4Co1 MLs but only for 0.25 Jcm^{-2} in Ag6Co ML. If Ag layers melt, they melt in the whole depth of MLs. The respective time of melting increases with the increasing fluence; e.g. at the surface of Ag4Co1 it is 30 and 56 ns for $F = 0.15$ and 0.2 Jcm^{-2}, respectively. The calculations are approximate as they do not reflect the structure of the layers and other parameters. The structural parameters of the prepared samples are summarized in Table 9.3.1

The effect of laser treatment on GMR is summarized in Table 9.3.2. The most important result was obtained for Ag6Co1 MLs where the GMR increase of about 100% for both orientations of the magnetic field was observed. A typical GMR dependence on the applied magnetic field for Ag6Co1 sample irradiated at $F = 0.15$ Jcm^{-2} and 10 pulses at 4.2 K is shown in Fig 9.3.1. The GMR increase is explained by the breaking-up of thin Co layers due to the grain boundary diffusion of Ag. Supposing a typical value of the grain boundary diffusion coefficient at the laser produced temperature [LUB98], the diffusion length of 1 nm (separation of Ag layers) corresponds to the diffusion time of 600 ns, i.e. duration of 20 laser pulses, in a good agree-

Tab. 9.3.2. GMR ratio and coercive field H_c at 4.2 K of Ag/Co MLs at various laser irradiation conditions, measured with magnetic field in the film plane. F - fluence, N - number of pulses, E - deposited energy. For Ag6Co1 ML, also the results for the magnetic field perpendicular to the film plane are given in the parentheses.

sample	F [Jcm^{-2}]	N	E [Jcm^{-2}]	H_c [Oe]	GMR [%]
Ag3Co1	as-deposited	0	0	800	11.5
	0.15	1	0.15	1000	13.4
	0.15	10	1.5	650	2.5
	0.2	1	0.2	750	7.6
	0.2	20	4	850	9.3
Ag4Co1	as-deposited	0	0	200	5.8
	0.1	1	0.1	300	6.3
	0.1	10	1	360	5.5
	0.1	20	2	200	6.7
	0.1	200	20	310	5.3
	0.15	1	0.15	260	4.7
	0.15	20	3	270	4.7
	0.2	1	0.2	390	1.3
	0.2	20	4	—	—
Ag6Co1	as-deposited	0	0	430 (3900)	7.6 (7)
	0.1	10	1	345 (4200)	12.5(11.7)
	0.15	10	1.5	360 (3500)	14 (12.8)
	0.15	50	7.5	360 (3100)	11.5 (14)
	0.15	200	30	430 (3900)	15 (15)
	0.2	20	4	330 (900)	13.5 (13.1)

ment with our irradiation conditions. This assumption is also supported by our diffusion studies in Co/Ag/Co trilayers [LUB02]. The magnetization data confirm the breaking-up of Co layers. Fig. 9.3.2 shows the temperature dependences of magnetization at 10 Oe after zero field cooling (ZFC) and field cooling (FC) for the as-deposited and irradiated Ag/Co MLs. A clear difference between the ZFC and FC curves for irradiated samples indicates the presence of a granular like component [HON95].

For Ag4Co1 ML, the laser irradiation does not affect GMR in a systematical way. The largest increase from 5.8 to 6.7% is for $F = 0.1$ Jcm^{-2} and 20 pulses. At higher fluences, the GMR decreases to zero for $F = 0.2$ Jcm^{-2} and 20 pulses.

The different behaviours under laser treatment of Ag6Co1 and Ag4Co1 MLs correlates with their different structure. Therefore, detailed structural studies were performed by the X-ray reflectivity and XRIDS. We traced the distribution of XRIDS throughout the reciprocal space by the sample (detector) scans at a fixed detector (sample) position. Some examples of the reflectivity and XRIDS measurements with their simulations are shown in Figs. 9.3.3 and 9.3.4, respectively. The corresponding simulation parameters are summarized in Tables 9.3.3 and 9.3.4.

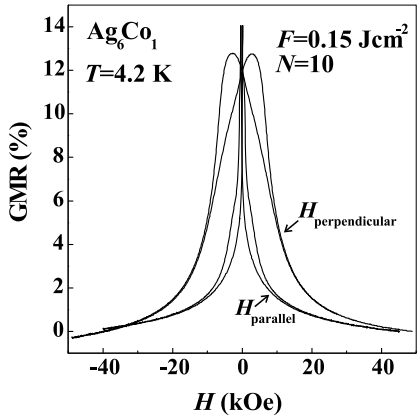

Fig. 9.3.1. GMR at 4.2 K for Ag6Co1 irradiated at $F = 0.15$ Jcm^{-2} and 10 pulses at two basic orientations of the magnetic field H.

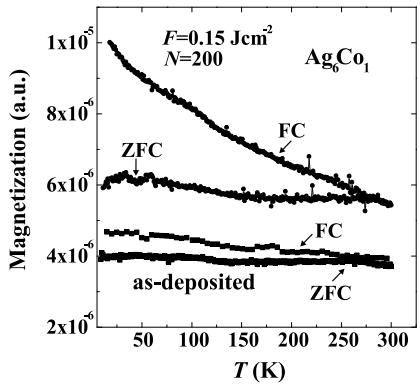

Fig. 9.3.2. Temperature dependence of the magnetization for zero field (ZFC) and field cooling (FC) conditions for Ag6Co1 as-deposited and irradiated at $F = 0.15$ Jcm^{-2} and 200 pulses.

The internal structure of the layers was checked by the XRD measurements and completed by CS TEM. The GI XRD patterns of Ag2Co1 and Ag6Co1 MLs taken at the angle of incidence $\alpha = 0.5^\circ$ are shown in Fig. 9.3.5. Both MLs exhibit a complete set of diffraction maxima of the face-centered cubic (fcc) Ag phase. Moreover, the maximum labeled as A may indicate the presence of a small amount of the close-packed hexagonal (hcp) Ag phase (203 diffraction). Co diffraction maxima cannot bet seen due to the small thickness of Co layers and a low scattering power of Co atoms. Moreover, 200 diffraction of the fcc Ag phase partially overlaps with a strong 002 one of the hcp Co phase (regular Co phase at room temperature). A trace of another diffraction of hcp Co, namely 200, is seen and it is labeled as B. The polycrystalline fcc Ag structure with random orientation of the grains persists after laser annealing at $F = 0.2$ Jcm^{-2}.

The Bragg-Brentano XRD pattern of the as-deposited Ag4Co1 (Fig. 9.3.6) shows only 111 and 222 diffractions of fcc Ag. Moreover, the satellites around 111 diffraction are recogniz-

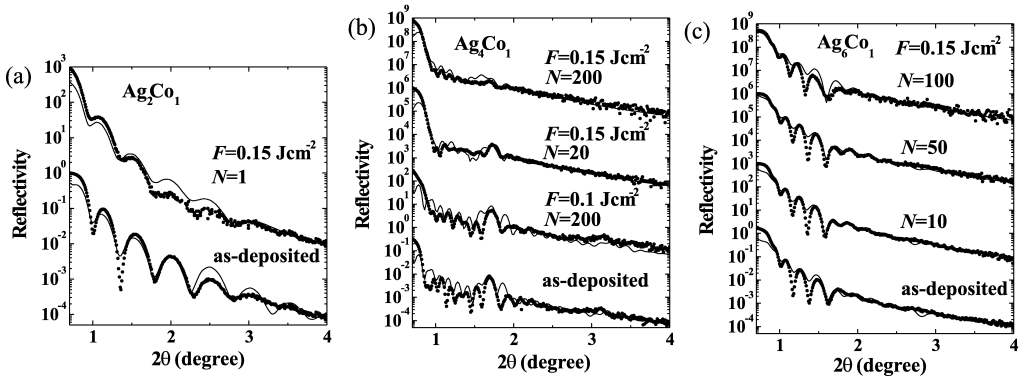

Fig. 9.3.3. Evolution of the specular XRR with laser irradiation for Ag2Co1 (a), Ag4Co1 (b), and Ag6Co1 (c) MLs. The measured curves (dots) were simulated by Fresnel optical computational code (line). For laser treated samples, the curves are multiplied by the factors of 10^3 (a), 10^3, 5×10^6, 10^9 (b), 5×10^2, 5×10^5, 5×10^8 (c) to shift them gradually upwards for clarity so that the scaling of the vertical axis is valid only for as-deposited MLs [JER00].

Tab. 9.3.3. Evolution of ML parameters with laser annealing obtained from the specular XRR simulations (Fig. 9.3.3). F, N, E, d_{Ag}, d_{Co}, d and σ_{eff} stand for the fluence, number of pulses, deposited energy, individual layer thickness, ML period and effective interface roughness, respectively. The layer thickness fluctuations included in the simulations reach 3 - 5%.

sample	F [Jcm^{-2}]	N	E [Jcm^{-2}]	d_{Ag} [nm]	d_{Co} [nm]	d [nm]	σ_{eff} [nm]
Ag4Co1	as-dep	0	0	4.7	1.1	5.8	0.6
	0.1	20	2	4.65	1.0	5.65	0.6
	0.15	10	1.5	4.4	1.1	5.5	1.0
	0.15	20	3	4.4	1.1	5.5	1.1
	0.15	200	30	3.5	1.8	5.3	1.8
Ag6Co1	as-dep.	0	0	5.5	1.2	6.7	1.1
	0.15	10	1.5	5.2	1.6	6.8	1.2
	0.15	50	7.5	4.65	2.0	6.65	1.3

able. These features imply a strongly textured structure with (111) planes in Ag layers oriented preferentially parallel to the surface which is confirmed also by CS TEM [MAJ99]. From the positions of the satellites, the period of 5 nm is calculated corresponding to the ML period found from the specular XRR. For $F = 0.1$ Jcm^{-2}, a strongly textured structure is preserved up to 200 pulses. For $F = 0.15$ Jcm^{-2}, the texture is gradually lost with increasing pulse number. The satellites disappear and another 200 diffraction of fcc Ag emerges from the background. For $F = 0.2$ Jcm^{-2}, further diffractions appear.

From the specular XRR simulations (Table 9.3.3) for Ag6Co1 ML it follows that the grain boundary diffusion of Ag atoms into Co layers is connected with a decrease of Ag layer thick-

Tab. 9.3.4. ML parameters obtained form the simulations of the XRIDS of laser treated samples (Fig. 9.3.4). The σ, ξ, L_{vert}, and h are the rms value of the geometrical interface roughness, lateral correlation length, vertical correlation length and Hurst (fractal) parameter, respectively.

sample	F [Jcm^{-2}]	N	E [Jcm^{-2}]	σ [nm]	ξ [nm]	L_{vert} [nm]	h
Ag4Co1	0.1	0	0	0.6	60	58	1
	0.1	200	20	0.6	60	56.8	1
Ag6Co1	0.15	0	0	1.1	50	33	1
	0.15	50	7.5	1.3	10	1	1

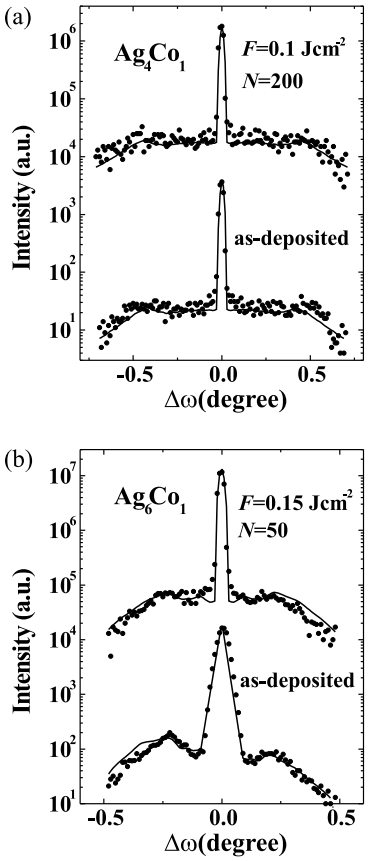

Fig. 9.3.4. Sample scans of Ag4Co1 (a) and Ag6Co1 (b) MLs before and after a laser irradiation. The measured curves (dots) were simulated within distorted-wave Born approximation (line) and for the laser treated samples, they are multiplied by a factor of 10^3 to shift them upwards for clarity so that the scaling of the vertical axis is valid only for as-deposited MLs. The $\Delta\omega$ means the offset from the specular position.

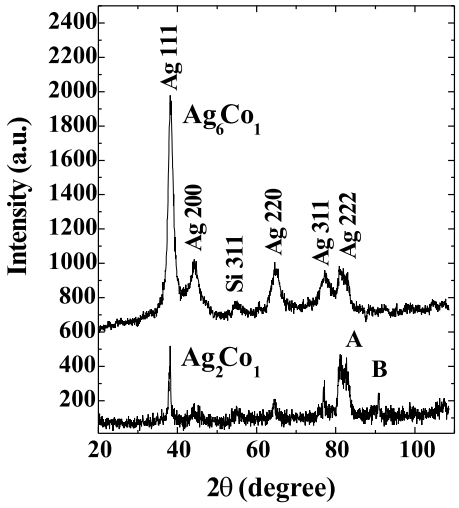

Fig. 9.3.5. X-ray diffraction patterns of the as-deposited Ag2Co1 and Ag6Co1 MLs taken at a grazing angle of incidence of 0.5°. The pattern of Ag6Co1 ML is shifted upwards by 600 for clarity so that the scaling of the vertical axis is valid only for Ag2Co1. The diffractions A and B are discussed in the text. Si 311 diffraction comes from the substrate.

nesses while opposite is the case for Co layers, the ML period being generally reduced. An enhanced refractive index of Co layers (by 10%), which had to be taken into account in the simulations, implies that these Co layers are in fact no more pure but "polluted" with Ag atoms penetrating between Co grains. When Ag layers start melting, one can assume a mixing of the liquid Ag/solid Co interfaces with a rapid solidification for each laser pulse. In the resulting granular-like structure, the GMR value is determined by number, size, shape and distribution of Co clusters depending solely on the details of a highly non-equilibrium solidification process.

For the as-deposited Ag4Co1 ML, the layer thicknesses remain rather unchanged under laser treatment (Table 9.3.3) and the satellites around 111 diffraction of fcc Ag persist up to $F = 0.15$ Jcm^{-2} and $N = 20$ irradiation while the interface roughness increases. For $N = 200$, Ag layers start melting and the GMR is unpredictably controlled by the granular-like structure formed.

As the interface roughness values determined from the specular XRR and diffuse scattering simulations (Tables 9.3.3 and 9.3.4) are equal for all samples, the values of the interface roughness found from the specular XRR simulations are the real (geometrical) ones and are fully controlled by the grain morphology as may be expected owing to the immiscibility of Ag and Co. Therefore, any change of the interface correlation, either lateral or vertical, is closely related to the grain morphology and size evolution induced by laser treatment. For Ag6Co1 ML, the vertical correlation length, comparable with the total ML thickness in the as-deposited state, decreases to the level of Co layer thickness for $F = 0.15$ Jcm^{-2} and $N = 50$. This means that the grain boundary diffusion breaks the replication of interface profiles completely. Simultaneously, the lateral correlation length decreases 5 times which suggests the formation of smaller grains in discontinuous ML, promoting the GMR ratio. A small value of the interface roughness

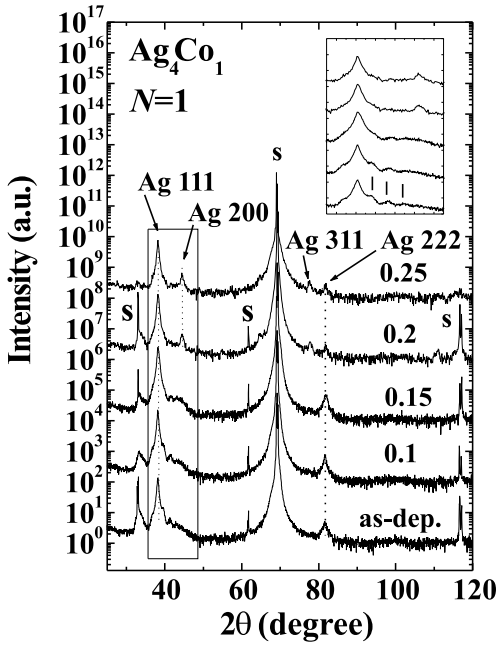

Fig. 9.3.6. X-ray diffraction patterns of Ag4Co1 ML taken in Bragg-Brentano geometry before and after one pulse irradiation with different fluences. The patterns of laser treated samples are multiplied by the factors of 10^2, 10^4, 10^6, and 10^8 to shift them gradually upwards for clarity so that the scaling of the vertical axis is valid only for the as-deposited ML. The superlattice satellites around Ag 111 diffraction are shown in more detail in the inset. The diffractions coming from the substrate are labeled as "S" [JER00].

in the as-deposited Ag4Co1 ML is connected with its textured character resulting into ordered grains, as observed by electron microscopy. Contrary to Ag6Co1 ML, the vertical and lateral correlation lengths of the interface profiles are little affected by the laser treatment and remain nearly the same for $F = 0.1$ Jcm^{-2} and $N = 200$ annealing. The interface roughness is also unchanged. For $F = 0.15$ Jcm^{-2}, the interface roughness increases implying a small reorientation of the grains while the texture character of the ML structure is basically still preserved up to the melting threshold for Ag layers, as indicated by the XRD measurements.

Considering the results of structural and interface analyses, the behaviour of the GMR laser irradiated MLs can be discussed as follows. When Ag layers are polycrystalline and do not melt under laser treatment, the Co layers become discontinuous due to the grain boundary diffusion of Ag into Co. Assuming that the main contribution to GMR originates from random orientation of the magnetic moments, this can explain the increase of GMR observed for Ag3Co1 ML at $F = 0.15$ Jcm^{-2}, $N = 1$ irradiation and Ag6Co1 ML for $F = 0.1$ - 0.2 Jcm^{-2} (Table 9.3.2). The grain boundary diffusion at the interfaces is significantly suppressed when interfaces are partially coherent and therefore, only slight changes of GMR are observed in Ag4Co1. When Ag layers melt, the subsequent rapid solidification can produce granular-like structures independently whether the interfaces were coherent or not in the solid state. In addition to the number,

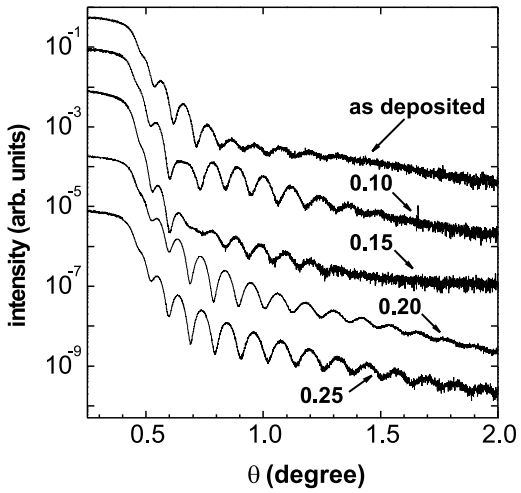

Fig. 9.4.1. XRR spectra of a trilayer Co(2 nm)/Ag(40 nm)/Co(1.5 nm) in the as-deposited state and after a treatment by 1 KrF laser pulse at various fluences [LUB02].

size, shape and distribution of Co clusters determined by the details of the irradiation process, the GMR value of such structures is affected also by a possible appearance of demagnetizing interparticle interactions (cf. [VIE97]).

9.4 Sharpening of Ag/Co interfaces

Possible "back-diffusion" effect and/or sharpening of the Ag/Co interfaces under laser heat treatment was studied in Ag/Co bilayers and trilayers [DAN99, LUB02]. Co thickness ranged between 1 and 10 nm and Ag thickness between 15 and 50 nm.

The XRR spectra (Fig.9.4.1) show considerable changes under laser treatment. At $F = 0.10$ Jcm^{-2}, the interfaces become sharper due to the densification of the structure and stress release. At higher fluence, they deteriorate due to the solid-state diffusion. After melting of Ag at $F = 0.20$ Jcm^{-2}, the spectrum shows sharpening (number of the peaks increases again) which may be attributed to the back-diffusion process. With further increase of the fluence, the spectrum deteriorates again. The sheet resistance (Fig. 9.4.2) correlates with the XRR data. After the initial decrease due to annealing-out of defects, the sharpening and intermixing effects compete at higher fluences, controlling the R_s values.

The diffusion studies can be summarized as follows:

a) In the case of solid-solid interface, the results indicates the grain boundary diffusion. The diffusion coefficient is $D = 10^{-8}$ cm^{2}s^{-1} at 1210 K and the activation energy of diffusion is $Q = 0.4$ eV.

b) In the case of solid-liquid interface, the diffusion coefficient with the pre-exponential factor $D_o = 3.8 \times 10^{-7}$ cm^{2}s^{-1} and activation energy $Q = 1.5$ eV were obtained. At 1380 K,

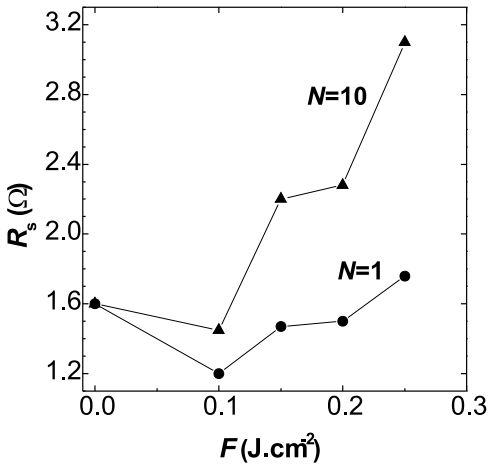

Fig. 9.4.2. Sheet resistance of the trilayer from Fig. 9.4.1 in the as-deposited state and after treatment by $N = 1$ and 10 laser pulses at various fluences [LUB02].

$D = 1.3 \times 10^{-8}$ cm^{2}s^{-1} for $F = 0.20$ Jcm^{-2} (not shown here). These values are typical for diffusion in liquid metals and amorphous alloys [WAN99].

9.5 Fe/W and Co/W multilayers

GMR in MLs has been studied mostly in the stacks combined from mutually immiscible material combinations, e.g. Cu/Co, Ag/Co. Their heat of formation ΔH is positive [MIE76]. Therefore, interfaces are chemically sharp and formation of magnetically dead layers is suppressed [GRU00]. For GMR applications, also tungsten spacer is of some interest because of its refractory nature and low electrical resistivity. Moreover, the heat of formation $\Delta H = 0$ for the Fe/W pair and is negative but of a low absolute value for Co/W ($\Delta H = -2$ kJ/g.at). Thus, some level of immiscibility is expected also in these structures.

The intermixing at interfaces of excimer KrF laser irradiated Co/W and Fe/W MLs was investigated in some of our papers [MAJ02, MAJ03b, CHU05]. These MLs have never been reported to exhibit giant magnetoresistance to our knowledge. The Fe/W and Co/W MLs with magnetic layers of 1 or 2 nm nominal thickness and W layers of 1, 2, 5, or 7 nm thickness were e-beam deposited in UHV of 10^{-7} Pa at 70 - 200°C onto Si substrates with a 300 nm thermal oxide layer. MLs with 5 and 10 periods were prepared. W was the top layer to avoid surface corrosion. The samples were irradiated by an excimer KrF laser ($\lambda = 248$ nm) with a homogenizer (homogeneity $> 95\%$) in dry vacuum (5×10^{-4} Pa). Fluences $F = 50$ - 250 mJ/cm^2 and number of pulses $N = 1$ and 10 directed to the same spot were used. The length of pulses and their repetition rate were 30 ns and 5 Hz, respectively. The magnetoresistance was measured at RT and 4.2 K in the current-in-plane geometry by a standard four-probe method in the field up to 5 T in the plane of MLs and perpendicular to the current direction.

From the calculations of the temperature evolutions of the laser irradiated samples it follows that the MLs remain solid up to $F = 100$ mJcm^{-2} and Fe, Co melt completely and SiO_2 partly

Tab. 9.5.1. GMR ratio data at 4.2 K of (Fe/W)×5 and (Co/W)×5 MLs with the nominal thickness of 1 or 2 nm of Fe, Co and 2 or 5 nm of W. The d_{Fe}, d_{Co}, d_W are the values of the respective thicknesses from the XRR spectra simulations. The saturated magnetization values M_s are also shown. The samples denoted by asterix were irradiated at $F = 100$ mJcm^{-2} by 10 pulses. (A decrease of the layer thickness $\approx$ 5 - 10% was observed only at $F \geq 150$ mJcm^{-2}.)

#	sample	$d_{Fe,Co}$ [nm]	d_W [nm]	GMR [%]	M_s [10^{-3} emu]
1	Fe/W	0.9	0.8	—	—
3	Fe/W	2.2	2.3	0.60	0.17
4	Fe/W	0.9	5.2	0.16	0.07
5	Fe/W*	0.9	5.2	0.30	0.06
6	Co/W	1.3	2.5	0.22	0.07
7	Co/W*	1.3	2.5	0.05	0.07

at $F \geq 200$ mJcm^{-2}. W remains solid at all fluences used [MAJ02, MAJ03b].

From the XRR we concluded that the effective interface roughness (including intermixing) was similar for both types of MLs in the as-deposited state, namely $\sigma_{eff} = 0.5$ - 0.8 nm for Co/W and $\sigma_{eff} = 0.4$ - 0.9 nm for Fe/W. Differences appear when the geometrical roughness inferred from the XRIDS is considered, being $\sigma = 0.3$ nm for Co/W and $\sigma = 0.3$ - 0.8 nm for Fe/W. Thus, intermixing given by the difference between these two types of roughness is higher for Co/W MLs which probably corresponds to the negative heat of formation. After the laser irradiation, the interface parameters of Co/W MLs including intermixing are almost doubled for the fluence $F = 150$ mJcm^{-2} and $N = 10$. For Fe/W MLs, σ_{eff} increases only slightly, being 1 nm after $F = 250$ mJcm^{-2} and $N = 10$ irradiation. Thus, Fe/W interfaces are more resistant against laser irradiation. With the exception of the MLs with nominal layer thicknesses of 1 nm, which were amorphous, both types of MLs show one-axial texture along [110] direction. For Co/W ML, also superlattice-like satellites corresponding to a strongly coherent structure and the formation of Co_3W phase are visible in the XRD pattern. After the laser irradiation of both types of MLs, the crystallization proceeds from top downwards.

Some GMR measurements performed at 4.2 K are summarized in Table 9.5.1. Obviously, MR is quite low. The best results for #3 are presented in Fig. 9.5.1. For #1, no GMR was measured. This is a consequence of the interface roughness and intermixing which are comparable with the W spacer thickness. However, it was found that the GMR ratio can be increased two times by laser irradiation of Fe/W MLs which are less prone to the intermixing (#4 vs. #5). On the other hand, the GMR ratio decreased four times in Co/W MLs (#6 vs. #7) where the intermixing under irradiation increases. Following this conclusions, we tried to improve the GMR in Fe/W MLs by the deposition at an elevated substrate temperature assuming that *in-situ* heating is a more effective way to influence the ML structure than a post-deposition treatment. A substantial MR enhancement was achieved in the (1.35 nm Fe/ 1.15 nm W)×10 ML deposited at 190°C. Here, the MR ratio increased up to 2% already at RT (Fig. 9.5.2) and no hysteresis was observed. Still several times larger value can be expected at 4.2 K. An increased number of periods should not influence this result considerably [GRU00]. The sample #8 (Table 9.5.2) was

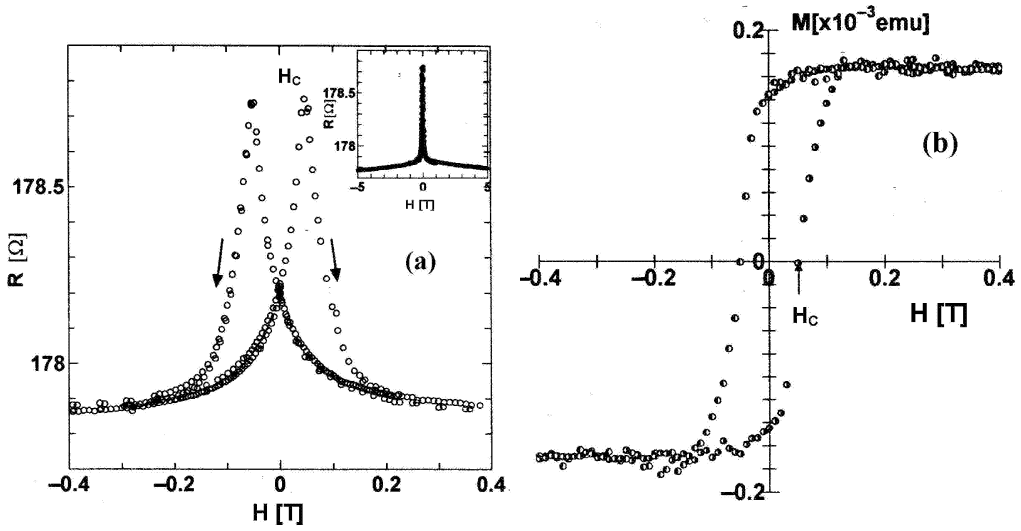

Fig. 9.5.1. Magnetoresistance curves (a) and magnetization loops (b) for ML #3 (Table 9.5.1) deposited at RT and measured at liquid helium temperature. The GMR ratio defined as $(R - R_{min})/R_{min}$ is 0.6% (a). H_c - coercivity.

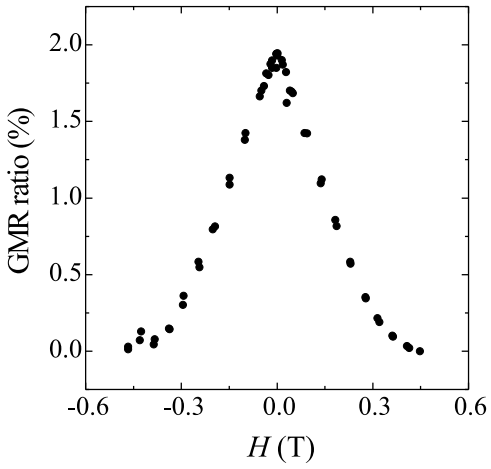

Fig. 9.5.2. MR curve for (1.35 nm Fe/ 1.15 nm W)×10 ML deposited at 190°C and measured at RT.

chosen for a detailed study of the effect of the ML structure on GMR. It will be compared with a similar sample #9 deposited at RT (Table 9.5.3).

Sample #8 deposited at 190°C exhibits two distinct diffraction peaks (Fig. 9.5.3) (sample #9 deposited at RT was amorphous) which can only be explained as superlattice-like satellites due to a structural coherency between the Fe and W layers with bcc (110) planes oriented parallel

Tab. 9.5.2. Simulation parameters of the bcc 110 diffraction satellites measured on the 190°C deposited ML. The quantities d, d^{is} and Δn stand for the layer thickness, (110) interplanar spacing (normal to the substrate) and Gaussian fluctuation of the lattice plane number inside the layers, respectively. The last parameter is related to a discontinuous interface roughness. The bulk values of the (110) interplanar spacing in JCPD/ICDD PDF-2 diffraction database are 0.20268 nm and 0.2238 nm for Fe and W, respectively.

#	d_{Fe} [nm]	d_W [nm]	d^{is}_{Fe} [nm]	d^{is}_W [nm]	Δn_{Fe}	Δn_W
8	1.41	1.20	0.2024	0.2228	1.17	0.25

Tab. 9.5.3. Parameters of the XRR and XRIDS simulations of the RT (#9) and 190°C (#8) deposited MLs; d, σ_{eff}, σ, ξ, L_{vert} stand for the layer thickness, effective interface roughness, geometrical interface roughness, lateral and vertical interface correlation lengths, respectively.

#	d_{Fe} [nm]	d_W [nm]	σ_{eff} Fe on W [nm]	σ_{eff} W on Fe [nm]	$\sigma_{\text{Fe on W}}$ [nm]	$\sigma_{\text{W on Fe}}$ [nm]	ξ [nm]	L_{vert} [nm]
8	1.34	1.14	0.6	0.9	0.4	0.7	9.0	25
9	1.00	0.85	0.5	0.7	0.3	0.5	2.2	7

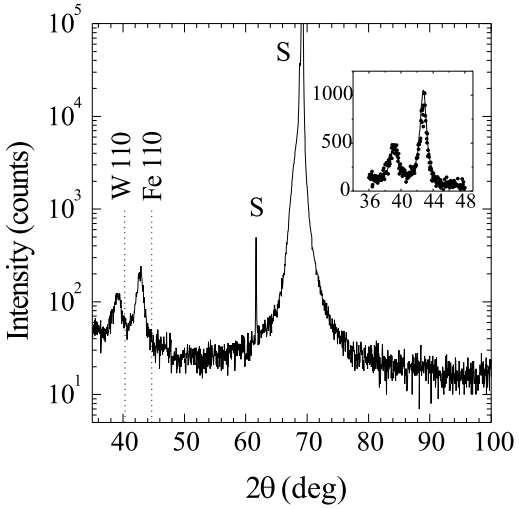

Fig. 9.5.3. The XRD pattern measured on the sample #8 (Table 9.5.2) with indicated bulk diffractions for bcc structure taken from JCPD/ICDD PDF-2 diffraction database. S marks substrate diffractions. The simulation of the 110 satellites is shown in the inset (dots - measured points, line - simulation).

to the substrate. The satellite simulation and its parameters are shown in the inset of Fig. 9.5.3 and Table 9.5.2, respectively. Using Scherrer equation, the coherency length of $\approx$ 10 nm was

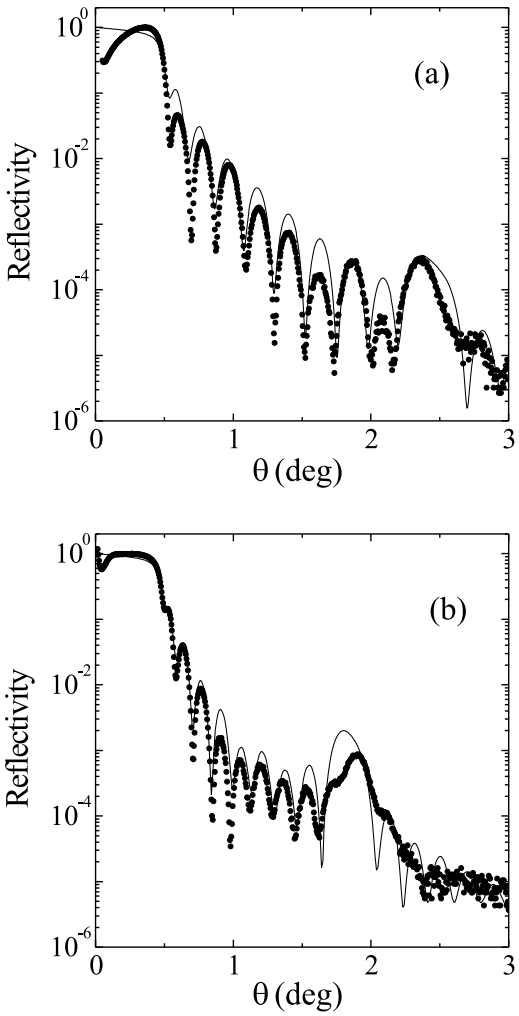

Fig. 9.5.4. The XRR curves (dots) and their simulations (lines) measured on ML #9 deposited at RT (a) and ML #8 deposited at 190°C (b). The θ is the angle of incidence with respect to the sample surface.

assessed from the satellite widths, i.e. the coherency stretches over ≈ 5 ML periods. The lattice parameter normal to the substrate is smaller than the bulk value both in the Fe and W layers. In the presence of one-axial texture, such result indicates a lateral tensile stress inside the layers.

The specular XRR curves of samples #8, #9 (Fig. 9.5.4) exhibit a large Bragg peak and dense Kiessig fringes suggesting that the interfaces are well resolved despite the nanometer-scale layer thicknesses. The interface characteristics obtained by the simulation of XRR and XRIDS measurements are summarized in Table 9.5.3. The effective interface roughness σ_{eff} is larger for 190°C deposited sample. The XRIDS measurements (Fig. 9.5.5) show an enhancement of the diffuse scattering around the specular ridge in both samples called resonant diffuse scattering

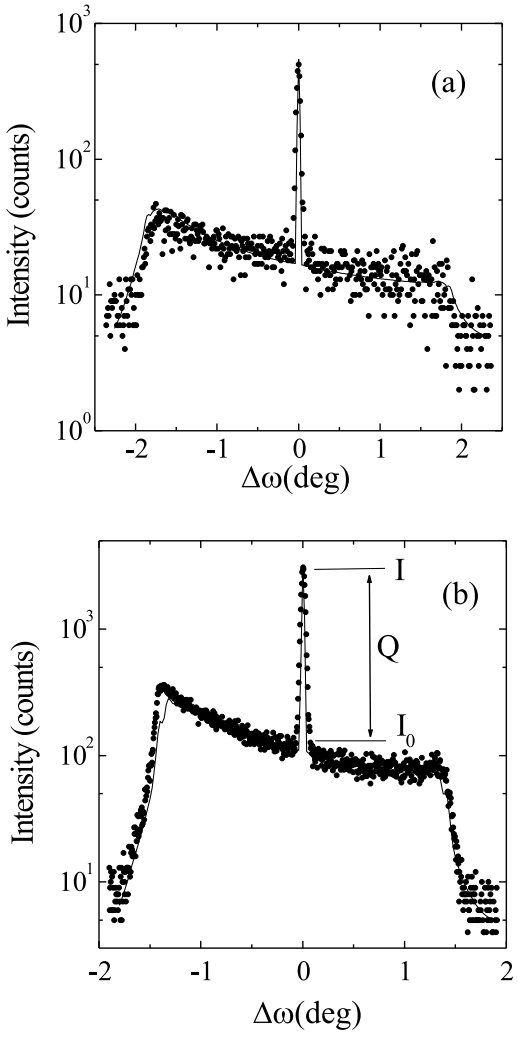

Fig. 9.5.5. The rocking curves (dots) and their simulations (lines) measured on MLs #9 deposited at RT (a) and #8 deposited at 190°C (b). The $\Delta\omega$ is the offset from the specular position. The rocking curves were measured with the rotating sample and the detector fixed at the first Bragg maximum.

(RDS). It is a clear sign of at least partial replication of the interface profiles. For simulations, an exponentially decaying vertical interface correlation function containing a single vertical correlation length L_{vert} proved to be a good choice. A lateral correlation function for self-affine interfaces suggested in [SIN88] was taken for all interfaces, being controlled by the lateral correlation length ξ, root-mean-square (rms) value of the (geometrical) interface roughness σ, and fractal parameter h (Table 9.5.3).

A comparison of the σ_{eff} and σ values for given samples shows again a rather low intermix-

ing. Therefore, the larger effective interface roughness in the 190°C sample is attributed solely to an enhanced geometrical interface roughness, presumably induced by the crystalline grains affecting the interface morphology. This fact is obvious already from an apparently higher level of the RDS above the instrumental background in the 190°C deposited sample (Fig. 9.5.5) which is produced solely by geometrical interface imperfections.

The strength of the interface replication (vertical interface correlation) in the two samples may be simply quantified and compared by a $Q = I/I_0$ parameter [BEL94, COL96] (Fig. 9.5.5b) which reaches the values of 25 and 28 for the RT and 190°C depositions, respectively. The ξ and L_{vert} values obtained from the DWBA simulations (Table 9.5.3) confirm rigorously not only a stronger vertical but also lateral correlation of the interface profiles in the 190°C deposited sample. The same lateral correlation length of 9 nm was found in the Fe/Cr MBE grown ML with high GMR ratio [SCHA98a, SCHA99]. The vertical correlation length is comparable with the whole ML thickness in sample #8 while in sample #9, the interface replication is lost over the distances much smaller than the multilayer thickness.

There may be several reasons for the considerably higher MR in the 190°C deposited ML. The textured crystalline structure with well developed coherency between the layers produces undoubtedly less bulk scattering regardless its spin nature with the positive effect on the MR if the bulk and interface scattering are counteracting. A less-defect structure contains also fewer pinholes changing unfavorably the magnetization directions [SCHA98a, SCHA99]. On the other hand, our results show that the intermixing is not promoted by the 190°C deposition so that there is no enhanced contribution of the mixed regions to the bulk scattering. A further factor which could contribute directly to the GMR enhancement is the larger interface roughness if it results in a larger spin asymmetry of the interface scattering. The most prominent difference, however, represent the substantially larger lateral and vertical correlation lengths of the interfaces in the 190°C deposited sample which indicate slowly varying and well replicated interface profiles. Therefore, the magnetic shortcuts formation is suppressed. The role of the vertical interface correlation in the GMR has been rather neglected so far but may be of importance in presence of thin layers and rough interfaces. Different vertical interface correlations may explain controversial results reporting either a decrease [BAR96] or increase [BAR97] of the GMR with an increasing lateral correlation length in the multilayers. Nevertheless, slightly different layer thicknesses in the two samples under study may also contribute to the GMR difference observed.

9.6 Néel coupling in spin valve structures

One of the most important tasks in CIMS spin valve research and development (Sec. 4) is the minimization of the interlayer magnetic coupling between the free and pinned ferromagnetic layers in order to achieve their parallel as well as antiparallel orientations. The interlayer morphology has an impact on the magnetic coupling of free and pinned layers due to the magnetostatic interaction of magnetic dipoles induced by the interlayer roughness (waviness) also known as Néel or orange peel coupling (Sec. 9.2) [NEE62, KOO99]. A number of experimental studies linked the structural properties of conventional spin valves obtained by scanning probe techniques [PAR00, TEG01], transmission electron microscopy [SCH00a], and X-ray reflectivity [LAN01].with their magnetic properties. The GMR/TMR (giant/tunnel magnetoresistance) and M-H hysteresis curves were measured in order to characterize the Néel coupling mechanism. Only a very limited number of experimental works [LAN01, BAB02] used diffusely scattered

X-rays from the spin valves, mainly because of a low scattered intensity. A complete X-ray mapping of the reciprocal space [HOL99] near the origin of CIMS spin valve structures was done for the first time to our knowledge in our recent paper [SIF07a].

We deposited simultaneously identical spin valve structures on substrates with and without a bottom Au layer used as electrode in CIMS structures. The roughness of the Au layer typically 40 nm thick is considerably higher in comparison to that of a common Si substrate. Different roughness implicates also an altered interface roughness replication during the growth process. The impact of a bottom Au electrode on the interface roughness, its vertical and lateral correlations on magnetic properties was studied. X-ray measurements of reciprocal space maps present convenient, fast and non-destructive statistical analysis of buried layers and interfaces of spin valve structures.

The samples were deposited by e-beam evaporation technique in an UHV chamber with the base pressure of 10^{-7} Pa. A set of Co(18 nm)/Au(5.4 nm)/Co(3.2 nm)/Au(0.8 nm) spin valves was deposited on Si(100)/SiO_2 (300 nm) wafers. In this pseudo spin valve structure, the thicker Co layer with higher coercivity is a pinned layer and the thinner Co layer is a free layer. Prior to the spin valve deposition, a part of Si/SiO_2 wafer was *in-situ* coated with a bottom electrode Cr(3.5 nm)/Au(41.6 nm) for the future CIMS functionality. Subsequently, the CoBAu/Co spin valve structure was deposited on both parts of the substrate simultaneously. In this way, the layer thicknesses are identical for both samples and any differences in the structure and interface characteristics are induced solely by the presence of the bottom Au layer. Sample A refers to the spin valve without the bottom Au electrode and sample B stands for the spin valve with the bottom Au electrode. We studied the spin valves with Au spacers because of their high electron density contrast with the adjacent Co ferromagnetic layers allowing a better analysis of the X-ray diffuse scattering data. Full X-ray reciprocal space maps of diffusely scattered radiation around the origin of the reciprocal space as well as common cuts – X-ray reflectivity, detector scans and rocking curves were measured on X-ray diffractometer (Bruker D8 Discover Super Speed) equipped with Cu rotating anode (wavelength 0.154 nm) and Goebel mirror yielding 10^9 photons/s in the primary beam. A high X-ray photon flux is a prerequisite for measurements of the diffuse scattering from CIMS spin valve structures. Coplanar grazing incidence (1°) X-ray diffraction was measured on the same X-ray diffractometer with a long Soller slit and a LiF monochromator on the detector arm. For magnetic characterization, a home-built longitudinal magnetooptical Kerr effect (MOKE) apparatus with s-polarized light incident at 50° on the sample was used [SIF07a]. The external magnetic field with an amplitude of 500 Oe and frequency of 0.125 Hz was applied in sample surface plane. The sample was mounted on a rotational stage allowing the measurement of the angular dependence of in-plane magnetic anisotropy.

Measured X-ray reciprocal space maps of diffusely scattered X-rays for sample A and sample B are shown in Fig. 9.6.1. An overall diffusely scattered intensity for sample B is larger than that for sample A which is a simple indicator of a larger total roughness of interfaces for the spin valve grown on the bottom Au electrode. The scattered X-ray waves from mutually correlated rough interfaces add coherently giving rise to the sheets of a higher intensity in q_x direction called resonant diffuse scattering (RDS) bananas. These sheets cross the specular direction ($q_x = 0$) at the points of the interference maxima. In the case of a weak or none vertical roughness correlation, the scattered X-ray waves from all interfaces add incoherently without generation of specific features in the reciprocal space map. The RDS bananas are much more pronounced in the reciprocal space map of sample B (Fig. 9.6.1b) showing a higher degree of the interface

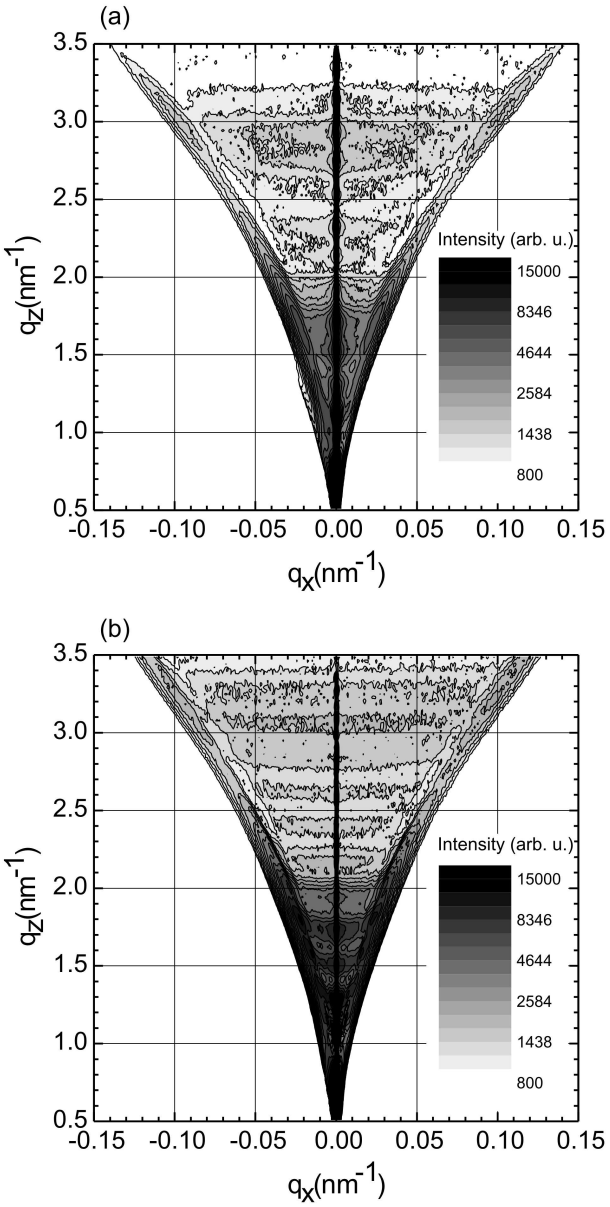

Fig. 9.6.1. Measured reciprocal space maps of diffusely scattered intensity from the spin valve structures. (a) sample A, (b) sample B.

profile replication in the vertical direction if compared to sample A (Fig. 9.6.1a). The upward bending of RDS bananas is due to refraction on interfaces. The lateral correlation length ξ of

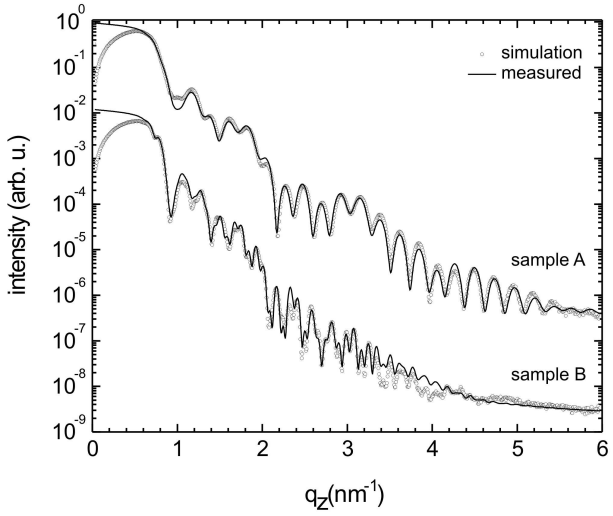

Fig. 9.6.2. Measured and simulated X-ray reflectivity scans for samples A and B.

spin valve interfaces is of the order of material grain size which is especially true for mutually immiscible polycrystalline layers, such as Co and Au in our case, where the interface morphology is controlled mainly by crystalline grains. We used Williamson-Hall plot [WIL54] to estimate the average Au grain size and microstrain. A significant (111) texture of Au layers restricted our analysis to the Au 111, 220 and 311 diffractions. The estimated grain size is 5 ± 1 nm for sample A and 12 ± 1 nm for sample B. The microstrain was found similar for both samples.

The X-ray reflectivity curves ($q_x = 0$) and their fits (Leptos software of Bruker AXS GmbH) are plotted for samples A and B in Fig. 9.6.2. A genetic fitting algorithm and reflectivity calculation based on the Parratt formalism with a Névot-Croce interface roughness model (Sec. 7) were used to estimate the individual thickness and effective roughness of each layer (Table 9.6.1). The effective roughness includes the topological roughness and interdiffusion at interfaces but in our case of immiscible materials the interdiffusion at the Au/Co or Co/Au interfaces can be neglected. For the layer densities, the tabulated values of bulk materials were used. The X-ray reflectivity of sample A was fitted independently of sample B and *vice versa*. In spite of this fact, the results for the thicknesses of the active spin valve layers (Co/Au/Co/Au) are very well correlated as expected from the simultaneous deposition process. The average roughness increase of the spin valve layers for sample B is 0.3 ± 0.1 nm with respect to sample A. The path direction of a detector scan in reciprocal space map intersecting the RDS bananas justifies its utilization for the quantitative estimate of the vertical correlation length. The measured and simulated detector scans are shown in Fig. 9.6.3. For the simulation of the diffuse scattering, the DWBA was used. The Hurst h parameter related to the fractal dimension of interfaces as $D^f = 3 - h$ was set to unity in all simulations implicating rather smooth interfaces. To include vertical correlation of the interface roughness, the Ming model [MIN93] that correlates the interface profiles within a single vertical correlation length L_{vert} gave satisfactory results. The only free parameter in the simulations of diffusely scattered intensity was then the vertical correlation length. The values

Tab. 9.6.1. Simulated thickness d and effective interface roughness σ_{eff} of individual layers of samples A and B.

SV layer	sample A		sample B	
	d[nm]	σ_{eff} [nm]	d [nm]	σ_{eff}[nm]
Au	0.8	0.5	0.9	0.9
Co	3.2	0.8	3.2	0.8
Au	5.4	0.5	5.3	0.8
Co	18.1	0.6	17.8	0.9
Au	—	—	41.6	0.7
Cr	—	—	3.5	0.7
SiO_2	300	0.3	300	0.3
Si	bulk	0.3	bulk	0.3

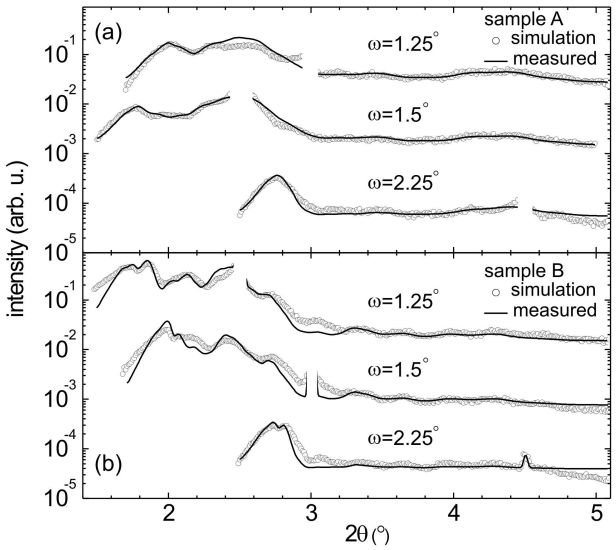

Fig. 9.6.3. Measured and simulated X-ray detector scans at various ω for samples A and B. The specularly reflected beam was removed for scaling reasons.

15 ± 5 nm and 35 ± 5 nm were estimated for samples A and B, respectively, which are comparable or larger than the layer thicknesses in the spin valve stack.

The higher vertical correlation length of sample B was already identified qualitatively from the RDS bananas in the reciprocal space map. As the thickness of the non-magnetic Au spacer (5.3 - 5.4 nm) is for both samples almost equal and smaller than the evaluated vertical correlation length, the Néel coupling model is applicable.

The quantitative analysis of the diffusely scattered and specularly reflected X-rays gives clear

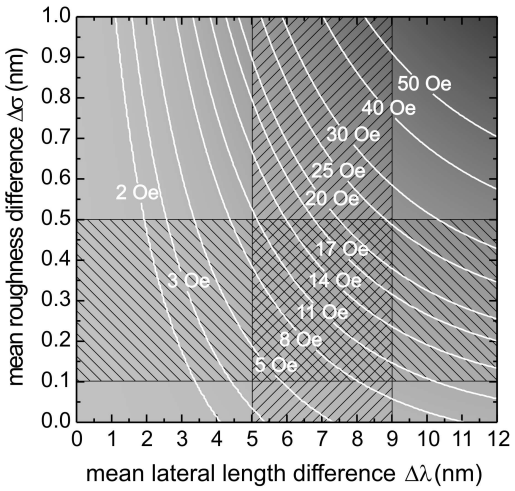

Fig. 9.6.4. Calculated change ΔH_N of the Néel coupling field as a function of the mean lateral length difference and mean roughness difference.

evidence of a higher roughness and vertical and lateral correlations for CIMS spin valves grown on the Au bottom electrode. It is accepted that full or at least partial vertical correlation of rough interfaces in a spin valve system is the origin of the Néel magnetostatic coupling mechanism [NEE62, KOO99]. For CIMS structures, it is sufficient to take into account only the ferromagnetic coupling between the two interfaces separated by a nonmagnetic spacer and the antiferromagnetic coupling between the upper free layer interface and the upper pinned layer interface. The magnetostatic coupling with the lower interface of the pinned layer is negligible. The Néel coupling field H_N is given by Eq. (9.2.1). Here, the height of the interface corrugation was assumed to be twice the interface roughness obtained from the X-ray reflectivity simulations. The Au bottom electrode of CIMS spin valve structures introduces an increase of the roughness, vertical and lateral correlation lengths and therefore enhances the Néel coupling. We used the formula (9.2.1) to simulate the expected increase of the Néel coupling ΔH_N stemming from a changed roughness and lateral correlation length. The ΔH_N as a function of the mean roughness difference $\Delta\sigma$ and mean lateral correlation length difference $\Delta\xi$ for our spin valve structure is shown as a contour plot in Fig. 9.6.4. The hatched area in the plot shows the theoretically predicted changes in the Néel coupling ΔH_N based on the values from the X-ray analysis: $\Delta\sigma = 0.3 \pm 0.1$ nm and $\Delta\xi = 7 \pm 2$ nm. The set of possible ΔH_N spans from 4 Oe to 25 Oe. The experimental uncertainty of 0.1 nm for the interface roughness and 1 nm for the lateral correlation length is the reason for this rather large variation of ΔH_N .

The longitudinal magnetooptical Kerr effect was employed to measure M-H curves of the samples A and B. Each sample was rotated around the surface normal by an angle φ and the corresponding M-H curves were recorded. Our results show the presence of an easy axis oriented in the plane of the spin valve samples. According to the published data, the critical thickness of Co layers for the transition from the out-of-plane to the in-plane easy magnetization axis state is around 2.4 - 1.8 nm [AYA02, PAR05]. A polar plot of the measured spin valve coercivity as

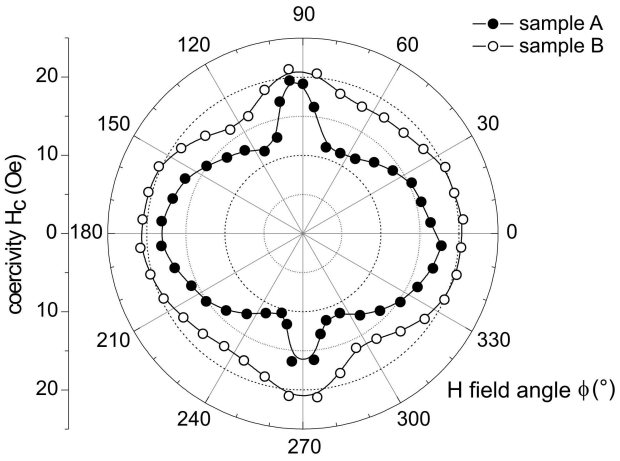

Fig. 9.6.5. A polar plot of spin valve coercivity as a function of the angle φ of the applied field for samples A and B.

a function of the angle of the applied field is shown in Fig. 9.6.5. The coercivity plot shows a four-fold symmetry for both samples. The polar coordinate system for the angle φ was oriented in order to match the four-fold symmetry at the angles of 0° and 90°. No spontaneous preferential magnetization orientation with respect to the substrate crystallographic axes was observed which is not surprising considering the 300 nm thick SiO_2 layer covering the Si (100) wafer. The four-fold symmetry of magnetic anisotropy for sample B is reduced which could be attributed to the increased Néel coupling, stress and interface roughness. A systematic increase of coercivity for sample B is observed. As the active spin valve structure is identical for sample A and B, the increase of coercivity is first of all because of the increased Néel coupling. However, the H_c value can be affected also by the stress in thicker Co layers which is probably different for Co layer growing on textured Au bottom layer and on amorphous SiO_2 substrate. The analysis of the measured coercivity increase ΔH_N has a mean value of 4.5 Oe with a standard deviation of 1.5 Oe. The experimentally determined values of ΔH_N fall well within the theoretically calculated range (Fig. 9.6.4) of coercivity change due to the Néel coupling. This qualifies the Néel coupling as a main contributing mechanism to the changed spin valve coercivity of CIMS spin valves grown on Au bottom electrodes.

The presented X-ray mapping of the reciprocal space of spin valve structures is a non-destructive approach suitable for a rapid statistical characterization of the interlayer properties which is able to reveal the origin of Néel magnetostatic coupling.

10 Nanoparticles as building blocks of nanostructures

10.1 Synthesis and self-assembling of magnetic nanoparticles

Nanoparticles (NPs) and nanoclusters are a special category of nanostructures which form a broad transition between bulk matter and isolated atoms or molecules. Their properties are determined by reduced dimensions and dimensionality, proximity effects, and surface dominating over the bulk [DOSCH01]. In spite of their finite size, nanoparticles are often categorized as zero-dimensional ($0D$) structures.

Two basic approaches to the preparation of nanostructures are top-down and bottom-up. Top-down methods are broadly used in semiconductor technology employing different types of lithography patterning, like electron beam, scanning tunneling and interference lithography. The structures are regular and can be distributed on regular lattices. Both the shape and size accuracy of the structures are limited by the resolution of patterning. This is important for diverse applications in memories and circuits but also for the study of new collective phenomena. Before 2015, the patterning should reach the production level of 25 nm [PARK97, LAW00].

The bottom–up approach utilizes physical or chemical deposition methods to build nanostructures from atoms or atomic clusters. The regular arrays of nanostructures can be fabricated by a variety of methods like focusing of deposited atoms by "atomic" laser lenses [McC00], deposition of atoms onto atomically accurate steps on the surface of crystals (vicinal surfaces) [KIR01], STM or AFM tip–assisted depositions [WIR99], etc. However, chemical "wet" methods are most extended at present. Here, NPs are prepared by chemical reactions from appropriate precursors in the form of colloid solution [NANO] and regular arrays of particles are formed by assembling on an appropriate surface.

The era of metal colloidal solutions began with the experiments of Faraday on gold sols in the mid-nineteenth century [FAR57]. Colloidal gold was prepared by reduction of $AuCl_4$ compound using phosphorus as the reducing agent. The first systematic studies of the effect of preparation conditions on particle size in colloids were performed by Zsigmondy [ZSI] at the beginning of 20th century. An intense research in this field began with the commencement of the era of nanoscience and nanotechnology. Nanometer-scale colloidal particles of semiconductors, noble and transition metals have attracted much attention over the last two decades due to their new electronic, magnetic, optical and structural properties. It should be noted that colloidal particles of micrometer and submicrometer size have been known for a relatively long time but only recently, suitable tools for their characterization and engineering enabling to create nanoparticle devices were elaborated. Nowadays, nanoparticles are suitable blocks for building of various structures, filling the gap between the standard lithographic techniques reaching 100 nm size and chemical synthesis on atomic and molecular level. Wet chemical methods enable us to prepare nanostructures in relatively large amounts and at reasonable expenses. In this work, only metallic colloid nanoparticles prepared by wet chemical approaches [NANO, CAO, MUR00] will be discussed.

Metal colloidal solutions are stable dispersions of nanoscale clusters or fine particles – either crystalline or amorphous – in a solvent. The surface of particles is covered by surfactant (typically 1 - 2 nm thick) preventing their agglomeration and oxidation. If the material dispersed in the solution exhibits ferromagnetic behaviour in the bulk, the colloidal suspensions are called ferrofluids or magnetic fluids. The most important prerequisite for the preparation of magnetic

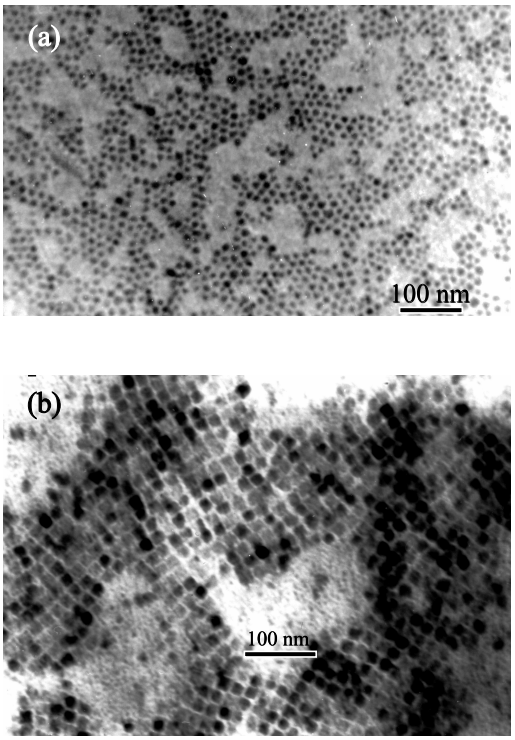

Fig. 10.1.1. SEM image of (a) an ordered array of Co-Fe-O nanoparticles with a diameter of 7.6 nm on Si substrate and (b) Fe-O nanoparticles with a diameter of 15 nm on a carbon coated TEM grid.

nanoparticle superstructures from ferrofluids is the control over the particle size and size distribution during synthesis [NANO, DOSCH01].

Colloidal nanoparticles can serve as building blocks for complex layered structures. The most attractive property of colloidal nanoparticles is their tendency to self-assembling. In particular, they spontaneously organize themselves into ordered $2D$ and $3D$ arrays (monolayers and artificial crystals, respectively) under specific conditions [COL98, PET98, MUR00, SHE03]. These arrays (prepared by variety of methods) show unique behaviour which is different from that of the bulk and isolated particles (c.f. [COL98] and references therein). Such structures move nowadays the frontiers in advanced materials and devices development. Self-assembling is attractive because no additional energy for formation of ordered arrays is needed.

Various techniques making use of spontaneous self-assembling have been reported. In the simplest case, a drop of colloidal nanoparticle solution is applied on a substrate. Subsequently, the process of solvent evaporation induces formation of single or multiple layers resulting in an ordered nanoparticle array. Hexagonal or cubic arrangements of nanoparticles are usually observed [NANO, MUR00] (Fig. 10.1.1).

Another effective way of preparation of ordered arrays of nanoparticles over large areas is the Langmuir-Blodgett deposition. This technique has been basically used for producing extremely

thin organic films with a high degree of control over the thickness and molecular architecture. However, it allows also preparation of insoluble nanoparticle monolayers floating on a water surface with subsequent deposition onto solid substrates whilst retaining the particle arrangement in the monolayer.

The third method is spin coating elaborated in the semiconductor device production for the formation of photoresist and electron-resist masks. By this method, it is possible to create monolayers over large areas, however, particles are not well ordered inside the layers as a rule.

The self-assembling is a complex process with various interactions between nanoparticles, substrate and solvent. At the microscopic level, interplay between localized interactions such as van der Waals attraction and hard-core (steric) repulsion (combined with long-range magnetic dipolar interaction if the particles are magnetic) determines the assembling process. However, type and thickness of the surfactant, interaction between the forming nanoparticle array and substrate, drying kinetics and solution/substrate interfacial energy affect dramatically the final array.

The particles dispersed in a medium undergo constant Brownian motion and their interactions could be described by an effective potential that accounts for all solvent effects. In a stabilized dispersion, the attractive and repulsive forces are in balance [HEN70]. Let us further to consider colloidal dispersion as a fluid of N particles at a temperature T and occupying a volume V. The interaction energy of two particles is characterized by the effective pair potential $U(r)$. If the total potential energy is an additive contribution to the pair potential, the fluid equation of state can be written as

$$\frac{pV}{N\mathrm{k_B}T} = 1 - \frac{2\pi\rho}{3\mathrm{k_B}T}\int\limits_0^\infty \frac{dU(r)}{dr} g(r) r^3 dr, \tag{10.1.1}$$

where $U(r)$ is the interaction energy of two particles, $\rho = N/V$ is the density, p is the pressure of the fluid, $g(r)$ is the radial distribution function probability of finding two particles separated by r and $\mathrm{k_B}$ is the Boltzmann constant. The function $g(r)$ holds information about the structure of the isotropic materials. When $r \to \infty$, $g(r) \to 1$. In general, the radial distribution function is unknown. It can be measured experimentally or it may be derived theoretically using Percus-Yevick equation [PER58] if the pair potential is given. To calculate $g(r)$, simple forms of the pair potential are used. The simplest approximation which describes the interaction between nanoparticles is a so called hard-core model. In this approximation, the spherical particles of radius R do not interact for distances larger than $2R$. At distance $2R$, the interaction becomes harshly repulsive. This is due to the fact that the particles are assumed as solid bodies that cannot interpenetrate. The interaction potential has the following analytical expression:

$$\begin{aligned} U(r)_{\mathrm{hard-core}} &= \infty, \qquad r < 2R \\ U(r)_{\mathrm{hard-core}} &= 0, \qquad r > 2R \end{aligned} \tag{10.1.2}$$

For high-density fluids, the behaviour of the spherical particles of radius R is dominated by the repulsive potential and can be described by the hard-core potential. For the hard-core potential, the equation of state can be written as

$$\frac{pV}{Nk_\mathrm{B}T} = \frac{1 + \phi + \phi^2}{(1-\phi)^3}, \tag{10.1.3}$$

where $\phi = N\pi(2R)^3/6V$ is a packing fraction. The hard-core repulsion interaction can induce positional ordering of the particles. Usually, particles form a close-packed lattice with the maximum packing fraction $\phi = 0.74$ or a random close-packed state $\phi = 0.64$ [THI63, RIN96]. Of course, for the maximum density of regular closed packed structures, values ϕ could be obtained also from simple geometrical considerations.

The pair potential of the colloidal suspension of charged particles can be described by the Derjaguin-Landau-Verwey-Overbeek (DLVO) potential. It includes the hard-core repulsion, van der Waals attraction, and Coulomb repulsion interactions

$$\begin{aligned} U(r)_{\mathrm{DLVO}} &= \infty, \qquad r < 2R \\ U(r)_{\mathrm{DLVO}} &= U(r)_{\mathrm{vdW}} + U(r)_{\mathrm{Coulomb}}, \qquad r > 2R. \end{aligned} \tag{10.1.4}$$

The van der Waals forces between the particles can be expressed as

$$U(r)_{\mathrm{vdW}} = -\frac{A}{6}\left\{\frac{2R^2}{r^2-4R^2} + \frac{2R^2}{r^2} + \ln\frac{r^2-4R^2}{r^2}\right\}, \tag{10.1.5}$$

where

$$A = \frac{3\mathrm{h}\nu(n_p+n_s)^2(n_p-n_s)^2}{16\sqrt{2}(n_p^2+n_s^2)^{3/2}} \tag{10.1.6}$$

is a Hamaker constant that accounts for materials properties derived by Israelachvili [ISR73], h is Planck constant, ν is a characteristic frequency and n_p and n_s are the refractive indices of the particles and the solvent, respectively.
The electrostatic Coulomb interaction can be described as

$$U(r)_{\mathrm{Coulomb}} = \left(\frac{Z^*\mathrm{e}\exp(kR)}{1+kR}\right)^2 \frac{\exp(-kr)}{\varepsilon r}, \tag{10.1.7}$$

where

$$k = \sqrt{\frac{4\pi\rho_c(qe)^2}{\varepsilon \mathrm{k_B}T}} \tag{10.1.8}$$

is the Debye screening length where ρ_c denotes the density of the free counter-ions and q their valence, ε is a dielectric constant of the continuous medium, e electron charge and Z is the effective charge of the colloid. From these equations it follows that we can tune the interaction between the particles by adjusting the solvent composition (i.e. changing ε; q, ρ_c).

When the particles are magnetic, the magnetostatic interaction is defined as

$$U(r)_{dd} = \left[\frac{\mu_\iota\mu_j}{r_{ij}^3} - \frac{3(\mu_\iota r_{ij})(\mu_j r_{ij})}{r_{ij}^5}\right], \tag{10.1.9}$$

where μ_i is the magnetic dipole of the particle i, r_{ij} is the vector joining particle i and j. The $U(r)_{dd}$ potential is anisotropic in contrast to the $U(r)_{\mathrm{DLVO}}$ which is isotropic. This leads to the dramatic change in self-assembling behaviour.

Different self-assembly behaviours of magnetic nanoparticles were confirmed experimentally. It was shown that Co monodomain magnetic particles self-assemble forming head-to-tail structures, linear and branched chains. Under an external magnetic field of 0.5 T, FeAu particles of 10 nm size aggregated along the direction of the magnetic field and formed micrometer chains [LIN01].

In the next part, we will show examples of our self-assembly studies of Co, Fe_3O_4 and $CoFe_2O_4$ nanoparticles.

Cobalt nanoparticles were prepared using a combination of oleic acid and oleyl amine to stabilize the monodisperse Co colloids. The synthesis is based on the thermal decomposition of dicobaltoctacarbonyl $Co_2(CO)_8$. A typical procedure is as follows: Under airless condition, a mixture of oleyl amine ≈ 1 mmol, deoxygenated decane ≈ 100 ml, and oleic acid ≈ 1 mmol is heated to 343 K. 1 mmol of dicobaltoctacarbonyl is added and stirred for 15 min. Finally, the solution is allowed to simmer for 1 h. After cooling to room temperature, the particles were separated from the solvent by a magnet. Ultrasmall particles remain in the solvent due to their smaller effective magnetic moment and the separated larger particles are redispersed in 100 ml toluene. This procedure is repeated until all fractions of particles of the same size are obtained [SPA02].

Fe_3O_4 and$CoFe_2O_4$ nanoparticles were synthesized by a high-temperature solution phase reaction of metal acetylacetonates ($Fe(acac)_3$, $Co(acac)_2$) with 1,2-hexadecanediol, oleic acid and oleylamine in phenyl ether. Fe(acac)3 (2 mmol), 1,2-hexadecanediol (10 mmol), oleic acid (6 mmol), oleylamine (6 mmol), and phenyl ether (20 mL) were mixed and magnetically stirred under a flow of oxygen-free argon (in a dry-box). The mixture was then transferred into a reactor and heated to 195 - 205°C for 30 min and then, under a blanket of argon, heated to reflux at 265°C for 20 - 30 min. The black-brown mixture was cooled down to room temperature by removing the heat source. Under ambient conditions, ethanol (40 mL) was added to the mixture, and a black material was precipitated and separated via centrifugation. The black product was dissolved in toluene in the presence of oleic acid (≈ 0.05 mL) and oleylamine (≈ 0.05 mL). Centrifugation (6000 rpm, 10 min) was applied to remove any undispersed residue. The product was then precipitated with ethanol, centrifuged (6000 rpm, 10 min) to remove the solvent and redispersed into toluene [SUN04, CHIT07b].

For the spontaneous self-assembling studies, we used the following approach: 5 μL drops of a solution were deposited onto the substrates of area of 1 cm^2. The particle arrays were created by drying in air at room temperature without a magnetic field (a), in the presence of an external magnetic field $B = 0.26$ - 0.9 T perpendicular or parallel to the substrate surface (b), and by spin coating (c). Si (001) wafers with 500 nm thick layer of Si_3N_4 and carbon coated Cu grids were used as substrates. Substrates were carefully cleaned prior to the deposition to remove all dust particles and impurities which could serve as additional pinning centers during drying the drop.

The size, shape and ordering of nanoparticles can be studied by high-resolution transmission electron microscopy (CS TEM) and scanning electron microscopy (SEM). For SEM, only field emission gun FEG machines give reliable results. The reason is the insulating surfactant covering the particles. Deposition of a thin conductive metallic and/or carbon layer onto particles to suppress charging effects by SEM observation could results in loss of the resolution if we inspect particles of 5 - 7 nm diameter. TEM is useful for evaluation of the surfactant layer thickness. As follows from Fig. 10.1.2, the nanoparticles do not touch each other. This is due to the surfactant layer which is transparent for electrons. Using HR TEM it is possible to analyze the internal

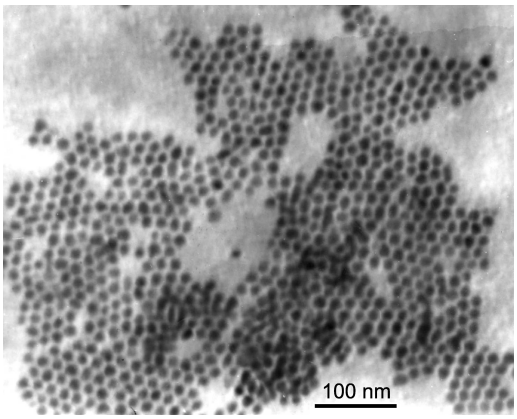

Fig. 10.1.2. TEM image of Co nanoparticle array (10 nm in diameter) prepared by drying a drop in air in the perpendicular magnetic field of 0.8 T on a carbon coated grid.

structure of nanoparticles. For composite nanoparticles like AgCo, the internal structure can be determined by TEM as shown in [CHI07a]. Composition can be determined using EDX, XRD and/or TEM techniques.

Crystalline structure inside nanoparticles can be studied by XRD. For a layer of nanoparticles on a substrate, grazing incidence X-ray diffraction (GI XRD) is the most effective (Fig. 10.1.3). Alternatively, transmission geometry with a capillary or a layer deposited onto a suitable transparent foil can be used. The ordering, average size and shape and interparticle distance can easily be determined by grazing-incidence small-angle X-ray scattering (GISAXS). GISAXS is also useful for an *in-situ* tracking of the ordering process. It should be noted that the resolution of common AFM instruments is usually not sufficient to distinguish the details of NPs.

In Fig 10.1.4, the evolution of structure of Co nanoparticles with temperature obtained by *in-situ* annealing is shown. For the as-prepared particles, only one broad maximum corresponding to the interplanar spacing of 0.203 nm is determined. This value corresponds neither to the fcc Co (111) nor to the hcp Co (002) phases known in the bulk metal. For bulk, the fcc Co (111) interplanar spacing is 0.2046 nm and the hcp Co 002 interplanar spacing is 0.2023 nm. The broad maxima indicate a poorly developed crystalline structure of nanoparticles. The most significant structural changes appear between 400 and 450°C. Here, the formation of a well developed fcc phase is observed. Above 450°C, the maxima of the fcc Co phase Co(111), Co(200), Co(220) and Co(311) become more narrow and their intensity increases with increasing temperature. Small reflections suggest the presence of poorly-developed CoO. We did not find any clear evidence of hcp Co phase or ε-Co phase formation in the whole temperature range of our *in-situ* and *ex-situ* heat treatments. The narrowing of the diffraction maxima with increasing temperature is caused by the subsequent increase of the coherently diffracting domains between 450-700°C. Apparent particle size ("diameter") was estimated for several temperatures using a simple Scherrer equation with the widths of (311) diffractions (Fig. 10.1.5). It was assumed that the broadening is caused mostly by the particle size effect and stress had just a small contribution. However, the widths were not corrected for instrumental contribution so that the values in Fig. 10.1.5 reveal

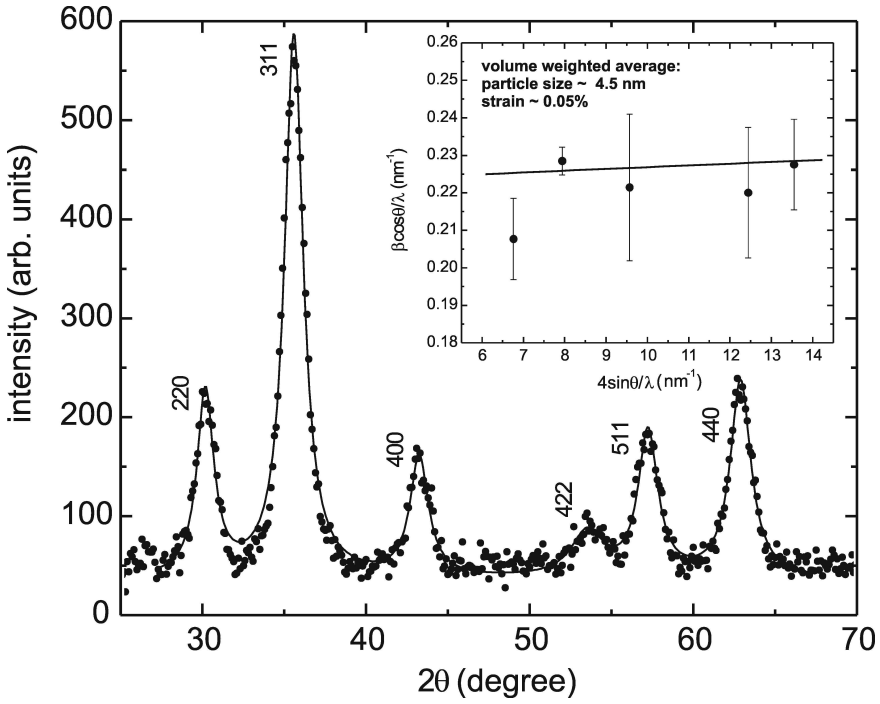

Fig. 10.1.3. Grazing incidence X-ray diffraction pattern of a multilayer stack of Fe-O nanoparticles on silicon substrate measured at 1.5° angle of incidence. The inset shows a WilliamsonHall plot based on the positions and widths of the measured diffraction peaks [SIF07b].

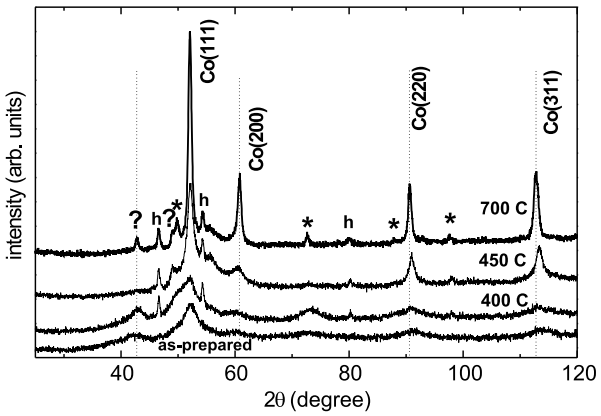

Fig. 10.1.4. XRD patterns of Co nanoparticles annealed *in-situ* using Pt heating element. For the temperature $\geq 450^{o}$C, fcc Co maxima can be seen (* - poorly crystalline CoO phase, ? - unidentified phase, h - maxima coming from the heating element) [CHI07a].

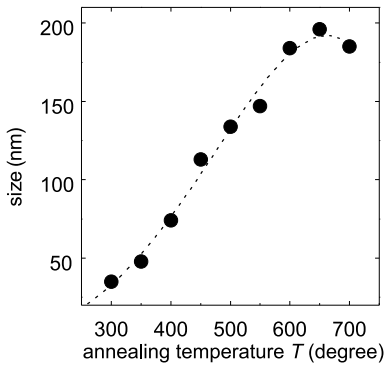

Fig. 10.1.5. Particle size ("diameter") vs. annealing temperatures determined using a simple Scherrer equation with the widths of (311) diffraction.

just an overall trend.

The increase of the coherently diffracting domains can be explained by the coalescence of Co particles during the heat treatment. For the temperatures between 200 and 400°C, the organic surfactant is destroyed and particles can agglomerate. This process was confirmed also by TEM studies. The formation of single crystal clusters can be understood taking into account the well known fact that the melting point of a metal cluster T_M depends on its radius r as [PAW]

$$T_M(r) = T_B(1 - L/r), \tag{10.1.10}$$

where T_B is the melting point of the bulk material and$L$ is the length parameter which depends on the type of material. For pure metallic Co clusters of $r = 4$ nm radius, coalescence at the temperatures approx. 100°C was reported in Ref. [PEN01]. Molecular dynamics studies showed [HEN03] that for the coalescence of two spherical particles, an increase of the thermal energy of the coalescing cluster balances the reduction of the surface energy. If the increase of temperature exceeds the cluster melting point, one can expect the cluster to melt during coalescence. Then, also the formation of larger single crystal clusters can be assumed.

For a drop of a colloidal solution deposited on a substrate, a nonzero contact angle is often observed with the contact line pinned to its initial position as the solvent evaporates. In this case, the nanoparticles move towards the contact line due to a higher evaporation rate at the drop edge. Also in absence of the pinning line, a convective particle flux towards substrate driven by the solvent evaporation may act in favour of the formation of ordered arrays [DEE97]. A so called stick-slip motion of the drop contact line accompanies the formation of arrays on the substrate with more pinning centers [ADA95, SHM02].

Model calculations of the self-assembling process based on the dynamics of the evaporating solvent indicate a crucial effect of the solvent, nanoparticle size and thermodynamic state on the morphology of the final structure [RAB03], as it was observed also experimentally. For example, formation of well ordered self-assembled arrays of dodecanthiol-passivated Au nanoparticles was achieved when the evaporation dynamics was modified by the surfactant molecules added to the colloidal solution [XLIN01, NAR04, BIG06]. On the other hand, a large variety of possible

resulting patterns of the self-assembled nanoparticles is a serious limitation for targeted technological applications of self-assembling. A deeper understanding of the self-assembling process, especially its initial stages, is essential for a better control of the nanoparticle ordering. This issue is closely related to answering the question where the ordering takes place. In contradiction with a common concept that the self-assembling process occurs at the substrate/colloid interface, formation of monolayer islands of dodecanthiol-passivated Au nanoparticles on the top surface of the drop (liquid/air interface) was confirmed by *in-situ* X-ray scattering experiments as well [NAR04].

In the next part we will present typical results on the self-assembling.

Formation of $2D$ ordered arrays of Co nanoparticles

Typical arrays of Co particles prepared by drying in air, by drying with the application of an external magnetic field, and by spin coating using SEM are shown in Fig. 10.1.6 [CHI07]. The tendency to form hexagonal $2D$ ordered Co nanoparticles can be found for all three types of deposition. The type of the substrate and concentration of particles affect the ordering, too. The assembled arrays are not perfect. One can find a coherent length or size of well ordered regions. Typically air-dried $2D$ ordered arrays are of 100 nm $\times$ 100 nm in size, being separated by disordered inclusions and empty areas (Fig. 10.1.6a). The $2D$ ordered arrays are observed also by spin coating, being smaller here (Fig. 10.1.6c). The application of the external perpendicular magnetic field improves the ordering of particles considerably. The size of ordered arrays increased e.g. to 200 nm $\times$ 500 nm, as shown in Fig. 10.1.6b. For all deposition procedures, the $2D$ hexagonal close-packed ordering was observed. The deposition procedure slightly modifies the distance between the nearest neighbours (see Table 10.2.1 further). The mean interparticle distance can be determined from SEM and TEM images and an average value from GISAXS [CHU03].

The interparticle distance (center-to-center) from TEM pictures is larger than the particle diameter because of the presence of the surfactant transparent for electron beam. The TEM and SEM analyses show the mean thickness of the surfactant layer of ≈ 2.8 nm. The ordering inside the array is relatively good. Nevertheless, various types of defects can be identified in the arrays. These defects are created first of all by the particles differing in shape and size from the statistical average. Therefore, a direct analogy with the atom ordering in crystals cannot be used but many resemblances are obvious. Fluctuation of the particle size deteriorates the long-range ordering and basic sub-arrays are often separated by quasi-dislocations. Considerably smaller areas of ordered arrays are formed on carbon coated Cu-grids (Fig. 10.1.2) in comparison to Si/Si_3N_4 substrates which is due to the higher roughness and imperfections of the carbon film deposited on the Cu grid.

Formation of $3D$ ordered arrays of nanoparticles

For Co nanoparticles prepared by the synthesis described above, we observed formation of $3D$ arrays of nanoparticles - columns - in an external magnetic field. In the field perpendicular to the substrate surface, most of the columns are aligned with the field direction (Fig. 10.1.7a). The columns are 1 - 4 μm long with a diameter of 300 - 400 nm. The columns are formed at the magnetic field $B \geq 0.20$ T which corresponds to the onset of saturation of magnetization in

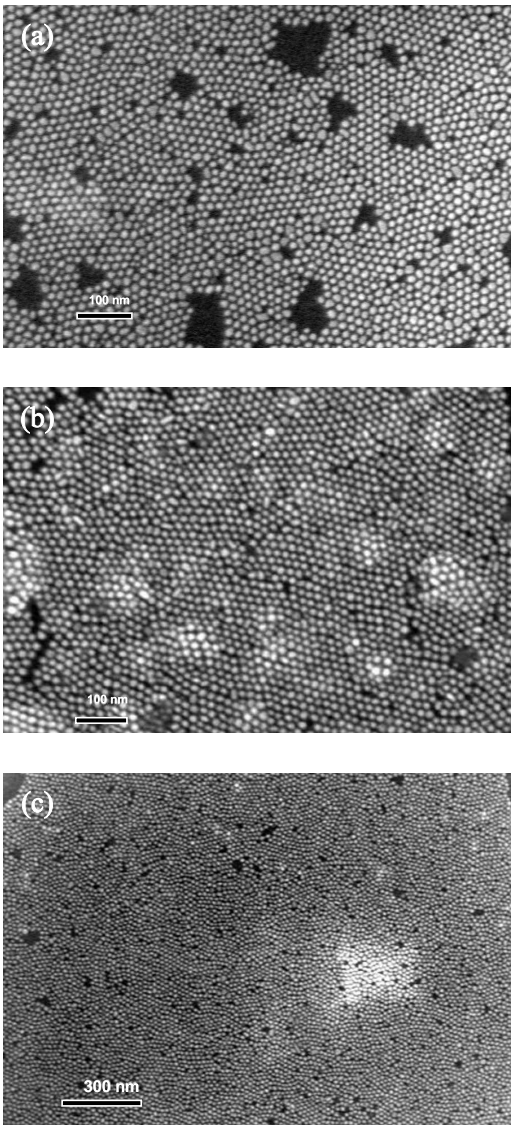

Fig. 10.1.6. SEM images of nanoparticle arrays prepared on Si/Si_3N_4 substrates (a) by drying in air, (b) by drying in the perpendicular magnetic field of 0.75 T and (c) by spin coating at 3000 rpm.

$M(H)$ dependences. Under appropriate conditions (higher concentration of nanoparticles than for preparation of $2D$ arrays, magnetic field perpendicular to the substrate surface), an ordered array of columns is formed. Various disordered areas with broken columns, tilted columns, etc. were found (Fig. 10.1.7b).

Similar columns were formed in a parallel magnetic field (Fig. 10.1.8). Here, the columns

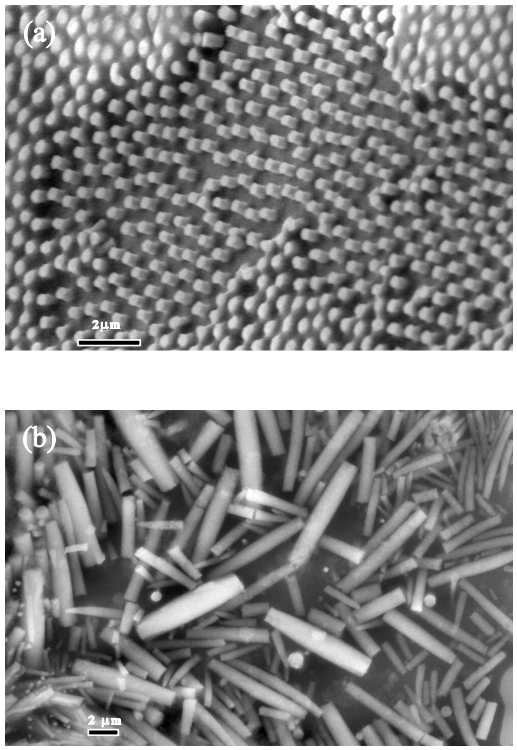

Fig. 10.1.7. SEM images of the columns prepared by drying in air on Si/Si_3N_4 substrate in the magnetic field of 0.8 T. (a) Random array of perpendicular columns, (b) damaged area with broken and tilted columns.

lay on the substrate surface along the field direction. The diameter of columns is similar as before (200 - 400 nm) but they are considerably longer (several 10 μm). This is due to the fact that in parallel geometry the extent of particle chaining is much larger, not being limited by the thickness of the drop.

The inner part of a column etched by an ion beam is shown in Fig. 10.1.9. The Co particles inside the column can be clearly distinguished. The samples were prepared from Co columns created on a NaCl crystal and covered by a thin carbon layer. Then the NaCl substrate was dissolved and a small part of columns was put onto a TEM grid and etched by Ar^+ beam (800 eV). Here, it is not possible to study the ordering of particles because it is influenced by the ion bombardment.

The formation of $3D$ clusters of magnetic nanoparticles is well known in magnetic ferrofluids. It was already predicted by de Gennes and Pincus [DGE70] that the magnetic dipole-dipole interaction induces a spontaneous formation of chains or rings of particles with the magnetic moment parallel to each other. In an external magnetic field, these chains align in the direction of the field. A pseudo-crystalline ordering of cobalt core-shell particles in ferrofluid has been reported elsewhere [WIE03].

Columns of close-packed magnetic particles formed in ferrofluids and ordered into a lattice were reported by Jiang et al. [JIA00]. The ordering follows the magnetic field orientation.

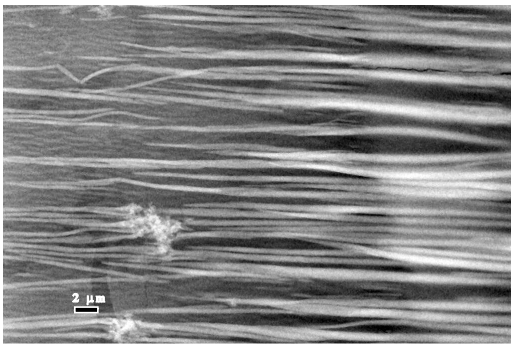

Fig. 10.1.8. SEM image of the columns prepared with the magnetic field of 0.8 T parallel to the substrate.

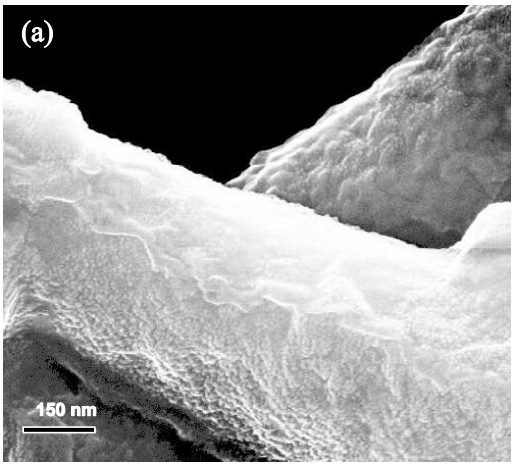

Fig. 10.1.9. SEM image of the inner structure of the ion beam etched column (a) and top of a column of the same type as in Fig. 10.1.7a (b).

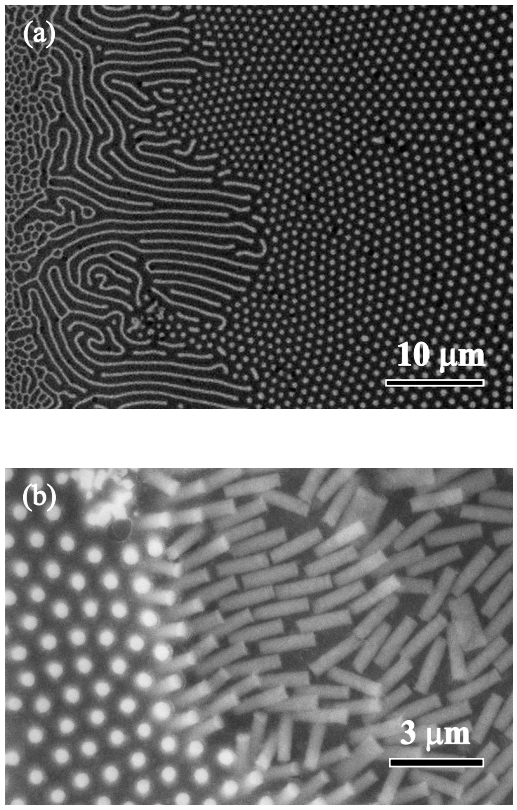

Fig. 10.1.10. SEM image (top view) of a periodic array of columns composed from Co nanoparticles (a) formed in perpendicular magnetic field $B = 0.2$ T; a labyrinthine structure is visible on the left side; (b) detailed image of a disturbed region.

Molecular dynamics studies [ENO03] show that when an external field is applied, a quick formation of chains aligned with the field direction appears and afterwards a coagulation of chains into columns takes place. In ferrofluids, this process is reversible: when the field is switched off, the particles re-arrange and the columns disappear. The column diameter depends on the magnetostatic interaction. At a certain length, the lateral growth of the column is not energetically favourable because the demagnetization factor increases. A similar mechanism as for ferrofluids is supposed to be responsible for our column formation. However, the ordering of particles is time-limited due to the evaporation of the solvent. Under favourable conditions, the particles have enough time to arrange into column (Fig. 10.1.10).

When inspecting the entire array of nanoparticles after drying a drop of concentrated colloid, we can see that the morphology of the layer changes from the center of the droplet towards the border. In [PUN01, LEO03, CHU03], $2D$ hexagonal arrays of Co nanoparticles have been observed in the central part of the droplet after toluene evaporation. Instead, a less uniform film has been observed near to the border of the droplet. Fig. 10.1.10 shows a similar morphology at

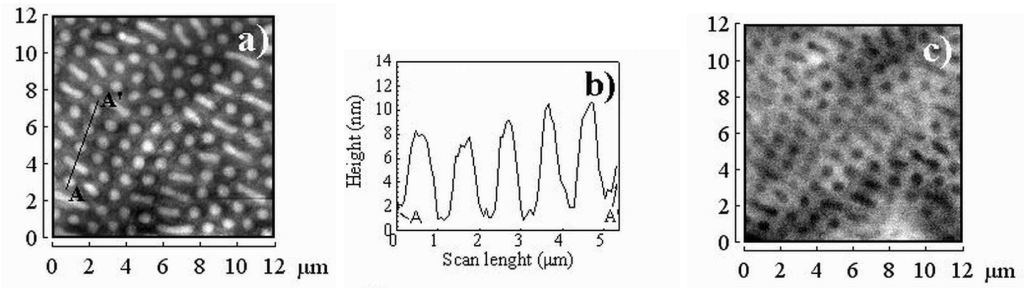

Fig. 10.1.11. AFM/MFM images of the Co NP column array: (a) 20 μm $\times$ 8 μm non-contact AFM topography, z scale $=$ 40 nm; (b) surface scan plot along the line AA$'$ from Fig. 10.1.11a; (c) corresponding MFM micrograph, scan lift 100 nm.

the droplet border. Hexagonally ordered arrays of columns perpendicular to the substrate (on the right of the image) can be seen together with a labyrinthine structure (on the left of the image). The average diameter of the columns is 600 ± 30 nm with average center-to-center distance of 940 ± 60 nm. Occasionally, collapsed columns have also been observed close to the droplet border (Fig. 10.1.10). The average length of the columns estimated from the ensemble of the collapsed columns is 1.98 ± 0.25 μm. Both columns (Fig. 10.1.9) and labyrinthine structure (not shown) are composed from close packed Co nanoparticles. Moreover, the aggregates of surfactant and disordered clusters of NPs are observed in the region between the columns.

Arrays of columns with the hexagonal symmetry on an area of several μm^2 were also observed by AFM. The period of the array and the average diameter of the columns were obtained by Fast Fourier Transform (FFT) and particle analysis of AFM images. In agreement with the SEM results, an average diameter of 560 ± 90 nm and a center-to-center separation of 870 ± 40 nm have been obtained. In addition to the columns, stripes with the width and height corresponding to the column dimensions were also found in the AFM images (Fig. 10.1.11a), probably due to the column coalescence. In Fig. 10.1.11b, the surface profile along the line AA$'$ in Fig. 10.1.11a is shown. The average height of both columns and stripes is about 10 nm, one order of magnitude lower than the value estimated from the length of the collapsed columns. In agreement with SEM observations, this result confirms definitely that the space between the columns is not empty. Fig. 10.1.11c shows the MFM image recorded simultaneously with the topography with a tip lift scan height of 100 nm. The black MFM contrast can be identified with either all domains oriented up or with all domains oriented down perpendicularly to the substrate. The sharp contrast of the MFM image and its clear correlation to the topological AFM image shows that the Co NP columns comprise aligned magnetic moments. This is in agreement with our magnetization measurements of the colloidal solution showing that the field $B = 0.2$ T corresponds to the onset of saturation [CHI06].

Labyrinthine structure and ordered arrays of columns of nanoparticles have been reported in ferrofluids. In a ferrofluid confined in a glass cell and subjected to a magnetic field, the particles form chains with the diameter of a single particle which conjugate together into columns. Columns can form disordered, ordered and/or labyrinthine patterns [CHI07a]. This field-induced phase transition has been experimentally well documented by Hong [HON97, HON99]. Depend-

ing on the field strength, the disordered column phase transforms into the hexagonal arrangement. The process is reversible, as it was already mentioned, and the columns decompose when the field is switched off even after application of a saturation field. The long-range attraction between the chains resulting in columns formation is not well understood yet [YTR00]. It is assumed that the column diameter depends on the dipolar interaction.

The formation of the $3D$ structures strongly depends on the nanoparticle preparation route and in particular, on the surfactant. The $3D$ columns are formed when oleic acid is used as surfactant while $3D$ artificial crystals of NPs (and self-assembled $2D$ arrays) are obtained when Co nanoparticles capped with a mixture of trioctylphosphine oxide (TOPO) and oleic acid are assembled [PUN01]. We observed a similar behaviour also for Fe-O and Co-Fe-O nanoparticles as we show below.

The coexistence of columns and labyrinthine patterns in close neighbourhood (Fig. 10.1.10) and the fact that they appear at the border of the droplet point to the role of the drying process in the pattern formation. The SEM images show that the concentration of Co NPs increases from the central region outward to the border area where the columns and labyrinthine structures form. The appearance of the concentration gradient of nanoparticles from the center to the border can be understood within a model of a drying drop of colloid [DEE97]. In a droplet with a circumference contact line pinned to the substrate, there is a flow carrying material from the center to the border during the evaporation of the solvent. Considering this, one can assume a flow of Co nanoparticles in the direction outward from the central part of the droplet. The coexistence of the ordered and labyrinthine pattern for our samples could be thus qualitatively understood within the approach given by Lacoste et al. [LAC01]. The authors proposed a model of pattern formation depending on the concentration of particles and the degree of alignment of the magnetic moments of particles. They show that under the applied field, the hexagonal phase can coexist with the labyrinthine structure if a varying density of particles in ferrofluid is assumed.

Using a similar method of preparation and replacing the oleic amine with TOPO, a new type of Co nanoparticles was prepared [HIL]. These particles assembled in a different way. In Fig. 10.2.6a, b, we will show a monolayer and a $3D$ artificial crystal formed by self-assembly. In this case, the application of the magnetic field did not affect the self-assembled array. The average radius of the particles is again 5.7 ± 0.05 nm.

10.2 Analysis of ordering, time-resolved GISAXS studies

Ordering and formation of ordered arrays were studied by GISAXS. This method is not as common as XRD. Therefore, in the next part we will give a short introduction to this useful technique.

GISAXS was introduced by Levine et al.[LEV89] as a method of studying discontinuous thin films. GISAXS is an innovation of the small-angle X-ray scattering (SAXS). It is surface sensitive, non-destructive and provides statistical information over the irradiated area. The method has been applied to study structures of metallic or semiconductor islands, dots or clusters [NAU98, STA99, NAU00, STA00] as well as for real-time monitoring of growing nanoparticles [REN03]. The geometry of the GISAXS experiment is shown in Fig. 10.2.1. The incident beam with the wave vector $\vec{k}_i$ is scattered by the wave vector transfer $\vec{q}$ with the q_y, q_z. components in the y - z plane. The scattered radiation is analyzed as a two-dimensional function of q_y, q_z.

The description of the X-ray scattering from the free-standing particles is based on the

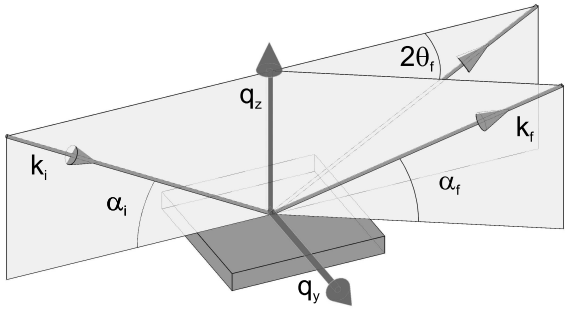

Fig. 10.2.1. Geometry of the GISAXS experiment.

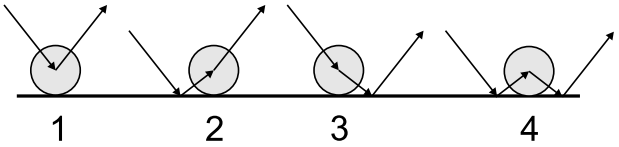

Fig. 10.2.2. To the GISAXS explanation - four scattering processes.

distorted-wave Born approximation (DWBA). The scattering potential V of the system is divided into two parts $V = V_A + V_B$ where V_A represents the scattering potential of the undisturbed system (a semi-infinite substrate) and V_B describes the scattering from the free-standing Co particles [STA00]. The differential cross-section of the scattering process in the DWBA approach is given as

$$\frac{d\sigma}{d\Omega} = \frac{1}{16\pi^2} \left\langle \left| \left\langle E_f^{(A)} \left| V_A \right| E_i^{(0)} \right\rangle + \left\langle E_f^{(A)} \left| V_B \right| E_i^{(A)} \right\rangle \right|^2 \right\rangle . \tag{10.2.1}$$

The averaging $\langle\ \rangle$ is performed over all random configurations of the particles on the surface. $\left|E_i^{(A)}\right\rangle$ and $\left|E_f^{A}\right\rangle$ are the known solutions of the wave equation $\left(\Delta + \vec{K}^2\right) E^{(A)} = V_A E^{(A)}$. The solution of Eq. (10.2.1) provides the Fresnel reflection and transmission coefficients.

The scattering potential of the disturbed system for the small angles of incidence has the form $V_B = 2\vec{K}^2 \delta(r)$ where $\vec{K}$ is the wave vector in vacuum, $\delta(\rho) = 1 - n(r)$ and $n(r)$ is the refractive index. The differential scattering cross-section of the diffuse component reads

$$\left(\frac{d\sigma}{d\Omega}\right)_{diff} = \frac{1}{16\pi^2} \mathrm{Cov}\left(\nu_{\mathrm{B}}, \nu_{\mathrm{B}}\right) \quad , \tag{10.2.2}$$

where $\nu_{\mathrm{B}} = \left\langle E_f^{(A)} \left| V^B \right| E_i^{(A)} \right\rangle$. For the nanoparticles deposited onto the substrate surface, four different scattering events (Fig. 10.2.2) have to be taken into account when X-rays interact with the sample.

The quantity ν_B can be written as

$$\nu_{\mathrm{B}} = \int d^3\vec{r}\, 2\vec{K}\delta\left(\vec{r}\right) E_i^{(A)} E_f^{(A)*} = 2\vec{K}^2 \sum_{j=1}^{4} A_j F\left(\vec{q}_j\right). \tag{10.2.3}$$

The amplitude A_j acquires the values corresponding to the processes $A_j = \{1, r_i, r_f, r_i r_f\}$ where r_i and r_f and the Fresnel reflection coefficients for the angle of incidence α_i and α_f (Fig. 10.2.1). The $F\left(\vec{q}_j\right) = \delta \int d^3\vec{r}\,\Omega\left(\vec{r}\right) \exp\left(-\mathrm{i}\vec{q}_j\vec{r}\right)$ is the Fourier transform of the shape function $\Omega(\vec{r})$ which is 1 inside the particle and 0 elsewhere. The $\vec{q}_j$ is the wave vector transfer of the j^{th} scattering process. The diffuse component of the differential scattering cross section has the form

$$\left(\frac{d\sigma}{d\Omega}\right)_{diff} = \frac{\vec{K}^4}{4\pi^2} \left| \sum_{j=1}^{4} A_j\ F\left(\vec{q}_j\right) \right|^2 \sum_{n,m}^{n} \left\langle \mathrm{e}^{-\mathrm{i}\vec{q}\left(\vec{r}_n - \vec{r}_m\right)} \right\rangle. \tag{10.2.4}$$

The double sum $\sum\limits_{n,m}$ expresses the correlation function which characterizes the position of the particles $\vec{r}_n$, $\vec{r}_m$ on the surface. The correlation function

$$\sum_{n,m} \exp\left\langle -\mathrm{i}\vec{q}_{\parallel}\left(\vec{r}_n - \vec{r}_m\right)\right\rangle \tag{10.2.5}$$

can be extracted from the analysis of the GISAXS spectra. If the particles are randomly scattered over the surface, the correlation function (10.2.5) equals 1 and the scattering intensity is a function of the shape and size of the particles. If particles form perfectly ordered structures the correlation function has sharp peaks. The position of the peaks corresponds to the distance between adjacent particles.

In real structures, particles deflect from the ideal positions and several models have been proposed to describe the imperfection of the ordering [LAZ02]. For particle arrays, a hexagonal paracrystal model is often used where the particle positions are misaligned in a probabilistic way with increasing distance from a reference point. As we will show later, random packing of hard sphere was also observed [CHU03].

Most part of our assembling experiments including time-resolved *in-situ* studies were performed with Fe_3O_4 and $CoFe_2O_4$ nanoparticles prepared at the Polymer Institute of SAS by the method described above. The nanoparticles show a well-developed crystalline structure and they are superparamagnetic at room temperature. The blocking temperature is $T_B = 22$ K for Fe_3O_4 and 204 K for $CoFe_2O_4$. NPs are monodomain due to their small size and behave as single magnetic dipoles because the dipole-dipole interaction of magnetic iron oxide nanoparticles is weak [LAL03]. Particles are nearly spherical with the radius of 3.2 ± 0.3 nm for Fe_3O_4 and 3.8 ± 0.27 nm for $CoFe_2O_4$ and form hexagonally ordered arrays (Fig. 10.2.3.).

GISAXS studies of ordered arrays of Co nanoparticles

For Co nanoparticles, the GISAXS measurements [CHU03, CHU05a, CHU06] were carried out at ID10B beamline at ESRF (Grenoble) using a wavelength of 0.155 nm. GISAXS allows to

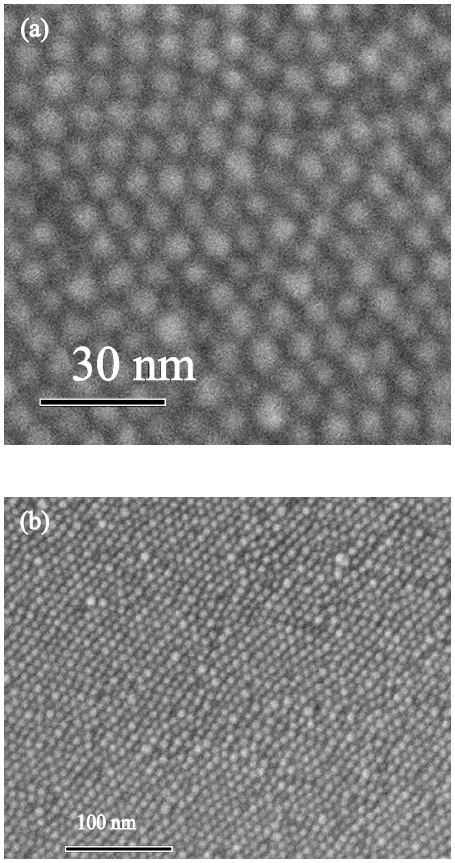

Fig. 10.2.3. SEM image of arrays of (a) Fe_3O_4 and (b) $CoFe_2O_4$ nanoparticles prepared by drying a droplet deposited onto Si/Si_3N_4 substrate.

study the ordering over large areas. For $3D$ arrays, only GISAXS can provide a reliable analysis of the ordering inside the columns (rods). The GISAXS patterns of the $2D$ nanoparticle array (Fig. 10.1.7) and columns (Fig. 10.1.10) are shown in Figs. 10.2.4 and 10.2.5, respectively.

For $2D$ arrays (monolayers), the local ordering with hexagonal symmetry observed by SEM was confirmed by GISAXS (Fig. 10.2.6). The monolayers consist of well-ordered regions with different orientations. Different type of ordering was determined by GISAXS for the array of columns. The ordering of particles inside columns is described by a close packed hard sphere model pointing at a rather random arrangement of the nanoparticles. The parameters of the arrays obtained by the simulation of the GISAXS spectra are summarized in Table 10.2.1.

The fact that for $3D$ arrays the ordering is better described by the hard sphere model indicates an increased randomness of the particle positions inside the columns. For $2D$ arrays, there is no substantial difference of ordering in the perpendicular magnetic field and in the absence of the field. The lower σ_a for the sample prepared in the magnetic field implies an improved ordering

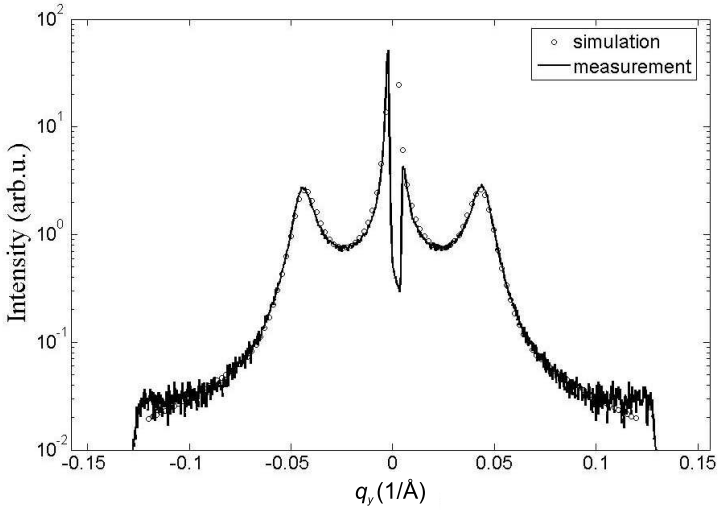

Fig. 10.2.4. Measured and simulated GISAXS scan along $q_z = 0.01$ Å^{-1} of the reciprocal space map of a $2D$ array of Co nanoparticles; the incidence angle $\alpha_i = 0.05^\circ$, the wavelength $\lambda = 0.155$ nm.

of the particles (Fig. 10.1.6b).

Time resolved GISAXS studies

As mentioned above, a large variety of possible resulting patterns of the self-assembled nanoparticles is a serious limitation for targeted technological applications of self-assembling. A deeper understanding of the self-assembling process, especially its initial stages, is essential for a better control of the nanoparticle ordering. This issue is closely related to answering the question where the ordering takes place. In contradiction with a common concept that the self-assembling process occurs at the substrate/colloid interface, formation of monolayer islands of dodecanthiol-

Tab. 10.2.1. Sample parameters obtained from the simulations of $2D$ and $3D$* arrays. N_{rel} is the relative concentration (volume fraction) of the colloid, R is particle radius, a is the lattice parameter of $2D$ arrays, a* is the diameter of a hard sphere for $3D$* arrays, σ_a is the standard deviation of the interparticle distance for $2D$ arrays and η is the packing fraction for $3D$* arrays.

magnetic field [T]	N_{rel}	R [nm]	a [nm]	a*	σ_a [nm]	η*
0	0.0625	5.7	16.8		3.3	
0.75	0.0625	5.7	16.8		2.9	
0.9*	0.125*	5.7*		14.7*		0.43*

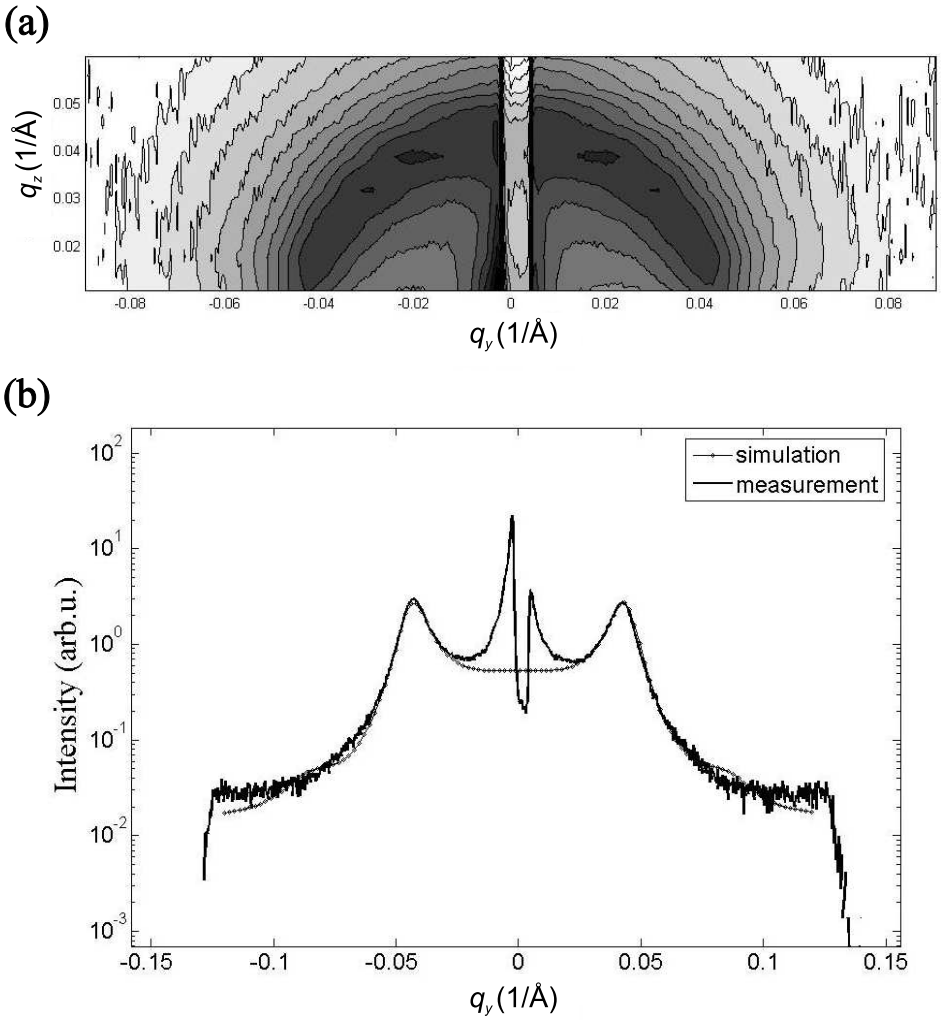

Fig. 10.2.5. (a) Reciprocal space map of columns composed from Co nanoparticles deposited in perpendicular magnetic field $B = 0.9$ T, the incidence angle $\alpha_i = 0.05^\circ$, the wavelength $\lambda = 0.155$ nm; (b) measured and simulated scan along $q_z = 0.01$ Å^{-1}.

passivated Au nanoparticles on the top surface of the drop (liquid/air interface) was confirmed by *in-situ* X-ay scattering experiments [NAR04]. Using the *in-situ* time-resolved GISAXS technique, we tried to analyze the region where the ordering starts. For these studies, we used our Fe-O nanoparticles [SIF07b].

A representative SEM image of the self-assembled monolayer is shown in Fig. 10.2.7. The inset shows the Fourier transform of the entire image. It can be seen that the nanoparticles are ordered in a perfect hexagonal close-packed (hcp) array within the domains of an apparent

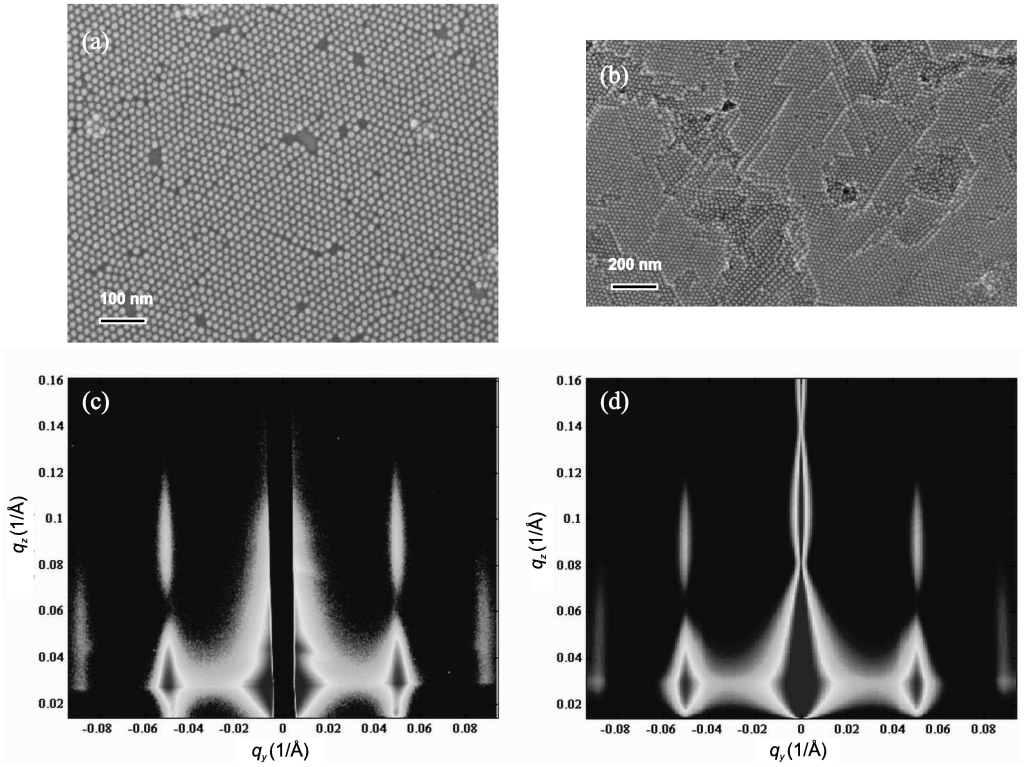

Fig. 10.2.6. SEM images of a monolayer (a) and artificial crystal (b). Measured (c) and simulated (d) GISAXS patterns of the self-assembled monolayer of Co nanoparticles prepared by mixture of trioctylphosphine oxide (TOPO) and oleic acid. The angle of incidence $\alpha_i = 0.186^\circ$, the wavelength $\lambda = 0.155$ nm. For the simulation, the particle radius of 5.4 ± 0.3 nm and hexagonal paracrystal model were used.

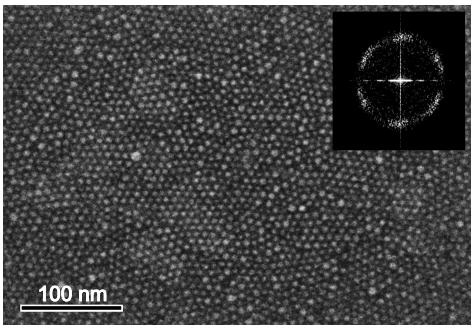

Fig. 10.2.7. Scanning electron microscope image of an Fe-O nanoparticle monolayer on Si substrate. Fourier transform of the image shown in the inset reveals hexagonal symmetry of the self-assemblying.

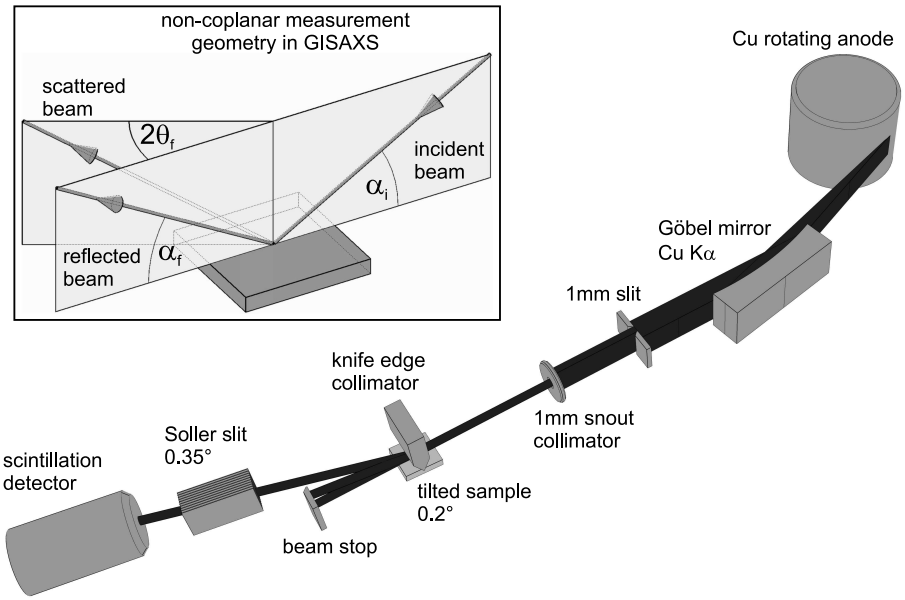

Fig. 10.2.8. Geometry of the GISAXS measurement using the Bruker D8 Discover SSS diffractometer.

size less than 100 nm. A partial smearing-out of the reciprocal lattice points is a consequence of mutually misaligned domains. The average particle size obtained from Fig. 10.2.7 is 6.4 ± 0.6 nm which is slightly larger than that determined by the transmission electron microscopy. This is mainly due to the fact the scanning electron microscope is more sensitive to the organic surfactant shell surrounding the Fe-O particle core. The average interparticle distance (center-to-center) was found to be 7.7 ± 0.6 nm.

The time resolved study was performed on the GISAXS beamline BW4 at the Hamburger Synchrotronstrahlungslabor [ROTH06]. The size of the focused beam at the substrate position, as determined from 1/e of the maximum intensity, was 65×3 μm^2 size (horizontal $\times$ vertical). The X-ray wavelength was 0.138 nm. We employed two measurement modes. In a substrate mode, the substrate was aligned in order to halve the primary beam intensity and subsequently tilted by 0.18° (standard GISAXS alignment with the angle of incidence of 0.18°). In a drop mode, the substrate was vertically translated downwards by 100 μm out of the primary beam after having been aligned and subsequently tilted by 0.1° in order to eliminate the X-ray scattering from the substrate. In this mode, solely the X-ray scattering from the drop (including its surface as it was crossing the primary beam during evaporation) was measured. The scattered X-ray radiation was detected by a two-dimensional X-ray CCD camera located at the distance of 1971-mm from the substrate. Each CCD pattern was acquired for 2.6-s if not stated otherwise.

The second part of our measurements was performed on a horizontal Xray diffractometer (Bruker D8 Discover Super Speed Solution) equipped with an 18-kW Cu rotating anode TXS generator (wavelength 0.154-nm). A parabolic Göbel mirror provided the primary beam of 0.03° FWHM horizontal divergence and intensity of 10^9 photons/s (Fig. 10.2.8). The horizontal and

vertical beam widths are formed to 1 mm by a pinhole collimator. A knife-edge collimator was moved downwards to the substrate surface to suppress the superfluous primary beam but not to influence the intensity of the useful GISAXS signal. The incident angle of 0.2° was adjusted by tilting the sample stage. A beamstop beyond the sample stage absorbed the passing primary beam. A Soller slit of 0.35° horizontal angular acceptance and a point scintillation detector set at a fixed angle were used to collect the GISAXS signal with a 100 ms temporal resolution. Using the laboratory source, we were able to measure the GISAXS signal few seconds after the deposition of the drop and to follow the early stage of the assembling process.

Monolayers of the Fe-O nanoparticles were prepared by the solvent evaporation from the drop of the colloidal solution applied on the substrate at room temperature. According to Ref. [POU05], three distinct stages of drying the drop are as follows: After the application on the surface, the radius of the drop grows and wets the substrate. After reaching the maximum diameter, the contact line is pinned for a certain time - the solvent evaporation and wetting of substrate are in balance. In the second stage, the evaporation moves the contact line in the stick-slip manner. The first one-two minutes can be characterized by a linear mass decrease of ≈45 μg/s. In the third stage, the evaporation-driven surface tension instability [YIA06] results in a fast drop migration over the substrate. The drop is completely dried within ≈ 5 min.

Time-resolved GISAXS studies with synchrotron radiation

A typical GISAXS pattern of the dried nanoparticle array on silicon substrate taken in the substrate mode after the solvent evaporation is shown in Fig. 10.2.9. The q_y and q_z components of the scattering vector are parallel and perpendicular to the substrate surface, respectively. The specularly reflected beam and diffuse scattering along q_z for $q_y = 0$ were blocked by a beamstop to avoid the CCD camera saturation. The empty areas in the left and right upper corners are due to the detection absence. The observed GISAXS pattern is formed by an interference of the diffusely scattered X-rays from each irradiated nanoparticle in the array. The side maxima at $q_y \approx \pm 0.82$ nm^{-1} indicate the interparticle spacing of $2\pi/q_y \approx 7.7$ nm, in agreement with the scanning electron microscopy.

The simulation of the measured GISAXS pattern was performed using the DWBA and hexagonal paracrystal model as mentioned above. The simulation and a selected line cut at the critical exit angle ($q_z = 0.31$ nm^{-1}) are shown in Figs. 10.2.9b and c, respectively. It can be seen that all measured features are well reproduced. From fitting the line cut, the following parameters were obtained: the average particle diameter of 6.1 ± 0.6 nm, the average interparticle distance of 7.5 ± 1 nm, and the lateral correlation length of the particle distribution of 87 nm. All these values are within the confidence intervals of the corresponding values determined by the X-ray diffraction and transmission and scanning electron microscopies.

In-situ temporal evolution of the GISAXS pattern was studied both in the substrate and drop modes. Three typical stages of the temporal evolution in the substrate mode are shown in Fig. 10.2.10a,b,c. The first stage is characterized by the X-ray scattering from the volume of the colloidal drop, the drop being larger than the beam size (Fig. 10.2.10a). Due to a high X-ray absorption coefficient of the colloidal solution, only a small part of the incoming radiation penetrates the drop and reaches the detector. The detected signal is featureless and the intensity decreases monotonously along q_y and q_z axes. No ordering of the nanoparticles in the solution is observed. In an intermediate stage of the solvent evaporation, the drop surface is crossing

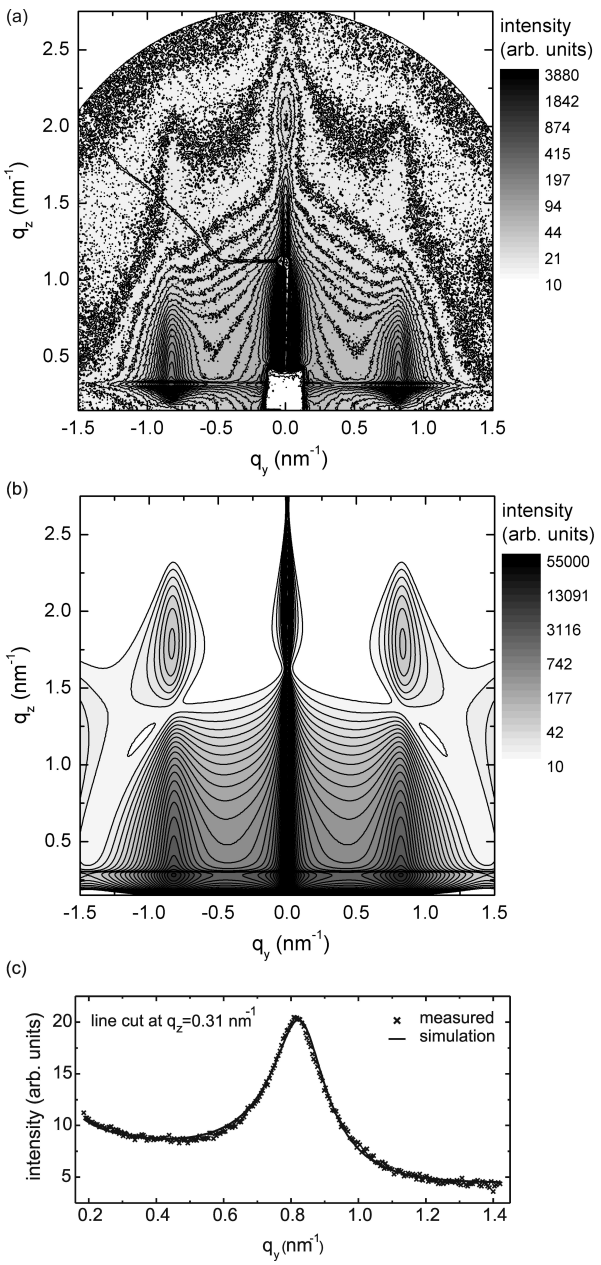

Fig. 10.2.9. Measured (a) and simulated (b) GISAXS patterns of the self-assembled nanoparticle array and a fit of a line cut of the measured GISAXS pattern along q_y at $q_z = 0.31$ nm^{-1} (c) (dots - measured points, line - fit). The central part along q_z is shadowed by a beamstop.

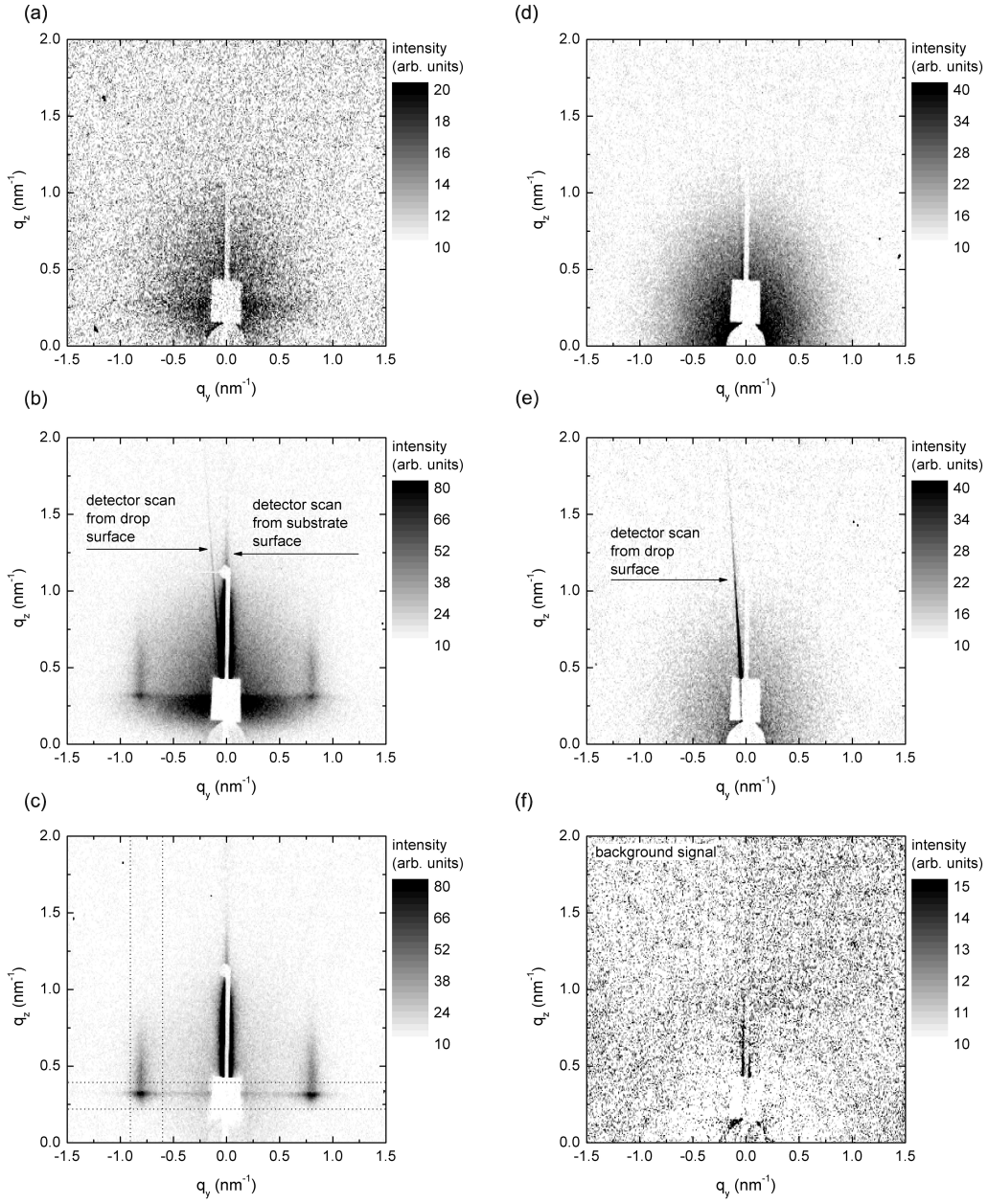

Fig. 10.2.10. GISAXS patterns taken in the substrate (a-c) and drop (d-f) modes measured at different phases of the drop evaporation.

the incident X-ray beam and the surface scattering from the already dried nanoparticle array on the substrate as well as the volume and surface scattering from the still evaporating drop are observed. Maxima at $q_y \approx \pm 0.8$ nm^{-1} appearing in this stage indicate a nanoparticle ordering on the substrate and/or the drop surface (Fig. 10.2.10b). The GISAXS maxima are well resolved in Fig. 10.2.10c which corresponds to an ordered array of nanoparticles after drying the drop. Moreover, we can see two stripes in the GISAXS pattern (marked by arrows in Fig. 10.2.10b) which can be understood as projections of the detector scans (in the language of the coplanar measurements with a point detector) in the q_x-q_z plane onto the q_y-q_z plane of the CCD camera (q_x is more than one order of magnitude smaller than q_z). The stripe parallel to q_z comes from the scattering from the substrate surface and can be observed also in Fig. 10.2.10c for the dried array of nanoparticles. The other stripe comes from the scattering from the drop surface. Though this surface is curved, the stripe is not fanned out because of the local surface sampling by the microfocus beam. The nonzero angle between the two stripes depends on mutual orientation of the respective surface normals. The shape of the drop surface is a complex function of time and may vary from drop to drop as a result of the statistical nature of the evaporation dynamics.

The GISAXS results obtained in the drop mode are shown in Fig. 10.2.10d,e,f. The first stage is dominated by the volume scattering from the colloidal drop (Fig. 10.2.10d). The signal decreases monotonously with increasing scattering vector in the reciprocal space. Similarly as in Fig. 10.2.10b, an abrupt change of the GISAXS pattern is observed when the drop surface is crossing the incident X-ray beam (Fig. 10.2.10e). Simultaneously, one sharp stripe (indicated by an arrow), which corresponds to the scattering from the drop surface as explained above, appears. The GISAXS signal comes from the drop volume and drop surface but no specific features indicating a nanoparticle ordering are observed. After the drop surface passed the incident beam, only a background signal is detected (Fig. 10.2.10f).

In order to visualize the temporal evolution of the GISAXS, we used $t - q_y$ intensity maps. The intensity corresponding to a particular (t, q_y) point is obtained by an integration of the measured intensity over the q_z interval of $\langle 0.22$ nm^{-1}, 0.39 m$^{-1}\rangle$ (marked by the horizontal dotted lines in Fig. 10.2.10c) at a constant q_y in the GISAXS pattern taken at the time instant t after starting the detection at $t = 0$. This zero time is shifted by ≈ 30 s with respect to the first contact of the drop with the substrate surface so that the used temporal scale is relative. Being not interested in the duration of the evaporation process itself, the absolute time is of little importance. In order to quantify the temporal evolution, we integrated further the scattered intensity also over the q_y interval of $\langle 0.6$ nm^{-1}, 0.9 nm$^{-1}\rangle$ to obtain a partial integrated scattering (PIS) as a function of time. The PIS plot shows the temporal evolution of the GISAXS intensity integrated over the area marked by the vertical and horizontal dotted lines in Fig. 10.2.10c where the side maximum appears.

Figure 10.2.11a shows the $t - q_y$ map measured in the substrate mode. The GISAXS signal comes from the already dried nanoparticles on the substrate, the drop volume and drop surface. Distinct lines at $q_y \approx \pm 0.8$ nm^{-1} are observable from the early stages, indicating the formation of an ordered nanoparticle array from the very beginning of the detection. The GISAXS signal along the q_y direction increases gradually with time and culminates at $t \approx 120$ s when the drop surface crosses and scatters strongly the X-ray beam in the form of a detector scan as explained above (compare with Fig. 10.2.10b). The corresponding PIS plot is shown in Fig. 10.2.11b. At the beginning, the scattered signal grows linearly while an exponential-like increase is observed when the drop surface crosses the primary X-ray beam before escaping from it completely. After

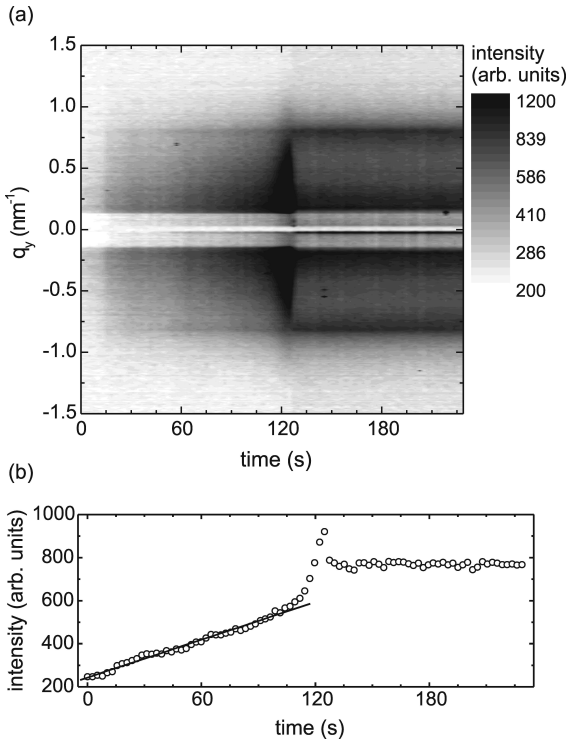

Fig. 10.2.11. A $t - q_y$ map of a drying colloidal drop forming a monolayer of ordered nanoparticles measured in the substrate mode (a) and the corresponding partial integrated scattering (PIS) plot (b).

this transient, the scattered intensity decreases to a stationary value produced solely by the dried self-assembled nanoparticle array on the substrate.

The overall initial increase of the GISAXS signal in the $t - q_y$ map is a result of the steadily increasing nanoparticle concentration in the drop volume as the solvent evaporates. For the PIS plot related to the region of the side maximum in the reciprocal space, the growing area of ordered nanoparticles on the substrate surface may play a role as well. In order to estimate the contribution of the scattering from the drop volume to the total scattered intensity during the drying process, we repeated the temporal analysis with the colloidal solution diluted by a factor of 10. The $t - q_y$ map and PIS plot are shown in Fig. 10.2.12a and b, respectively. The GISAXS signal in the $t - q_y$ map increases with time up to a maximum at $t \approx 120$ s before the drop escapes from the X-ray beam and a steady-state regime is established. Ordering lines at $q_y \approx \pm 0.8$ nm^{-1} can be resolved in the steady-state regime but their traces are visible already at earlier stages. A sub-monolayer coverage of the substrate consisting of isolated islands of the ordered nanoparticle arrays was observed by the scanning electron microscopy after drying the drop. The islands produce a smaller PIS signal than the monolayer. The PIS temporal plot exhibits again a linear increase up to $t \approx 100$ s followed by a transient and steady-state regions, the linear signal being higher than the steady-state one coming from the ordered nanoparticle

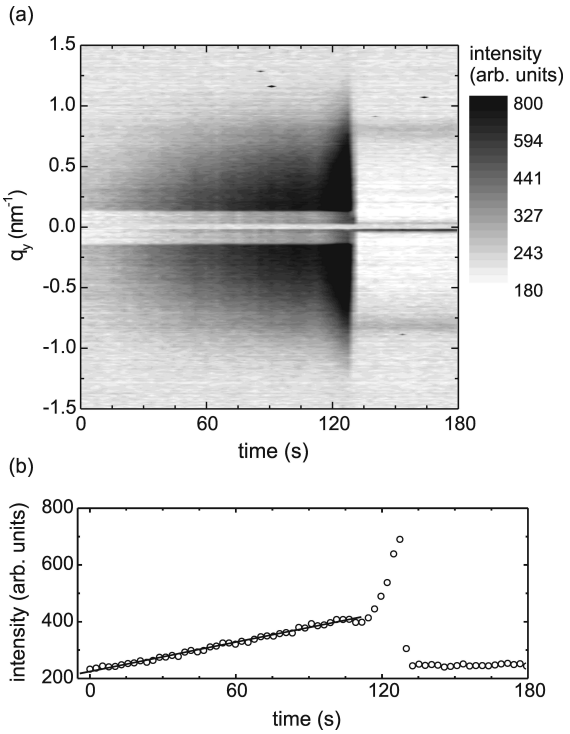

Fig. 10.2.12. A $t - q_y$ map of a drying diluted colloidal drop forming ordered sub-monolayer arrays of nanoparticles measured in the substrate mode (a) and the corresponding partial integrated scattering (PIS) plot (b).

array on the substrate. This fact indicates clearly that also in the PIS plot, the main contribution to the scattered intensity before the drop escapes from the X-ray beam comes from the nanoparticles inside the drop.

In view of these findings, the initial linear increase of the GISAXS signal can be attributed to the linear increase of the nanoparticle concentration as the drop is losing its mass during the solvent evaporation. The amount of the deposited nanoparticles is still negligible when compared to the number of the nanoparticles inside the drop. The growing nanoparticle concentration leads to the observed linear growth of the volume and surface scattering from the drop. Later, the evaporating drop surface crosses the X-ray beam and the drop position becomes unstable. Finally, the drop moves completely out of the X-ray beam and an abrupt intensity decrease resulting in a stationary time-independent GISAXS signal is observed in the PIS plot. This decrease is not connected with a loss of the nanoparticle order but with the absence of the drop scattering.

It still remains to determine the region of the nanoparticle self-assembling. Measurements in the substrate mode cannot distinguish between the signal scattered from the ordered nanoparticle assembly on the substrate surface and on the drop surface. Therefore, we utilized the drop mode which probes the drop exclusively. In order to minimize the impact of the read-out time on

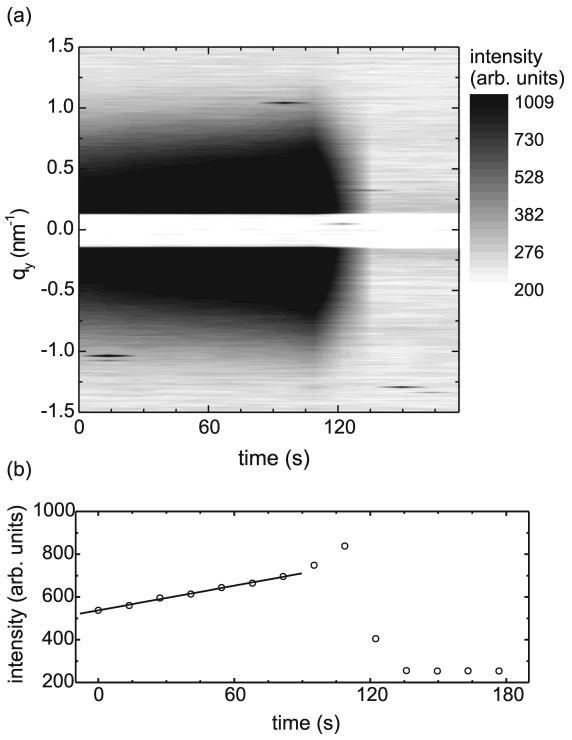

Fig. 10.2.13. A $t - q_y$ map of a drying colloidal drop measured in the drop mode (a) and the corresponding partial integrated scattering (PIS) plot (b).

possible short transients, we enhanced the integration time of a single GISAXS pattern from 2.6 s to 13.6 s. The measured $t - q_y$ map and PIS plot are shown in Fig. 10.2.13a and b, respectively. Differently to the substrate mode, the $t - q_y$ map shows no ordering lines and the GISAXS signal along q_y decays monotonously with time up to $t \approx 120$ s. The linear increase of the PIS plot is dominated by the volume scattering of the linearly densifying drop. The exponential-like final increase may be attributed to a combined effect of the volume and surface scattering from the colloidal drop (compare with Fig. 10.2.10e). Finally, the drop escapes from the X-ray beam and the measured scattering signal goes to a background value. No evidence of the existence of ordered nanoparticle arrays in the drop volume or on the drop surface within the employed statistics has an important implication. According to our calculations, $\approx 63\%$ of the incident X-ray intensity probed the drop volume located between 82 μm and 118 μm above the substrate surface. Therefore, the self-assembly process takes place no more than ≈ 80 μm above the substrate surface in the vicinity of the drop contact line. The contact line moves steadily in the stick-slip manner and the nanoparticles, which are ordering in its neighborhood, adhere to the substrate surface as the solvent evaporates.

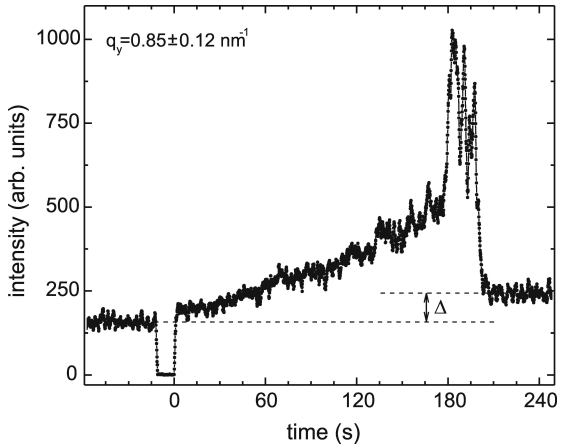

Fig. 10.2.14. Partial integrated scattering (PIS) plot of a drying colloidal drop in the substrate mode measured with X-ray rotating anode source.

Time-resolved GISAXS studies with X-ray rotating anode source

A poor temporal resolution poses a risk of data undersampling when monitoring fast dynamical processes. In order to avoid deceptive results, we measured the GISAXS at a fixed scattering angle using a rotating anode X-ray source. The GISAXS signal was sampled at 10 Hz, i.e. 26 times faster than it was possible with the X ray CCD camera. In this way, we were able to study the early stages of the self-assembling process. A horizontal Soller slit was positioned parallel to the substrate normal so that the measured GISAXS intensity was integrated along the q_z direction and convoluted with the slit acceptance along the q_y direction. A PIS plot integrated over the q_y interval of $\langle 0.73\ \mathrm{nm}^{-1}, 0.97\ \mathrm{nm}^{-1}\rangle$ is shown in Fig. 10.2.14. The zero time $t = 0$ refers to the start of the detection after the drop was applied on the substrate. For negative time, before the drop was applied, we observe diffuse scattering from the clean substrate. The application of the drop is displayed by a missing part of the signal. The drop evaporation is accompanied by a linear increase of the scattered intensity up to $t \approx 120$ s, as observed also by the time-resolved synchrotron measurements. This evaporation phase is dominated by an increasing volume scattering from the densifying colloidal drop, a small contribution of the already dried ordered nanoparticle array on the substrate being also possible. After this linear increase, several fast fluctuating transients are observed. These transients are a consequence of the evaporation-driven surface tension instability and vary from drop to drop. The drying drop with a fast modifying surface moves into and out of the X-ray beam and the contributions of the volume and surface scattering from the drop produce "revivals" of the GISAXS signal accordingly. These transients were undersampled in the CCD synchrotron measurements, resulting in the smooth exponential-like increase of the PIS plot. The difference between the initial and final PIS levels (denoted by the symbol Δ in Fig. 10.2.14) shows a contribution of the dried self-assembled nanoparticles to the GISAXS signal.

In summary, using time resolved GISAXS it was possible to separate the contributions of

the volume and surface X-ray scattering from the drop to the total GISAXS signal during the self-assembling. The colloidal nanoparticle solution used shows the absence of self-assembled clusters in the drop volume or self-assembled domains on the drop surface for the distances from the substrate surface larger than 80 μm. Relying on these results, we conclude that the self-assembling takes place in the vicinity of the three-phase (liquid-solid-air) drop contact line as the solvent evaporates, i.e. not inside or on the drop.

11 Summary and perspectives

A common denominator of the structures discussed in this work is their very small and all the time decreasing size. Consequently, the ratio between the number of surface and interface atoms and the number of atoms inside the bulk rapidly increases. Therefore, interfaces influence the properties of multilayers in a decisive way.

The interfaces play a key role in X-EUV and magnetic multilayers, used nowadays mostly in Bragg mirrors and spintronics devices, respectively. High-performance multilayer structures for X-EUV optics are often composed of several hundreds of layers of a nanometer or sub-nanometer thickness which must be controlled with the precision better than 0.1 nm. This requires also development of advanced *in-situ* methods to monitor and control the deposition process with picometer accuracy. The progress in X-EUV multilayers was first of all stimulated by the development of X-EUV lithography with resolution below 30 nm as a next generation tool for micro- and nanoelectronic device production. Simultaneously, mirrors for new imaging techniques, like water window microscopy, represent inevitable tools for new research in biology and material science. Though not discussed in this tutorial, significant advance in deposition technology was achieved in terms of the control of lateral grading of layer thickness along the substrate which is unavoidable for imaging multilayer mirrors deposited on figured substrates. Here, the control of layer thickness distribution along the substrate with an accuracy below 0.1 nm is necessary, too. One can assume that novel structures and novel devices not only for X-EUV optics will be prepared with further development of the lateral thickness control during the deposition process in a single technological run as a specific application of the bottom-up approach.

Ultrathin nanometer-size layers dictate the progress also in a new branch of electronics, viz. spintronics, with direct output for storage and retrieval of information. Here, the thickness of deposited layers must be also controlled with the precision better than 0.1 nm which is in agreement with predicted transition from nano- to picometer-size technology.

New properties and new phenomena in multilayer and spin valve physics are of primary interest for us. As it was shown, X-EUV multilayers serve as model systems for the interface studies where a complete set of roughness and interlayer characteristics must be known to understand the measured properties. The modelling approach is attractive because X-EUV MLs have a high quality of layering and contrast of optical constants. Only a deep understanding of interfaces may improve even at present controversial observations of giant magnetoresistance values vs. interface structure.

However, the GMR devices are only the vanguard of further opportunities in nanomagnetism covering spin injection, magnetic vortices and new magnetic materials. In classical GMR structures, the need of an external magnetic field sets limits for further miniaturization. Therefore, novel nanometer-size structures utilizing the current induced magnetization switching are studied as a future building blocks of ultra-high density media. Here, a detailed knowledge of interface phenomena and mechanisms of interdiffusion in both immiscible and miscible combinations of materials is also a prerequisite of further progress.

The research of MLs is closely connected with a continuous development and invention of proper analytical tools for interface analyses. We have demonstrated that X-ray scattering methods developed originally for X-EUV multilayers can be applied for detailed interface analyses of magnetic nanosized structures and that the grazing incidence small-angle X-ray scattering provides a new approach to the fundamental understanding of the structures under study. The

possibility to monitor and control the growth process with picometer accuracy by *in-situ* ellipsometry was presented.

Other nanometer-size structures studied in this work are colloidal magnetic nanoparticles with their ability to form spontaneously ordered arrays. A typical diameter of nanoparticles is approx. 10 nm and less which is beyond the possibilities of contemporary lithographic techniques. Uniform arrays of nanomagnets can be prepared from colloidal magnetic nanoparticles. Such bottom-up approach presents fast and cost-effective way of the fabrication of nanoparticle monolayers which can be combined with various layered systems. An ordered array of magnetic nanoparticles can be used as a natural double tunnel barrier of novel tunnel magnetoresistance structures or spin torque nanooscillators. For technological application of the self-assembling process, the formation of ordered arrays has to be understood in detail. However, metallic nanoparticles provide also new opportunities in the field of nanomedicine, local therapy and diagnostic procedures with better resolution.

Nowadays, nanoparticles are considered as an intermediate phase in the bottom-up strategies following the prophetic vision of R. Feynman from 50-ties of the 20^{th} century that structures and devices could be built atom by atom. This challenge stimulates broad research activities. Natural slowness of the process involved could be overcome using a huge parallelism of the building technique.

Acknowledgement: Our work has been supported by Scientific Grant Agency (SGA) VEGA, Bratislava, Science and Technology Assistance Agency (STAA), Slovakia, NATO, European Commission and by Slovak Academy of Sciences (SAS) in the last decade. S.L. acknowledges the support by Alexander von Humboldt Foundation, Germany. At present, our work is supported by SGA VEGA grants 2/6030/28 and 2/0047/08, by STAA grants LPP-0080-06 and APVV-0173-06, by NATO under the contract CLG 982748 and by Centre of Excellence SAS – Physics of Information, contract I/2/2008.

We are grateful for a long-time cooperation to Prof. Ulrich Heinzmann and his group from University Bielefeld, Germany, and to Prof. Armando Luches and his group from University Salento, Italy. A part of this work was performed during the stay of E.M. at the Tohoku University with the group of Prof. Masaki Yamamoto.

References

[ABD02] S. Abdali, L. Gerward, A.E. Yakshin, E. Louis, F. Bijkerk: *Materials Research Bulletin* **37** (2002) 279

[ACQ03] S. Acquaviva, A. P. Caricato, E. D'Anna, M. Fernandez, A. Luches, Z. Frait, E. Majkova, M. Ozvold, S. Luby, P. Mengucci: *Thin Solid Films* **433** (2003) 252

[ACQ05] S.Acquaviva, E. D'Anna, M. L. De Giorgi, M. Fernandez, A. Luches, G. Majni, S. Luby, E. Majkova: *Appl. Surf. Sci*. **248** (2005) 286

[ADA95] E. Adachi, A. S. Dimitriov, K. Nagayama: *Langmuir* **11** (1995) 1057

[ALI03] J. Alicea, S. Hershfield: *J. Appl. Phys.* **93** (2003) 7930

[ALS] J. Als-Nielsen, Des McMorrow: *Elements of Modern X-ray Physics*, (J. Wiley and Sons, Chichester), ISBN 0-471-49858-0

[AN06] Y. An, H. Zhang, B. Dai, Z. Mai, J, Cai, Z. Wu: *J. Appl. Phys.* **100** (2006) 023516

[AND03] S.S. Andreev, M.S. Bibishkin, N.I. Chkhalo, E.B. Kluenkov, K.A. Prokhorov, N.N. Salashchenko, M.V. Zorina, F. Schäfers, L.A. Shmaenok: *J. Synchrotron Radiation* **10** (2003) 358

[ANN96] E.D'Anna, A. Luches, M. Martino, M. Brunel, E. Majkova, S. Luby, R. Senderak, M. Jergel, F. Hamelmann, U. Kleineberg, U. Heinzmann: *Appl Surf Sci* **106** (1996) 166

[ANO01] A. Anopchenko, M. Jergel, E. Majková, Š. Luby, V. Holý, A. Aschentrup, I. Kolina, Y. Cheol Lim, G. Haindl, U. Kleineberg, U. Heinzmann: *Physica* **B 305** (2001) 14

[ARA93] S. Araki: *J.Appl.Phys.* **73** (1993) 3910

[ASP84] D. E. Aspnes, A. A. Studna, E. Kinsbron: *Phys. Rev*. B **29** (1984) 768

[ASP93] D. E. Aspnes: *J. Opt. Soc. Am. A* **10** (1993) 974

[ATT] D. Attwood: *Soft X-rays and Extreme Ultraviolet Radiation, Principles and Applications*, (Cambridge Univ. Press; Cambridge, 1999), p. 98

[AYA02] M. Ayadi, R. Belhi, N. Mliki, K. Abdelmoula, J. Ferre, J. P. Jamet: *J. Magn. Magn. Mater*. **247** (2002) 215

[AZZ] R. M. A Azzam, N. M. Bashara: *Ellipsometry and Polarized Light*, (Elsevier Science Pub Co., Amsterdam, 1987)

[BAB02] W. Babik: *Thesis* (RWTH Aachen, Germany, 2002)

[BAI88] M. N. Baibich, J. M. Broto, A. Fert, F. Nguyen Van Dau, F. Petroff, P. Eitenne, G. Creuzet, A. Friederich, J. Chazelas: *Phys. Rev. Lett.* **61** (1988) 2472

[BAR81] T. W. Barbee: *Proc. AIP* **75** (1981) 131

[BAR85] T. W. Barbee, Jr., S. Mrowka, M. C. Hettrick: *Appl. Opt*. **24** (1985) 883

[BAR89] J. Barnas, K. E. Camley: *Phys. Rev. Lett.* **63** (1989) 664

[BAR90a] T. W. Barbee: *Mater. Res. Bull.* (1990) 3744

[BAR90b] J. Barnas, A. Fuss, R. E. Camley, P. Grünberg, W. Zinn: *Phys.Rev.B* **42** (1990) 8110

[BAR95] J. Barnas, Y. Bruynseraede: *Europhys. Lett.* **32** (1995) 176; *Phys. Rev. B* **53** (1996) 5449

[BAR96] J. Barnas, Y. Bruynseraede: *Phys. Rev. B* **53** (1996) 5449

[BAR97] J. Barnas, G. Palasantzas: *J. Appl. Phys.* **82** (1997) 3950

[BEL94] P. Belién, R. Schad, C.D. Potter, G. Verbanck, V.V. Moshchalkov, Y. Bruynseraede: *Phys. Rev. B* **50** (1994) 9957

[BEN87] R.W. Bene: *J. Appl. Phys.* **61** (1987) 1826

[BER92] A. Berkowitz, J. R. Mitchell, M. J. Carey, A. P. Young, S. Zhang, F. E. Spada, F. T. Parker, A. Hutten, G. Thomas: *Phys.Rev.Lett.* **68** (1992) 3745

[BER96] L. Berger: *Phys. Rev. B* **54** (1996) 9353

[BHA06] D. Bhattacharyya, D. Joseph, A.K. Poswal: *Nucl. Instr. Meth. Phys. Res*. B **248** (2006) 264

[BHU] B. Bhushan (Ed.): *Springer Handbook of Nanotechnology*, (Springer, 2004)

[BIB05] M.S. Bibishkin, A.A. Fraerman, A.E. Pestov, K.A. Prokhorov, N.N. Salashchenko, Yu.A. Vainer: *Nucl. Instr. & Methods A* **543** (2005) 333

[BIG06] T. P. Bigioni, X. M. Lin, T. T. Nguyen, E. I. Corwin, T. A. Witten, H. M. Jaeger: *Nature Materials* **5** (2006) 265

[BIN89] G. Binasch, P. Grünberg, F. Saurenbach, W. Zinn: *Phys. Rev. B* **39** (1989) 4828

[BIR03] J. Birch, F. Eriksson, G. A. Johansson, H. M. Hertz: *Vacuum* **68** (2003) 275

[BIR06] J. Birch, T. Joellson, F. Eriksson, N. Ghafoor, L. Hultman: *Thin Solid Films* **514** (2006) 10

[BOR00] C. Borchers, P. Ricardo, C. Michaelsen: *Phil Mag A* **80** (2000) 1669

[BOR02] C. Borchers, C.Michaelsen: *Phil Mag* **A 82** (2002) 1195

[BOT03] T. Bottger D. C. Meyer, P. Paufler S. Braun, M. Moss, H. Mai, E. Beyer. *Thin Solid Films* **444** (2003)165

[BRA01] S. Braun, R. Dietsch, M. Haidl, T. Holz, H. Mai, S. Müllender, R. Scholz: *Microelectronic Engn*. **57-58** (2001) 9

[BRU91] M. E. Brubaker, J. E. Mattson, C. H. Sowers, S. D. Bader: *Appl. Phys. Lett.* **58** (1991) 2306

[BRU93] M. Brunel, S. Enzo, M. Jergel, Š. Luby, E. Majková, I. Vávra: *J. Mater. Res.* **8** (1993) 2600

[CAM] I. A. Campbell, A. Fert: *Ferromagnetic Materials 3,* E. P. Wohlfarth (Ed.), (North Holland, Amsterdam, 1982), p. 774

[CAM96] J. Camarero, T. Graf, J. J., De Miguel, R. Mireanda, W. Kuch, M. Zharnikov, A. Dittschar, C. M. Schneider, J. Kirschner: *Phys. Rev. Lett*. **76** (1996) 42

[CAO] G. Cao, *Nanostructures & Nanomaterials, Synthesis, Properties and Applications*, (Imperial College Press, London, 2004)

[CAO94] J. Cao, M. Yanagihara, M. Yamamoto, Y. Goto, T. Namioka: *Appl. Opt*. **33**, (1994) 2013

[CAR87] C. Carbone, S. F. Alvaredo, *Phys. Rev.* **B 36** (1987)2433

[CHA03] T. Chassé, H. Neumann, B. Ocker, B. M. Scherer, W. Frank, F. Frost, D. Hirsch, A. Schindler, G. Wagner, M. Loreny, G. Otto, M. Zeuner, B. Rauschenbach:. *Vacuum* **71** (2003) 407

[CHE00] V.A. Chernov, E. D. Chkalo, N. V. Kovalenko, S. V. Mytnichenko: *Nucl Instr & Meth* **A 448** (2000) 276

[CHI98] W. C. Chiang, W. P. Pratt, M. Herrold, D. V. Baxter: *Phys. Rev. B* **58** (1998) 5602

[CHI06] L. Chitu, Y. Chushkin, S. Luby, E. Majkova, G. Leo, A. Satka, M. Giersig, M. Hilgendorff: *Appl. Surface Sci.* **252** (2006) 5559

[CHI07a] L. Chitu, Y. Chushkin, S. Luby, E. Majkova, A. Satka, J. Ivan, L. Smrcok, A. Buchal, M. Giersig, M. Hilgendorff: *Mat. Sci. Eng. C* **27** (2007) 23

[CHI07b] L. Chitu, M. Jergel, E. Majkova, S. Luby, I. Capek, A. Satka, J. Ivan, J. Kovac, M. Timko: *Mater. Sci. Engn C* **27** (2007) 1415

[CHU03] Y. Chushkin, M. Ulmeanu, S. Luby, E. Majkova, I. Kostic, P. Klang, V. Holy, Z. Bochnicek, M. Giersig, M. Hilgendorff, T. H. Metzger: *J. Appl. Phys.* **94** (2003) 7743

[CHU05a] Y. Chushkin, M. Jergel, S. Luby, E. Majkova, M. Ozvold, Y. Kuwasawa, S. Okayasu, E. D'Anna, A. Luches, M. Martino: *Appl. Surf. Sci.* **243** (2005) 62

[CHU05b] Y. Chushkin, L. Chitu, S. Luby, E. Majkova, A. Satka, V. Holy, J. Ivan, M. Giersig, M. Hilgendorff, T. H. Metzger, O. Konovalov: D. Kumar et al. (Eds.), (Mater. Res. Soc. Symp. Proc. 877E, Warrendale, PA , 2005), S6.18

[CHU06] Y. Chushkin, L. Chitu, Y. Halahovets, S. Luby, E. Majkova, A. Satka, G. Leo, M. Giersig, M. Hilgendorff, V. Holy, O. Konovalov: *Mat. Sci. Eng. C* **26** (2006) 1136

[COL96] J. M. Colino, I. Schuller, V. Korenivski, K. V. Rao: *Phys. Rev. B* **54** (1996) 13030

[COL98] C. P. Collier, T. Vossmeyer, J. R. Heath: *Annu. Rev. Phys. Chem*. **49** (1998)371

[COL00] R. W. Collins, J. Koh, H. Fujiwara, P. I. Rovira, A. S. Ferlauto, J. A. Zapien, C. R. Wronski, R. Messier: *Appl. Surf. Sci.* **154-155** (2000) 217

[COM23] A. H. Compton : *Phil. Mag.* **45** (1923) 1121

[COM95] J. C. Comfort, F. K. Urban III: *Thin Solid Films* **270** (1995) 78

[CXRO] web site of Center for X-ray Optics, Lawrence Berkeley National Laboratory http://www-cxro.lbl.gov/optical_constants/

[CYR00] M. C. Cyrille, S. Kim, M. E. Gomez, J. Santamaria, K. M. Krishnan, I. K. Schuller: *Phys. Rev. B* **62** (2000) 3361

[DAI99] J. Daillant, A. Gibaud (Eds.): *X-ray and Neutron Reflectivity : Principles and Applications*, (Lecture Notes in Physics Vo. 23, Springer Verlag, Berlin, 1999), p.87

[DAN88] D'Anna, G. Leggieri, A. Luches: *Appl.Phys. A* **45** (1988) 325

[DAN96] E. D'Anna, A. Luches, M. Martino, M. Brunel, E. Majková, Š. Luby, R. Senderák, M. Jergel, F. Hamelmann, U. Kleineberg, U. Heinzmann: *Appl. Surf. Sci.* **106** (1996) 166

[DAN99] E. D'Anna, G. Leggieri, A. Luches, M. Martino, G. Majni, G. Barucca, P. Mengucci, S. Luby, E. Majkova, M. Jergel: *Thin Solid Films* **343 – 344** (1999) 206

[DEB94] D.K.G. de Boer: *Phys. Rev.* **B 49** (1994) 5817

[DEB95] D.K.G. de Boer: *Phys. Rev.* **B 51** (1995) 5297

[DEB96] D.K.G. de Boer: *Phys. Rev.* **B 53** (1996) 6048

[DEE97] R. D. Deegan, O. Bakajin, T. F. Dupont, G. Huber, S. R. Nagel, T. A. Witten: *Nature* **389** (1997) 827; *Phys. Rev E* **62** (2000) 756

[DEN93] N. D. Denkov, O. D. Velev, P. A. Kralchevsky, I. B. Ivanov, H. Yoshimura, K. Nagayama: *Nature* **361** (1993) 26

[DGE70] P.-G. de Gennes, P. Pincus : *J. Phys.: Condens. Matter*. **11** (1970) 189

[DHE87] P. Dhez: *Nucl. Instr. Methods A* **261** (1987) 66

[DIE88] R. Dietsch, T. Holz, H. Mai, C.F. Meyer, R. Scholz, B. Wehner: *Appl. Surf. Sci.* **127-129** (1988) 451

[DIE91] B. Dieny, V. S. Speriosu, S. S. P. Parkin, B. A. Gurney, D. R. Wilhoit, D. Mauri: *Phys. Rev. B* **43** (1991) 1297

[DIE02] R. Dietsch, T. Holz, T. Weissbach, R. Scholz: *Appl. Surf. Sci.* **197** (2002) 169

[DJA00] T. Djavanbakht, V. Carrier, J.M. Andre, R. Barchewitz, P. Troussel: *J. de Physique IV* **10** (2000) 281

[DIK90] J.W. Dikes. Y.K. Kim, A, Tsoukatos, S. Gupta, F. C. Sander: *J. Appl. Phys.* **79** (1990) 5584

[DOSCH01] H. Dosch: *Appl. Surf. Sci.* **182** (2001) 192

[DUE02] T.Duenas, A.Sehrbrock, M. Lohndorf, A. Ludwig J.Wecker, P.Grunberg, E. Quandt: *J. Magn. Magn. Mater.* **242–245** (2002) 1132

[DUM40] J. DuMond, J.P.Youtz: *Appl. Phys*. **11** (1940) 357

[DUP90a] V. Dupuis, M.F. Ravet, C. Tete, M. Piecuch, B. Vidal: *J. Appl. Phys.* **68** (1990) 3384

[DUP90b] V. Dupuis, M. F. Ravet, C.Tete, M. Piecuch, Y.Lepetre, R. Rivoira, E. Ziegler: *J Appl. Phys.* **58**: (1990) 5146

[EDW82] S.F. Edwards, D.R. Wilkinson: *Proc. Royal Soc. London* **A 381** (1982) 17

[EDW91] D. M. Edwards, R.B.Muniz, J.Mathon: *IEEE Trans.Magn*. **3**, (1991) 4941; J.Mathon: *Contemp.Phys.* **32** (1991) 143

[ENO03] Y. Enomoto, K. Oba, M. Okada *Physica A* **330** (2003) 496

[ESA70] L. Esaki, R. Tsu *IBM J. Res. Develop*. **14** (1970) 61

[FAR57] M. Faraday: *Phil. Trans. Roy. Soc.* **147** (1857) 145

[FAR98] R.F.C. Farrow: *IBM Journal of Research and Development* **42** (1998) 1

[FRI97] J. Friedrich, I. Diel, C.Kunz, S.Di Fonzo, B.R. Müller, W.Jark: *Appl. Optics* **36** (1997) 6329

[FUC04] G. D. Fuchs, N. C. Emley, I. N. Krivorotov, P. M. Braganca, E. M. Ryan, S. I. Kiselev, J. C. Sankey, D. C. Ralph, R. A. Buhrman, J. A. Katine: *Appl. Phys. Lett.* **85** (2004) 1205; Y. M. Huai, F. Albert, P. Nguyen, M. Pakala, T. Valet: *Appl. Phys. Lett.* **84** (2004) 3118; J. C. Slonczewski: *Phys. Rev. B* **71** (2005) 024411

[FUL92] E.E. Fullerton, D.M. Kelly, J. Guimpel, J.K. Schuller, Y. Bruynseraede: *Phys. Rev. Letters* **68** (1992) 859

[GER05] V. Germain, J. Richardi, D. Ingert, M. P. Pileni: *J. Phys. Chem. B* **109** (2005) 5541

[GRE85] A. L. Greer, F. Spaepen: *Synthetic modulated structures,* In: *Diffusion* (Eds. L. L. Chang, B. C. Giessen, Academic Press, 1985)

[GRE88] A. L. Greer, In: *Diffusion phenomena in thin films and microelectronics materials*, (Eds. D. Gupta, P. S. Ho, Noyes Publ., NewYork. 1988), p. 146

[GRU86] P. Grünberg, R. Schreiber, Y. Pangm M. B. Brodsky, H. Sowers: *Phys. Rev. Lett*. **57** (1986) 2442

[GRU00] P. Grünberg: *Acta Mater.* **48** (2000) 239

[GUI93] D.P. Guines, R.C. Spitzer, N.N. Ceglio, M. Krumrey, G. Ulm: *Appl. Optics* **32** (1993) 6991

[GUP06] A. Gupta, D. Kumar: *Nucl. Instr. Meth. in Phys. Res. B* **244** (2006) 202

[HAM00] F. Hamelmann, G. Haindl, J. Schmalhorst, A. Aschentrup, E. Majkova, U. Kleineberg, U.Heinzmann, A. Klipp, P. Jutzi, A. Anopchenko, M. Jergel, S. Luby: *Thin Solid Films* **358** (2000) 90

[HAM06] F. Hamelmann, A. Wonisch, W. Hachmann, U. Heinzmann: *Functional Properties of Nanostructured Materials*; R.Kassing (Ed.): (Springer, Netherlands, 2006); p 351

[HAT99] T. Hatano, H. Umetsu, M. Yamamoto: In: Y. Furukawa, Y. Mori, T. Kataoka (Eds.): *Proc. 9th Int. Conf. on Production Engineering,* (Osaka, 1999), p. 292

[HAT03] T. Hatano, S. Kubota, Y. Adachi, T. Tsuru, M. Yamamoto, In T. Warwick, J. Arthur, H. A. Padmore, J. Stohr (Eds.): *Proc. 8th International Conference on Synchrotron Radiation Instrumentation*,(San Francisco, AIP, 2004), p. 839

[HEI91] B. Heinrich, J. F. Cochran, M. Kowalewski, J. Kirschner, Z. Celinksi, K. Myrtle: *Phys. Rev. B* **44** (1991) 30

[HEN70] D. J. Henderson, J. A. Barker, R. O. Watts: *IBM J. Res. Develop.* **14** (1970) 668

[HEN03] S. Hendy, S. A. Brown, M. Hyslop: *Phys. Rev. B* **68** (2003) 241403(R)

[HIL] M. Hilgendorff private communication

[HOL77] T. Holz, R. Dietsch, H. Mai, L. Brügemann, S. Hopfe, R. Scholz, R. Krawietz, B. Wehner: *46 Ann. Denver X-ray Conf. and US X-Top*, (Steamboat Springs, Colorado, 1997)

[HOL88] K. Holloway, R. Sinclair: *J. Less Common Metals* 140 (1988) 1

[HOL89a] K. Holloway, R. Sinclair, M. Nathan: *J. Vac. Sci. Technol. A* **7** (1989)1479

[HOL89b] K. Holloway, K. Do, R. Sinclair: *J. Appl. Phys*. **65** (1989) 474

[HOL93] V. Holý, J. Kuba, I. Ohlídal, K. Lischka, W. Plotz: *Phys. Rev.* **B 47** (1993) 15896

[HOL94] V. Holý, T. Baumbach: *Phys. Rev.* **B 49** (1994) 10668

[HOL99] V. Holý, U. Pietsch, T. Baumbach: *High-Resolution X-Ray Scattering from the Thin Films and Multilayers,* (Springer, Berlin, 1999)

[HON95] J. Honda, K. Sato, Y. Aoki, R. Araki: *J. Phys. Soc. Jpn.* **64** (1995) 219

[HON97] C.-Y. Hong, I. J. Jang, H. E. Horng, C. J. Hsu, Y. D. Yao, H. C. Yang: *J. Appl. Phys.* **81** (1997) 4275

[HON99] C.-Y. Hong, H. E. Horng, F. C. Kuo, S. Y. Yang, H. C. Yang, J. M. Wu: *Appl. Phys. Lett.* **75** (1999) 4325

[HOU88] Ph. Houdy, P. Boher, C. Schiller, P. Luzeau, R. Barchewitz, N. Alehyane, M. Quahabi: *Proc. SPIE* **984** (1988) 95

[HUN78] W. R. Hunter: *Appl. Opt.* **17** (1978) 74

[HUW96] W. Hu, M. Yamamoto, M. Watanabe: *Proc. SPIE* **2873** (1996) 74

[HYL93] T. R. Hylton, K. R. Coffey, M. A. Parker, J. K. Howard: *Science* **161** (1993) 1021

[IBM03] IBM Research, "The Giant Magnetoresistive Head", J. Robert Lineback, The Semiconductor Reporter (2003), http://www.research.ibm.com/research/gmr.html

[ISH02] M. Ishino, O. Yoda, Y. Haishi, F. Arimoto, M. Takeda, S. Watanabe, S. Ohnuki, H. Abe: *Jpn. J. Appl. Phys*. **41** (2002) 3052

[ISR73] J. N. Israelachvili: *J. Chem. Soc. Faraday Trans. II*, **69** (1973) 1729

[JAM] R. W. James: *The optical principles of the diffraction of X-ray optics,* (Bell, London 1948)

[JAN90] A. F. Jankowski, L. R. Schrawyer, M. A. Wall: *J. Appl. Phys.* **68** (1990) 5162

[JAN04] A.F. Jankowski, C.K. Saw, C.C. Walton, J.P.Hayes, J. Nilsen: *Thin Solid Films* **469** (2004) 372

[JER93] M. Jergel, E. Majkova, S. Luby: *J. de Physique IV Coll*.**C8** (1993) 337

[JER95] M. Jergel, V. Holy, E. Majková, S. Luby, R. Senderák: *J. Phys. D* **28** (1995) A241

[JER96] M. Jergel, Z. Bochnícek E. Majkova, R. Senderak, S. Luby: *Appl. Phys. Leters.* **69** (1996) 919

[JER97] M. Jergel, V. Holy, E. Majkova, S. Luby, R. Senderák: *J. Appl. Crystallography* **30** (1997) 642

[JER98] M. Jergel, V. Holy, E. Majkova, S. Luby, R. Senderak, H.J. Stock, D. Menke, U. Kleineberg, U. Heinzmann: *Physica B* **253** (1998) 28

[JER00] M. Jergel, A. Anopchenko, V. Holy, E. Majkova, S. Luby, R. Senderák: *J. Appl. Crystallography* **33** (2000) 753

[JER00a] M. Jergel, V. Holy, E. Majkova, S. Luby, R. Senderak, H.J. Stock, D. Menke, U. Kleineberg, U. Heinzmann: *Mater. Sci. Forum* **21-24** (2000) 184

[JER00b] M. Jergel, A. Anopchenko, E. Majkova, M. Spasova, S. Luby. V. Holy, M. Brunel, A. Luches, M. Martino: *Thin Solid Films* **373** (2000) 216

[JER06] M. Jergel, M. Ožvold, R. Senderák, S. Luby, E. Majkova: *Zeitschrift für Kristallographie* **Suppl. 23** (2006) 305

[JER08] M. Jergel, E. Majkova, Ch. Borel, Ch. Morawe, I. Mako: *Multilayers with Ultra-short Periods*, In *Modern Developments in X-Ray and Neutron Optics*, Springer Series in Optical Sciences vol 137, A. Erko, M. Idir, Th. Krist, A.G. Michette (Eds.) (Springer Verlag, Berlin-Heidelberg 2008), pp. 375-390, ISBN 978-3-540-74560-0

[JIA89] Z. Jiang, X. Hiang, W. Liu, Z. Wu: *J. Appl. Phys.* **65** (1989) 196

[JIA00] I. M. Jiang, M. S. Wang, H. E. Horng, C. Y. Hong: *Physica* **A 281** (2000) 87

[JIA01] L. Jiang, B.Verman, B. Kim, Y. Platonov, Z. Al-Mosheky, R. Smith, N. Grupido: *The Rigaku Journal* **18** (2001) 13

[JIN95] Q. Y. Jin, M. Lu, Q. S. Bie, Y. B. Xu, H. R. Zhai, Y. H. Shen: *J. Magn. Magn. Mater.* **140-144** (1995) 565

[KAG96] V.M. Kaganer, S.A.S tepanov, R. Köhler: *Physica* **B 221** (1996) 34

[KAN93] H. Kano, K. Kagawa, A. Suzuki, A. Okabe, K. Hayashi, K. Asoa: Appl. Phys. Lett. **63** (1993) 2839

[KAR86] M. Kardar, G. Parisi, Y.Ch. Zhang: *Phys. Rev. Letters* **56** (1986) 889

[KAT00] J. A. Katine, F. J. Albert, R. A. Buhrman, E. B. Myers, D. C. Ralph: *Phys. Rev. Lett.* **84** (2000) 3149; F. J. Albert, J. A. Katine, R. A. Buhrman, D. C. Ralph: *Appl. Phys. Lett.* **77** (2000) 3809

[KAW94] T. Kawamura, H. Takenaka: *J. Appl. Phys.* **75** (1994) 3806

[KIM92] H. Kimura, M. Yamamoto, M. Yanigihara, T. Maehara, T. Namioka: *Rev. Sci. Instr.* **63** (1992) 1379

[KIN] T. Kingetsu, M. Yamamoto: *Surface Sci. Rep*. **45** (2002) 79

[KIN86] H. Kinoshita, K. Kurihara, Y. Ishii, Y. Torii: *J. Vac. Sci. Technol. B* **7** (1986) 1648

[KIN89] H. Kinoshita, K. Kurihara, Y. Ishii, Y. Torii: *J. Vac. Sci. Technol. B* **7** (1989) 1648

[KIN02] T. Kingetsu, M. Yamamoto: *Surf. Sci. Reports* **45** (2002) 81

[KIR01] A. Kirakosian, R. Bennewitz, J.N. Crain, Th. Fauster, J.-L. Lin, D.Y. Petrovykh, F.J. Himpsel: *Appl. Phys. Lett*. **79** (2001) 1608

[KJO04] B. Kjornrattanawanich, S. Bajt, J. F. Seely: *Appl. Opt.* **43** (2004) 1082

[KLE94] U. Kleineberg, H.J.Stock, A.Kloidt, B.Schmiedeskamp, U.Heinzmann, S.Hoppe, R.Scholz: *Phys. Stat. Sol.* **145** (1994) 539

[KNI88] L.V. Knight, J.M. Thorne, A. Toor, T.W. Barbee Jr.: *Revue de Physique Apl.* **23** (1988) 1631

[KOCH04] R. H. Koch, J. A. Katine, J. Z. Sun: *Phys. Rev. Lett.* **92** (2004) 088302

[KON93] V.V. Kondratenko, Yu.P. Pershin, O.V. Poltseva, A.I. Fedorenko, E.N. Zubarev, S.A. Yulin, I.V. Kozhevnikov, S.I. Sagitov, V.A. Chirkov, V.E. Levashov, A.V. Vinogradov: *Appl. Optics* **32** (1993) 1811

[KOO99] J. C. S. Kools, W. Kula, D. Mauri, T. Lin: *J. Appl. Phys*. **85**, (1999) 4466

[KOP03] M. Kopcewicz, F. Stobiecki, J. Jagielski, B. Szymanski, M. Schmidt, J. Dubowik, J. Kalinowska: *J. Appl. Phys.* **93** (2003) 5514

[KOR91] J.B. Korright, S. Joksch, E. Ziegler: *J. Appl. Phys.* **69** (1991) 168

[KOR97] J.B. Kortright; S.K. Kim, T. Warwick, N.V. Smith: *Appl. Phys. Letters* **71** (1997) 1446

[KOV03] N.V.Kovalenko, S.V.Mytnichenko, V.A.Chernov: *JETP Letters* **77** (2003) 80

[KUH02] T. Kuhlmann, S.Yulin, T.Feigl, N.Kaiser. T.Gorelik. U.Kaiser, W.Richter, W. *Appl. Opt.*, **41** (2002) 2048

[KWO87] J. Kwo, M. Hong, F. J. DiSalvo, J. V. Waszczak, C. F. Majkrzak: *Phys. Rev. B* **35** (1987) 7295

[LAC01] D. Lacoste, T. C. Lubensky: *Phys. Rev. E* **64** (2001) 041506

[LAL03] Y. Lalatone, J. Richardi, M. P. Pileni: *Nature Materials* **3** (2003) 121

[LAN01] J. Langer, R. Mattheis, B. Ocker, W. Maaß, S. Senz, D. Hesse, J. Kräußlich: *J. Appl. Phys.* **90** (2001) 5126

[LAR02] J. Larruquert: *Optics Comm*. **206** (2002) 259

[LAW00] R.A. Lawes: *Appl. Surf. Sci.* **154-155** (2000) 519

[LAY69] H. P. Layer, D. E. McClure, R. H. Muller: *Surf. Sci*. **16** (1969) 177

[LAZ02] R. Lazzari: *IsGISAXS: a program for GISAXS analysis of supported islands, J. Appl. Cryst*. **35** (2002) 406

[LEG01] J. Legrand, A.-T. Ngo, Ch. Petit, M. P. Pileni: *Adv. Mater.* **13** (2001) 58

[LEO03] G. Leo, Y. Chushkin, S. Luby, E. Majkova, I. Kostic, M. Ulmeanu, A. Luches, M. Giersig, M. Hilgendorff: *Mat. Sci. Engin.* **C 23** (2003) 949

[LEV84] D. Levine, P. Steinhards: *Phys. Rev. Lett* **53** (1984) 2477

[LEV89] J. R. Levine, J. B. Cohen, Y. W. Chung, P. Georgopoulos: *J. Appl. Cryst*. **22** (1989) 528

[LIF] E. M. Lifshitz, L. P. Pitaevskii: *Statistical Physics*, (A. Wheaton & Co., Exeter, 1981)

[LIM01] Y.C. Lim, T. Westerwalbesloh, A. Aschentrup, O.Wehmeyer, G. Haindl, U.Kleineberg, U.Heinzmann: *Appl. Phys. A* **72** (2001) 121

[LIN01] J. Lin, W. Zhou, A. Kumbhar, J. Wiemann, J. Y. Fang, E. E. Carpenter, C. J. O'Connor: *Journal of Solid State Chemistry*, **159** (2001) 26; J. S. Yin, Z. L. Wang: *Nanostructured Materials* **11** (1999) 845

[LOD96] G.S. Lodha, S. Pandita, A. Gupta, N.V. Nandedkar, K. Yamashita: *J. Electr. Spec. & Related Phenomena* **80** (1996) 453

[LOL95] R. Loloe, P.A, Schroeder, W.P. Pratt, J Bass, A. Fert: *Physica B* **204** (1995) 274

[LOU05] E. Louis, A.E. Yakshin, R.W.E. van der Kruijsr, I. Nedelcu, S.A. van der Westen, T. Tsarfati, F. Bijkerk, H. Enkish, S. Müllenedr, B. Wolshrijn, B. Mertens: *Proc. SPIE* **5900** (2005) 590

[LUB92] S. Luby, E.Majkova, P. Lobotka, I. Vávra, M.Jergel, R. Senderák, J. Grňo: *Physica* **C 197** (1992) 35

[LUB98] S. Luby, E. Majkova, M. Spasova, M. Jergel, R. Senderak, E. D'Anna, A. Luches, M. Martino, M. Brunel: *Thin Solid Films* **312** (1998) 15

[LUB99] S. Luby, M. Jergel, A. Anopchenko, A. Aschentrup, F. Hamelmann, E. Majkova, U. Kleineberg, U. Heinzmann: *Appl. Surf. Sci.* **150** (1999) 178

[LUB02] S. Luby, E. Majkova, M. Jergel, R. Senderak, A. Anopchenko, E. D'Anna, G. Leggieri, A. Luches, M. Martino, P. Mengucci, G. Majni, A. Di Cristoforo: *Mat. Sci. Engn. C* **694** (2002) 145

[MAC] G. Machula, J. Thieme, J.Niemeyer. In: *X-Ray Microscopy and Spectromicroscopy*; Eds. Thieme, J.; Schmahl, G.; Rudolph, D.; E. Umbach, E.; Springer-Verlag, Heidelberg, 1998; pp II-21 - II-28

[MAI92] H. Mai, W. Pompe, W. *Appl. Surf. Sci*., **54** (1992) 215

[MAJ96] E. Majkova, B.George, Ch.Bellouard, S. Luby, M. Jergel, R.Senderak, M.Babinsky,. *J. Magn. Magn. Mater*. **156** (1996) 415

[MAJ99] E. Majkova, M. Spasova, M. Jergel and S. Luby, S. Okayasu, A. Luches, M. Martino, E. N. Zubarev, M Brunel, *Thin Solid Films* **343-344** (1999) 214

[MAJ02] E. Majkova, S. Luby, M. Jergel, A. Anopchenko, Y. Chushkin, G. Barucca, A. DiCristoforo, P. Mengucci, E.D.'Anna, A. Luches, M. Martino, Hsin-Yi Lee*, Mat. Sci. Eng. C* **19** (2002) 139

[MAJ03a] E. Majkova, M. Yamamoto: *Optical Review* **10** (2003) 398

[MAJ03b] E. Majkova, S. Luby, M. Jergel, Y. Chushkin, E. D'Anna, A. Luches, M. Martino, P. Mengucci, G. Majni, Y. Kuwasawa, S Okayasu, Appl. Surf. Sci. **208-209** (2003) 394

[MAJ06] E. Majkova, Y. Chushkin, M. Jergel, S. Luby, V. Holy, I. Matko, B. Chenevier, L. Toth, T. Hatano, M. Yamamoto: *Thin Sol. Films* **497** (2006) 115

[MAJ08] E. Majkova, S. Luby, M. Jergel: *Interface Properties and Thermal Stability of Multilayers for X-EUV Optics,* In *Leading-Edge Materials Science Rsearch,* P. W. Lamont (Ed.), (Nova Sci. Publ. Inc., NY, 2008), pp. 5-39, ISBN 1-60021-798-2

[MAO99] P. H. Mao, F. A. Harrison, D. L. Windt, F. E. Christensen: *Appl. Opt*. **38** (1999) 4766

[MAT74] H. J. Matieu: *Rev. Sci. Instrum*. **45** (1974) 798

[MAT87] V. Matijasevic, M. R. Beasley: *Phys. Rev. B* **35** (1987) 3175

[MAT06] V. Matarello, V. Rigato, F. Borgatti, S. Nannarone: In: 8^{th} *Int. Conf. Phys. X-ray Mult. Struct.,* (Tohoku Univ.,Sapporo, 2006), p. 29

[McC00] J.J. McClelland, R.J. Celotta: *Thin Solid Films* **367** (2000) 25

[MCW] D. B. McWhan: *Synthetic Modulated Structures, Structure of Chemically Modulated Films*, (Academic Press, 1985), p. 43

[MEY90] L. Meyerheim, B. Lengeler, H.E. Goebel: *J. Appl. Phys.* **68** (1990) 2549

[MIC] C. Michaelson, P. Ricardo, D. Anders, M. Schuster, J. Schilling, H. Göbel: In *Adv. X-ray Anal.*, (Int. Center. for Diff. Data, Vo. **42**, 2000), p 308

[MIC00] C. Michaelsen, P. Ricardo, D. Anders, M. Schuster, J. Schilling, H. Goebel: *Adv. In X-ray Analysis* **42** (2000) 308

[MIC02] C. Michaelsen, J. Wiesmann, C. Hoffmann, K. Wulf, L. Brugemann, A. Strom: *Proc. SPIE* **4782** (2002) 43

[MIE76] A.R. Miedema: *Philips Tech. Rev.* **36** (1976) 217

[MIK95] P. Mikulik, V. Holy, J. Kubena, K. Ploog: *Acta Cryst. A* **51** (1995) 825

[MIL92] D.J. Miller, K.E. Gray, R.T. Kampwirth, J.M. Murduck: *Europhys. Letters* **19** (1992) 27

[MIN93] Z.H. Ming, A. Krol, Y.L. Soo, Y.H. Kao, J.S. Park, K.L. Wang: *Phys. Rev. B* **47** (1993) 16373

[MOL91] J.M. Molarius, S. Franssila, G. Drozdy, J. Saarilahti: *Appl. Surf. Sci.* **53** (1991) 383

[MOR91] D. Morris, C.J. Buckley, G.R. Morrison, A.G. Michette, P.A.F. Anastasi, M.T. Browne, R.E. Burge, P.S. Charalambous, G.F. Foster, J.R. Palmer, P.J. Duke: *Scanning* **13** (1991) 7

[MOR99] Ch. Morawe, J.C.Peffen, O. Hignette, E.Ziegler: *SPIE Proc*. **3773** (1999) 90

[MTA99] D. Meziane Mtalsi, M. ElHarfaoui, M. Faris, A. Qachaou J. Ben Youssef, H. Le Gall: *J. Cond. Mat.* **2** (1999) 1

[MUR83] S.P. Murarka: *Silicides for VLSI Applications*, (Academic Press; New York, 1983), p. 130

[MUR00a] Y. Muramatsu, Y. Ueno, E. M. Gullikson, R. C. C. Perera: *Appl. Phys. Lett.* **77** (2000) 2653

[MUR00b] C. B. Murray, C. R. Kagan, M. G. Bawendi: *Annu. Rev. Mater. Sci.* **30**, 545 (2000)

[NAG03] L. C. C. M. Nagamine, A. Biondo, L. G. Pereira, A. Mello, J. E. Schmidt, T. W. Chimendes, J. B. M. Cunha, E. B. Saitovitch: *J. Appl. Phys.* **94** (2003) 5881

[NANO] *Nanoparticles: From Theory to Application.* G. Schmid (Ed.) (Wiley Verlag GmbH & Co., Weinheim, 2004), ISBN: 3-527-30507-6

[NAK92] K. Nakajima, S. Aoki, S. Sudo, S. Fujiwara: *Jap. J. Appl. Phys.* **31** (1992) 2864

[NAR04] S. Narayanan, J. Wang, and X. M. Lin: *Phys. Rev. Lett*. **93** (2004) 135503

[NAU98] A. Naudon, D. Babonneau, F. Petroff, A. Vaures: *Thin Solid Films* **319** (1998) 81

[NAU00] A.Naudon, D. Babonneau, D. Thiaudiere, S. Lequien: *Physica B* **283** (2000) 69

[NEE62] L.Néel: *Comptes. Rendus* **255** (1962) 1676

[NEF01] A. Nefedov, H. Zabel, F. Schäfers: *Nucl. Instr. & Meth. A* **467-468** (2001) 345

[NES] A.N.Nesmeyanov: *Vapour Pressure of the Elements*, (Infosearch Ltd.; London, 1963), p. 451

[NEV80] L. Nevot, P. Croce: *Revue de Physique Apl.* **15** (1980) 761

[NEV88] L. Nevot, B. Pardo, J. Corno: *Revue de Physique Apl.* **23** (1988) 1675

[NOM92] N. Nomura, K. Mayama, T. Sasaki, M. Yamamoto, M. Yanagihara: *Proc. Soc. Photo-Opt. Instrum. Engn.* **1720** (1992) 395

[NTT-AT] http://www.ntt-at.com/products_e/beamsplitter/index.html

[NVE] http://www.nve.com/technicalTools.htm

[OHI03] T. Ohigashi, N. Watanabe, H. Yokosuka, S.Aoki: *J. Phys*. *IV France* **104** (2003) 53

[PAL] J.R.Palmer, G.R.Morrison, In: *X-Ray Microscopy III*; A. G. Michette, G. R. Morrison; C. J. Buckley (Eds.): (Springer Series in Optical Science, Springer-Verlag, Berlin, Vo. 67, 1992) p. 278

[PAL93] G. Palasantzas : *Phys. Rev.* **B 48** (1993) 14472

[PAN96] M. Panzer, R. Dietsch, Th. Holz, H. Mai, H. Voelmar: *Appl. Surf. Sci*. **96-98** (1996) 643

[PAR] S. S. P. Parkin: In *Ultrathin Magnetic Structures II*, B. Heinrich, J. A. C. Bland (Eds.), (Springer, Berlin 1994), p. 148

[PAR54] L.G. Parrat : *Phys. Rev.* **95** (1954) 359

[PAR90] S.S.P.Parkin, N. More, K. P. Roche: *Phys.Rev.Lett.* **64** (1990) 2304

[PAR91a] S. S. P. Parkin, R. Bhadra, K. P. Roche: *Phys. Rev. Let*t. **66** (1991) 2152

[PAR91b] S. S. P. Parkin, *Phys. Rev. Lett*. **67** (1991) 3598

[PAR93] S. S. P. Parkin: *Phys. Rev. Lett.* **71** (1993) 1641

[PAR94] S. S. P. Parkin, R. F. S. Farrow, R. F. Marks, A. Cebollada, G. R. Harp, R. J. Savoy: *Phys.Rev.Lett.* **72** (1994) 3718

[PAR00] D. C. Parks, P. J. Chen, W. F. Egelhoff, Jr., R. D. Gomez: *J. Appl. Phys*. **87**, (2000) 3023

[PAR05] Park, X. Zhang, A. Misra, J. D. Thompson, M. R. Fitzsimmons, S. Lee, C. M. Falco: *Appl. Phys. Lett*. **86** (2005) 042504

[PARK97] Y.D. Park, J.A. Caballero, A. Cabbibo, J.R. Children, H.D. Hudspeth, T.J. Schultz, F. Shari: *J. Appl. Phys.* **81** (1997) 4717

[PAT] A. Patelli, J.Ravagnan, V.Rigato, G.Salmaso, D.ilvestrini, E.Bontempi, L.E.Depero: *Appl. Surf. Sci*. **238** (2004) 262

[PAW] P. Pawlow: *Z. Phys. Chem* **65** (1909) 545; V. K. Semenchenko: *Surface phenomena in Metals and Alloys*, (Pergamon Press, NY 1981)

[PEN01] D. L. Peng, T. J. Konno, K. Wakoh, T. Hihara, K. Suniyama: *Appl. Phys. Lett*. **78** (2001) 1535

[PER58] J. K. Percus, G. Yevick: *Phys. Rev.* **110** (1958) 1

[PER02] Y.P. Pershin, Y.N. Zubarev, V.V. Kondratenko, O.V. Poltseva, A.G. Ponomarenko, V.A. Servryukova, J. Verhoeven: *Metallofizika i Noveishie Tekhnologii* **24** (2002) 795

[PET87] A.K. Petford-Long, M.B. Stearns, C.H. Chang, S.R. Nutt, D.G. Stearns, N.M. Ceglio, A.M. Hawryluk: *J. Appl. Phys.* **61 (**1987) 1422

[PET98] C. Petit, A. Taleb, M. P. Pileni: *Adv. Mater*. **10** (1998) 259

[PHA93] Y.H. Phang, D.E. Savage, R. Kariotis, M.G. Lagally: *J. Appl. Phys.* **74** (1993) 3181

[POU05] C. Poulard, G. Guén, A. M. Cazabat: *J. Phys.: Condens. Matter* **17** (2005) S4213

[PRA99] C. Prados, D. V. Dimitrov, G. C. Hadjipanayis: *J. Magn. Magn. Mater.* **192** (1999) 19

[PRI99] G. A. Prinz, *J. Magn. Magn. Mater.* **200** (1999) 57

[PUI91] E.I. Puik, M.J. Van der Wiel, H. Zeulenmaker, J. Verhoeven: *Appl. Surf. Sci.* **47** (1991) 251

[PUN01] V. F. Puntes, K. M. Krishnan, P. Alivisatos, *Science* **298** (2001) 2115

[RAB03] E. Rabani, D. R. Reichman, Ph. L. Geissler, L. E. Brus: *Nature* **426** (2003) 271

[RAV04] M. F. Ravet, F. Bridou, H. Zh. Song, A. Jerome, F. Delmotte, M. Bougnet, Ph. Bouyries, J.-P. Delaboudiniere: *Proc. SPIE* **5250** (2004) 99

[REN03] G. Renaud, R. Lazzari, Ch. Revenant, A. Barbier, M. Noblet, O. Ulrich, F. Leroy, J. Jupille, Y. Borensztein, C. R. Henry, J. P. Deville, F. Scheurer, J. Mane-Mane, O. Fruchart: *Science* **300** (2003) 1416

[RIF03] J.C. Rife, M.M. Miller , P.E. Sheehan, C.R. Tamanaha, M. Tondra, L. J. Whitman: *Sensors and Actuators A* **107** (2003) 209

[RIN96] M. D. Rintoul, S. Torquato: *J. Chem. Phys*. **105** (1996) 9258

[ROD93a] B. Rodmacq, M. Vaezzadeh, B. George, Ph. Mangin: *J. Magn. Magn. Mat*. **121** (1993) 213

[ROD93b] B. Rodmacq, G. Palumbo, Ph. Gerard: J. Magn. Magn. Mat. **118** (1993) L11

[ROTH06] S. V. Roth, R. Döhrmann, M. Dommach, M. Kuhlmann, I. Kröger, R. Gehrke, H. Walter, C. Schroer, B. Lengeler, P. Müller-Buschbaum: *Rev. Sci. Instr*. **77** (2006) 085106

[RUG] S. T. Ruggiero, M. R. Beasley: In*: Synthetic Modulated Structures*, L. L. Chang, B. C. Giessen (Eds.), (Academic Press, 1985), p. 365

[SAK99] K. Sakano, M. Yamamoto: *SPIE Proceedings* **3767** (1999) 238

[SAL96] T. Salditt, T. Lott, T.H. Metzger, J. Peisl, G. Vignaud, P. Høghøj, O. Schärpf, R. Hinze, R. Lauer: *Phys. Rev. B* **54** (1996) 5860

[SAL97] N.N. Salashenko, E.A. Shamov: *Optics Comm.* **134** (1997) 7

[SAN02] J. Santamaria, M.-E. Gomez, M.-C. Cyrille, C. Leighton, C. Kannan, M. Krishnan, I. K. Schuller: *Phys. Rev. B* **65** (2002) 012412

[SAT55] S. Sato, H. Maezawa, M. Yanagihara, E. Eshiguro, S. Matsuo: *Opt. Engn*. **34** (1955) 377

[SAT94] H. Sato, T. Matsudai, W. Abdul-Razzaq, C. Fierz, P. A. Schroeder: *J. Phys.: Cond. Mat.* **6** (1994) 6151

[SAV92] D.E. Savage, N. Schimke, Y.H. Phang, M.G. Lagally: *J. Appl. Phys.* **71** (1992) 3283

[SCH95] A.R. Schlatmann, J.D. Shindler, J. Verhoeven: *Phys. Rev. B* **51** (1995) 5345

[SCH96] A.R. Schlatmann, J.D. Shindler, J. Verhoeven: *Phys. Rev. B* **54** (1996) 10880

[SCH00a] F. Schäfers: *Physica* B **283** (2000) 119

[SCH00b] B. D. Schrag, A. Anguelouch, S. Ingvarsson, G. Xiao, Y. Lu, P. L. Trouilloud,A. Gupta, R. A. Wanner, W. J. Gallagher, P. M. Rice, S. S. P.Parkin: *Appl. Phys. Lett.* **77** (2000) 2373

[SCH05] E. Schubert, F. Frost, B. Ziberi, G. Wagner, H. Neumann, B. J. Raschenbach: *J. Vac. Sci. Technol. B* **23** (2005) 959

[SCHA94] R. Schad, C. D. Potter, P. Beliën, G. Verbanck, V. V. Moshchalkov, Y. Bruynseraede: *Appl. Phys.Lett.* **64** (1994) 3500

[SCHA95] R. Schad, C. D. Potter, P. Beliën, G. Verbanck, J. Dekoster, G. Langouche, V. V. Moshchalkov, Y. Bruynseraede: *J. Magn. Magn. Mat.* **148** (1995) 331

[SCHA98a] F. Schaefers, H.Ch. Mertins, F. Schmolla, I. Packe, N.N. Salashenko, E.A. Shamov: *Appl. Opt*. **37** (1998) 719

[SCHA98b] R. Schad, P. Belién, G. Verbanck, C.D. Potter, H. Fischer, Lefebvre, M. Bessière, V.V. Moshchalkov, Y. Bruynseraede: *Phys. Rev. B* **57** (1998) 13692

[SCHA99] R. Schad, P. Belien, G. Verbanck, V. V. Moschalkov, Y. Bruynsraede, H. E. Fischer, S. Lefebvre, M. Bessiere: *Phys. Rev. B* **59** (1999) 1242

[SCHA00] F. Schäfers , *Physica B* **283** (2000) 119

[SCHL94] R. Schlatmann, C.Lu, J. Verhoeven, E.J. Puik, M.J.van der Wiel: *Appl. Surf. Sci.* **78** (1994) 147

[SCHL95] A. R. Schlatmann, J. D. Schindler, J. Verhoeven: *Phys. Rev*. B **51** (1995) 5345

[SCHM] G. Schmid: *Nanoparticles: From Theory to Application*, (Wiley, Weinheim, 2004)

[SCHU05] E. Schubert, F. Frost, B. Ziberi, G. Wagner, H. Neumann, B. Raschenbach: *J. Vac. Sci. Technol. B* **23** (2005) 959

[SCHW83] R. B. Schwarz, W. L. Johnson: *Phys. Rev. Lett*. **51** (1983) 415

[SEE93] J. F. Seely, G. E. Holland, J. V. Giasson:. *Appl. Optics* **32** (1993) 6294

[SEN97] R. Senderak, M. Jergel, S. Luby, E. Majkova, V. Holy, G. Haindl, F. Hamelmann, U. Kleineberg, U. Heinzmann: *J. Appl. Phys*. **81** (1997) 2229

[SHE92] F. Shelp, G. Tosim, M. Carata. M.N. Baibich, A.A. Gomez, J.E.Schmidt: *Appl. Phys. Lett*. **61** (1992) 1858

[SHE03] E. V. Shevchenko, D. V Talapin, H. Schnablegger, A. Kornowski, O. Festin, P. Svedlinh, M. Haase, H. Weller: *J. Am. Chem. Soc*. **125** (2003) 9090

[SHI93] K. Shintaki, Y. Daitoh, T. Shinjo: *Phys. Rev. B* **17** (1993) 14584

[SHI03] M. Shiraishi, N. Kandaka, K. Murakami: *Proc. SPIE* **5037** (2003) 249

[SHM02] L. Shmuylovich, A. Q. Shen, H. A. Stone: *Langmuir* **18** (2002) 3441

[SIF07a] P. Siffalovic, L. Chitu, Y. Halahovets, M. Jergel, R. Senderak, E. Majkova, S. Luby: *J. Appl. Phys*. **101** (2007) 033538-1

[SIF07b] P. Siffalovic, E. Majkova, L. Chitu, M. Jergel, S. Luby, A. Satka, S. V. Roth: *Phys. Rev. B* **76** (2007) 195432-1

[SIN88] S.K. Sinha, E.B. Sirota, S. Garoff, H.B. Stanley: *Phys. Rev.* **B 38** (1988) 2297

[SIN95] S.K. Sinha: *MRS Symposium Proc.* **376** (1995) 175

[SIN02] R. Sinclair, T. Itoh, R. Chin: *Microscopy and Microanalysis* **8** (2002) 288

[SKU95] K.M.Skulina, C.S.Alford, R.M.Bionta, D.M.Makowiecki, E.M. Gullikson, R. Soufli, J.B. Kortright, J. H. Underwood: *Appl. Optics*, **34** (1995) 3727

[SLA94] J. M. Slaughter, D. W. Schulze, C. R. Hills, A. Mirone, R. Stalio, R. N. Watts, C. Tarrio, T. B. Lucatorto, M. Krumrey, P. Mueller, C. M. Falco: *J. Appl. Phys*. **76** (1994) 2144

[SLO96] J. Slonczewski: *J. Magn. Magn. Mater.* **159** (1996) 1

[SNY99] R.L. Snyder, J. Fiala, H.J. Bunge: *Defect and Microstructure Analysis by Diffraction*, (Oxford Univ. Press Inc.; New York, 1999), p. 1

[SPA99] M. Spasova, E. Majkova, M. Jergel, R. Senderak, S. Luby, E. D'Anna, A. Luches, M. Martino, E. N. Zubarev, M. Brunel: *J. Magn. Magn. Mater*. **198-199** (1999) 43

[SPA01] U. Wiedwald, M. Spasova, M. Farle, M. Hilgendorff, M. Giersig: *J. Vac. Technol. A* **19** (2001) 1773

[SPA02] M. Spasova, U. Wiedwald, R. Ramchal, M. Farle, M. Hilgendorff, M. Giersig: *J. Magn. Magn. Mater.* **240** (2002) 40

[SPI72] E. Spiller: *Appl. Phys. Lett.* **20** (1972) 365

[SPI74] E. Spiller: *Space Optics, Proc. 9$^{\text{th}}$ ICO, Santa Monica, 1972, (National Academy of Science, Washinton D.C., 1974) p.581*

[SPI80] E. Spiller, J. Segnmüller, J. Rife, R.P. Haelbich: *Appl. Phys. Lett*. **37** (1980) 1048

[SPI81] E. Spiller: *AIP Conf. Proc.* No.75, Low Energy X-ray Diagnostics, (1981) 124

[SPI88] E. Spiller: *Multilayer Optics for X-rays*, in *Physics, Fabrication, and Applications of Multilayered Structures*, in NATO ASI Series B: Physics, vol. **182** (1988); P. Dhez, C. Weisbuch eds.,: p. 271

[SPI93] E. Spiller, D.G. Stearns, M. Krumrey: *J. Appl. Phys.* **74** (1993) 107

[SPI] E. Spiller: *Soft X-Ray Optics*, (SPIE Opt. Engn. Press; Bellingham, 1994), p. 1

[STA99] J. Stangl, V. Holy, P. Mikulik, G. Bauer, I. Kegel, T. H. Metzger, O. G. Schmidt, C. Lange, K. Eberl: *Appl. Phys. Lett.* **74** (1999) 3785

[STA00] J. Stangl, V. Holy, T. Roch, A. Daniel, G. Bauer, J. Zhu, K. Brunner, G. Abstreiter: *Phys. Rev B*. **62** (2000) 7229

[STE89] D.G. Stearns: *J. Appl. Phys.* **65** (1989) 491

[STE90] D.G. Stearns, M.B. Stearns, Y. Cheng, J.H. Smith, N.M. Ceglio: *J. Appl. Phys.* **67** (1990) 2415

[STE91] D. G. Stearns, R. S. Rosen, S. P. Vernon: *Proc. SPIE* **1457** (1991) 2

[STE92] M.B. Stearns, C.H. Chang, D.G. Stearns: *J. Appl. Phys.* **71** (1992) 187

[STE98] D.G. Stearns, D.P. Gaines, D.W. Sweeney, E.M. Gullikson: *J. Appl. Phys.* **84** (1998) 1003

[STO] J. Stohr, H. C. Siegmann: *Magnetism: From Fundamentals to Nanoscale Dynamics*, (Springer Series in Solid State Science, Springer Berlin Heidelberg New York, 2006), ISBN – 10-3-540-30282-4

[STO93] H.J. Stock, U. Kleineberg, A. Kloidt, B. Schmiedeskamp, U. Heinzmann, M. Krumrey, P. Müller, F. Scholz : *Appl. Phys. Letters* **63** (1993) 2207

[SU03] M.-H. Su, C.-C. Hwang, J.-G. Chang, S.-H. Wang: *J. Appl. Phys.* **93** (2003) 4566

[SUN04] Sh. Sun, H. Zeng, D. B. Robinson, S. Raoux, Ph. M. Rice, Sh. X. Wang, G. Li: *J. Am. Chem. Soc*. **126** (2004) 273

[SWA94] P.P. Swadding, D.F. McMorrow, B.A. Cowley, R.C.C. Ward, M.R. Wells: *Phys. Rev. Letters*, **73** (1994) 2232

[SWI03] P. Swift, D.M. Solina, R.W. Cheary, G.M. McCredie: *Thin Solid Films* **440**, (2003) 117

[SZE] S. M. Sze, *VLSI Technology*; (McGraw-Hill Int. Ed.; New York, 1988), p 393

[TAK93] R. Takatani, T. Dei, Y. Sugita: *J. Appl. Phys.* **73** (1993) 6375

[TAK96] H. Takenaka, T. J. Kawamura : *Electron Spectr. Relat. Phenom.* **80** (1996) 381

[TAK01] H. Takenaka, H. Ito, K. Nagai, Y. Marumatsu, E. Gullikson, R.C. Perera: *Nucl. Instr. & Meth. A* **467-468** (2001) 341

[TEG01] S. Tegen, I. Mönch, J. Schumann, H. Vinzelberg, C. M. Schneider: *J.Appl. Phys.* **89** (2001) 8169

[THI63] E. Thiele, *J. Chem. Phys.* **39** (1963) 474

[THO57] W. Thomson: *Proc. R. Soc. London A* **8** (1857) 546

[TOM] H. G. Tompkins, E. A. Irene: *Handbook of Ellipsometry*, (Springer, Heidelberg, 2005)

[TSA86] T. Tsakalakos: *J. Vac. Sci. Technol.* **B 4** (1986) 144

[TSU03] T. Tsuru, T. Tsutou. T. Hatano, M.Yamamoto: In T. Warwick, J. Arthur, H. A. Padmore, J. Stöhr (Eds.): *Proc. 8th International Conference on Synchrotron Radiation Instrumentation*, (San Francisco, AIP, 2004), p. 732

[TSU04] T. Tsuru, T. Tsutou, M. Yamamoto: *Thin Solid Films* **455-456** (2004) 705

[TSU05] T. Tsuru, T. Tsutou, T. Hatano, M. Yamamoto: *J. Electron Spectrosc. Relat. Phenom*. **144-147** (2005) 1083

[TSU06] T. Tsuru, M. Yamamoto: *Thin Solid Films* **515** (2006) 947

[TSU08] T. Tsuru, M. Yamamoto: *Phys. Stat. Sol.* (2008) in print

[TSY01] E. Tsymbal, D. G. Pettifor: *Solid State Physics* **56** (2001) 113

[ULM00] M. Ulmeanu, A. Serghei, I.N. Mihailescu, P. Budau, M. Enachescu: *Appl Surf Sc*i **165** (2000) 109

[ULY00] A. Ulyanenkov, R. Matsuo, K. Omote, K. Inaba, J. Harada, M. Ishino, M. Nishii, O. Yoda: *J. Appl. Phys.* **87** (2000) 7255

[UND81] J.H. Underwood, T.W. Barbee Jr.: *AIP Conf. Proc.* **75** (1981) 170

[URB94] F. K. Urban III, J. C. Comfort: *Thin Solid Films* **253** (1994) 262

[VIE97] A. D. C. Viegas, J. Geshev, L. F. Shelp, J. E. Schmidt: *J. Appl. Phys.* **82** (1997) 7058; J. D. Jarrat, J. A. Barnard: *J. Appl. Phys.* **79** (1996) 5606; E. A. M. van Alphen, W. M. J. de Jonge, *Phys. Rev. B* **51** (1995) 8182; M. Iijima, Y. Shimizu, N. Kojima, A. Tanaka, K. Kobayashi: *J. Appl. Phys.* **79** (1996) 5602

[VOL92] C. Volkert, A. Polman: *Mat. Res. Soc. Symp. Proc.* **235** (1992) 3

[VOO97] H.J. Voorma, E. Louis, F. Bijkerk, F.S. Abdali: *J. Appl. Phys*. **82** (1997) 1876

[WAN94] W.K. Wang, W.H. Wang, H.Y. Bai: *Materials Sci. Engn. A* **179 – 180** (1994) 234

[WAN99] W.H. Wang, H.Y. Bai, M. Zhang, J.H. Zhao, X.Y. Zhang, W.K. Wang: *Phys. Rev.* **B 59** (1999) 10811

[WAN00] J-Q Wang, L. M. Malkinski, Y. Hao, C. A. Ross, J. A. Wiemann, Ch. J. O'Connor: *Materials Science and Engineering B* **76** (2000) 1

[WIE03] A. Wiedenmann, A. Hoell, M. Kammel, P. Boesecke: *Phys. Rev. E* **68** (2003) 031203

[WIL54] G. K. Williamson, W. M. Hall: *Acta Metall*. **1** (1954) 22

[WIN99] D.L. Windt: *Appl. Phys. Letters* **74** (1999) 2890

[WIN00] D.L. Windt, F.E. Christensen, W.W. Craig, C. Hailey, F.A. Harrison, M. Jimenez-Garate, R. Kalyanraman, P.H.J. Mao: *J. Appl. Phys.* **88** (2000) 460

[WIR99] S. Wirth, S. von Molnar, M. Field, D.D. Awschalom: *J. Appl. Phys.* **8** (1999) 5249

[WOL01] S. A. Wolf, D. D. Awschalom, R. A. Buhrman, J. M. Daughton, S. von Molnar, M. L. Roukes, A. Y. Chtchelkanova, D. M. Treger: *Science* **294** (2001) 1488; M. Ziese, M. J. Thornton: *Spin Electronics*, Springer (2001); I. Žuti J. Fabian, S. Das Sarma: *Rev. Mod. Phys.* **76** (2004) 323

[XLIN01] X. M. Lin, H. M. Jaeger, C. M. Sorensen, K. J. Klabunde: *J. Phys. Chem*. **B 105** (2001) 3353

[XU04] W. Xu, L. E. De Long, T. Charlton, M. Chisholm, D. Lederman: Appl. Phys. Lett. **85** (2004) 408

[XU07] W. Xu, L. E. De Long, T. Charlton, M. Chisholm, D. Lederman: *J. Appl. Phys.* **101** (2007) 103920

[YAM80] M. Yamamoto, O. S. Heavens: *Surf. Sci*. **96** (1980) 202

[YAM89] M. Yamamoto, J. Cao, T. Namioka: *Proc. Soc. Photo-Opt. Instr. Eng*. **1140** (1989) 448

[YAM92] M. Yamamoto, T. Namioka: *Appl. Opt.* **31** (1992) 1612

[YAM93] M. Yamamoto: *Proc. SPIE* **2010** (1993) 152

[YAM99a] M. Yamamoto, H. Nomura, M. Yanagihara, M. Furudate, M. Watanabe: *J. Electr. Spectr. Rel. Phenom.* **101-103** (1999) 869

[YAM99b] M. Yamamoto, K. Sakano, Y. Hotta: *Inst. Phys. Conf. Ser.* (1999) No. 159, p. 601

[YAM01] M. Yamamoto: *Nucl. Instrum. Methods A*, **467-8** (2001) 1282

[YAM03] M. Yamamoto, Y. Hotta, M. Sato: *Thin Solid Films* **433** (2003) 224

[YAM_1] http://www.tagen.tohoku.ac.jp/labo/m_yamamoto/bodyJava.htm

[YAMK92] K. Yamashita, M. Watanabe, O. Matsudo, J. Yamazaki, I. Hatsukade, T. Ishigami, S. Takahama, K. Tamura, M. Ohtani: *Rev. Sci. Instr.* **63** (1992) 1217

[YAN96] M. Yanagihara, T. Sasaki, M. Furudate, M. Yamamoto: *Optical Review* **3** (1996) 65

[YAN97] K. H. Yanagihara, K. Pettit, M. B. Salamon, E. Kita, S. S. P. Parkin: *J. Appl. Phys.* **81** (1997) 5197

[YIA06] S. G. Yiantsios, B. G. Higgins: *Phys. Fluids* **18** (2006) 082103

[YUL03] Yulin, S.: *Optical Interference Coatings*; N. Keiser, H. Pulker (Eds.).; (Springer Series in Photonics, 2003)

[YUL05] S.A. Yulin, N. Benoit, T. Feigl, N. Kaiser: *Proc. SPIE* **5645** (2005) 289

[YTR00] F.M.Ytreberg, S.R. McKay: *Phys.Rev. E* **61** (2000) 4107

[ZAH98] P. Zahn, J. Binder, I. Mertig, R. Zeller, P. H. Dederichs: *Phys. Rev. Lett.* **80** (1998) 4309

[ZAM02] A. Zambano, K. Eid, R. Loloee, W. P. Pratt, J. Bass: *J. Magn. Magn.Mater.* **253** (2002) 51

[ZHA92] S. Zhang, P. M. Levy, A. Fert: *Phys. Rev. B* **45** (1992) 8689; S. Zhang, P. M. Levy: *Phys. Rev. Lett.* **77** (1996) 916

[ZHA04] A. M. Zhang, X. S. Wu, L. Sun, W. T. Sheng, B. You, J. Du, M. Lu, A. Hu, S. S. Jiang: *J. Appl. Phys.* **95** (2004) 7294

[ZIE92] E. Ziegler, G. Marot, A.K. Freund, S. Joksch, H. Kawata, L.E. Berman, M. Jarocci: *Rev. Sci. Instr.* **63** (1992) 496

[ZSI] R. Zsigmondy: *Colloids and the Ultramicroscope*, (English Edition), (Wiley, New York, 1909)